AN ABSTRACT OF THE THESIS OF

Robin Robertson for the degree of Doctor of Philosophy in Oceanography presented on February 18, 1999.

Title: Mixing and Heat Transport Mechanisms in the Upper Ocean in the Weddell Sea

Redacted for privacy

Abstract approved: _____

Laurie Padman

Vertical heat transport mechanisms in the Weddell Sea were investigated with the long-term objective of evaluating their roles in the upper ocean heat flux. The mechanisms explored include double-diffusion, shear instabilities, surface mixing, and the influence of tides. This evaluation was comprised of three separate efforts; 1) an analysis of observational data in the western Weddell Sea, 2) a barotropic tidal model for the entire Weddell Sea, and 3) a primitive equation model to simulate internal tide generation for transects in the southern Weddell Sea.

Temperature, conductivity, current shear, and velocity data were obtained from a drifting ice station in the western Weddell Sea during February-June 1992. From this data, the diapycnal heat flux through the permanent pycnocline was estimated to be about 3 W m^{-2} and to be predominantly attributable to double-diffusive convection. The estimated mean rate of heat transfer from the mixed layer to the ice was 1.7 W m^{-2}, although heat fluxes of up to 15 W m^{-2} occurred during storms.

The 1992 data along with other observations suggested that mixing rates in the pycnocline might be related to local tidal effects. A high-resolution barotropic tidal model was used to predict tidal elevations and currents in the Weddell Sea, including under the Filchner-Ronne Ice Shelf. Tides were found to influence the mean flow by modifying the effective bottom drag. Additionally, a parameterization of internal tide generation from interactions of the barotropic tide with topography suggested that internal tides are generated at the continental shelf break in the southern Weddell Sea.

In order to further investigate the internal tides, an attempt was made to utilize the Princeton Ocean Model (POM) to investigate M_2 internal tide generation at the

continental shelf/slope break in the southern Weddell Sea using the barotropic model to provide boundary conditions. A two-dimensional transect application of POM was used for this study. Although POM does give some indication of internal tide generation over the upper continental slope, POM in its present form proved to be unsuitable for simulating the internal tides in the southern Weddell Sea. Its unsuitability stemmed from systematic errors associated with the baroclinic pressure gradient term.

Mixing and Heat Transport Mechanisms in the Upper Ocean in the Weddell Sea

by

Robin Robertson

A THESIS

submitted to

Oregon State University

in partial fulfillment of
the requirements for the
degree of

Doctor of Philosophy

Presented February 18, 1999
Commencement June 1999

Doctor of Philosophy thesis of Robin Robertson presented on February 18, 1999

APPROVED:

Redacted for privacy

Major Professor, representing Oceanography

Redacted for privacy

Dean of the College of Oceanic and Atmospheric Sciences

Redacted for privacy

Dean of the Graduate School

I understand that my thesis will become part of the permanent collection of Oregon State University libraries. My signature below authorizes release of my thesis to any reader upon request.

Redacted for privacy

Robin Robertson, Author

ACKNOWLEDGEMENTS

First and foremost I would like to thank my advisor, Laurie Padman, for technical, financial, and moral support and additionally for taking me to the Antarctic during the austral winter 1994. (The latter was better than it sounds.) He did a superb job of advising me and made my experience here both enjoyable and productive. I also appreciate the advice and support provided by Murray Levine, particularly with respect to internal waves and tides and his contributions as a co-author. I would also like to thank my other co-author, Gary Egbert, for providing both the barotropic tidal model and advice on its use. Other COAS professors, including Andrew Bennett, John Allen, Ricardo Matano, and Bob Miller, were an invaluable resource for useful advice on numerical modeling.

I would like to thank my friends, Liz Brown, Sara Harris, Julie Arrington, Diana Greenslade, Sabine Lamprecht, Matt Zacate, Peter Langner, and Melanie and Patrick Volz for providing moral support and keeping me sane and my climbing partners, Tina Kienzle, Suzanne Remillard, Lothar Schindele, Pete Hower, Gent Mende, and Günter Schneider for keeping me more balanced both on the rocks and in my life.

The study for chapter two was supported by NSF, contracts DPP-9024695 and OPP-9317319. CTD data were kindly provided by Arnold Gordon and current meter data were provided by Robin Muench. I also thank Robin Muench, Miles McPhee, Dan Kelley, Vicki Lytle, Steve Ackley, and an anonymous reviewer for their critical comments on the draft manuscript for this chapter.

The work for chapter three was funded by grants DPP-9024695 and OPP-9317319 from the National Science Foundation. I am grateful to Ed Zaron for his assistance with the barotropic tidal model and to Mark Abbott for providing the CM-5 Connection Machine computing resources. Eberhard Fahrbach and Keith Nicholls provided tidal analyses for their recent-acquired current meter data. I would also like to acknowledge the assistance of Robin Muench, Michael Smithson, and Christoph Kottmeier. Ole Andersen and three anonymous reviewers provided valuable comments on the original manuscript for chapter three.

For chapter four, I am grateful to Andrew Bennett, John Allen, Ricardo Matano, and Jorge Mesias for their assistance with POM. Peter Holloway's paper on internal tides was of invaluable help. The work for chapter four was funded by grants OPP-9317321 and OPP-9615524 from the Office of Polar Programs, National Science Foundation.

CONTRIBUTION OF AUTHORS

For chapter two, Dr. Murray Levine provided insight on the effects of shear instabilities and on how to estimate their heat flux contribution. For the tidal model in chapter three, Dr. Gary Egbert provided the original tidal model and advice on how to operate the model. He also helped with the energy flux estimations. For the model of internal tides for chapter four, Dr. Murray Levine provided advice on the behavior of internal waves and tides.

TABLE OF CONTENTS

TABLE OF CONTENTS (continued)

LIST OF FIGURES

LIST OF FIGURES (continued)

LIST OF FIGURES (continued)

LIST OF FIGURES (continued)

LIST OF FIGURES (continued)

LIST OF TABLES

"A long rock climb is a series of problems, each one different from the rest, which have to be solved by ingenuity of mind and versatility of body." John Buchan

My Ph.D. seemed to be similar to a long, long rock climb, only a versatility of numerical techniques and of mind was used instead of the versatility of the body.

Mixing and Heat transport Mechanisms in the Upper Ocean in the Weddell Sea

1: GENERAL INTRODUCTION

The Weddell Sea affects global climate and the global circulation both through Antarctic Bottom Water (AABW) formation and through heat exchange with the atmosphere [*Broecker et al.*, 1998]. The Weddell Sea is the primary location (80-90 %) for deep and bottom water formation, including AABW, for the Southern Ocean [*Weppernig et al.*, 1996]. The ocean heat exchange with the atmosphere is controlled by the thickness and concentration of the ice cover and by upward flux of heat from the warm subsurface water to the ocean surface. The ice cover acts as an insulator and drastically reduces the heat flux between the ocean and the atmosphere when it is present. Its thickness depends on both the atmospheric and ocean temperatures near the interface. The mechanisms that can transport heat through the upper ocean or can cause mixing resulting in AABW formation are the focus of this thesis.

The major water masses for the Weddell Sea are shown schematically in Figure 1.1, with their temperature and salinity specifications given in Table 1.1. Throughout most of the Weddell Sea, a layer of Warm Deep Water (WDW) is found below the fresher, colder surface layers. This WDW layer originates from North Atlantic Deep Water (NADW) which is upwelled near the Antarctic Front and is transported through the Weddell Sea by the Weddell Gyre. A weak permanent pycnocline lies along the upper edge of this layer and inhibits heat transport from the WDW to the surface layers [*Weppernig et al.*, 1996]. Nevertheless, sufficient heat is transported from the WDW to form a transition layer, Modified Warm Deep Water (MWDW). In winter, the surface layer generally has a temperature near freezing for its salinity and is quite thick, roughly 100 m. This water mass is designated Winter Water (WW). In summer, a seasonal pycnocline develops, separating a shallow, fresher surface mixed layer (SML) from the remnant WW layer. Over the shelf, salt rejection due to ice formation results in cold, salty water denoted as High Salinity Shelf Water (HSSW) or Western Shelf Water (WSW) in the western Weddell Sea. Under the ice shelves, melting and heat loss to the ice along with the lower

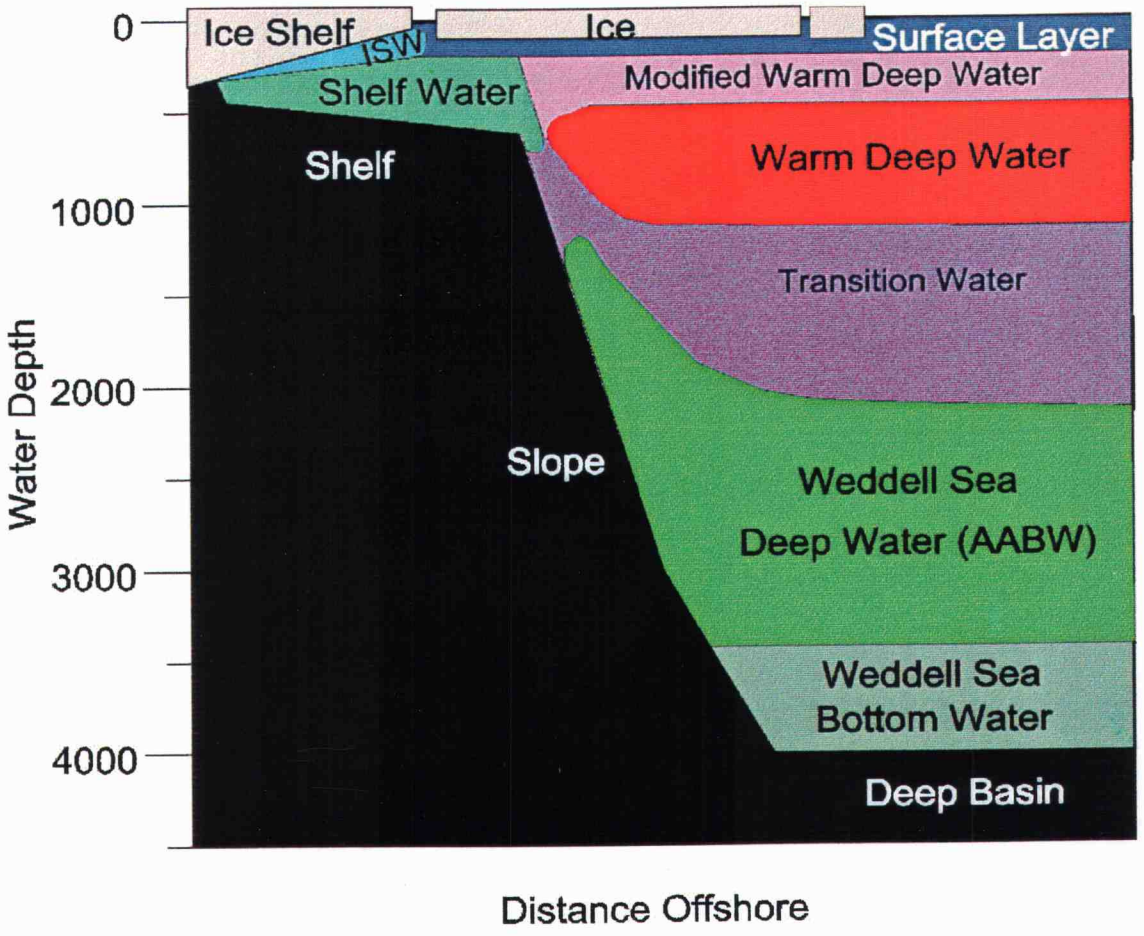

Figure 1.1 Idealized hydrography for the Weddell Sea. The major water types from the bottom to surface are Weddell Sea Bottom Water (WSBW), Weddell Sea Deep Water (WSDW), which is a subclass of Antarctic Bottom Water (AABW), Warm Deep Water (WDW), Modified Warm Deep Water (MWDW), Shelf Water (SW), and Ice Shelf Water (ISW). The surface layer is also shown and represents both the surface mixed layer (SML) and Winter Water (WW) during summer conditions.

freezing temperature due to increased pressure, result in an extremely cold, fresher water mass type known as Ice Shelf Water (ISW). Mixing of WDW with either WSW or ISW can result in the formation of the denser Weddell Sea Bottom Water (WSBW) and/or Weddell Sea Deep Water (WSDW), the latter being a subclass of AABW [*Gordon*, 1998]. These combinations may also include various amounts of the surface waters, SML, WW, and/or MWDW.

Water Mass	Potential Temperature Range (°C)	Salinity Range (psu)
Winter Water (WW)	-1.88* to -1.7	34.25 to 34.52
High Salinity Shelf Water (HSSW)	-1.88* to -1.7	34.56 to 34.84
Ice Shelf Water (ISW)	< -1.9	34.2 to 34.7
Modified Warm Deep Water (MWDW)	-0.7 to -1.7	34.4 to 34.6
Warm Deep Water (WDW)	0.0 to 1.0	34.6 to 34.75
Weddell Sea Deep Water (WSDW)	-0.8 to 0.0	34.62 to 34.68
Weddell Sea Bottom Water (WSBW)	-1.3 to -0.8	34.62 to 34.68

*-1.88 or surface freezing temperature for the salinity present

Table 1.1 Potential temperature and salinity ranges for Weddell Sea water masses, adapted from *Weppernig et al.* [1996] following definitions by *Carmack and Foster* [1976].

Significant progress has been made in defining the circulation, and heat and freshwater budgets for the Weddell Sea using classical hydrographic techniques augmented by tracer studies [for example, see *Orsi et al.*, 1993; *Gouretski and Danilov*, 1993; *Farhbach et al.*, 1994; *Muench and Gordon*, 1995; *Weppernig et al.*, 1996]. However, ultimately mixing and water mass conversion occur on the very small scales where molecular processes become important (O(1cm)). Additionally, several intermediate-scale processes determine the coupling between the large and small scales. At present most of these processes are crudely parameterized in basin- and global scale models. Such models can be tuned to match present observations, but only an improved understanding of these processes can lead to predictive models that can continue to be reliable under a changing large-scale environment. In this thesis, I concentrate on the small and intermediate-scale processes.

The three questions that I have attempted to address are:

1) *What mechanisms are capable of transporting heat from the WDW across the permanent pycnocline and through the upper water column?*

2) *How much heat do these mechanisms transport?*

3) *What mechanisms are capable of inducing mixing leading to AABW formation?*

Mechanisms capable of transporting heat across the permanent pycnocline or mixing the different water masses to form AABW include:

- Surface mixing from wind
- Large-scale convection
- Double-diffusion
- Cabbeling
- Shear instabilities resulting from internal waves
- Upwelling mechanisms
- Intrusions
- Eddies
- Tidal effects including
    - Generation of internal waves
    - Deformation of the ice pack
    - Facilitation of mixing near the continental shelf/slope break
    - Injection of warmer water into the ISW production cycle
    - Increasing benthic and under-ice stresses

Investigation of all of these mechanisms is beyond the scope of this study. Consequently, I focused on surface mixing from wind, double-diffusion, shear instabilities, and some of the tidal effects.

Mixing, heat transport, and circulation are affected by tides through several mechanisms. Large-scale tides interact with the continental shelves and other topographic features to generate smaller scale continental shelf waves and internal tides and waves. By setting up the conditions for shear or advective instabilities, internal tides and waves can increase mixing through the permanent pycnocline, thereby increasing the heat flux. Tidal current interactions with topography can also induce "rectified mean flows". Tides also have the potential to retard the mean circulation by increasing the effective benthic stress. If different water types are present near the bottom, increased benthic stress can also lead to higher benthic stirring, mixing, and heat transport. In polar regions, tidal shear and strain fracture the sea ice causing lead formation through periodic ice divergence. A higher lead percentage greatly increases the mean heat loss from the

ocean to the atmosphere, since the heat flux through leads is much higher than that through ice.

This thesis consists of three papers, two published and the third in preparation. The heat flux contributions from surface mixing from wind, double-diffusion, and shear instabilities as estimated from a drift camp in the western Weddell Sea are described in chapter 2. Chapter 3 discusses tidal effects determined using a two-dimensional barotropic tidal model. An attempt is then made to investigate the internal tides in the southern Weddell Sea using a three-dimensional primitive equation model (chapter 4). A general summary is provided in chapter 5.

Chapter 2

FINESTRUCTURE, MICROSTRUCTURE, AND VERTICAL MIXING PROCESSES IN THE UPPER OCEAN IN THE WESTERN WEDDELL SEA

Robin Robertson, Laurie Padman and Murray D. Levine

Published in *Journal of Geophysical Research*,
Vol. 100, 18,517-18,535, September 15, 1995.

2.1. Abstract

The upward flux of heat from the subsurface core of Warm Deep Water (WDW) to the perennially ice-covered sea surface over the continental slope in the western Weddell Sea is estimated using data obtained during February-June 1992 from a drifting ice station. Through the permanent pycnocline the diapycnal heat flux is estimated to be about 3 W m^{-2}, predominantly due to double-diffusive convection. There is no evidence that shear-driven mixing is important in the pycnocline. The estimated mean rate of heat transfer from the mixed layer to the ice is 1.7 W m^{-2}, although peak heat fluxes of up to 15 W m^{-2} are found during storms. It is hypothesized that isopycnal mixing along sloping intrusions also contributes to the loss of heat from the WDW in this region, however we are unable to quantify the fluxes associated with this process. Intrusions occur intermittently throughout this experiment but are most commonly found near the boundary of the warm-core current and the shelf-modified water to the east. These heat fluxes are significantly lower than the basin-averaged value of 19 Wm^{-2} [*Fahrbach et al.*, 1994] that is required to balance the heat budget of the Weddell Gyre. Other studies suggest that shelf processes to the west of the ice station drift track and more energetic double-diffusive convection in the mid-gyre to the east could account for the difference between our flux estimates for this region and those based on the basin-scale heat budget.

2.2. Introduction

The Weddell Sea is believed to be an important component of the ocean-atmosphere system and is a significant source region for Antarctic Bottom Water (AABW) [e.g., *Gordon et al.*, 1993a, b]. The circulation is dominated by the Weddell Gyre, the structure of which is described in detail by *Orsi et al.* [1993]. The Gyre is a clockwise circulation of about 30 Sv (1 Sv = 10^6 m^3s^{-1}) with most (~90%) of the transport being contained in a boundary current located within 500 km of the shelf break [*Fahrbach et al.*, 1994]. Water in the Gyre loses a significant amount of heat as it travels from the eastern Weddell Sea to the northern tip of the Antarctic Peninsula. *Fahrbach et al.* [1994] estimate that the oceanic heat loss is equivalent to a flux to the atmosphere of 19 Wm^{-2} when averaged over the entire Weddell Sea.

Several different mechanisms are responsible for the observed cooling. For example, *Muench et al.* [1990] found that double-diffusive fluxes in the central Gyre, away from boundaries, were comparable to the basin-scale average flux of 19 W m^{-2}. High fluxes might also occur over the broad, deep continental shelves in the southern and western Weddell Sea. Complex physical oceanographic interactions occurring on the shelves and near the shelf/slope front can contribute to the formation of AABW, including the extremely cold and dense Weddell Sea Bottom Water (WSBW) [e.g., *Carmack*, 1986; *Foster et al.*, 1987]. These processes include those due to nonlinearities in the equation of state, such as cabbeling [*Fofonoff*, 1956; *Foster*, 1972; *Foster and Carmack*, 1976a] and thermobaricity [see *Gill*, 1973]. This wide range of distinct but interacting processes implies that understanding the sensitivity of the Gyre circulation to perturbations in large-scale forcing requires first that the dominant physical processes in each region of the Weddell Sea be identified and understood.

Several physical oceanographic studies have been made in regions of the Weddell Sea where the ice cover either disappears in summer or is sufficiently thin to allow ship access. The western margin, however, is relatively inaccessible to ships because it is perennially covered with thick, second-year ice that has been advected into the region from the east. The problem of access is particularly acute in winter when the ice cover is most compact. Consequently, prior to 1992, most data in this region consisted of ice drift and ice concentration measurements obtained from satellite or aircraft-borne sensors and satellite-tracked ice-mounted buoys. Even basic features of the bathymetry, such as the location of the continental slope, were inferred primarily from satellite altimetry [*LaBrecque and Ghidella*, 1993]. To increase the data coverage, a manned camp, *Ice Station Weddell 1* (CISW), was established on the mobile pack ice near 52° W, 71.5° S in January 1992 by the Russian icebreaker *Akademik Federov*. A wide variety of oceanic, atmospheric, sea-ice, and biological data were collected as CISW drifted approximately northward over the central continental slope [*Gordon et al.*, 1993b]. The camp was recovered near 52° W, 66° S in early June (Figure 2.1). More recently (January 1993), the German research vessel Polarstern has obtained data from a cross-slope transect to the face of the Larsen Ice Shelf near 69°S [*Bathmann et al.*, 1994].

Our primary goals in this paper are to estimate the upward oceanic heat flux from the WDW to the surface in the western Weddell Sea and to identify the principal physical mechanisms responsible for this flux. Toward these goals, we summarize our observations of oceanic finestructure and microstructure at CISW and describe the processes responsible for this flux. The following section describes the data and section 2.4 gives an overview of the spatial and temporal variation of the upper ocean hydrography. Section 2.5 discusses the various processes responsible for vertical heat flux in the upper ocean. A discussion and summary are provided in section 2.6.

2.3. The Experiment

Ice Station Weddell 1 (CISW) was established in late January 1992 on a floe of multi-year ice located over the continental slope. CISW initially drifted southwest toward shallower water, then turned northward and traveled downslope to deeper water, after which it continued northward roughly following the 3000 m isobath (Figure 2.1). *Gordon et al.* [1993b] review CISW and its associated measurements.

We collected approximately 700 microstructure profiles using the Rapid-Sampling Vertical Profiler (RSVP) [*Caldwell et al.*, 1985; *Padman and Dillon*, 1987, 1991] between February 26 and May 27, 1992. These dates correspond to year-days 57 and 148. Throughout this paper, time t will be given in decimal day-of-year 1992 (UTC), where $t = 1.0$ is 0000 on January 1. Most profiles reached from the surface to a depth of about 350 m, which is within the permanent pycnocline. During intensive investigations of the seasonal pycnocline, however, shallower profiles were taken, typically to 100 m. The cycling time between profiles varied from about 15 minutes to days. Several profiles were obtained on most days (Figure 2.2a), with the exception of the ten-day data gap from $t = 115$ to 124.

The RSVP is a tethered, free-fall profiler about 1.3 m long. Sensors for measuring temperature (T), conductivity (C), pressure (P), and microscale velocity shear ($u_Z = \partial u/\partial z$ and $v_Z = \partial v/\partial z$) are located on the nose. Each data channel was sampled at 256 Hz. The fall rate was about 0.85 m s^{-1}; therefore, each profile to 350 m required about 7 minutes.

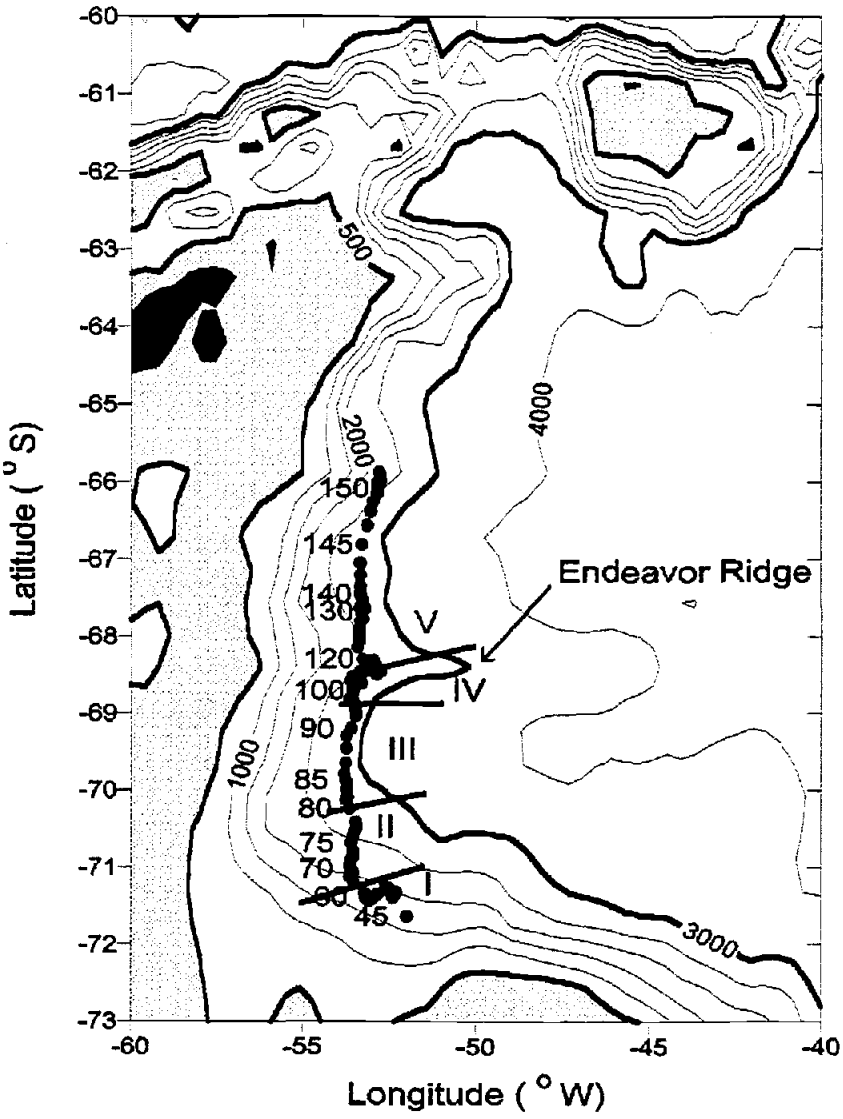

Figure 2.1. Drift track of Ice Station Weddell: daily positions indicated by dots. Depth contours are in meters, with depths less than 500 m being shaded. The 500 and 3000 m isobaths are shown bold. Time along drift track is in day of year. Roman numerals refer to the regimes defined in section 2.4.

Sensors to measure T and C were a Thermometrics FP07 thermistor and a Neil Brown Instruments Systems microconductivity cell, respectively. The conductivity required frequent recalibration, which was achieved by comparison with the closest (in time) CTD profiles obtained by Lamont Doherty Earth Observatory (LDEO). Least significant bit (*lsb*) resolutions of the raw 16-bit records are about 1.5×10^{-4} °C in T and 1.5×10^{-5} S m^{-1} for C. Typical *rms* noise levels based on measurements in non-turbulent mixed layers are comparable to the *lsb* resolution in T (2.1×10^{-4} °C) and an order of magnitude larger for

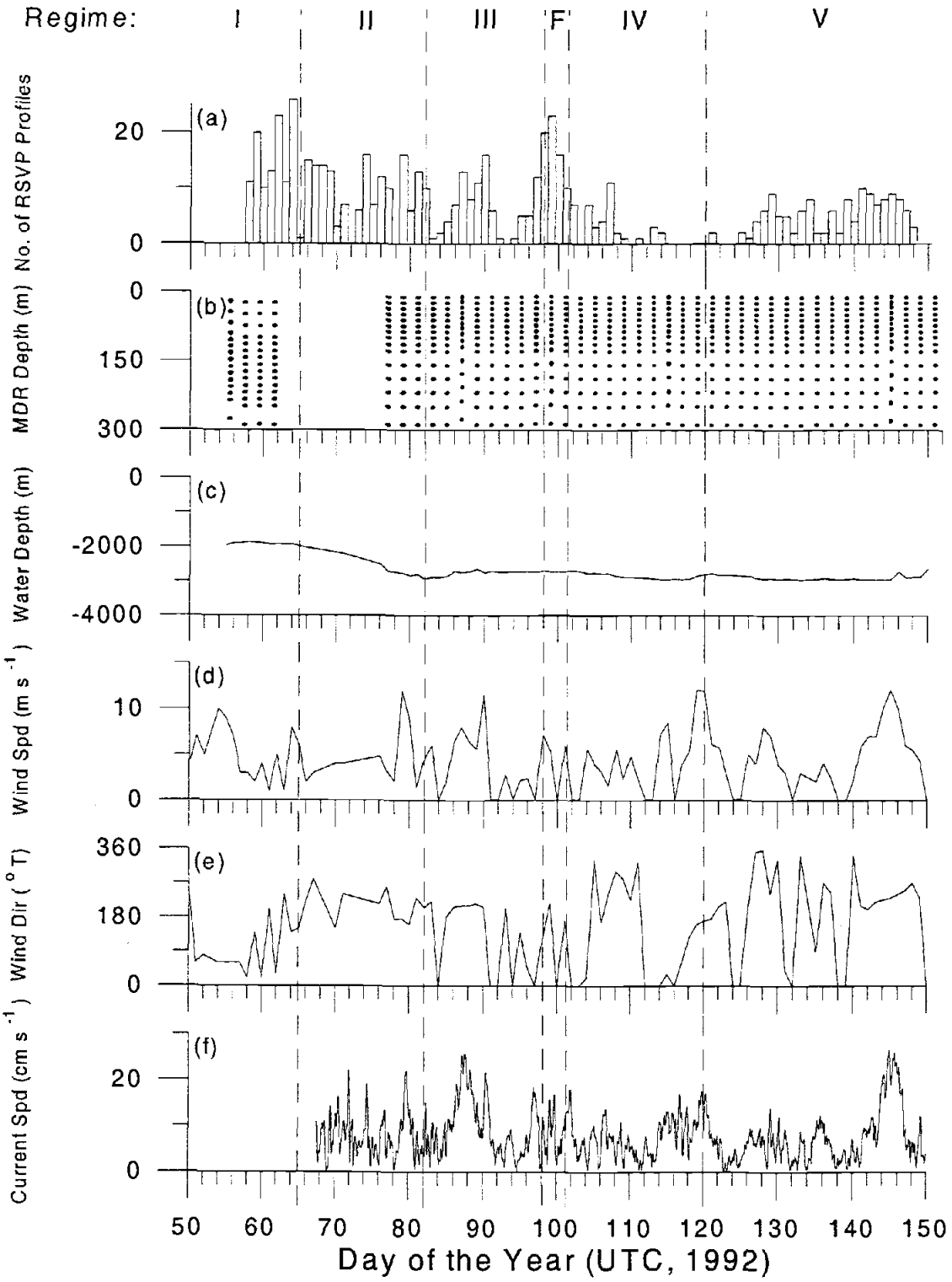

Figure 2.2. (a) Number of RSVP profiles per day, (b) MDR depths, every two days, (c) water depth (m), (d) wind speed (m s^{-1}), and (e) wind direction (°T) and (f) ice-relative current speed at 50 m (cm s^{-1}) at CISW.

C (1.1 x 10^{-4} S m^{-1}). For calculating salinity (S) and potential density (σ_θ), the mismatch between the time constants and locations of the T and C sensors was taken into account by lagging C by 0.075 m. The lag was determined by optimizing the correlation coefficient between temperature and conductivity gradients and minimizing salinity spiking. After incorporating the lag, T and C were averaged over 2 s (512 points) and used to generate values of S and σ_θ at approximately 1.7 m depth intervals. Temperatures were converted to potential temperature (θ) using S and measured P.

Two orthogonally-mounted airfoil shear sensors on the RSVP measured the velocity shear microstructure (u_Z and v_Z). The spatial resolution of these probes, approximately 0.03 m [*Osborn and Crawford*, 1980], can resolve most of the Kolmogorov shear spectrum [*Tennekes and Lumley*, 1992] for typical oceanic turbulence levels. The velocity shear spectra were integrated for wave numbers between 2.5 and 40 cycles per meter (cpm) to estimate the turbulent kinetic energy dissipation rate (ε) at approximately 1.7 m depth intervals (2 s of data). This dissipation rate is related to the microscale shear variance by

$$\varepsilon = 7.5\upsilon\left(\frac{\langle u_z^2\rangle + \langle v_z^2\rangle}{2}\right) \tag{2.1}$$

where υ is the kinematic viscosity of seawater, approximately 1.85 x 10^{-6} m^2 s^{-1} for these temperatures and salinities, and the angle brackets $\langle\ \rangle$ indicate vertical averaging. The factor 7.5 results from assuming that the velocity fluctuations are isotropic [*Tennekes and Lumley*, 1992]. This assumption is generally valid when ε is sufficiently large that the buoyancy or "Ozmidov" length scale $L_b = (\varepsilon/N^3)^{1/2}$ is much greater than the viscous or "Kolmogorov" scale, $L_k = (\upsilon^3/\varepsilon)^{1/4}$ [*Dillon*, 1984]. This condition can be written in terms of an "activity" index $A_T = \varepsilon/\upsilon N^2$: if A_T is greater than about 24 [*Stillinger et al.*, 1983], then a significant fraction of the total velocity shear variance will be found at spatial scales that are unaffected by buoyancy.

Prior to calculating ε, the velocity shear records were edited for obvious spikes resulting from anomalous fall speeds or encounters with biota. Additionally, shear values greater than 3 standard deviations from the mean shear for each 2-second interval were

excluded from the variance calculations, since the majority of these large shears were believed to be related to biota impacts or electronic noise. For ε above the noise floor of about 2×10^{-9} m^2 s^{-3}, this latter stage of editing made little difference to the estimates of ε.

To provide background information on thermal structure and internal gravity waves, an ice-mounted mooring consisting of fifteen miniature data recorders (MDRs) was deployed twice, with the positions of some sensors being changed between deployments. The mean depths of the MDRs over two day intervals are shown in Figure 2.2b for both deployments. A Yellow Springs Instruments model YSI40006 thermistor was installed in each MDR. The MDRs have a resolution of approximately 0.001° C and a long-term stability of 0.03° C. In the deepest MDR, a Veritron Corp. model 3000 pressure sensor was installed to monitor the mooring motion. This pressure sensor had a resolution of 0.5 psi (~0.3 m). The variations in the sensor depths near t = 87 and 145 in Figure 2.2b are due to mooring motion. The depths of sensors above the bottom MDR were interpolated using a mooring model forced by a depth-independent, ice-relative current. Temperature was recorded at two minute intervals by the upper fourteen MDRs, and both T and P at four minute intervals by the deepest MDR. Sensors were calibrated before and after the experiment.

Additional data collected at CISW by other investigators included CISW location, water depth, currents, CTD profiles, and meteorological and ice data [*Gordon et al.*, 1993b]. The drift track of the camp (Figure 2.1) is based on global positioning system (GPS) measurements after smoothing with the complex demodulation algorithm described by *McPhee* [1988]. A precision depth recorder and an acoustic pinger mounted on the LDEO CTD wire were used to determine water depths. To supplement water depth measurements at CISW, satellite and aircraft gravimetric data were used by *LaBrecque and Ghidella* [1993] to develop a bathymetric chart for the western Weddell Sea. Current velocities at CISW were measured at three depths under the ice, 25 m, 50 m, and 200 m (Figure 2.2f) [*Muench et al.*, 1993]. CTD profiles to the bottom were collected by LDEO roughly at 10 km intervals along the drift track, *i.e.* several times per week [*Gordon et al.*, 1993b; *Huber et al.*, 1994].

2.4. CISW Upper Ocean Hydrography

The hydrographic structure of the upper ocean helps determine the physical processes that can cause the vertical transport of heat and salt. We therefore first review the principal features of the upper ocean hydrography at CISW. For reference, a profile taken at $t = 76.018$ is shown (Figure 2.3). A thin, well-mixed surface layer that was present during the earlier portion of the experiment typically extended to a depth of 20-50 m and was bounded below by the seasonal pycnocline. Below the seasonal pycnocline, a weakly-stratified layer was found. This layer has potential temperatures (-1.9° to -1.5° C) and salinities (typically 34.3 to 34.6 psu), which are characteristic of the Winter Water layer described by *Foster and Carmack* [1976b] and *Muench et al.* [1990]. This layer is believed to be a remnant of the surface mixed layer from the previous winter. The lower portion of this layer has been, and continues to be, modified substantially by intrusions and vertical mixing. Intrusions like those in Figure 2.3a were typically found between 150 and 300 m depth throughout the experiment. They are clearly visible in θ-S diagrams (e.g. Figure 2.3b) as the kinks in the θ-S curve. Below this weakly stratified layer was the permanent pycnocline, which was roughly 300 m thick with a potential density change of about 0.08 kg m^{-3}. The maximum buoyancy frequency N in the permanent pycnocline was about 2 cycle per hour (cph). Within both the permanent pycnocline and the region of intrusions, double-diffusive steps were found.

Below the permanent pycnocline there was a core of relatively warm water with a potential temperature ranging from 0.4° to 0.6° C and a salinity of 34.68-34.70 psu. This water lies within the θ-S space denoted as Warm Deep Water (WDW) by *Foster and Carmack* [1976b]. The maximum potential temperature (θ_{max}) and salinity (S_{max}) values and their depths ($Z_{\theta max}$ and Z_{Smax}) (Figure 2.4) were determined from the CTD profiles collected by LDEO and kindly provided by A. Gordon. The value of θ_{max} generally decreased as the ice camp moved north [*Gordon et al.*, 1993a]. During the first few days of the camp, both the θ_{max} (~0.5° C) and the S_{max} (34.67-34.68) were lower than elsewhere along the drift path. Also during this period, both the permanent pycnocline and the $Z_{\theta max}$ were approximately 200 m deeper than during the remainder of the experiment. The

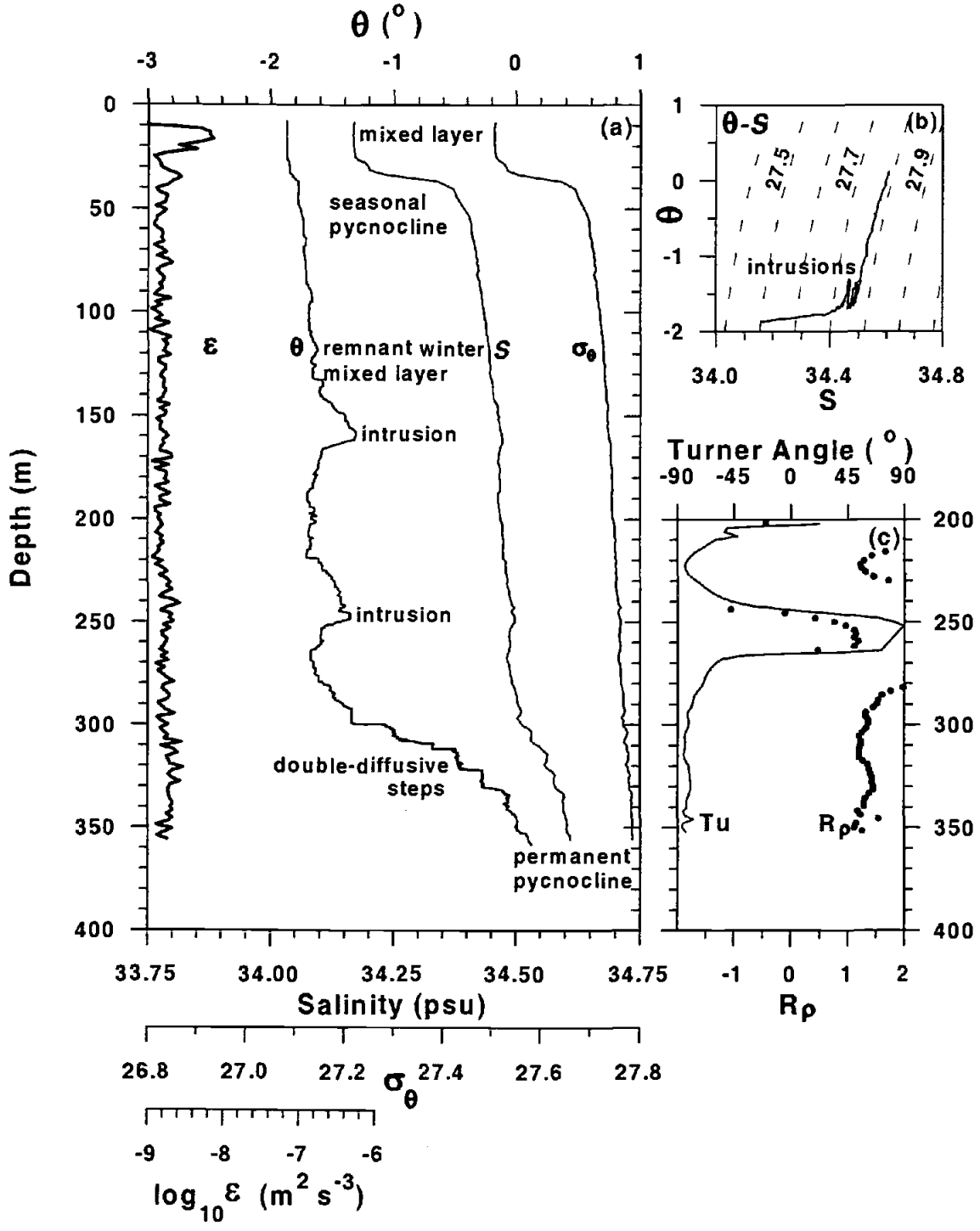

Figure 2.3. (a) Profiles of potential temperature θ (°C), salinity S (psu), potential density σ_θ, and the log of the dissipation rate ε ($m^2\ s^{-3}$) collected on t = 76.0184. (b) The θ-S diagram for this profile with constant density lines shown dotted; and (c) the density ratio R_ρ and Turner angle Tu (°) profiles for this drop are also shown.

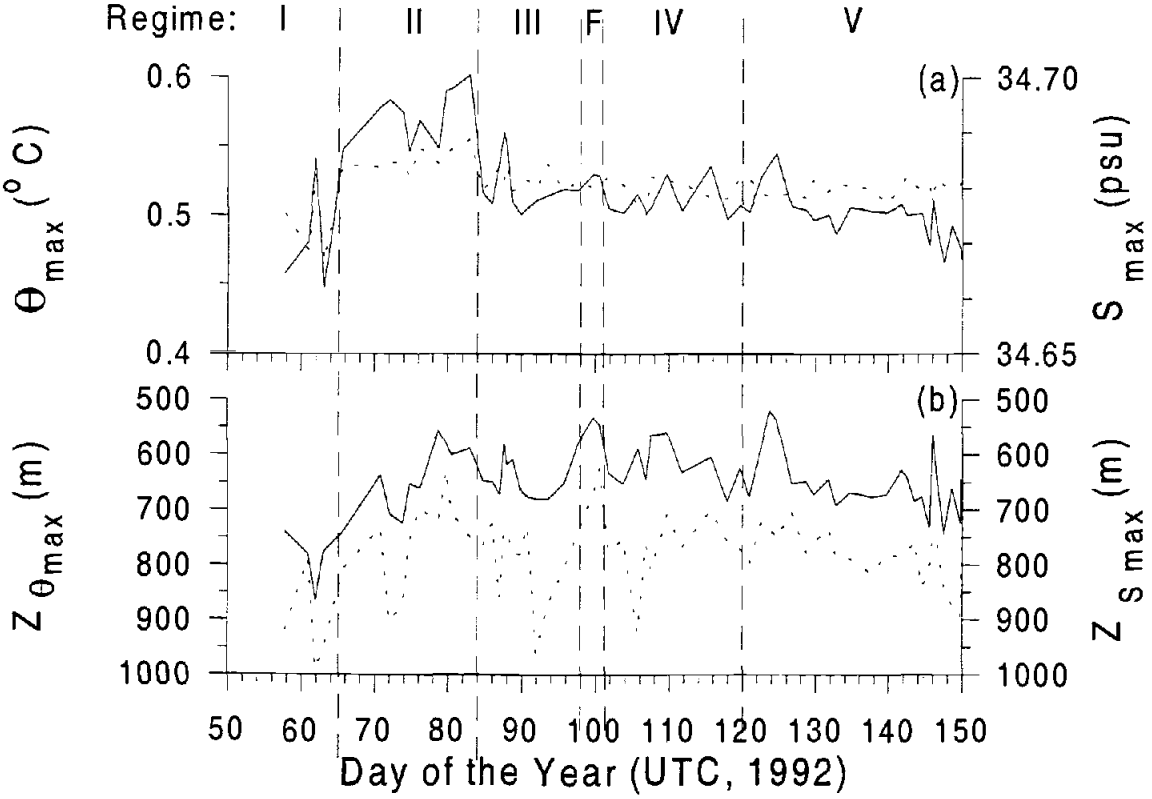

Figure 2.4. (a) The maximum potential temperature θ_{max} and (°C) (solid line) and salinity S_{max} (psu) (dashed line) as observed at the camp from LDEO CTD proflies. (b) Also shown are the depth of θ_{max}, $Z_{\theta max}$ (solid line) and the depth of S_{max}, Z_{Smax} (dashed line) (m).

Z_{Smax} was observed to be about 200 m deeper than $Z_{\theta max}$ during most of the experiment, a feature also found in the eastern Weddell Sea [*Gordon and Huber*, 1990].

Analysis of CTD data from both the main camp and cross-slope helicopter transects indicates that CISW generally drifted near the warm core of the northward-flowing western arm of the Weddell Gyre [*Gordon et al.*, 1993a; *Muench and Gordon*, 1995]. Measurements from early in the experiment were inshore of the warm core of the current, which roughly follows the 2500 m isobath. On the basis of changes in bathymetry and upper-ocean hydrographic structure, the experiment was divided into five time periods, or regimes (see Figures 2.1, 2.2, 2.4, and 2.5).

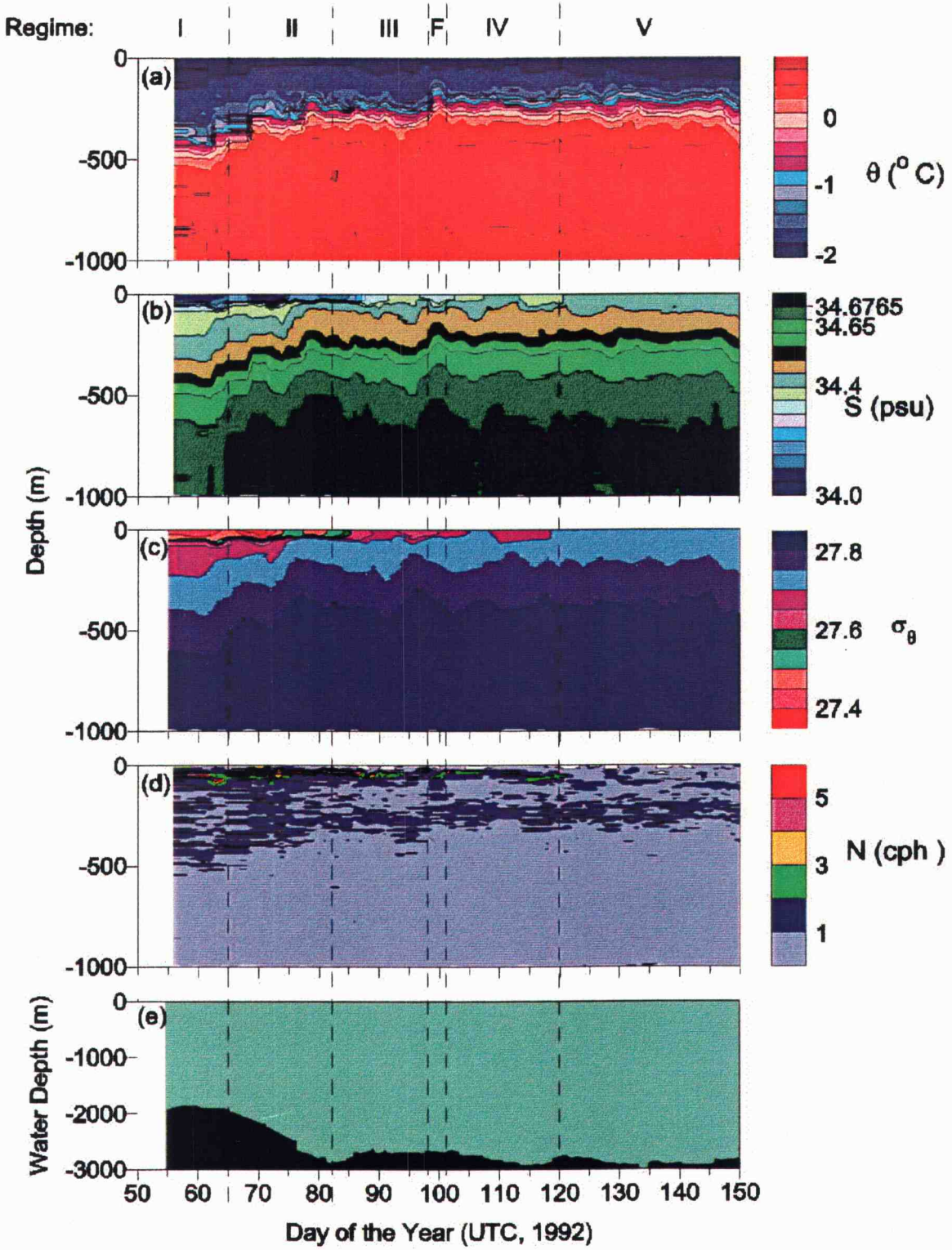

Figure 2.5. Transects along the camp drift track of (a) potential temperature θ (°C), (b) salinity S (psu), (c) potential density σ_θ, (d) buoyancy frequency N (cph), and (e) water depth D (m) from the LDEO profiles.

• Regime I ($57 \leq t < 65$): The ice camp traveled over the upper continental slope, where water depths were less than 2000 m. There was a thin, deep seasonal pycnocline (~50-75 m) and $Z_{\theta max}$ was near 800 m.

• Regime II ($65 \leq t < 82$): The ice camp drifted across the continental slope into deeper water with the water depth increasing from 2000 to 2700 m. There was a shallower seasonal pycnocline (~30 m) and $Z_{\theta max}$ (~700 m) than in regime I.

• Regime III ($82 \leq t < 101$): The seasonal pycnocline was weaker than in the previous regimes with a typical density difference across the seasonal pycnocline of 0.05-0.1 kg m^{-3}, compared with differences of approximately 0.2 earlier in the experiment. This decrease in density difference was caused by an increase in salinity and a slight decrease in temperature in the surface layer. This temperature decrease (~0.03° C) is apparent in the MDR records but is not noticeable in Figure 2.5a. The temperature maximum was shallower than in regimes I and II ($Z_{\theta max}$ ~ 600-650 m). The ice station traveled over a deeper portion of the continental slope during this period.

• Regime IV ($101 \leq t < 120$): During this regime, the upper water column was in transition from regime III to V with a very weak seasonal pycnocline. The $Z_{\theta max}$ was at ~650-700 m, a slight deepening relative to regime III. This regime is also characterized by extremely variable ice drift (Figure 2.1) compared with the relatively smooth northward motion during regimes III and V. Analyses of measured and geostrophic currents [*Muench and Gordon*, 1995] indicated a strong inflow of 9 Sv from the east during this period, possibly associated with bathymetric steering of the primarily barotropic currents by Endeavor Ridge.

• Regime V ($120 \leq t < 150$): The seasonal pycnocline was absent, and CISW remained over a deeper portion of the continental slope. The upper mixed layer now includes the remnant mixed layer from the previous winter. The water column below 200 m was similar to that in regime IV.

The LDEO profiles from regimes IV and V have been averaged together to produce representative profiles (Figures 2.6a). The lack of a seasonal pycnocline during these regimes is apparent, especially when compared with Figure 2.3a, which is a profile taken from regime II.

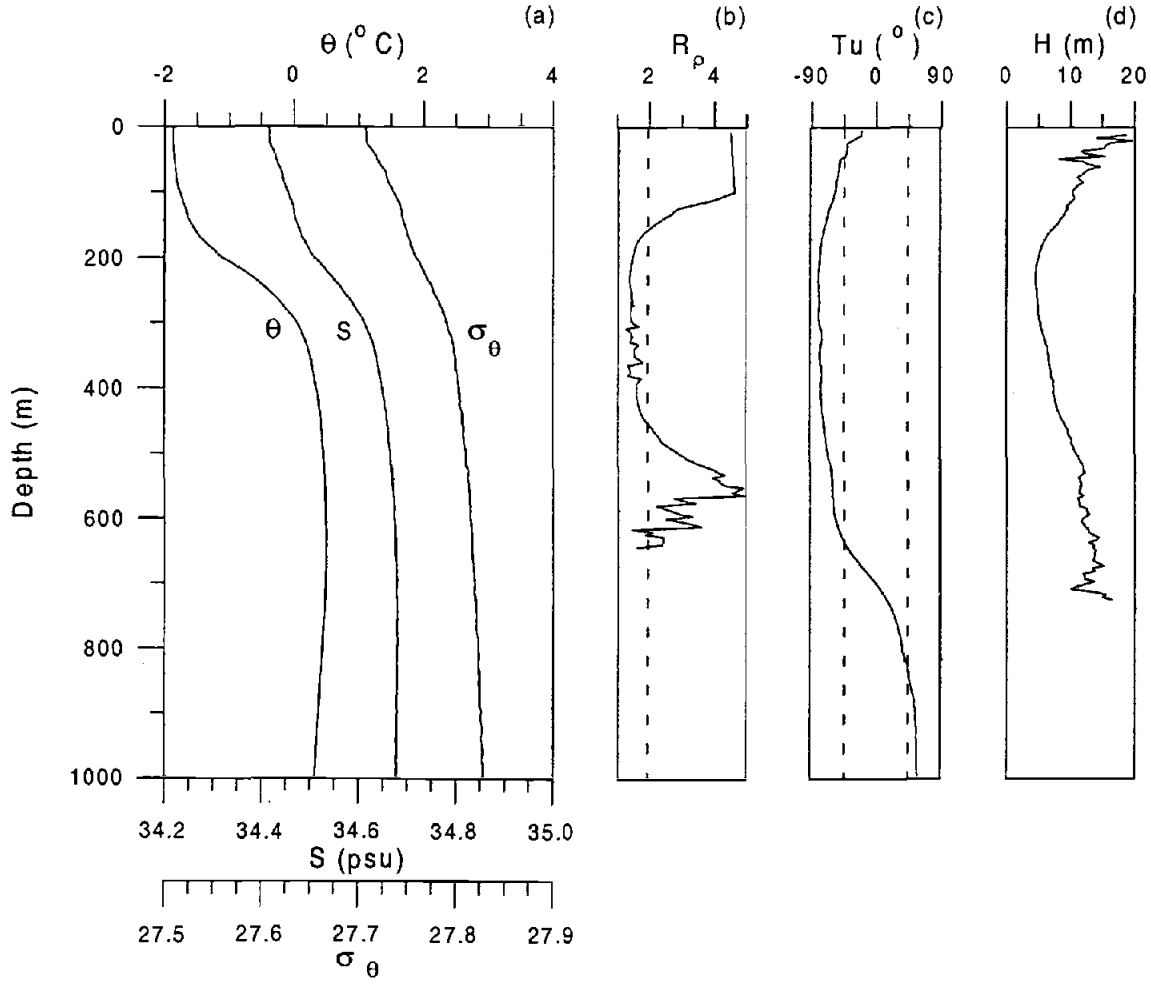

Figure 2.6. Average profiles for regimes IV and V for (a) potential temperature θ (°C), salinity S (psu), and potential density σ_θ, (b) density ratio R_ρ, (c) Turner angle Tu (°), and (d) modeled step height H (m). Thirty-three LDEO profiles were used for the averages.

In a twelve hour period on Day 99, near the end of regime III, CISW passed over an unusual hydrographic feature (denoted in Figures 2.2, 2.4 & 2.5 by "F"). This feature, which might be a small eddy, has been excluded from further analyses of these data.

2.5. Vertical Mixing Processes and Rates

The primary purpose of this study was to investigate the rate of heat transport from the subsurface Warm Deep Water (WDW) to the ocean surface. We concentrated on

processes which occur within the permanent and seasonal pycnoclines, since they act as barriers for heat flux. In this section we first discuss the heat transport processes expected to be important in the permanent pycnocline, then review the transport mechanisms in, and destruction of, the seasonal pycnocline.

2.5.1. The Permanent Pycnocline

On the basis of the hydrographic structure discussed in the previous section, the most likely processes responsible for heat transport through the permanent pycnocline are double-diffusion, internal wave-induced shear instabilities, and intrusions. These are discussed independently below.

2.5.1.1. *Double-diffusion*

Double-diffusive staircases are often found when the vertical gradients of T and S have the same sign [see *Turner*, 1973; *Schmitt*, 1994]. If T and S both decrease with depth, salt fingering may occur; if T and S both increase with depth, double-diffusive convection is possible. We will concentrate on the latter case, since in polar regions cold, fresh water generally lies above warmer, saltier water. Salt fingering is possible, however, below the temperature and salinity maxima and also on the lower edges of warm, salty intrusions.

In double-diffusive convection (see Figure 2.3), the density gradient due solely to the temperature stratification is intrinsically unstable, while the salinity gradient provides the necessary static stability. Staircases are characterized by homogeneous layers that are bounded above and below by thin interfaces (or "sheets") in which both T and S change rapidly with depth. The layers are convectively stirred by the destabilizing buoyancy flux arising from the diffusive transport of heat through the interfaces, which is only partly offset by the diapycnal salt flux. This combination of diffusion and convection can significantly increase the diapycnal fluxes of heat, salt, and momentum.

One indicator of double-diffusive activity is the Turner angle (Tu), defined by

$$Tu = \tan^{-1}\left(\frac{(1+R_\rho)}{(1-R_\rho)}\right) \tag{2.2}$$

where R_ρ is the density ratio, given by

$$R_\rho = \frac{\beta\ \partial S/\partial z}{\alpha\ \partial T/\partial z} \tag{2.3}$$

In (2.3), β and α are the haline contraction and thermal expansion coefficients, respectively. A Turner angle between -90° and -45° indicates a potential for double-diffusive convection; a value between +45° and +90° indicates a potential for salt fingering. As *Tu* approaches -90°, which implies that the destabilizing density gradient due to $\partial T/\partial z$ is becoming comparable to the stabilizing gradient due to $\partial S/\partial z$, the likelihood of finding strong double-diffusive activity increases [*Ruddick*, 1983]. Equivalently, values of R_ρ greater than 1.0 are indicators of double-diffusive activity, with $1.0 < R_\rho < 2.0$ indicating strongly double-diffusive conditions. For salt fingering, $0.0 < R_\rho < 1.0$. Favorable conditions for double-diffusive convection were found in a band below about 200-250 m during regimes I and II and below about 100-150 m during regimes III to V (Figures 2.7a, 2.3c, 2.6b, and 2.6c). Double-diffusive steps were frequently found in this band, some examples of which are shown in Figure 2.3a.

Observed step heights varied from ~0.05 m, near the vertical resolution of the RSVP's temperature sensor, to about 20 m, although most steps had heights less than 10 m. The temperature differences across interfaces adjacent to thick layers (5-10 m) typically ranged from 0.1 to 0.5° C and occasionally reached 0.8° C. The largest temperature steps were usually associated with large intrusions. Intrusions and double-diffusion interact: intrusions establish the large-scale conditions necessary for the double-diffusive instability, and double-diffusion supplies a driving force for intrusions [*Toole and Georgi*, 1981; *Walsh and Ruddick*, 1995].

Smaller steps, with heights of about 2 m and temperature differences less than 0.1° C, were observed in regimes II to V and were much more common than the larger steps. Double-diffusive steps have been previously observed in the Weddell Sea by *Foster and Carmack* [1976a] and *Muench et al.* [1990]. The latter paper divided steps into two size classifications: type A (1-5 m) and type B (>10 m). The most common size steps

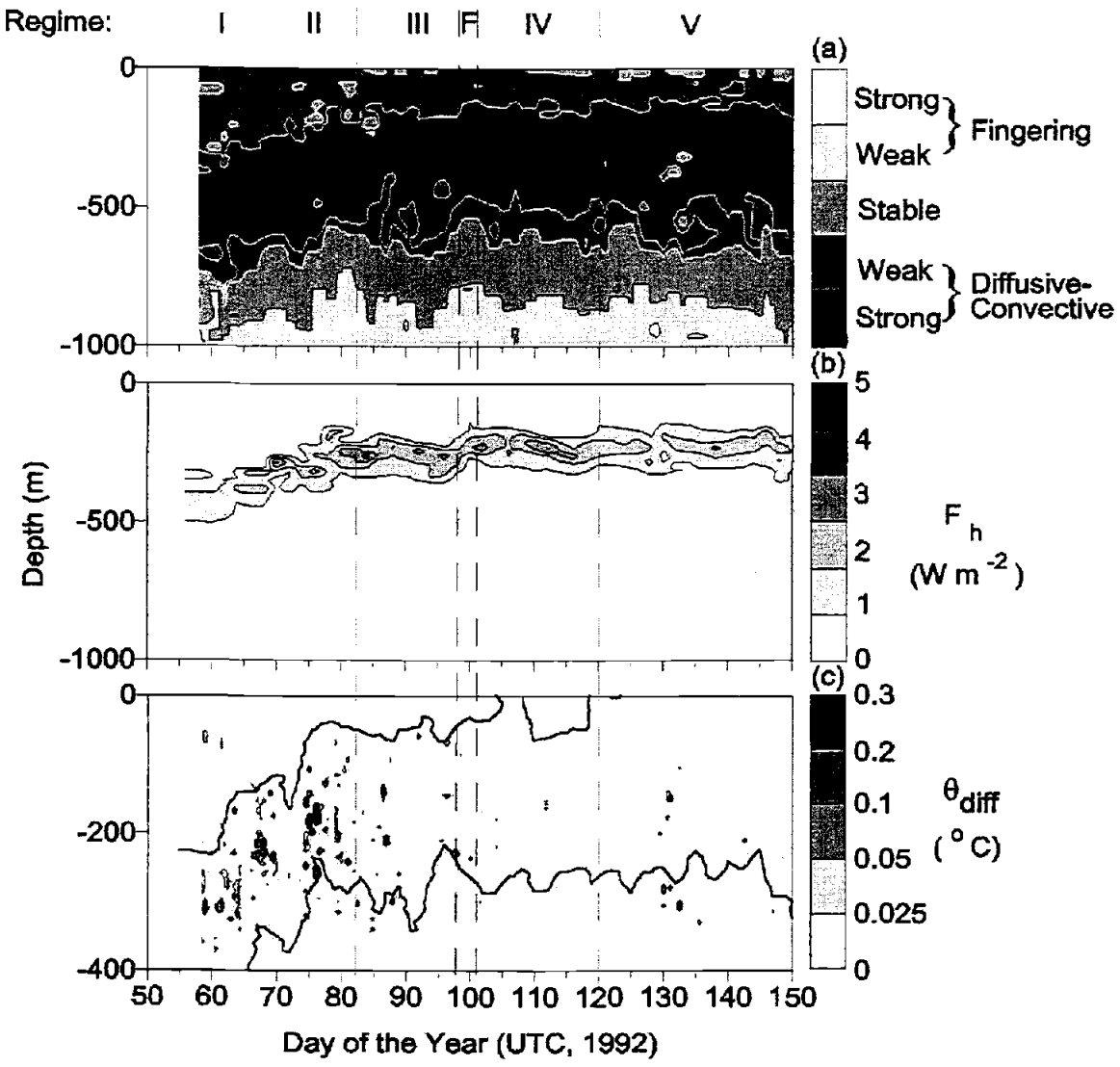

Figure 2.7. Transects of (a) the Turner angle Tu and (b) vertical heat fluxes F_H (W m $^{-2}$) according to the formulation of *Kelley* [1990]; and (c) locations of major intrusions (see text). In (c) the lower line is the $\sigma_\theta = 27.78$ isopycnal and the upper line is the $\sigma_\theta = 27.70$ isopycnal. Tu is scaled with strong salt fingering as $67.5 < Tu < 90$, weak salt fingering as $45 < Tu < 67.5$, stable as $-45 < Tu < 45$, weak diffusive-convective as $-45 < Tu < 67.5$, and strong diffusive-convective as $-67.5 < Tu < -90$.

observed here correspond to type A. *Muench et al.* [1990] found that type B steps typically occurred deeper than type A in the weaker stratification just above the broad temperature maximum. If such steps were present in the western Weddell, they would have been present below the maximum depth sampled by the RSVP. The larger steps observed here are more likely to be related to intrusions than to type B steps, which were

found only in a more central region of the Weddell Gyre where no intrusive features were present.

Models for estimating the vertical heat flux (F_H) through double-diffusive steps have been developed by several investigators, including *Marmorino and Caldwell* [1976], *Taylor* [1988], *Fernando* [1989], *Kelley* [1990], and *Rudels* [1991]. We refer to these studies below as MC76, T88, F89, K90, and R91 respectively. The heat fluxes predicted by each model are denoted $F_{H\text{-}MC}$, $F_{H\text{-}T}$, $F_{H\text{-}F}$, $F_{H\text{-}K}$, and $F_{H\text{-}R}$, respectively. All of these formulations are parameterized using the temperature difference across the step ($\Delta\theta$) and the density ratio R_ρ (2.3). (These investigators use ΔT in their heat flux formulations; however, the formulas are quote with $\Delta\theta$ here.) With the exception of F89, the models assume that the heat flux is proportional to $(\Delta\theta)^{4/3}$, based on a model developed for heat flow between two parallel plates [*Turner*, 1973]. Heat flux parameterizations (in Wm^{-2}) for four of these models are presented below:

$$F_{H-MC} = 0.00859\,\rho_o c_p \alpha^{-1} \exp\left\{4.6\exp\left[-0.54\left(R_\rho - 1\right)\right]\right\}\left(g\kappa_t^2\upsilon^{-1}\right)^{1/3}\left(\alpha\Delta\theta\right)^{4/3} \quad (2.4)$$

$$F_{H-T} = 0.00272\,\rho_o c_p \alpha^{-1} R_\rho^{-2.1}\left(g\kappa_t^2\upsilon^{-1}\right)^{1/3}\left(\alpha\Delta\theta\right)^{4/3} \quad (2.5)$$

$$F_{H-K} = 0.0032\,\rho_o c_p \alpha^{-1} \exp\left[4.8\,R_\rho^{-0.72}\right]\left(g\kappa_t^2\upsilon^{-1}\right)^{1/3}\left(\alpha\Delta\theta\right)^{4/3} \quad (2.6)$$

$$F_{H-R} = \frac{5}{3}\pi^{-5/3}\rho_o c_p \alpha^{-1}\left[1-\sqrt{\kappa_s\kappa_t^{-1}}\right]^{4/3}\left(g\kappa_t^2\upsilon^{-1}\right)^{1/3}\left(\alpha\Delta\theta\right)^{4/3} \quad (2.7)$$

where ρ_o is the mean density (kg m^{-3}), c_ρ is the specific heat (J kg^{-1} $°C^{-1}$), g is the gravitational acceleration (m s^{-2}), and κ_s and κ_t are molecular diffusivities (m^2 s^{-1}) for salt and heat, respectively. The parameterization by F89 is only self-consistent for a specific value of R_ρ ($\approx$1.2) and therefore has not been used. (However, readers interested in the physical processes involved in double-diffusive convection with varying density ratio will find a clear description in that paper.) The model of R91 was developed for R_ρ = 1.0; consequently, it should only be applied to regions of low R_ρ.

For regions of fairly constant R_ρ, the fundamental parameter required for estimating the double-diffusive heat flux is the thermal step at the interface, $\Delta\theta$. Methods for locating interfaces have been developed for application to data from the Arctic Ocean

[*Padman and Dillon,* 1987, 1988]. Automated searching in the present data is, however, complicated by the wide range of step scales, the intermittency of steps, and the irregular structure in the interfaces separating the quasi-homogeneous layers. The thermal step $\Delta\theta$ was estimated from the layer height H using $\Delta\theta = \langle\partial\theta/\partial z\rangle H$. Two methods were followed to determine the thermal gradient and H.

1. For the range of temperatures for which steps were commonly found, each profile was categorized as consisting of "large", "medium", and "small" steps, based on visual inspection of profiles and ignoring layers less than 0.5 m thick. The layer thickness, H, for each category was then estimated from a more detailed inspection of several typical profiles for each category. The mean thermal gradient was estimated using the difference in θ over the depth range in which steps were found.

2. We estimated H from the large scale stratification parameters using the relation proposed by *Kelley* [1984]:

$$H = \left[0.25x10^{-9}\ R_\rho^{1.1}\ \upsilon\ \kappa_t^{-1}\ \left(R_\rho - 1\right)\right]^{0.25} \sqrt{\kappa_t \langle N^{-1}\rangle} \qquad (2.8)$$

The thermal gradient was then estimated from a vertically smoothed average of θ, where the averaging scale was much greater than a typical layer height.

For regimes II to V, mean layer heights evaluated using method 1 are about 2 m, and for the mean thermal stratification of 0.015°C m^{-1}, the resultant value of $\Delta\theta$ is 0.03°C. Examples of step heights obtained using method 2 are shown in Figure 2.6d, and in the region of well-defined steps (*Tu* near –90°), step heights range from 4-7 m. In sections of the profiles with well-defined steps, the step heights from both methods were similar. However, when the steps are poorly defined or absent, the heights from method 1 are much lower than the modeled heights from method 2.

To demonstrate the differences between the heat flux models described by (2.4)-(2.7), and to define a reasonable upper bound on double-diffusive fluxes, we apply each model to the layer heights determined by method 2 (Figure 2.8). Both K90 and T88 predict essentially the same values, hence the T88 estimates are not shown. Heat flux estimates from R91 are only shown in Figure 2.8 when $R_\rho < 1.5$. The estimates made using MC76 exceed those using K90 (Figure 2.8) by a factor of 2-2.5 for $1.4 < R_\rho < 1.5$ (typical values

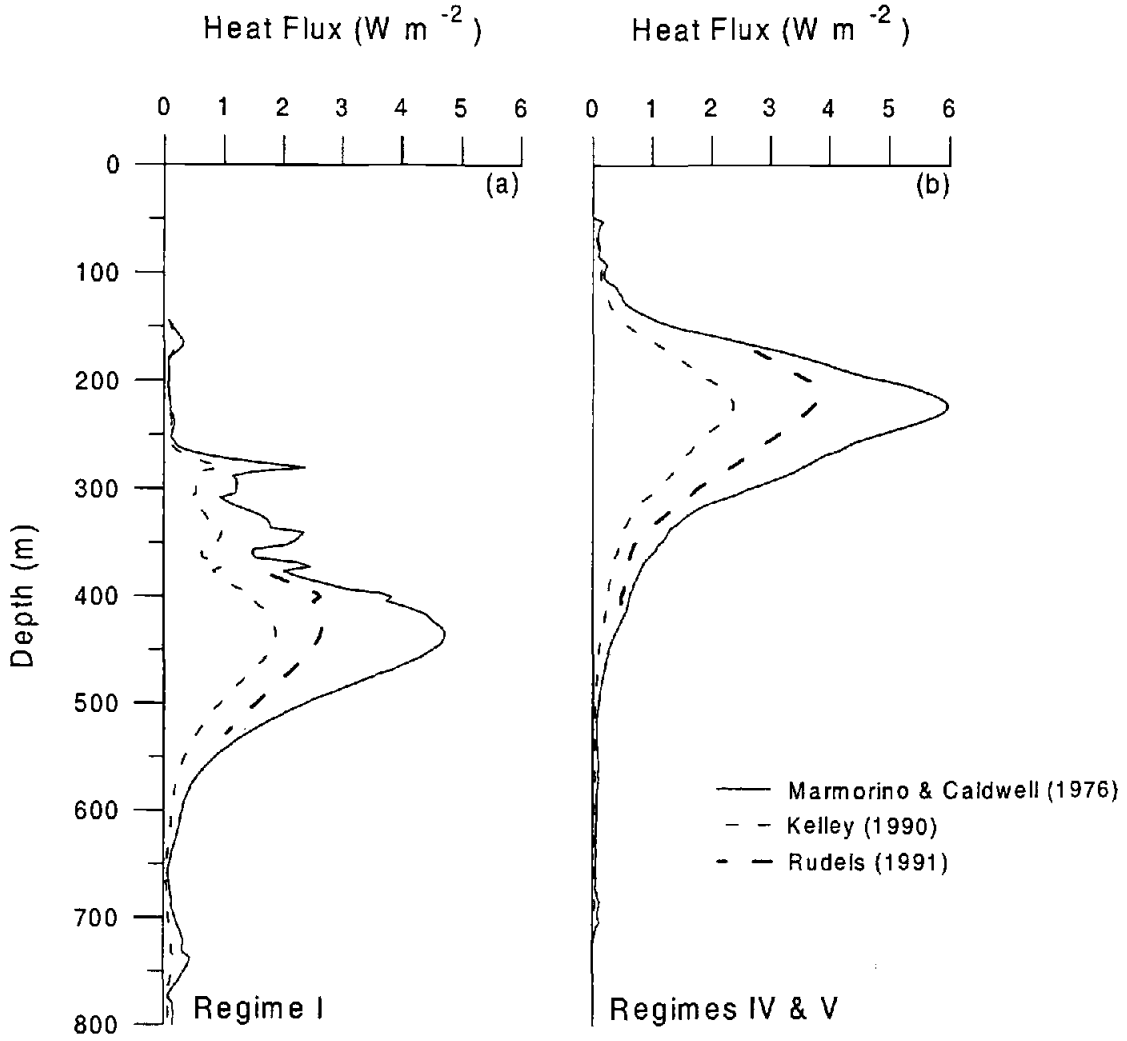

Figure 2.8. Intercomparison of heat flux estimates from the formulations of *Marmorino and Caldwell* [1976] (solid line), *Kelley* [1990] (dashed line), and *Rudels* [1991] (heavy dashed line) for representative profiles from (a) regime I and (b) regimes IV and V. (Note that heat flux estimates from *Rudels* are only shown for $R_\rho < 1.5$).

for these data). At $R_\rho = 1.0$, the MC76 and K90 predictions differ by a factor of 4. For $1.0 < R_\rho < 1.5$, there is a wide scatter in the laboratory data on which these formulations are based, with very little data available at all for $R_\rho < 1.2$. The discrepancy between these models is therefore explained primarily by the authors' different choices of functions for fitting the R_ρ dependence. Note, however, that MC76 heat flux exceeds those from R91 (Figure 2.8), the latter being assumed to be an upper bound because it is formally applicable only at neutral static stability, i.e. $R_\rho = 1$.

The heat fluxes evaluated using method 1 for the mean layer height range from 1 to 2 W m^{-2}. Note that this is an average over the depth range for which steps are found. This is comparable to the heat flux estimate using method 2 (Figure 2.8) when averaged over the diffusive-convective depth range. Our interpretation, based on our observations of both layer heights and intermittency, is that the double-diffusive flux is 1-2 W m^{-2} on average, with peak values, when steps are well-defined, of about 4 W m^{-2}.

Ideally, the flux laws above should be applied to the properties ($\Delta\theta$ and R_ρ) of each observed diffusive-convective step, followed by averaging of the modeled fluxes appropriate time and/or depth ranges (see, for example, *Padman and Dillon*, [1987]). In the present case, however, the steps are difficult to find automatically in the RSVP data due to their intermittency and the variability of their sizes, as discussed above. Furthermore, steps are seldom resolved by the LDEO CTD data, which have been used here to extend our flux calculations to the depth of the temperature maximum. *Padman and Dillon* [1987] found for Arctic data that the actual mean heat flux was about 50% higher than would be predicted from (2.4) and (2.8), primarily because the large steps in the measured distribution of temperature differences dominated the average flux due to the $\Delta\theta^{4/3}$ dependence in (2.4)-(2.7). Analyses on a few characteristic profiles in the present data set suggest that some increase in mean heat flux would occur by considering the true distribution of interfacial $\Delta\theta$ and R_ρ; however, the increase is small, less than 20%.

Transects of $F_{H\text{-}K}$ obtained using method 2 are shown in Figure 2.7b. Maximum fluxes were reasonably constant throughout all regimes, although the heat flux of regime I was slightly smaller. Maximum fluxes of 4 W m^{-2} (following K90) occurred in a band centered near 250 m in regimes III-V. In regime II, this band was approximately 50 m deeper (300 m), which corresponds to the deeper location of the band of double-diffusive steps. Likewise, the band was significantly deeper (~400-450 m) in regime I and the heat fluxes were smaller (< 3 W m^{-2}). The maximum heat flux of 4 W m^{-2} corresponds to a buoyancy flux of about 4 x 10^{-10} m^2 s^{-3}. T88 noted that the buoyancy flux should be approximately balanced by the dissipation rate ε in the layers, however we are unable to

test this hypothesis in the present case because the expected buoyancy flux is less than the noise level for ε.

In data obtained from the Canada Basin, *Padman and Dillon* [1988] were able to trace individual layers between adjacent profiles, allowing estimates of along-layer variability of T and H to be made. With the present data set, however, this is not possible. This may be due to the relatively rapid motion of the ice camp, combined with significant horizontal spatial gradients of T and S in the steps. Temporal evolution may also be more rapid, because vertical heat fluxes are much higher here, being $O(1)$ W m^{-2} compared with 0.04 W m^{-2} in the Canada Basin. *Muench et al.* [1990] noted that the large (type "B") steps found to the east of the CISW drift track were observable over hundreds of kilometers.

Below the salinity maximum (Figure 2.5b), gradients of both T and S are favorable for salt-fingering. The Turner angle, however, indicates only weak salt fingering conditions (Figure 2.7a).

2.5.1.2. *Shear Instabilities*

In the permanent, mid-latitude thermocline, a significant component of the total diapycnal flux is usually provided by mixing associated with shear instabilities of the internal gravity wave field [*Gregg*, 1989]. In the few experiments from polar regions that have investigated both mixing and internal waves, a wide range of diapycnal heat fluxes have been found. For example, *Padman and Dillon* [1987] found that the contribution of shear-driven mixing to the local diapycnal flux was negligible (less than 0.1 W m^{-2}) in the central Canada Basin. In contrast, measurements in the eastern Arctic revealed heat fluxes of up to 30 Wm^{-2}, due to energetic mixing events associated with large-amplitude, high-frequency wave packets [*Padman and Dillon*, 1991]. One difference between these two sites is their proximity to internal wave sources. The measurements described by *Padman and Dillon* [1991] were made in a region where strong tidal flows were able to interact with the steep topography of the continental slope, whereas the Canada Basin measurements were taken well away from significant topographic features.

Given our poor understanding of both the topography and currents in the western Weddell Sea prior to the present program, it was not known whether current/topography interactions would be important in this region. In the observed microstructure profiles, the dissipation rate ε in the permanent pycnocline never exceeded the noise level of about $2 \times 10^{-9} m^2 s^{-3}$. What would be the heat flux if the true value of ε was always near the noise level? Following *Osborn* [1980], we estimate the effective diapycnal eddy diffusivity as

$$K_T \approx \frac{\Gamma \varepsilon}{N^2} \tag{2.9}$$

where Γ is the mixing efficiency, generally assumed to be about 0.2 [*Gregg*, 1987]. For a buoyancy frequency N = 1 cph (0.0017 s^{-1}), the diffusivity associated with the noise level for ε is about 10^{-4} $m^2 s^{-1}$. Since the diapycnal heat flux is given by

$$F_H = \rho c_p K_T \partial T / \partial z \tag{2.10}$$

the noise-level of ε is equivalent to a heat flux of about 4 W m^{-2}. This value is, however, an upper bound. Shear-driven turbulence tends to be extremely variable in both space and time [*Baker and Gibson*, 1987], with the average value being dominated by the presence of a few large but intermittent events. Since we do not find any events significantly above the noise floor, we expect that the mean value of heat flux is actually much less than 4 W m^{-2}. An alternative technique for estimating the vertical diffusivity and heat flux from internal wave based on a model by *Gregg* [1989] and extended by *Wijesekera et al.* [1993], implies a mean heat flux of about 1 W m^{-2}.

2.5.1.3. *Intrusions*

Intrusions such as those shown in Figure 2.3 are often associated with large along-isopycnal gradients of temperature and salinity, and hence are frequently found at fronts between contrasting water types. Isopycnal mixing can be quite energetic and effective, since it does not have to overcome any buoyancy gradient. It is, however, extremely difficult to evaluate its magnitude: *Ledwell et al.* [1993] is one of very few studies to have estimated an isopycnal diffusivity by tracking the lateral diffusion of released tracers. In the present study, we are unable to quantify the mixing rates suggested by the presence of

intrusions. However, intrusions can play an important role in the ultimate ventilation of the subsurface oceanic heat to the sea surface.

During CISW, large intrusions were frequently found in the weakly stratified region above the permanent pycnocline. An intrusion is most accurately identified as a region of anomalous θ-S characteristics relative to some 'background" θ-S relation. The background relationship can be determined by scale separation (see, for example, *Ruddick and Walsh* [1995]), or by averaging several profiles together to define a "mean" state. In the present study, the mean hydrography varies in the vertical on scales comparable to intrusion heights, hence the former method is impractical. The latter method is also difficult to apply in this case because of the rapid change in "mean" hydrographic properties in the region where most intrusions are found. Since our present goal is simply to describe the distribution of intrusions, we search for regions where the temperature decreases with increasing depth, contrary to the large-scale trend of increasing θ (above the temperature maximum). For such regions, we calculate the maximum value of $\Delta\theta$ representing the difference between a local temperature maximum and the adjacent (in depth) local minimum. These values are contoured from the RSVP data in Figure 2.7c. Note that, according to our search algorithm, locally high values of $\Delta\theta$ occur on the lower edges of warm and salty intrusions. Most intrusions are found in regimes I and II, i.e., while CISW was located over the upper slope. This observation is consistent with most intrusions being located on the inshore side of the warm-core current, between this current and the shelf/slope front revealed by the cross-slope transect in the work by *Muench and Gordon* [1995].

We also indicate on Figure 2.7c two isopycnals that represent the approximate upper and lower bounds of intrusive activity. The lower isopycnal, $\sigma_\theta = 27.78$, slopes upward both to the west (inshore) and east of the warm core, reaching the bottom of the winter mixed layer over the upper slope and in the central Gyre. Isopycnal mixing associated with the intrusions therefore provides a mechanism for venting upper WDW heat to the surface over a broader region than would be possible by diapycnal (near-vertical) fluxes alone. A similar mechanism has been described by *Boyd and D'Asaro* [1994] for explaining the heat lost by the West Spitsbergen Current as it enters the Arctic Ocean.

Large intrusions, defined by us as having heights of 25-35 m and temperature anomalies of 0.1°- 0.6°C (see Figure 2.9) were usually found in regimes I and II. Smaller intrusions with heights of 5-20 m and smaller temperature anomalies were found in all regimes but may not appear in Figure 2.6c because of the analysis method.

In general, intrusions could not be tracked between RSVP profiles to allow estimations of their horizontal extent or lifetime. However, the horizontal extent of the intrusions in a series of RSVP drops from t = 74 was estimated using the ice-relative velocities at 200 m, kindly provided by R. Muench. One intrusion approximately 50 m high was observed for almost 4 km (Figure 2.9); however, most of the intrusions were traceable less than 1 km. We caution, however, that much of the variability in the

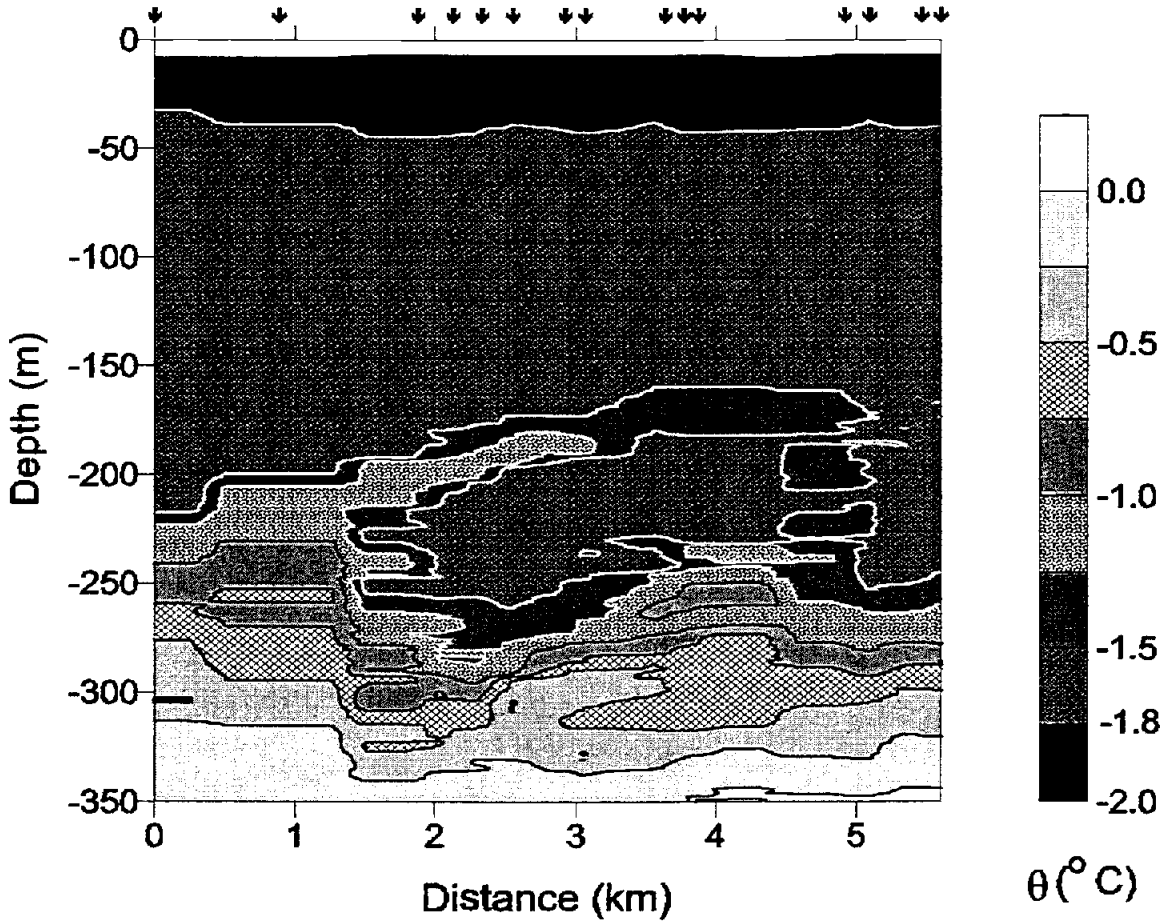

Figure 2.9. A map of potential temperature, θ, showing the horizontal extent of the intrusions of t = 74 using the ice-relative velocity u_{rel} at 200 m to determine distance. Arrows at the top of the plot indicate the locations of the RSVP profiles.

intrusion properties probably occurs in the direction normal to the CISW drift track, since most of the large-scale hydrographic variability is across-slope (see *Muench and Gordon* [1995]). The observed vertical scales of intrusion, defined as the vertical distance from one temperature maximum to the next, were about 50-100 m. This is consistent with the vertical scale of $O(100)$ m that is obtained from the model of *Toole and Georgi* [1981], using the observed mesoscale horizontal gradient of salinity obtained from the cross-slope CTD transects.

2.5.2. The Seasonal Pycnocline and the Mixed Layer

The final obstacle to the upward flux of heat from the WDW towards the sea ice is the seasonal pycnocline which isolates surface effects, such as mixing driven by surface stress and cooling, from the deeper waters of the remnant winter mixed layer. The seasonal pycnocline is located at the base of the surface mixed layer (SML), which is a water layer of nearly constant θ and S in contact with the ice (Figure 2.3a). In most cases, weak vertical gradients of both θ and S exist in the SML, particularly deeper. For purposes of discussion, we therefore define the lower depth bound of the SML as the depth at which the temperature is 0.04° greater than θ_{ML}, the average temperature of the upper 20 m. Potential temperature was used rather than density because θ was better resolved in the RSVP data than S. This is a reasonable approach since the seasonal thermocline and halocline coincided during most of the experiment. The mixed layer temperature, θ_{ML}, ranged from -1.85 to -1.89° C during the experiment and was near or slightly above freezing (typically within ~0.02° C, based on the corresponding salinity range of 34.10 to 34.45 psu).

The seasonal pycnocline is visible in transects of both σ_θ (Figure 2.5c) and buoyancy frequency N (Figure 2.5d). Values of N in the seasonal pycnocline decreased from greater than 5 cph early in the experiment to less than 3 cph just before it disappeared near $t = 120$. The seasonal pycnocline began to deteriorate significantly around $t = 82$ (Figures 2.5c and 2.5d), finally disappearing completely near $t = 120$. Most of the decay occurred during storm events, with about 40% of the total density change across the seasonal pycnocline occurring during the storm event of $t = 86$-91. Another 40% is

associated with two other storms (~20% each). Thus, 80% of the mixed layer density change was associated with three storm events.

During one storm event (t = 86-91), *McPhee and Martinson* [1994] used frame-mounted clusters measuring u, v, w, T, and S to obtain direct measurements of the turbulent vertical heat flux $\langle w'T' \rangle$, the covariance of temperature and vertical velocity fluctuations T' and w', respectively, in the upper SML (4-24 m depth). Peak fluxes near 15 W m^{-2} were measured. *McPhee* [1992] found that the turbulent heat flux in the upper mixed layer could be estimated from

$$F_H = \rho c_p c_H u_* \left(T_{ML} - T_f\right) \tag{2.11}$$

where c_H is a constant (~0.005 to 0.006 [*McPhee*, 1992]), T_f is the freezing point temperature for the measured SML salinity, and the friction velocity u_* is determined from

$$u_* = \sqrt{c_{D,25}}\ u_{rel} \tag{2.12}$$

In (2.12), u_{rel} is the measured ice-relative velocity at 25 m and $c_{D,25}$ is the appropriate ice/water drag coefficient. For rough ices, a reasonable value of $c_{D,25}$ is about 0.005. Using (2.11) and (2.12), turbulent heat fluxes (Figure 2.10) were estimated using the T at ~12.5 m depth (the uppermost MDR) for T_{ML} and interpolating S from the LDEO CTD profiles in order to determine T_f. The highest turbulent heat fluxes occurred during storms, when the ice-relative current speed was greatest. Times of major storms are marked by arrows in Figure 2.10. The maximum flux of about 15 W m^{-2} for the storm of t = 86-91 is comparable with the *McPhee and Martinson's* [1994] estimate. Between storms, the turbulent heat fluxes were typically less than 2 W m^{-2}. The mean flux for the entire record was 1.7 W m^{-2}. For comparison, *Lytle and Ackley* [1996] estimated an average heat flux through the ice of 7 W m^{-2} using measurements of ice and snow conditions combined with modeling of the conductive and convective fluxes through the ice and snow cover. While these two estimates disagree, both indicate that the local loss of oceanic heat to the surface is less than the large-scale average of 19 W m^{-2}.

McPhee and Martinson [1994] postulated that the increase in turbulent heat flux due to storms resulted from mixing of the slightly warmer and saltier water of the remnant winter mixed layer into the SML. An example of this mixing can be seen in microscale

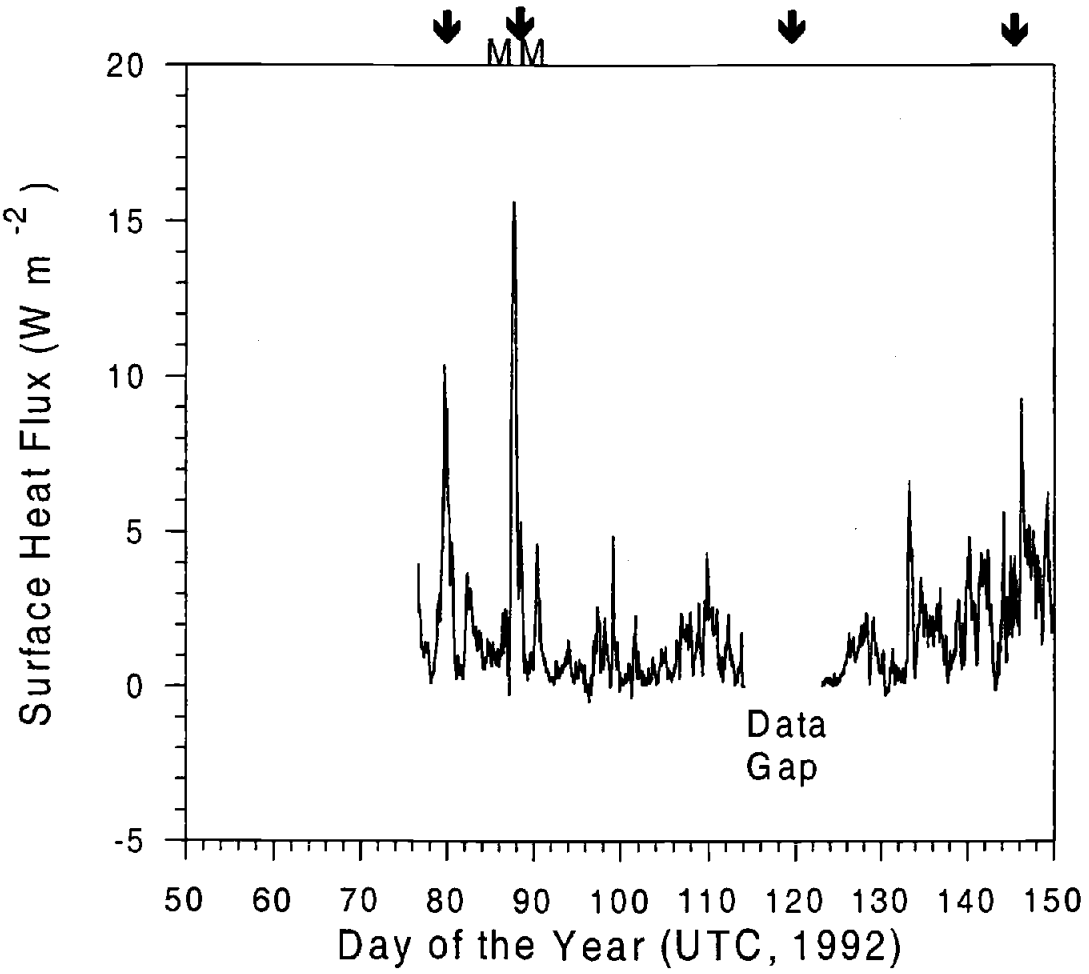

Figure 2.10. Turbulent heat flux estimates versus time from u_* following *McPhee* [1992]. Times of principal storms are marked with arrows. "MM" denotes the storm of t = 86-91, for which *McPhee and Martinson* [1994] measured a peak turbulent heat flux of 15 Wm^{-2}.

profiles of θ and velocity shear (u_z) during a storm on day 79 (Figure 2.11a). The turbulent velocity shear is high throughout the mixed layer. During storm events, surface generated turbulence frequently extended to the pycnocline (Figure 2.12). In such cases, mixing entrains water into the mixed layer, thus deepening the SML and at the same time bringing heat and salt upward into the SML [e.g. *McPhee and Martinson*, 1994]. Mixing can also continue across the pycnocline after the surface stress has decreased (Figure 2.11b). In this case, the source of turbulent kinetic energy is presumably the velocity shear across the seasonal pycnocline, which might be due to mean flow or internal gravity waves.

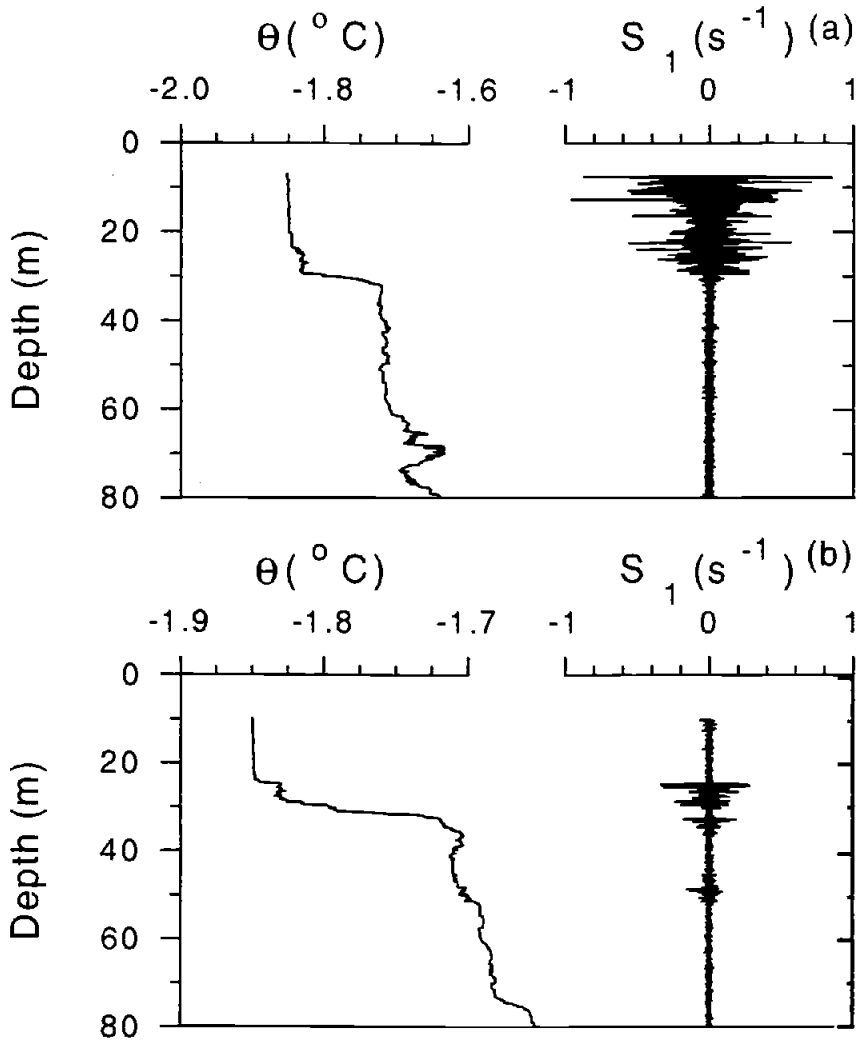

Figure 2.11. Profiles of potential temperature θ (°C) and one of the orthogonal velocity shears, S_1,(s^{-1}), (a) at $t = 87.4635$, showing entrainment through the seasonal pycnocline by surface stress and (b) at $t = 80.9341$, showing cross-pycnocline mixing in the absence of surface stress.

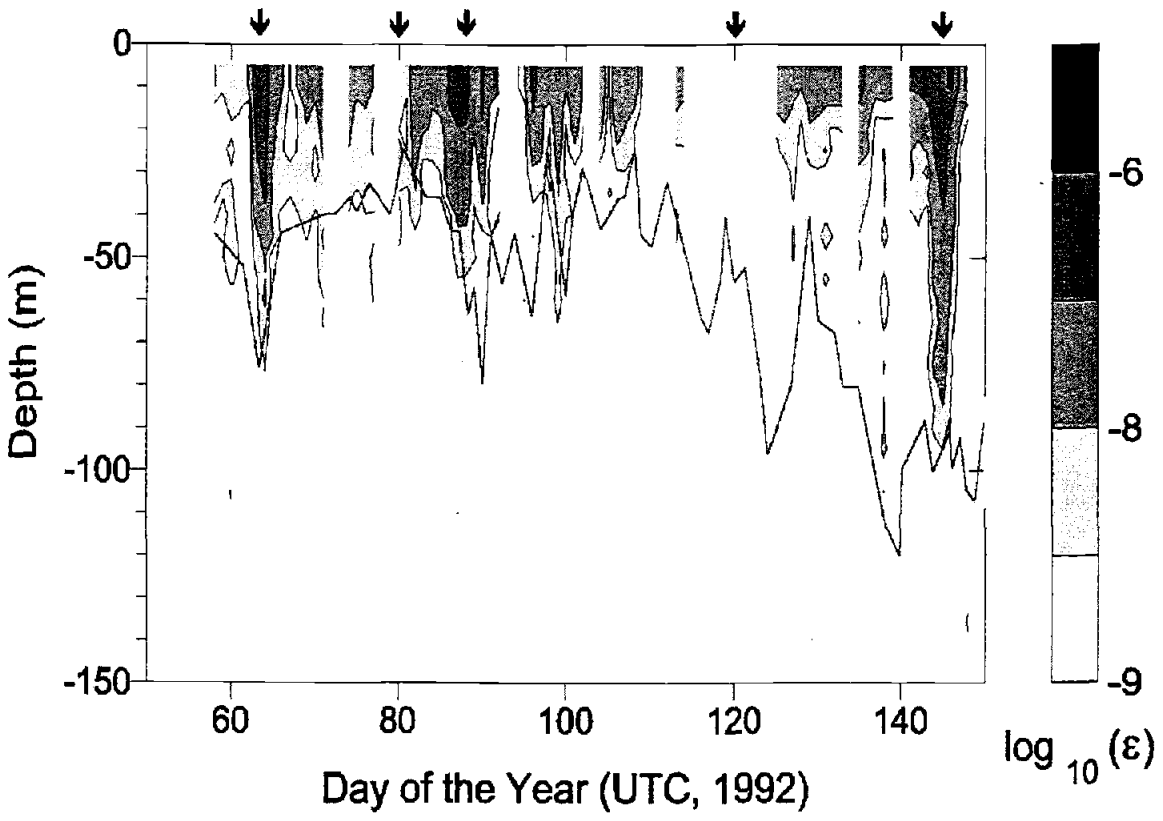

Figure 2.12. Transects of the mixed layer depth, H_{ML}, as determined from the LDEO profiles (solid line) and the log of the dissipation rate, ε (shaded). Times of principal storms are marked with arrows.

2.6. Discussion and Summary

The heat fluxes associated with the various processes described in section 2.5 are summarized in Figure 2.13. This figure represents average conditions from late February to late May, 1992 during CISW. About 3 W m^{-2} of upward heat flux occurs in the permanent pycnocline, primarily due to double-diffusive convection. We estimate that 1.7 W m^{-2} finally reaches the base of the pack ice through stress-driven turbulent entrainment of heat from the underlying seasonal pycnocline and remnant winter mixed layer. An additional loss of heat from the warm core occurs through mixing along isopycnals, as suggested by the presence of large intrusions on the inshore side of the warm core. While we are unable to quantify the isopycnal heat flux, we note that the deepest isopycnal for which intrusions are found slopes upward into the surface mixed layer to the east and west of the CISW drift track. Isopycnal mixing therefore provides a plausible mechanism for venting the upper WDW heat to the surface over a broader area than by diapycnal mixing processes alone.

These heat fluxes are significantly less than the 19 W m^{-2} average flux required to explain the overall observed cooling of the water in the Weddell Gyre [*Fahrbach et al.*, 1994]. This should not be surprising: the thicker second-year ice in this region is a much more efficient insulator between the ocean and atmosphere than the thinner seasonal ice further to the east. In addition the hydrographic and current fields are not amenable to the energetic mixing processes that are possible on the upper slope and shelf. It is nonetheless, important to understand the heat transport processes, which are present, so that the region's sensitivity to perturbations in oceanic and atmospheric conditions can be assessed.

Some support for this inference of low mean fluxes from the ocean to the surface is provided by *Lytle and Ackley* [1996], who used time series of ice and snow thicknesses and temperatures to model the thermodynamic evolution of the ice at several sites on the CISW floe. They conclude that the mean conductive flux through the ice (denoted F_{cond} on Figure 2.13) varies between 10 and 30 W m^{-2} during the freeze-up period (days 70 to

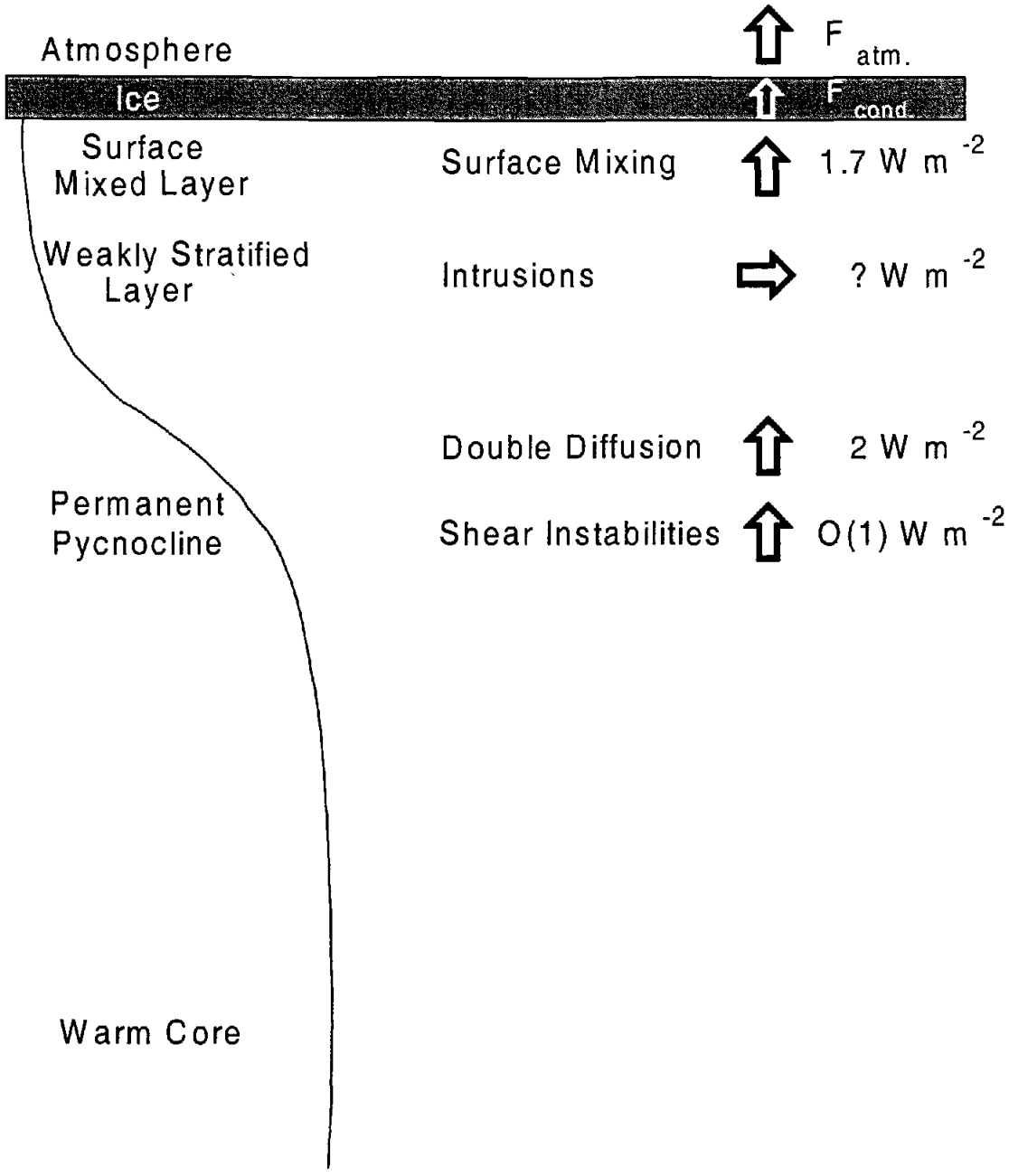

Figure 2.13. Heat budget for the water column in the western Weddell Sea during CISW. F_{cond} and F_{atm} represent the conductive flux through the ice and the heat loss to the atmosphere from the snow surface, respectively.

92), and between 0 and 15 W m^{-2} during the fall (days 92 to 145). The flux of heat from the snow surface to the atmosphere averaged 9-17 W m^{-2}. From the observed mass balance the required heat flux from the ocean was 7 W m^{-2}, which is significantly larger than our estimate of 1.7 W m^{-2}.

Several processes might contribute to the mismatch between these two estimates of oceanic heat loss to the ice. Since our estimate agrees well with direct measurements of the turbulent heat flux $\langle w'T' \rangle$ made by *McPhee and Martinson* [1994], we tend to favor the lower value. The complexity of the ice thermodynamics in this region, where much of the new ice formation is via flooding of snow-loaded sea ice rather than growth on the ice base, makes modeling more difficult [*Lytle and Ackley*, 1996]. Significant variability in ice and snow thickness also raises concerns about the applicability of data from the five ice-monitoring sites to the overall transfer of oceanic heat to the sea ice. Nevertheless, both estimates are much lower than the 19 W m^{-2} mean flux required for the Gyre-scale heat budget.

The high dissipation rates that we found at CISW during storms were primarily due to stress-driven mixing caused by the surface-layer water moving relative to the rough ice base. The observed evolution of the SML is not, however, solely due to stress-driven mixing. One possibility is that much of the observed variation in the depth of the SML is due to lateral variability rather than local temporal change. This would not be surprising, given the variability of the mesoscale velocity field as determined from geostrophy by *Muench and Gordon* [1995]. For example, the strong westward mesoscale flow of about 9 Sv that they find between 67.5° and 68.5°S (t = 101-120) could also advect in the new, deeper surface mixed layer structure that is found subsequent to that time.

The presence of a highly variable mesoscale flow, combined with the sampling constraints imposed by CISW's drift track, precludes simple comparisons between the estimated flux profiles an the observed downstream hydrographic variability of the warm-core current. Some of the hydrographic variability in Figures 2.4 and 2.5 is clearly due to the camp's transit over a spatially variable hydrographic field, for example the variation in temperature maxima (T_{max}) between regimes I-II and II-V. Any attempt to explain the apparent downward trend in T_{max} between t = 85 and t = 145 in terms of the observed

diapycnal heat fluxes is confused by the addition of fluid to the boundary flow near the Endeavor Ridge [*Muench and Gordon*, 1995].

Considering these caveats our principal conclusions are given below.

1. Double-diffusive convection is the dominant diapycnal heat transport mechanism in the permanent pycnocline, with a maximum estimated upward flux of 2 W m^{-2}. (Figures 2.7 and 2.8).
2. Mixing due to shear instabilities in the permanent pycnocline appears to provide a maximum of about 1 W m^{-2} of upward heat flux.
3. Intrusions are frequent in the depth range above the permanent pycnocline. This depth range is associated with isopycnals that intersect the surface mixed layer to the east and west of the CISW drift track. We hypothesize that mixing along these sloping isopycnals could be responsible for further heat loss from the warm core of the boundary current.
4. The seasonal pycnocline, which in summer and early fall protects the remnant of the previous year's winter mixed layer from surface effects, weakens during the ice drift, disappearing entirely near the end of April. The decay is strongly correlated with energetic stress-driven mixing during rapid ice motion in storms, however additional variability may be imposed by mixed-layer lateral advection associated with the mesoscale velocity field described by *Muench and Gordon* [1995].
5. The mean heat loss from the ocean to the ice is 1.7 W m^{-2}.

Ice Station Weddell was the first oceanographic study in the western Weddell Sea to obtain modern finescale and microscale measurements that allow direct estimates of fluxes in this region. Further measurements would be necessary to fully understand the small-scale mixing processes in the various hydrographic and current regimes revealed by the concurrent large-scale surveys described by *Muench and Gordon* [1995]. In many ways, the warm core current that was under CISW for most of the experiment is an anomalous component of the general northward flow of the western Weddell Gyre. This flow includes the shelf circulation to the west and the more horizontally homogeneous hydrography of the central Gyre to the east of the CISW drift track. Mixing mechanisms over the upper slope and broad continental shelf [e.g. *Carmack*, 1986] differ significantly

from those revealed by the present study. From data collected in the southern Weddell Sea, *Foster et al.* [1987] proposed that barotropic shelf waves could advect the WDW, which is generally confined seaward of the shelf/slope front, onto the shelf where mixing could be accomplished by shear instabilities in the semidiurnal tides and perhaps higher-frequency internal gravity waves. Nonlinearities in the equation of state, such as cabbeling [*Fofonoff*, 1956; *Foster*, 1972; *Foster and Carmack*, 1976a] and thermobaricity [*Gill*, 1973] also become critical as the density contrast between surface and deeper waters is reduced. Similar processes are presumably operating over the shelf and slope in the western Weddell Sea, since the cross-slope hydrographic structure [see *Muench and Gordon*, 1995] is similar to the southern shelf/slope. It is suggested that future studies in this region concentrate on mixing processes over the upper slope and central shelf, in particular the interaction between shelf water and WDW at the shelf/slope front.

2.7. References

Baker, M. A. and C. H. Gibson, Sampling turbulence in the stratified ocean: Statistical consequences of strong interactions, *J. Phys. Oceanogr.*, *17*, 1817-1836, 1987.

Bathmann, U., V. Smetacek, H. De Baar, E. Fahrbach, and G. Krause, The expeditions ANTARKTIS X/6-8 of the research vessel "*Polarstern*" in 1992/93, *Rep. Polar Res. 135*, Alfred-Wegener Institute for Polar and Mar. Res., Germany, 1994.

Boyd, T. J., and E. A. D'Asaro, Cooling of the West Spitsbergen Current, *J. Geophys. Res.*, *99*, 22,597-22,618, 1994.

Caldwell, D. R., T. M. Dillon, and J. N. Moum, The rapid-sampling vertical profiler: An evaluation, *J. Atmos. Oceanic Technol.*, 2, 615-625, 1985.

Carmack, E. C., Circulation and mixing in ice-covered waters, in *The Geophysics of Sea Ice*, edited by N. Untersteiner, pp. 641-712, Plenum, New York, 1986.

Dillon, T. M., The energetics of overturning structures: Implications for the theory of fossil turbulence, *J. Phys. Oceanogr.*, *14*, 541-549, 1984.

Fahrbach, E., G. Rohardt, M. Schröder, and V. Strass, Transport and structure of the Weddell Gyre, *Ann. Geophysicae, 12*, 840-855, 1994.

Fernando, H. J. S., Oceanographic implications of laboratory experiments on diffusive interfaces, *J. Phys. Oceanog.*, *19*, 1707-1715, 1989.

Fofonoff, N. P., Some properties of sea water influencing the formation of Antarctic bottom water, *Deep Sea Res.*, *4*, 32-35, 1956.

Foster, T. D., An analysis of the cabbeling instability in sea water, *J. Phys. Oceanogr.*, *2*, 294-301, 1972.

Foster, T. D., and E. C. Carmack, Temperature and salinity structure in the Weddell Sea, *J. Phys. Oceanogr.*, *6*, 36-44, 1976a.

Foster, T. D., and E. C. Carmack, Frontal zone mixing and Antarctic Bottom Water formation in the southern Weddell Sea, *Deep Sea Res.*, *23*, 301-317, 1976b.

Foster, T. D., A. Foldvik, and J. H. Middleton, Mixing and bottom water formation in the shelf break region of the southern Weddell Sea, *Deep Sea Res.*, *34*, 1771-1794, 1987.

Gill, A. E., Circulation and bottom water production in the Weddell Sea, *Deep Sea Res.*, *20*, 111-140, 1973.

Gordon, A. L., and B. A. Huber, Southern Ocean winter mixed layer, *J. Geophys. Res.*, *95*, 11,655-11,672, 1990.

Gordon, A. L., B. A. Huber, H. H. Hellmer, and A. Ffield, Deep and bottom water of the Weddell Sea's western rim, *Science*, *262*, 95-97, 1993a.

Gordon, A. L., and Ice Station Weddell Group of Principal Investigators and Chief Scientists, Weddell Sea exploration from ice station, *EOS Trans., AGU*, *74*, 121-126, 1993b.

Gregg, M. C., Diapycnal mixing in the thermocline: A review, *J. Geophys. Res.*, *92*, 5249-5286, 1987.

Gregg, M. C., Scaling turbulent dissipation in the thermocline, *J. Geophys. Res.*, *94*, 9686-9698, 1989.

Huber, B. A., P. A. Mele, W. E. Haines, A. L. Gordon, and V. I. Lukin, Ice Station Weddell 1, CTD/Hydrographic Data, *Tech. Rep. LDEO-94-2*, Lamont-Doherty Earth Obs., Palisades, N. Y., 1994.

Kelley, D., Effective diffusivities within thermohaline staircases, *J. Geophys. Res.*, *89*, 10,484-10,488, 1984.

Kelley, D., Fluxes through diffusive staircases: A new formulation, *J. Geophys. Res.*, *95*, 3365-3371, 1990.

LaBrecque, J. L., and M. E. Ghidella, Estimates of bathymetry, depth to magnetic basement, and sediment thickness for the western Weddell Basin, *Antarc. J. U.S.*, *27*, 68-70, 1993.

Ledwell, J. R., A. J. Watson, and C. S. Law, Evidence for the slow mixing across the pycnocline from an open-ocean tracer-release experiment, *Nature*, *364*, 701-703, 1993.

Lytle, V. I., and S. F. Ackley, Heat flux through sea ice in the western Weddell Sea: Convective and conductive transfer processes, *J. Geophys. Res.*, *101*, 8853-8868, 1996.

Marmorino, G. O., and D. R. Caldwell, Heat and salt transport through a diffusive thermohaline interface, *Deep Sea Res.*, *23*, 59-67, 1976.

McPhee, M. G., Analysis and prediction of short-term ice drift, *J. Offshore Mech. Arct. Eng.*, *110*, 94-100, 1988.

McPhee, M. G., Turbulent heat flux in the upper ocean under sea ice, *J. Geophys. Res.*, *97*, 5365-5379, 1992.

McPhee, M. G., On the turbulent mixing length in the oceanic boundary layer, *J. Phys. Oceanogr.*, *24*, 2014-2031, 1994.

McPhee, M. G., and D. G. Martinson, Turbulent mixing under drifting pack ice in the Weddell Sea, *Science*, *263*, 219-220, 1994.

Muench, R. D., and A. L. Gordon, Circulation and transport of water along the western Weddell Sea margin, *J. Geophys. Res.*, *100*, 18,503-18,516, 1995.

Muench, R. D., H. J. S. Fernando, and G. R. Stegun, Temperature and salinity staircases in the northwesten Weddell Sea, *J. Phys. Oceanogr.*, *20*, 295-306, 1990.

Muench, R. D., M. D. Morehead, and J. T. Gunn, Regional current measurements in the western Weddell Sea, *Antarc. Journal U.S.*, *27*, 108, 1993.

Orsi, A. H., W. D., Nowlin, Jr., and T. Whitworth III, On the circulation and stratification of the Weddell Gyre, *Deep Sea Res., 40*, 169-203, 1993.

Osborn, T. R., Estimates of the local rate of vertical diffusion from dissipation measurements, *J. Phys. Oceanog.*, *10*, 83-89, 1980.

Osborn, T. R., and W. R. Crawford, An airfoil probe for measuring turbulent velocity fluctuations in water, in *Air-Sea Interactions: Instruments and Methods*, 369-386, Plenum, New York, 1980.

Padman, L., Small-scale physical processes in the Arctic Ocean, In: *Arctic Oceanography: Marginal Ice Zones and Continental Shelves, Coastal Estuarine Stud.*, vol. 49, edited by W. O. Smith and J. M. Grebmeier, pp. 97-129, AGU, Washington, D. C., 1995.

Padman, L., and T. M. Dillon, Vertical heat fluxes through the Beaufort Sea thermohaline staircase, *J. Geophys. Res.*, *92*, 10,799-10,806, 1987.

Padman, L., and T. M. Dillon, On the horizontal extent of the Canada Basin thermohaline steps, *J. Phys. Oceanogr.*, *18*, 1458-1462, 1988.

Padman, L., and T. M. Dillon, Turbulent mixing near the Yermak Plateau during the Coordinated Eastern Arctic Experiment, *J. Geophys. Res.*, *96*, 4769-4782, 1991.

Ruddick, B., A practical indicator of the stability of the water column to double-diffusive activity, *Deep Sea Res.*, *30*, 1105-1107, 1983.

Ruddick, B., and D. Walsh, Observations of the density perturbations which drive thermohaline intrusions, in *Proceedings of the Chapman Conference on Double-Diffusive Convection*, Scottsdale, AZ, 1995.

Rudels, B., The diffusive interface at low stability: The importance of non-linearity and turbulent entrainment, *Tellus Series A 43*, 153-167, 1991.

Schmitt, R.W., Double diffusion in oceanography, *Ann. Rev. Fluid Mech., 26*, 255-285, 1994.

Stillinger, D. C., K. N. Helland, and C. W.Van Atta, Experiments of the transition of homogeneous turbulence to internal waves in a stratified fluid, *J. Fluid Mech., 131*, 91-122, 1983.

Taylor, J., The fluxes across a diffusive interface at low values of the density ratio, *Deep-Sea Res., 35*, 555-567, 1988.

Tennekes, H., and J. L. Lumley, *A First Course in Turbulence*, 300 pp., MIT Press, Cambridge, MA, 1992.

Toole, J. M., and D. T. Georgi, On the dynamics and effects of double-diffusively driven intrusions, *Prog. Oceanogr., 10*, 123-145, 1981.

Turner, J. S., *Buoyancy Effects in Fluids*, 368 pp; Cambridge University Press, New York, 1973.

Walsh, D., and B. Ruddick, Double-diffusive interleaving: The influence of non-constant diffusivities, *J. Phys. Oceanogr., 25*, 348-358, 1995.

Wijesekera, H. W., L. Padman, T. M. Dillon, M. D. Levine, C. A. Paulson, and R. Pinkel, The application of internal wave dissipation models to a region of strong mixing, *J. Phys. Oceanogr., 23*, 269-286, 1993.

Chapter 3

TIDES IN THE WEDDELL SEA

Robin Robertson, Laurie Padman, and Gary D. Egbert

Published in
Ocean, Ice and Atmosphere: Interactions at the Antarctic Continental Margin,
Antarctic Research Series, Vol. 75, edited by S. S. Jacobs and R. Weiss, 341-369,
AGU, Washington, D. C., 1998.

3.1. Abstract

We use a high-resolution barotropic tidal model to predict tidal elevations and currents in the Weddell Sea. The ocean cavity under the Filchner-Ronne Ice Shelf is included in the model domain. Tidal elevations exceed 1 m at the back of the Filchner-Ronne and Larsen Ice Shelves. Tidal velocities are small over the deep basins but are generally greater than 10 cm s^{-1} over the continental shelves. Velocities occasionally reach 1 m s^{-1} in the shallow water near the General Belgrano Bank and under the Ronne Ice Shelf near the ice front. Model performance was evaluated through comparisons with TOPEX/Poseidon altimetry, bottom pressure gauge records, and current meter data. The largest discrepancies between the model results and measurements occur over the continental slope and under the ice shelves. The principal error sources are believed to be inaccurate bathymetry in our model, tidal analysis limitations associated with short data record lengths, and omission of baroclinic tides. Model results indicate that tides play a significant role in the circulation and heat flux in the Weddell Sea. We discuss the influence of tides on mean flow through the modified effective bottom drag, and the generation of baroclinic tides and other internal gravity waves through interactions of the tide with topography.

3.2. Introduction

Recent studies have greatly improved our understanding of the ways in which tides can influence lower-frequency ocean variability [e.g., *Hatayama et al.*, 1996; *Ffield and Gordon*, 1996]. These authors focused on the potential for added vertical mixing in the pycnocline caused by shear instabilities initiated by baroclinic tides and other internal gravity waves, that can be generated when barotropic tides encounter steep or rough topography. This mixing can modify sea surface temperatures and salinities and, where the spatial gradient in the pycnocline mixing rate is large, generate geostrophically-balanced flows. Tidal current interactions with topography can also cause "rectified mean flows" [*Robinson*, 1981], which are Lagrangian circulations that may be an important component of net advective transport in some regions [e.g., *Loder*, 1980; *Kowalik and Proshutinsky*, 1995].

Studies of tides in high-latitude seas confirm these general influences discussed above. For example, *Polyakov* [1995] used a baroclinic tidal model to demonstrate that mixing associated with tidal currents near the basin boundaries can explain much of the spatial structure of the salinity field in the Arctic. *Parsons* [1995] found, using a three-dimensional model that included both tides and wind forcing, that the hydrographic field over the shallow shelf seas of the eastern Arctic is significantly modified by the addition of the tide. When the response of sea ice to the underlying oceanic tidal field is also considered, the influence of tides in the Arctic becomes even more profound. Tidal-frequency shear and strain fracture the sea ice, while open-water formation by periodic ice divergence greatly increases the mean loss of heat from the ocean to the polar atmosphere, with a subsequent increase in upper-ocean salinity as additional ice forms in the leads [*Kowalik and Proshutinsky*, 1994].

The present study explores the possibility that, as in the Arctic, tides in the Weddell Sea affect the lower-frequency oceanographic variability of the region. The Weddell Sea is an important element of the global "conveyor belt" [*Broecker and Peng*, 1982], being responsible for much (perhaps 50%) of the world ocean's Antarctic Bottom Water (AABW) production [e.g., *Carmack*, 1977]. For at least a decade, tides have been suspected of aiding this production, which involves the formation and mixing of distinct water types including cold, saline Western Shelf Water (WSW) and Warm Deep Water (WDW). *Foster et al.* [1987] suggested that mixing of WSW and WDW at the shelf/slope front is increased by energetic baroclinic tides and internal waves on the upper slope. *Foldvik and Gammelsrød* [1988] noted that the formation of high-salinity WSW was enhanced by increased open water near the Ronne ice front due, in part, to tidal divergence. *Levine et al.* [1997] suggested that the properties of the dense plume that flows off the shelves to become Weddell Sea Deep and Bottom Water and, ultimately AABW, will be modified by the increased benthic stirring due to tides. Increases in mean benthic stress due to tides might also retard the general oceanic circulation, which in this region consists of the wind- and thermohaline-forced Weddell Gyre.

Several measurements of tidal elevations and velocities have been made in the Weddell Sea [e.g., *Lutjeharms et al.*, 1985; *Pedley et al.*, 1986; *Foldvik et al.*, 1990;

Levine et al., 1997], but their spatial coverage is far from complete. Data are particularly sparse over the continental shelf and slope of the southwestern Weddell Sea, where much of the water mass formation and mixing responsible for AABW production is expected to occur. Numerical models provide the most effective method for improving our knowledge of tides in this region. The tides under the Filchner-Ronne Ice Shelves (FRIS) have been modeled by *Smithson et al.* [1996]; however, much of the Weddell Sea and the entire Scotia Sea were excluded from their domain. We have, therefore, constructed a high-resolution, non-linear, finite-difference, barotropic tidal model of the Weddell and Scotia Seas. The model is described in section 3.3, and available tidal measurements are reviewed in section 3.4. Output tidal fields are described in section 3.5. Model performance is evaluated with respect to observations, and the output from three global tidal models. The tidal energy budget is described in section 3.6. In section 3.7, we review two mechanisms by which tides might modify the Weddell Sea circulation and hydrographic structure: the reduction of the mean flow by the increase in the effective bottom friction; and generation of baroclinic tides. The influence of tides on the sea-ice cover is addressed in a separate paper [*Padman et al.*, 1998]. A summary, including ideas for future work, is provided in section 3.8.

3.3. Modeling Approach

3.3.1. Model Domain, Bathymetry, and Grid

Our model domain extends from 83°10'S to 55°00'S, and from 84°00'W to 10°00'E (Figure 3.1). This region includes the ocean cavity under the FRIS, and other ice shelves. Over most of the domain, we obtained bathymetry from the ETOPO-5 database, which provides depths on a 1/12° global grid [*National Geophysical Data Center*, 1992]. However, modifications to the model bathymetry were made in several regions where more recent data have become available. Bathymetry based on satellite altimetry and aircraft gravimetric surveys, as well as depth measurements from Ice Station Weddell [*LaBrecque and Ghidella*, 1993] was used in the western Weddell Sea in the region 73°S to 65°S, and 60°W to 44°W. Minor additional modifications were made along the edges

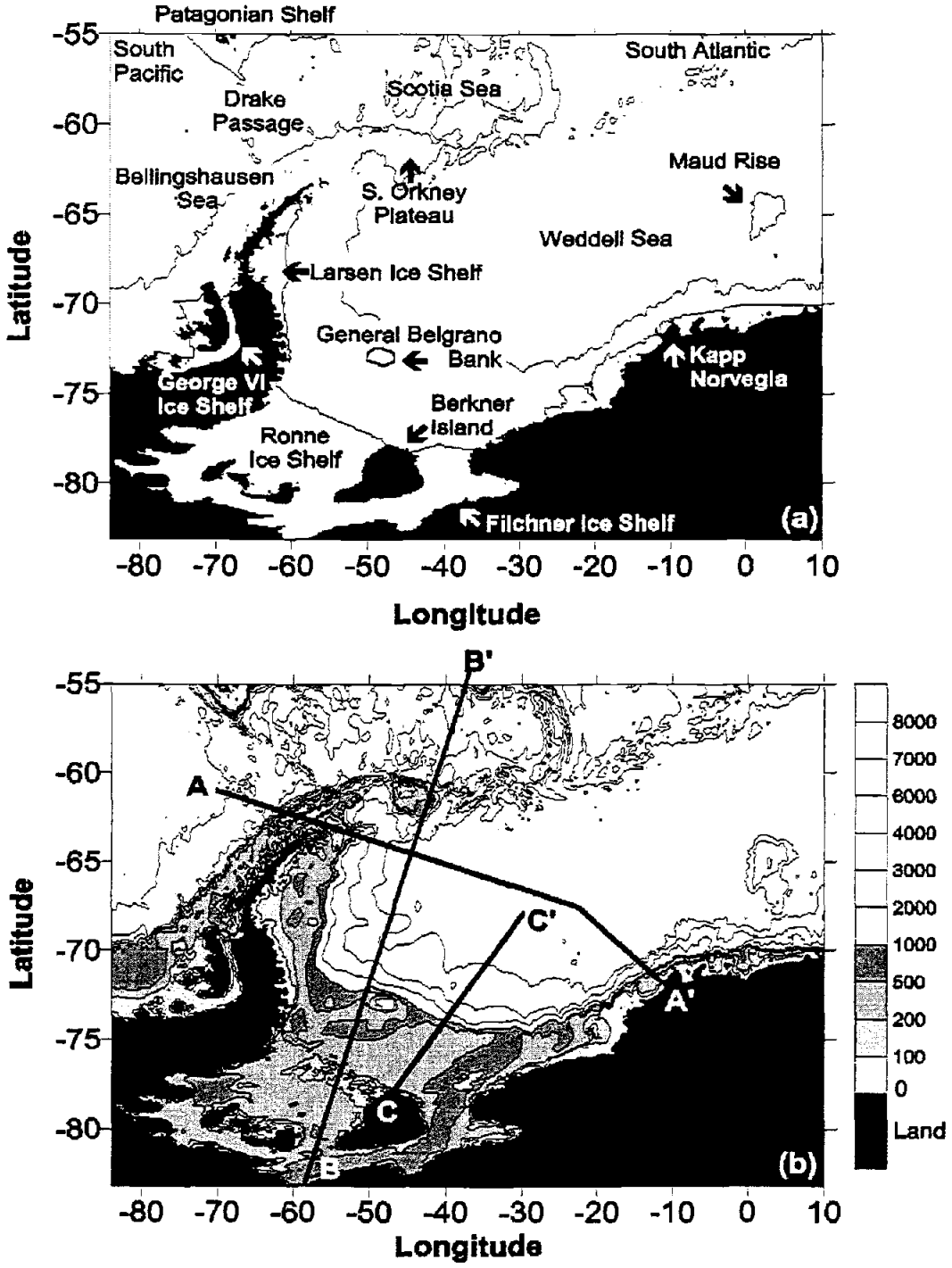

Figure 3.1. (a) The model domain with important topographic features noted. Ice shelves are shaded gray and the 3000 m isobath is indicated. (b) Water column height over the model domain, which is water column thickness under the FRIS and bathymetry elsewhere. Depths less than 1000 m are shaded, and the other contours that are shown are indicated on the scale. The locations of three transects, A-A', B-B', and C-C' (see Figure 3.5), are shown.

of this region to smooth the transition between the two data sets. Under the FRIS, measurements of water column thickness were used instead of bathymetry [*Vaughan et al.*, 1994]. Bathymetry in front of the FRIS was modified to agree with *Gammelsrød et al.* [1994]. Throughout the domain, depths less than 2 m have been converted to land to avoid the occurrence of negative water column thickness, which can otherwise result as tidal elevation fluctuates.

An Arakawa-C grid was used. The grid spacing is 1/6° in longitude and 1/12° in latitude, resulting in a 565 x 339 array. This grid size provides acceptable computational speed, and is also comparable to the resolution of the depth databases. We note, however, that ETOPO-5 is a gridded data set that has been interpolated from available, irregularly spaced, ship track data. In several parts of the model domain, especially over the southwestern shelves and under the ice shelves, no real depth data are available [see *Padman et al.*, 1998]. Additionally, *Smith* [1993] cautioned that the ETOPO-5 bathymetry is generally smoother than the actual topography. He also noted that the interpolation scheme could add unrealistic bathymetric structure in regions without ship tracks.

3.3.2. Equations and Boundary Conditions

Analyses of data from moorings with current meters at more than one depth suggest that tidal kinetic energy in the Weddell Sea is generally dominated by the barotropic (i.e., depth-independent) component. *Middleton and Foster* [1977] found that the barotropic tide accounted for 50% and 72% of the tidal energy in the southern Weddell Sea, for the semidiurnal and diurnal constituents, respectively. Data from Ice Station Weddell, in the western Weddell Sea, showed that there was only a very small velocity difference between currents at 50 m and 200 m below the drifting ice camps [*Levine et al.*, 1997], again consistent with a predominantly barotropic tide. For this first modeling effort, we have chosen a two-dimensional, depth-integrated barotropic model and therefore ignore variations of currents with depth.

The model uses the mass conservation and depth-integrated shallow water momentum equations:

$$\eta_t + \frac{\partial U}{\partial x} + \frac{\partial V}{\partial y} = 0 \tag{3.1}$$

$$U_t = -\frac{U}{H}\frac{\partial U}{\partial x} - \frac{V}{H}\frac{\partial U}{\partial y} + 2\Omega \sin\theta V - \beta g H \frac{\partial \eta}{\partial x} - \frac{C_D U|\mathrm{U}|}{H^2} + \left(\frac{\partial^2 U}{\partial x^2} + \frac{\partial^2 U}{\partial y^2}\right) + F_U \tag{3.2a}$$

Advection Coriolis Pressure Bottom Stress Lateral Viscosity Astronomical Forcing

$$V_t = -\frac{U}{H}\frac{\partial V}{\partial x} - \frac{V}{H}\frac{\partial V}{\partial y} - 2\Omega \sin\theta U - \beta g H \frac{\partial \eta}{\partial y} - \frac{C_D V|\mathrm{U}|}{H^2} + \left(\frac{\partial^2 V}{\partial x^2} + \frac{\partial^2 V}{\partial y^2}\right) + F_V \tag{3.2b}$$

where η is the height above mean sea level, U and V are volume transports in the east-west and north-south directions, respectively, and $\mathbf{U}$ $(=Ui+Vj)$ is the volume transport vector. In the open ocean, $H(x,y)$ represents the water depth, while under the ice shelves it represents the water column thickness. In the Coriolis term, Ω is the angular rotation of the earth ($=7.292\text{x}10^{-5}\ \text{s}^{-1}$) and θ is the latitude. The pressure term includes g, the gravitational acceleration ($9.8\ \text{m s}^{-2}$), and a simplified scalar factor to correct for tidal loading and ocean self-attraction ($\beta = 0.9$) [*Schwiderski*, 1980]. Bottom frictional stress is represented by a quadratic drag formulation with a drag coefficient, C_D, of 0.003. We chose this value because it was within the range of observed values, 0.001 to 0.003 [*Gallagher and Munk*, 1971], and is similar to those used in other numerical models, [e.g. *Ramming and Kowalik*, p. 17, 1980; *MacAyeal*, 1984; *Parker*, 1991; *Kowalik and Proshutinsky*, 1994; *Le Provost et al.*, 1994]. Sensitivity tests in which C_D was varied between 0.0025 and 0.0035 indicate only minor variations in tidal heights and currents. Under the ice shelves, C_D was doubled to account for the additional drag at the ice/water interface [*MacAyeal*, 1984]. The ice shelf edge location was obtained from the *Central Intelligence Agency* [1972] coastline data set (Figure 3.1a).

A lateral viscosity coefficient, (A_H) of 1000 m^2s^{-1} is used. This value is at the top of the range of 50-1000 m^2s^{-1} used in the Arctic by *Kowalik and Proshutinsky* [1994], and is an order of magnitude higher than that used in the Ross Sea (100 m^2s^{-1}) by *MacAyeal* [1984]. It is, however, within the range of estimated values and provides the necessary model stability. The forcing functions for the velocities, F_U and F_V, are determined from

the astronomical tide-generating potentials [e.g., *Cartwright and Taylor*, 1971] and corrected for solid earth tides in the standard way.

Four tidal constituents were modeled, two semidiurnal (M_2 and S_2), and two diurnal (O_1 and K_1). Although the relative strengths of tidal constituents vary with location, these four constituents generally account for about 70-80% of the total tidal elevation [*Pond and Pickard*, 1978, p 260]. The available tidal elevation data in our model domain support this estimate.

For land boundaries, both the no-normal flow and no-slip conditions are used. At open boundaries, setting either the elevation or the normal flow leads to a mathematically well-posed problem. We used tide height coefficients obtained from TPXO.3, an updated version of the global inverse solution described in *Egbert, Bennett, and Foreman (EBF)* [1994] based on assimilation of approximately three years of TOPEX/Poseidon altimetry data. This model was chosen due to its availability and its known good performance [*Andersen et al.*, 1995].

The model was implemented on a Thinking Machines CM-5. A 12 s time step was used to satisfy the *Courant-Friedrichs-Levy* stability condition [*Haltiner and Williams,* 1980]. The model simulations were run for 105 days. For the parameters we used, the model stabilized after approximately 50 days. After stabilization, the model elevation results were harmonically analyzed for 45 days, producing fields of the amplitude and phase for each tidal constituent. The velocity components were also harmonically analyzed for 45 days to obtain estimates of the major and minor axes, inclination, and phase for the tidal ellipses, following the definitions of *Foreman* [1978].

3.3.3. Sources of Error in the Model

The primary sources of error for the model are uncertainties in boundary conditions and bathymetry, and the use of simplified shallow water equations (including the barotropic assumption). The boundary condition errors are dependent on the quality of the TPXO.3 global solution. For our model domain, the worst performance for TPXO.2 (the global model that preceded TPXO.3) was in Drake Passage where root mean square (rms) differences were 3.6, 1.3, 1.3, and 1.0 cm for the M_2, S_2, O_1, and K_1 constituents,

respectively [*Andersen et al.*, 1995]. These estimates should be viewed as upper limits, however. They were generated when only one year of altimetry data was available for the *EBF* model. Presently, the *EBF* model incorporates three years of altimetry data and its performance has improved significantly, particularly in the region of Drake Passage and the Patagonian Shelf.

In the shallow water equations, the physics for both the bottom stress term and the lateral viscosity term have been parameterized and thus are potential sources of error. Exclusion of processes such as baroclinicity, and stress at the interface separating the sea ice from the ocean, are additional error sources. We believe, however, that poor bathymetric information is likely to be most significant single error source for our model. The bathymetry is poorly known in several parts of the model domain, especially over the southwestern shelves [see *Padman et al.*, 1998], and under the ice shelves. *Padman et al.* [1998] demonstrate that changing the model bathymetry based on observations of iceberg grounding [*Viehoff and Li*, 1995] can change predicted currents in some regions of our model by as much as a factor of four.

3.4. Validation Data

3.4.1. Elevation Measurements

Two types of elevation measurements, satellite altimetry and tide gauges, were available for comparison with the model. The satellite data consist of coefficients determined by harmonic analysis of sea surface elevation at 356 crossover points from three years of TOPEX/Poseidon data (1993-1996). The southern limit for these data is about 66°S. Tide gauge data consist of elevation time series at a few coastal stations on the Antarctic continent in the Weddell Sea [*Smithson*, 1992; *Genco et al.*, 1994], and several records obtained from the "open" water [*Middleton and Foster*, 1977; *Middleton et al.*, 1982, 1987; *Lutjeharms et al.*, 1985; *Foldvik et al.*, 1990] and under the FRIS [*Thiel et al.*, 1960; *Pratt*, 1960; *Hisdal*, 1965; *Stephenson et al.*, 1979; *Eckstaller and Miller*, 1984; *Smith*, 1991; *Doake*, 1992]. Thirty-one elevation observations were found within the model domain (Figure 3.2a). These observations are summarized in Table 3.1,

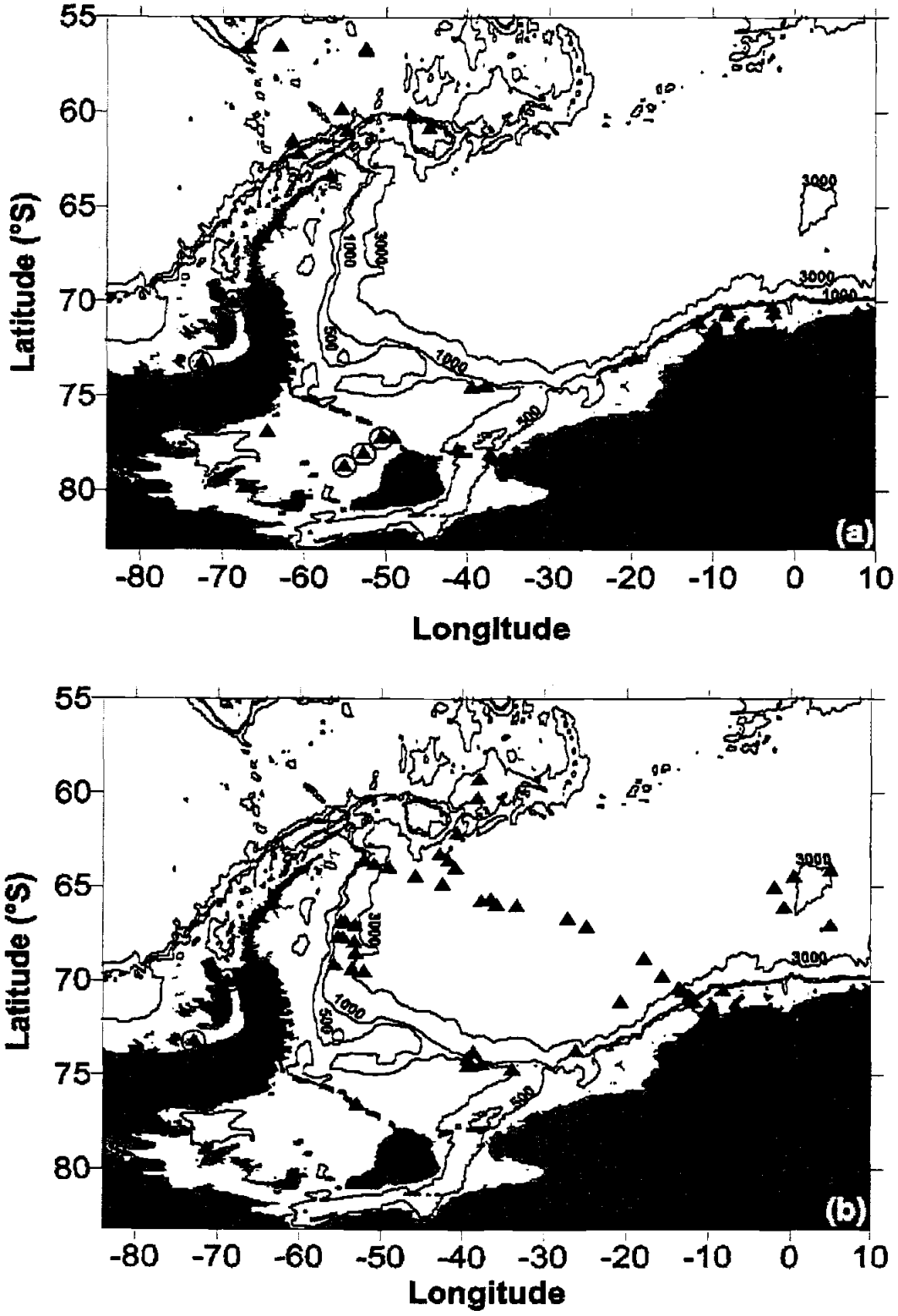

Figure 3.2. (a) The location of the tide gauge observations, with the locations shown as triangles. Circled triangles indicate instruments that were ignored. The 500, 1000, and 3000 m isobaths (or water column thickness isolines under the FRIS) are shown. (b) The locations of the current meter observations, with the locations shown as triangles.

First Author	Year	Latitude	Longitude	Depth observation (m)	Depth model (m)	Record Length (days)	rms error (cm)	Category
Smith	1991	79°44'S	67°21'W	N/A	194	43	>12	Ice Shelf
Eckstaller	1984	78°37'S	55°8'W	N/A	371	5 to 10	N/A	ignored
Stephenson	1979	78°33'S	82°58'W	N/A	10	4	N/A	Ice Shelf
Pratt	1960	77°58'S	37°10'W	N/A	481	51	N/A	Open Water
Eckstaller	1979	77°53'S	52°45'W	N/A	178	5 to 10	N/A	Ignored
Thiel	1960	77°42.6'S	41°8.0'W	792	591	30	2,4,8,4 †	Ice Shelf
Eckstaller	1984	77°8'S	50°30'W	N/A	236	5 to 10	N/A	Ignored
Foldvik	1982a	77°7'S	49°3'W	260	252	4.2	3,2,2,2 †	Ice Shelf
Doake	1992	76°45'S	64°30'W	N/A	375	9	N/A	Ice Shelf
Foldvik	1985b	74°26'S	39°24'W	450	466	30	1	Open Water
Middleton	1982	74°23'S	37°39'W	470	521	180	4	Open Water
Potter	1985	73°8'S	72°32'W	583	100	357	N/A	Ignored
Smithson	1992	72°53'S	19°37'W	461	1793	316	N/A	Open Water
Smithson	1992	71°3'S	11°45'W	430	416	367	N/A	Open Water
Lutjeharms	1985	70°37'S	8°32'W	N/A	107	27	N/A	Open Water
Hisdal	1965	70°30'S	2°32'W	N/A	27	3	N/A	Open Water
Smithson	1992	70°26'S	8°18'W	468	407	324	N/A	Open Water
Lutjeharms	1985	70°12.5'S	2°43.5'W	307	173	20	7	Open Water
Potter	1985	69°58'S	68°51'W	512	100	16	N/A	Ignored
Genco	1994	63°17'S	56°55'W	N/A	188	N/A	N/A	Open Water
Smithson	1992	62°8'S	60°41'W	500	369	358	3	Open Water
Smithson	1992	61°28'S	61°17'W	3946	4264	320	3	Open Water
Smithson	1992	60°51'S	54°43'W	1020	1736	378	4	Open Water
Genco	1994	60°43'S	44°39'W	N/A	136	N/A	N/A	Open Water
Smithson	1992	60°3'S	47°5'W	2010	2272	408	3	Open Water
Smithson	1992	60°2'S	47°6'W	2180	2657	208	3	Open Water
Smithson	1992	59°44'S	55°30.'W	3690	3565	377	8	Open Water
Smithson	1992	56°42'S	52°32'W	3150	4943	349	5	Open Water
Smithson	1992	56°40'S	52°29'W	2891	4218	375	5	Open Water
Smithson	1992	56°32'S	67°0'W	500	1162	364	2	Open Water
Smithson	1992	56°29'S	62°59'W	3925	3965	320	6	Open Water

† For these two records, rms errors are errors on individual constituents, M_2, S_2, O_1, and K_1, respectively.

Table 3.1. The first author and location for the tide gauge elevation observations. The depth of the observation and the depth used by the model for that location are also given along with the record length and the measurement uncertainty. N/A denotes that the quantity is unknown. The category used for comparison against the model results is included. The designation 'ignored' indicates an observation was not included in the determination of the standard deviation of the differences between model results and observations. Multiple values for the uncertainty indicate the uncertainties for the M_2, S_2, O_1, and K_1 constituents, respectively.

using the first author of each reference as an identifier. (For the *Genco et al.* [1994] and *Pratt* [1960] observations, measurements were published only for the M_2 constituent.) Twenty-one observations were in open water and ten records were obtained under, or at the edge of, an ice shelf (Figure 3.2a). Five of the ice shelf observations were discarded due either to the instrument type or inaccurate bathymetry. These have been circled in Figure 3.2a.

Two types of instrument were used to obtain tidal elevation under the ice shelves. Tiltmeters measure the tilting of the ice shelf, and gravimeters, which convert variations in gravity to tidal displacements as described by *Thiel et al.* [1960]. *Doake* [1992] compared a tiltmeter and a gravimeter located in close proximity and observed that "the gravity amplitudes were about 30% higher than the amplitudes from the tilt records". He postulated that the ice shelf tilt measurements were erroneous due to the use of an inadequate parameterization of the tidal flexure in their calibration. Consequently, three tiltmeter observations [*Eckstaller and Miller,* 1984] have been excluded from the data comparisons with our model. Because the ETOPO-5 bathymetry under the George VI ice shelf is inconsistent with water depths reported by *Potter et al.* [1985], two tide gauge observations from under the George VI ice shelf [*Potter et al.*, 1985; *Pedley et al.*, 1986] were also excluded from the comparisons (Figure 3.2a).

Both the satellite and the tide gauge data are subject to measurement errors, which need to be considered when determining the quality of the tidal model solution. In standard tidal analysis (see, e.g., *Foreman* [1978]), a set of sine and cosine waves with specific tidal frequencies is fit to the time series of height (or velocity). The resultant coefficients then describe both the amplitudes and the phases of the best-fit tidal constituents. A time series of data residuals can also be calculated, representing that part of the signal that cannot be explained by the set of tidal constituents that were generated by the multivariate fit. Data residuals include instrument errors, as well as true oceanic signals at frequencies that have not been included in the fitting scheme. The latter signals include tidal energy at excluded frequencies, doppler-shifted tidal energy (particularly due to baroclinic currents), and non-tidal energy.

For the satellite data, the estimated error in the amplitude of each tidal constituent was about 3-4 cm. Errors for the tide gauge observations depend on the instrument used to make the measurement. When known, the estimated *rms* residual error for each measurement is given in Table 3.1. The amplitude error for each tidal constituent in a multivariate fit is provided by the fitting procedure, and is typically much less than the *rms* residual error. When more than one number is shown in Table 3.1, the numbers represent the reported errors for the M_2, S_2, O_1, and K_1 constituents, respectively. If the *rms* residual error was not reported, 4 cm was used for the open water measurements and 10 cm for the ice shelf ones. Errors are also larger when the record being analyzed is too short to allow all the energetic tidal constituents to be resolved. At least 15 days of hourly data is required to resolve M_2 from S_2, and O_1 from K_1, and errors in specific constituents will become much larger as record lengths become shorter than this. Many of the ice shelf observations suffer from short record lengths.

3.4.2. Velocity Measurements

Sixty-four current meter records were found within the model domain (Figure 3.2b). Observations were not used if they were in the bottom boundary layer, defined as within 50 m of the seabed: currents in the boundary layer may not represent the mean water column velocity, which is being simulated by our barotropic model. Table 3.2 lists these observations using the first author of the reference as an identifier.

Two of these measurements were made under, or at the edge of, the Ronne Ice Shelf. Ninety-five days of current meter measurements were obtained by deploying a current meter through the ice shelf (K. Nicholls, personal communication, 1996), and *Nygaard* [1995] collected over a year of current meter measurements at a site at the ice shelf edge. Two current meter observations made under the George VI ice shelf [*Potter et al.*, 1985; *Pedley et al.*, 1986] have been excluded in the comparisons because we do not have any reliable bathymetric data in the region surrounding these measurement sites.

Of the sixty open-water locations, thirty observations were provided by *Fahrbach et al.* [1992, 1994], who moored current meters at various locations between the tip of the Antarctic Peninsula and Kapp Norvegia. Most of these moorings provided more than one

First Author	Year	Latitude	Longitude	Depth for observation (m)	Depth for model (m)	Depth of instrument (m)	Record Length (Days)	Category
Nicholls	-	78° 52.0'S	71° 20.3'W	485	525	N/A	95	Ice Shelf
Nygaard	1995	76° 29'S	53° 0'W	431	414	411	435	Ice Shelf
Middleton †	1982	74° 40'S	33° 56'W	475	437	375	410	C. Shelf
Middleton †	1982	74° 26'S	39° 24'W	475	466	375	630	C. Shelf
Middleton †	1982	74° 24'S	39° 6'W	465	448	400	510	C. Shelf
Foldvik	1990	74° 23'S	37° 39'W	475	521	450	31	C. Shelf
Foldvik	1990	74° 8'S	39° 19'W	650	655	627	460	C. Slope
Middleton †	1982	74° 6'S	39° 22'W	720	763	620	600	C. Slope
Middleton †	1982	73° 43'S	38° 36'W	1915	1852	1815	420	C. Slope
Fahrbach	1994	73° 37.6'S	26° 7'W	3360	1658	3197	250	Deep
Fahrbach	1992	72° 52.8'S	19° 37.5'W	415	1793	280	310	ignored
Potter	1985	73° 9'S	72° 49'W	720	100	249	25	ignored
Fahrbach	1992	71° 7.7'S	12° 11.9'W	682	352	255	330	C. Slope
Fahrbach	1994	71° 5.8'S	20° 47.1'W	4440	4289	4277	370	Deep
Fahrbach	1992	71° 3.3'S	11° 44.1'W	380	416	260	300	C. Shelf
Fahrbach	1994	71° 3.0'S	11° 46.0'W	467	416	462	300	C. Shelf
Fahrbach	1994	71° 2.7'S	11° 45.4'W	425	416	325	30	C. Shelf
Fahrbach	1994	71° 2.4'S	11° 44.6'W	676	416	293	360	C. Slope
Fahrbach	1994	70° 59.2'S	11° 49.4'W	2364	481	706	430	C. Slope
Fahrbach	1994	70° 56.4'S	11° 57.7'W	1522	1029	320	420	C. Slope
Fahrbach	1994	70° 54.7'S	11° 57.8'W	1555	1029	760	380	C. Slope
Fahrbach	1994	70° 42.6'S	12° 21.5'W	2123	1760	978	310	C. Slope
Fahrbach	1994	70° 29.7'S	13° 8.9'W	2450	2726	340	400	C. Slope
Fahrbach	1994	70° 29.5'S	13° 7.0'W	2364	2726	856	430	C. Slope
Fahrbach	1992	70° 26.0'S	8° 18.0'W	408	407	330	310	C. Shelf
Fahrbach	1994	70° 22.8'S	13° 32.5'W	2950	3988	940	400	C. Slope
Fahrbach	1994	70° 19.1'S	13° 39.6'W	4330	4392	1130	320	Deep
Potter	1985	69° 58'S	68° 51'W	512	100	N/A	N/A	ignored
Fahrbach	1994	69° 39.6'S	15° 42.9'W	4728	4777	988	430	Deep
Levine	1997	69° 24.9'S	52° 10.3'W	N/A	3217	200	15	Deep
Levine	1997	69° 19.0'S	53° 37.8'W	2700	2890	200	15	C. Slope
Levine	1997	69° 6.8'S	55° 46.1'W	N/A	1535	50	15	C. Slope
Fahrbach	1994	68° 49.7'S	17° 54.5'W	4740	4759	4240	700	Deep
Levine	1997	68° 27.7'S	53° 8.9'W	2900	2584	200	19	C. Slope
Levine	1997	67° 50.2'S	53° 18.4'W	2900	2591	200	15	C. Slope
Levine	1997	67° 40.1'S	54° 43.0'W	N/A	2180	200	15	C. Slope
Levine	1997	67° 37.7'S	55° 18.8'W	N/A	1693	50	15	C. Slope
Fahrbach	1994	67° 3.6'S	24° 52.1'W	4840	4747	4340	400	Deep
Levine	1997	66° 59.4'S	53° 11.4'W	2900	2816	200	15	C. Slope
Bersch	1992	66° 59.2'S	4° 59.4'E	4158	4054	959	180	Deep
Levine	1997	66° 48.7'S	54° 26.9'W	N/A	2238	200	15	C. Slope
Levine	1997	66° 48.5'S	55° 1.0'W	N/A	1721	50	15	C. Slope
Fahrbach	1994	66° 37.4'S	27° 7.1'W	4830	4788	293	430	Deep
Middleton	1977	66° 26.3'S	41°2.6'W	3540		4510	349	Deep
Fahrbach	1994	66° 16.6'S	30° 17.8'W	4750	4788	2840	370	Deep
Bersch	1992	66° 3.2'S	0° 47.1'W	4100	4594	1180	110	Deep
Fahrbach	1994	65° 58.2'S	33° 20.3'W	4800	4896	4300	390	Deep
Barber	1995	65° 55.2'S	35° 49.4'W	4770	4696	4270	270	Deep
Fahrbach	1994	65° 39.9'S	37° 42.5'W	4730	4650	4455	400	Deep
Fahrbach	1994	65° 38.1'S	36° 30.2'W	4710	4701	2534	410/700	Deep
Bersch	1992	64° 58.6'S	2° 0.2'W	4331	5012	901	180	Deep
Fahrbach	1994	64° 48.9'S	42° 29.3'W	4650	4635	1000	400	Deep
Fahrbach	1994	64° 25.1'S	45° 51.0'W	4390	4434	220	430	Deep
Bersch	1992	64° 24.5'S	0° 22.2'E	5019	3624	1120	180	Deep

Table 3.2. (continued)

First Author	Year	Latitude	Longitude	Depth for observation (m)	Depth for model (m)	Depth of instrument (m)	Record Length (Days)	Category
Bersch	1992	64° 1.2'S	1° 20.8'E	3721	2844	1043	180	Deep
Fahrbach	1994	63° 57.0'S	49° 9.2'W	3480	3279	2970	420	Deep
Barber	1995	63° 10.7'S	42° 46.0'W	3855	3660	3355	350	Deep
Barber	1995	62° 4.5'S	40° 35.7'W	3375	3352	3365	340	Deep
Barber	1995	60° 11.3'S	38° 8.6'W	2969	3133	2959	290	C. Slope
Barber	1995	59° 8.8'S	37° 57.6'W	2870	2930	2070	160	C. Slope

† *Foldvik et al.* [1990] is a more useful reference for these observations..

Table 3.2. The first author and location for the velocity observations. The depth of the observation and the depth used by the model for that location are also given along with the record length. The category used for comparison against the model results is included.

year of continuous data. At some sites, currents were measured at more than one depth. In these cases we excluded data from within 200 m of the ocean surface. The remaining mid-water column measurements at one site usually agreed with each other within the measurement uncertainty, consistent with our barotropic assumption. For those cases where the observations disagreed, the measurement with the longer time series was used. For two sites, we averaged the mid-water column current meters. One of the *Fahrbach et al.* sites was excluded from the model evaluation because of a large discrepancy between the reported water depth at the measurement location, 415 m, and the model bathymetry, ~1800 m. The velocity is known to be strongly dependent upon bathymetry, therefore comparing modeled and measured currents at this location seemed inappropriate. Ten observations were provided by *Levine et al.* [1997], who analyzed current meters located at 50 m and 200 m below the various camps of Ice Station Weddell. Since the camps were moving, the current meter data were broken into 15-day segments for analysis. The average location for the camp during each time segment was used for the observation location. Eight observations were collected as part of a Weddell Sea tidal study [*Foldvik and Kvinge*, 1974; *Middleton and Foster*, 1977; *Foldvik et al.*, 1982a,b, 1985a,b; *Middleton et al.*, 1982, 1987; *Foldvik et al.*, 1990]. All but one of these observations were made in the southwestern Weddell Sea near the shelf/slope break, and record lengths were typically from one to two years. A mid-basin observation described in these studies was excluded because the current meter was within 30 m of the bottom

[*Middleton and Foster*, 1977]. *Barber and Crane* [1995] made seven observations near the tip of the Antarctic Peninsula. Finally, five observations with lengths of about a half-year were collected by *Bersch et al.* [1992] near Maud Rise. *Foreman*'s [1978] analysis software was used to determine the tidal constituents for these observations.

As with the elevation data, estimates of velocity errors are needed before measurements can be used to evaluate model performance. Typical rms residual errors for the *Levine et al.* [1997] and *Bersch et al.* [1992] records were about 2-3 cm s^{-1}, with the exception of the two northernmost Ice Station Weddell camp locations, which had values of about 6 cm s^{-1}. We attribute these higher residual errors to greater motion of the camp during this time period. For locations for which error estimates were not available, we used an *rms* residual error of 2 cm s^{-1}, which is consistent with the measurement error for Aanderaa current meters [*Aanderaa Instruments*, 1979]. Record length is also a significant factor in the accuracy of the tidal constituents: errors increase with shorter record length, and are particularly severe for records of less than 30 days. As described in section 3.4.1, the error on individual constituent velocities will be less than the *rms* residual error. For comparison purposes, the uncertainty in each constituent was therefore taken to be 1 cm s^{-1}, which represents a relatively small percentage error for regions of strong tidal flows in our model.

3.5. Model Results

3.5.1. Tidal Elevations

The largest tidal elevations are due to the semidiurnal constituents. The M_2 constituent has a tidal amplitude greater than 1.5 m at the southwestern end of the Ronne Ice Shelf (Figure 3.3a), and greater than 1.0 m under the Larsen Ice Shelf. For M_2, there are two amphidromic points, one in the northeastern Weddell Sea and one near the edge of the Ronne Ice Shelf. Phase generally propagates from east to west along the Antarctic continent, and clockwise under the FRIS. The S_2 constituent (Figure 3.3b) is structurally similar to M_2, although it's amplitude is smaller and there is an additional amphidromic point near the tip of South America.

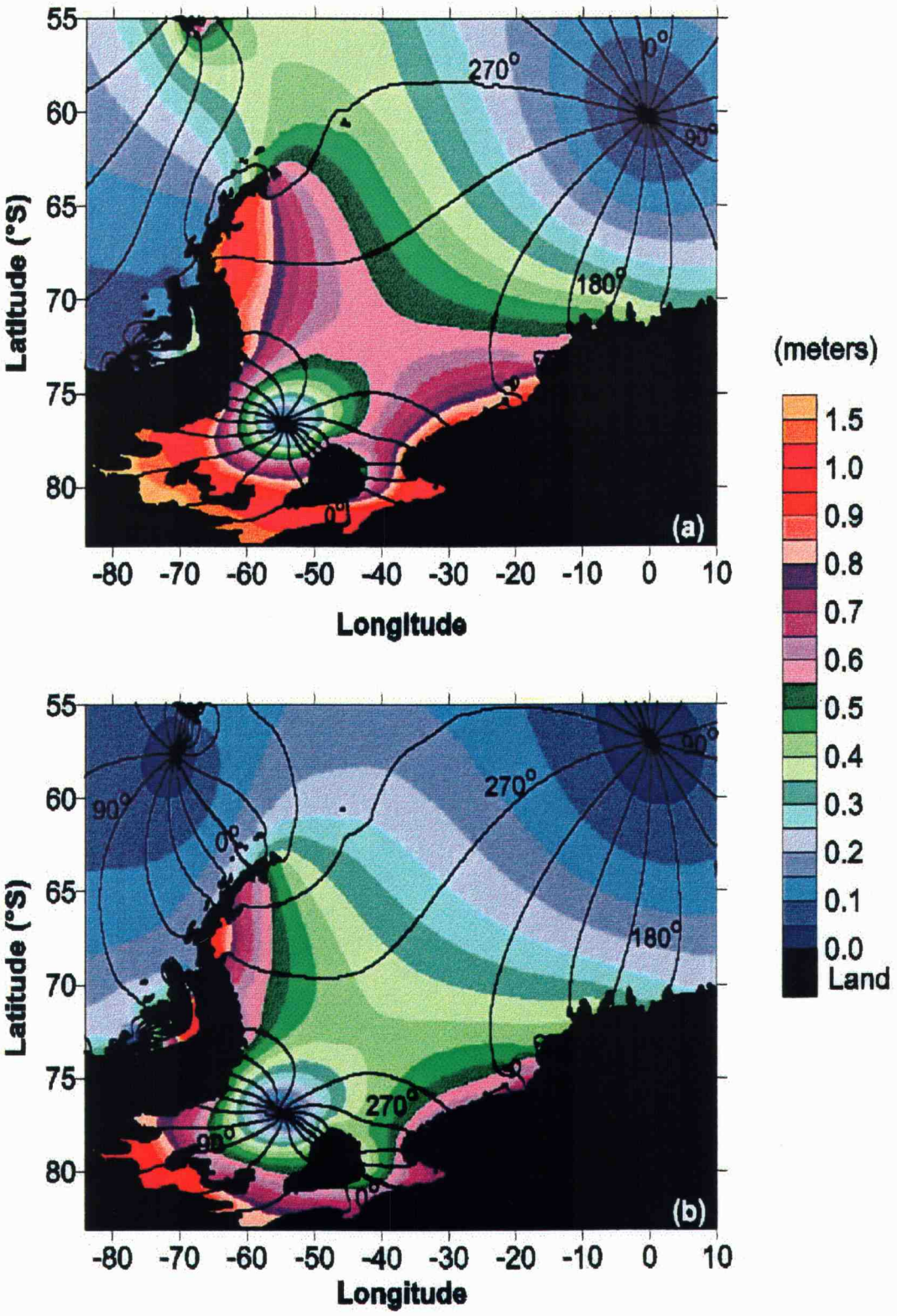

Figure 3.3. The elevation amplitude and phase for the (a) M_2, (b) S_2, (c) K_1, and (d) O_1 constituents, with the amplitude given by the color scale and the phase by the contour lines. The contour interval is 22.5° in phase.

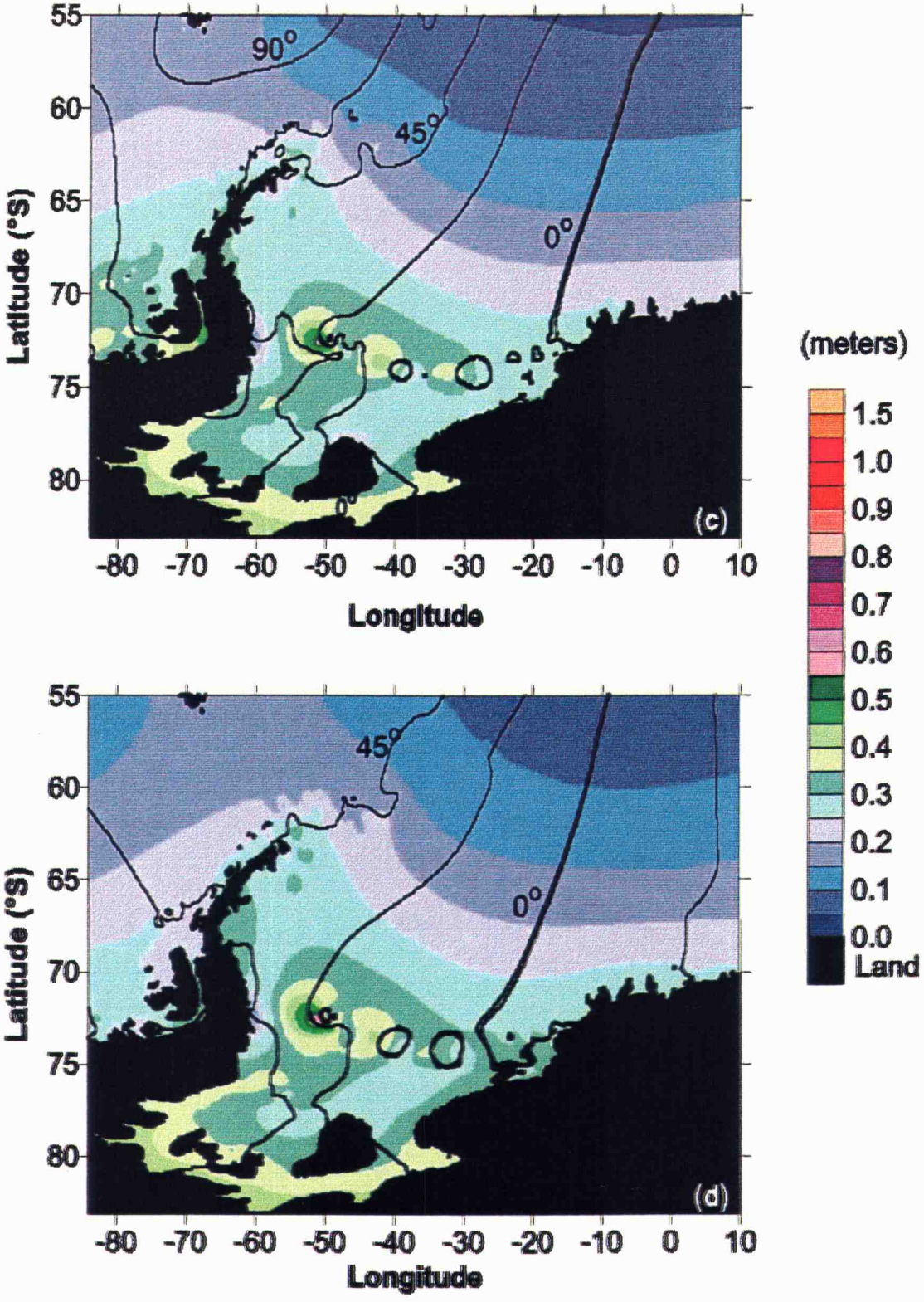

Figure 3.3 (continued)

The tidal amplitude for the diurnal constituent, K_1, generally increases towards the Antarctic continent, except for an area along the outer southern shelf including the General Belgrano Bank (Figure 3.3c). The structure of the O_1 constituent (Figure 3.3d) is very similar to K_1. No amphidromic points occur within our model domain for the diurnal constituents, and the phase propagates roughly from east to west, except for a region of complex structure along the southern slope, which can be ascribed to the presence of diurnal shelf waves along the southern shelf and slope. These shelf modes will be considered in more detail in a future study.

3.5.2. Tidal Velocities

The lengths of the major axes for the modeled current ellipses (U_{maj}) for the M_2 and O_1 components are shown in Figure 3.4. The value of $U_{maj}(M_2)$ exceeds 5 cm s^{-1} over most of the shelf and upper slope. Values greater than 30 cm s^{-1} are found under the leading edge of the Ronne Ice Shelf west of Berkner Island, on the Patagonian Shelf, under the Brunt and Riiser-Larsen Ice Shelf (near 20°W on the Antarctic coast), and in Bransfield Strait. Other regions of strong M_2 currents are: the General Belgrano Bank; a region from 15°W to 25°W along the Antarctic coast; and much of the western Weddell Sea shelf adjacent to, and under, the Larsen Ice Shelf.

For the diurnal constituents, $U_{maj}(O_1)$ is largest over the General Belgrano Bank, exceeding 75 cm s^{-1} in this region. Other regions of strong diurnal currents include: the entire outer shelf in the southern Weddell Sea; the front of the Ronne Ice Shelf; and near the northern tip of the Antarctic Peninsula, including Bransfield Strait and the South Orkney Plateau. Diurnal tides are expected to exist in these regions as topographically-trapped shelf modes, and thus tend to be strongest over the upper continental slope where the bottom slope is steep and the water depth is relatively shallow [*Loder*, 1980; *Middleton et al.*, 1987; *Padman et al.*, 1992]. Because of the sensitivity of diurnal currents to topography, relatively small errors in bathymetry can radically alter the modeled currents. We have made several model runs with varying bathymetry to investigate this sensitivity, and some comparisons will be presented by *Padman et al.* [1998]. One sensitivity run involved modifications of the southern shelf/slope between

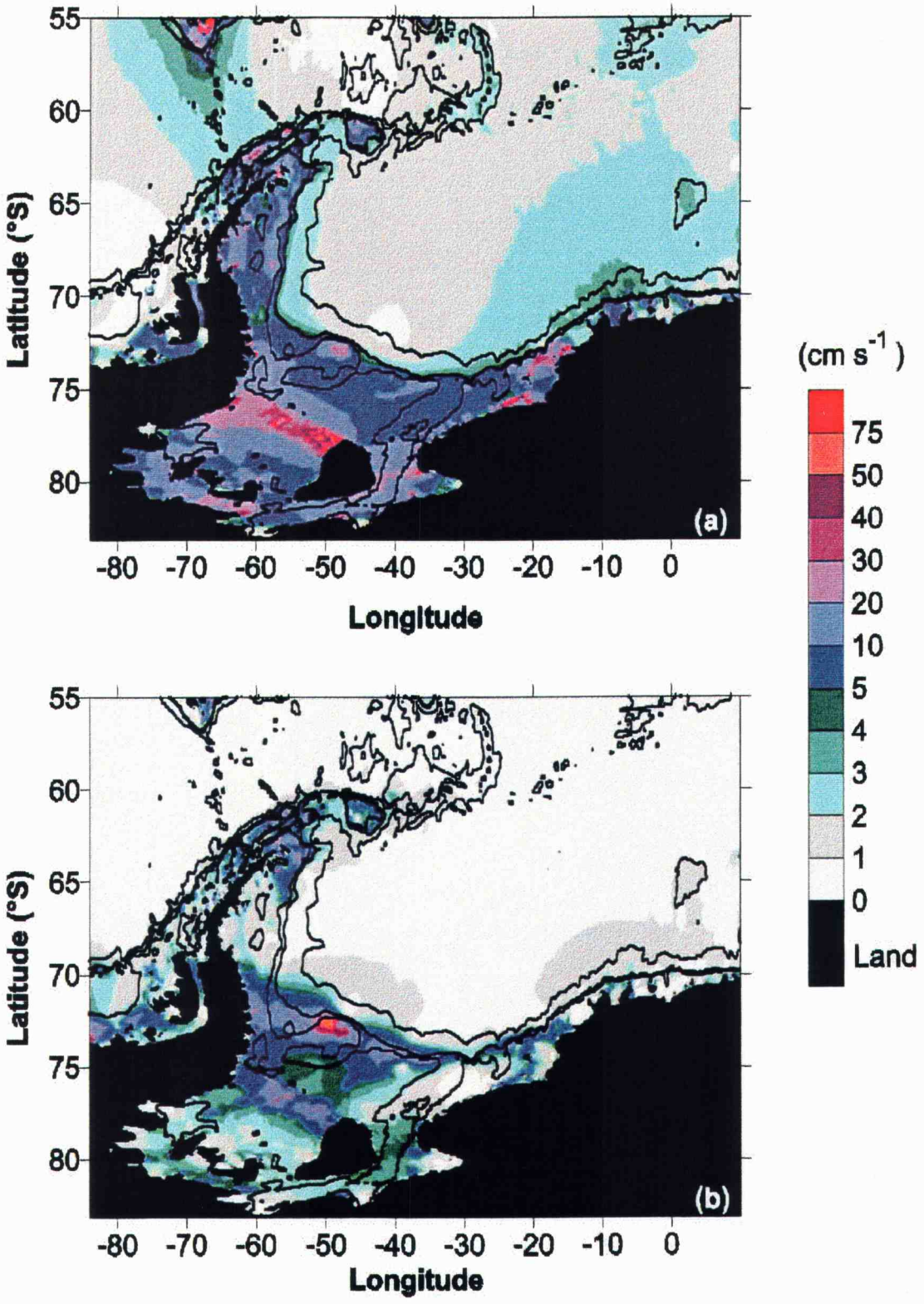

Figure 3.4. Length of major axis of the modeled tidal ellipse for (a) the M_2 and (b) O_1 constituents. Isobaths (or water column thickness isolines under the FRIS) for 500, 1000, and 3000 m are shown. Note that the color ranges are not evenly spaced.

50°W and 60°W, in a region with very little available bathymetric data. It is possible, with model bathymetry that is not inconsistent with available depth data, to reduce $U_{maj}(O_1)$ over the General Belgrano Bank to less than 20 cm s^{-1}, i.e., less than 25% of the value shown in Figure 3.4b. At present we favor the lower value of $U_{maj}(O_1)$ for this region, based on observed tidal-frequency ice motion [*Padman et al.*, 1998]. However, the results shown here are appropriate for the bathymetry given by GEBCO chart 5.18 with the revisions we have made based on *LaBrecque and Ghidella* [1993].

The relationship between tidal currents and bathymetry can be seen in transects of $U_{maj}(M_2)$ and $U_{maj}(O_1)$ (Figure 3.5) along the lines A-A', B-B', and C-C' (Figure 3.1b). As we noted above, the strongest M_2 currents tend to occur in shallow water, e.g., at the front of the Ronne Ice Shelf (~77°S in Figure 3.5b) and over the broad southern shelf (south of ~74°S in Figure 3.5c). Diurnal currents are usually strong at the upper continental slope and at other rapid changes in bathymetry. One exception is over the narrow shelf near Kapp Norvegia (Figure 3.5a): this is typical of most of the Antarctic coastline east of about 20°W in our model (Figure 3.4b).

A useful measure of a typical tidal current magnitude is given by

$$u_{typ}^2 = \sum_{i=1}^{4} \left(u_i^2 + v_i^2 \right), \tag{3.3}$$

where u_i and v_i are the amplitudes of the east and north components of velocity for tidal constituent '*i*'. Values of u_{typ} are usually small over the deep basin but increase to over 5 cm s^{-1} near the shelf break (Figure 3.6). Currents greater than 10 cm s^{-1} are common over the continental shelves and are significantly larger than the mean boundary currents of 4-6 cm s^{-1} [*Fahrbach et al.*, 1994] associated with the Weddell Gyre. The largest tidal currents occur in regions where the bathymetry changes rapidly. Maximum values of u_{typ} are greater than 1 m s^{-1} and occur near General Belgrano Bank, where diurnal constituents dominate the total tidal signal (Figure 3.5b and Figure 3.6b). Velocities greater than 75 cm s^{-1} also occur under the Ronne Ice Shelf near the ice front, where semidiurnal constituents dominate (Figure 3.5b and Figure 3.6b).

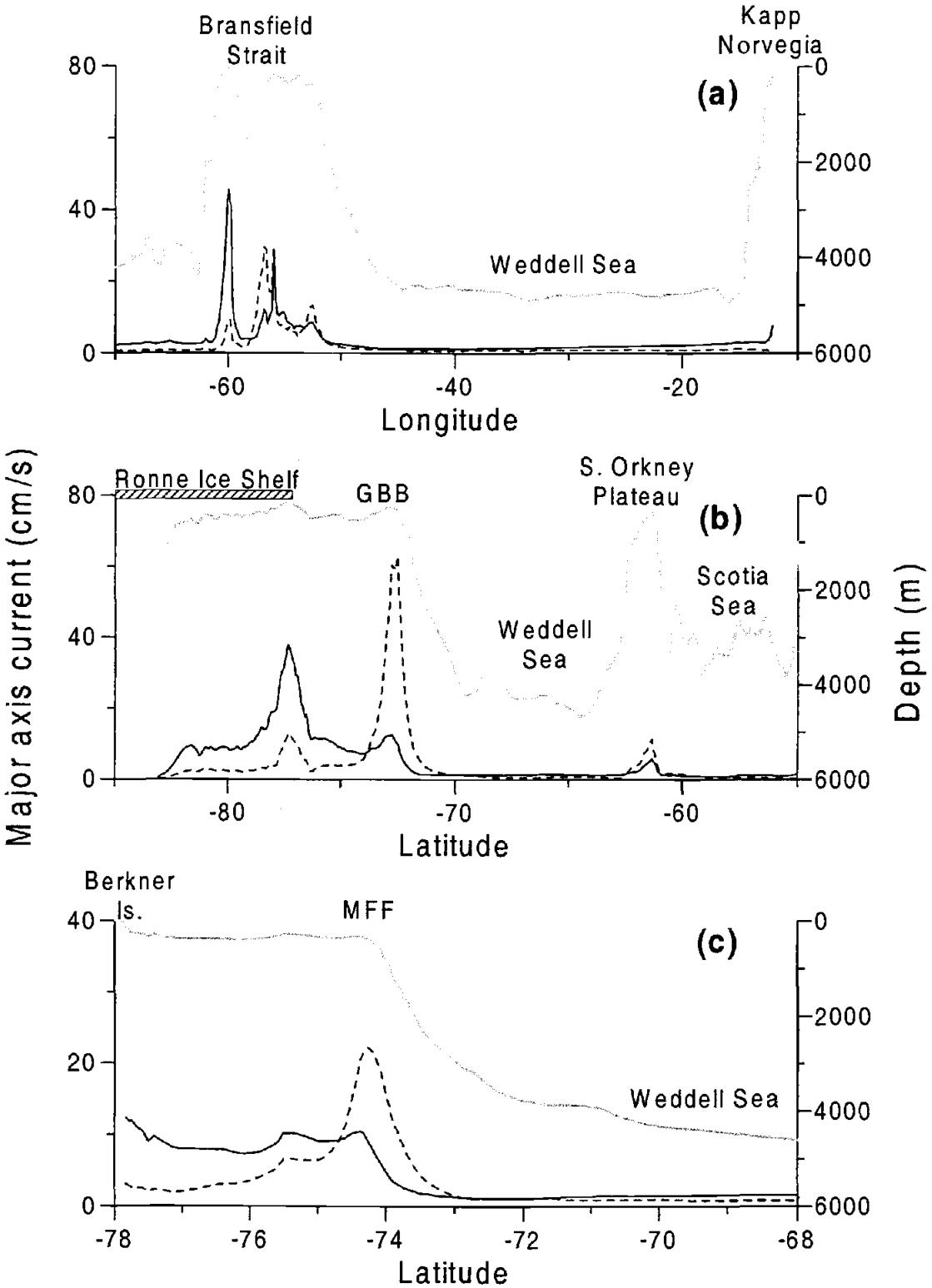

Figure 3.5. Transects of bathymetry (gray line) and M_2 and O_1 major axis lengths (solid line, $U_{maj}(M_2)$; dashed line, $U_{maj}(O_1)$) for the three transects on Figure 1b: (a) transect A-A'; (b) transect B-B'; (c) transect C-C'. Features shown include the General Belgrano Bank ("GBB" in (b)), and the *Middleton et al.* [1987] moorings ("MFF" in (c)).

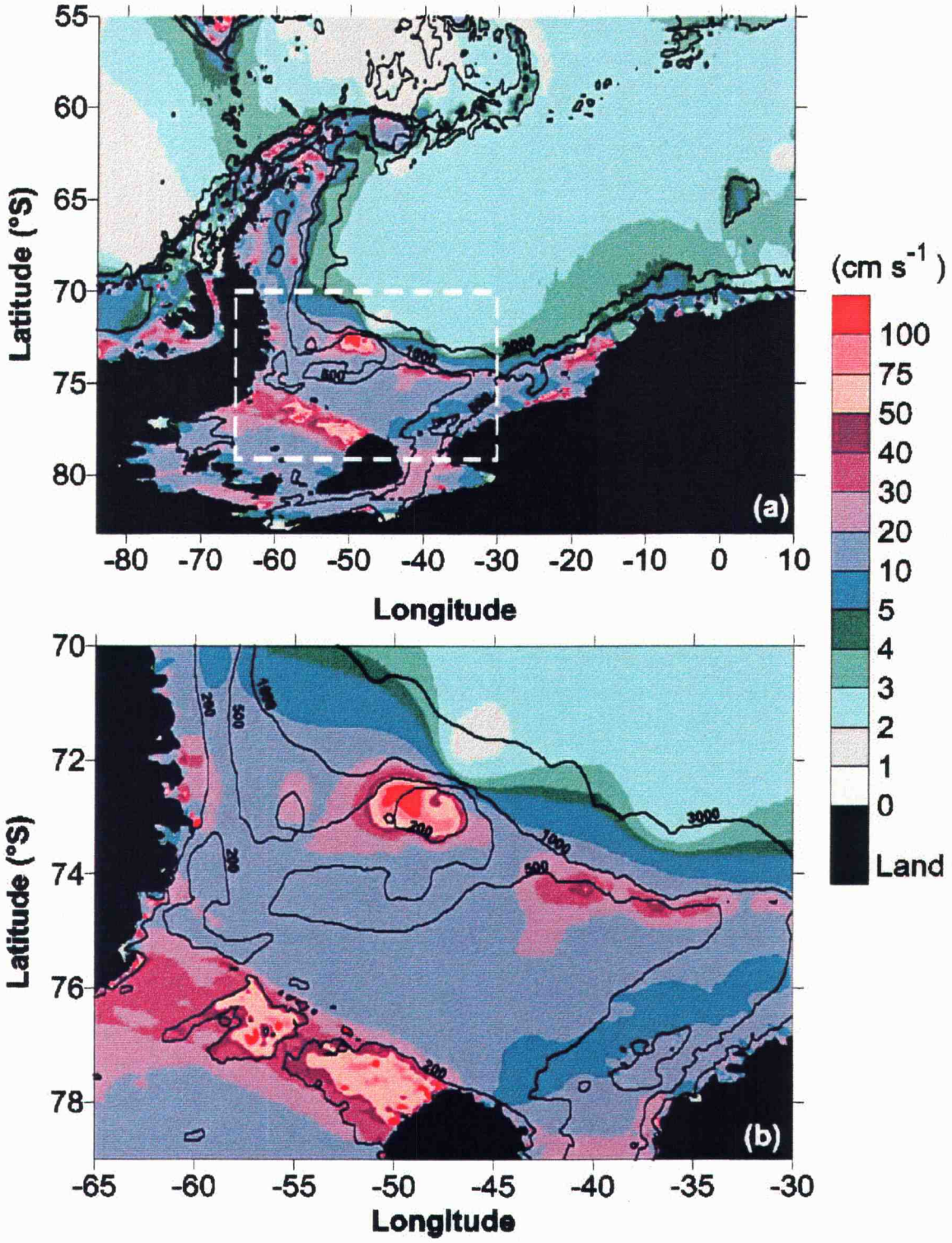

Figure 3.6. (a) The combined typical current speed (U_{typ}: (eq. 3.3)) for the four principal tidal constituents for the entire model domain. The 500, 1000, and 3000 m isobaths (or water column thickness isolines under the FRIS) are shown. (b) As for (a), but for only the central southern shelf region. The 200 m water column thickness line has been added. Note that the color ranges are not evenly spaced.

3.5.3. Comparisons Between Model Results and Measurements

3.5.3.1. *Elevations*

For comparison purposes, the model domain was broken into two categories: open water; and under the ice shelf or at its edge (Table 3.1). All of the satellite altimetry data lie in the open water. Twenty-one non-satellite tidal elevation measurements are in the open water category and five in the ice shelf category. For each measurement location and for each tidal constituent, we first calculate the difference (δ_i) between the model-predicted elevation amplitude ($a_{m,i}$) and the amplitude based on data ($a_{d,i}$), where subscript '*i*' identifies a specific tidal constituent. Then, for each ocean category with M comparison sites, we determine the standard deviation of δ_i. A similar calculation is made for phase. These values are given in Table 3.3. The equivalent *rms* percentage errors, for amplitudes, were determined from $\{M^{-1}\Sigma[(100\delta_i/a_{d,i})^2]\}^{1/2}$, where the *rms* error is used for $a_{d,i}$ if $a_{d,i}$ is less than the *rms* error.

Model results agree quite well with the satellite data. The standard deviation of the differences between the model results and measurements, for all four constituents, were 3 cm or less in amplitude and 9 to 32° in phase. Good agreement was found for tide gauge data in the open water. The standard deviation of the amplitude errors was 5 cm or less, and 5-8° for phase. The percentage error for these standard deviations ranged from 8 to 19%, which is lower than the percentages for the satellite data, 16 to 47%. Since the percentages are based on the magnitude of the elevation, and the elevations are typically larger in the shallower water where the tidal gauges are usually located, equivalent absolute differences for the standard deviation result in smaller percentages. Under the ice shelves, the agreement between model results and measurements was poorer, with standard deviation errors of 8-14 cm for amplitude and 12-70° for phase. The largest phase errors under the ice shelves were associated with the diurnal constituents. Due to the higher mean amplitudes, the percentages of error for these standard deviations were still reasonably low, less than 25% except for S_2.

Comparisons of model elevation coefficients and measurements are shown in Figures 3.7a-d for the M_2, S_2, O_1, and K_1 constituents, respectively. As we noted above, there are

Model	Category	Data Source	N[a]	M_2		S_2		O_1		K_1	
				A[b] (cm)	Phase (°)	A[b] (cm)	Phase (°)	A[b] (cm)	Phase (°)	A[b] (cm)	Phase (°)
Robertson et al.	Open Water	Satellite Data	356	2 (16 %)	16	3 (47 %)	32	1 (16 %)	9	3 (25 %)	20
Robertson et al.	Open Water	Tide Gauges	18 (21)	5 (8 %)	7	3 (13 %)	8	2 (8 %)	5	5 (19 %)	6
Robertson et al.	Under the Ice Shelf	Tide Gauges	5	12 (24 %)	12	14 (51 %)	20	8 (16 %)	62	9 (22 %)	70
TPXO.3: Egbert et al.	Open Water	Tide Gauges	17 (19)	5 (11 %)	11	4 (12 %)	12	2 (8 %)	7	4 (20 %)	5
FES95.2: Le Provost et al.	Open Water	Tide Gauges	17 (19)	5 (12 %)	26	6 (29 %)	38	5 (19 %)	18	4 (20 %)	20
AG95: Andersen-Grenoble	Open Water	Tide Gauges	15 (16)	3 (28 %)	8	1 (19 %)	5	3 (33 %)	26	2 (14 %)	31

a. Number of Observations
b. Amplitude

Table 3.3. Standard deviations of the differences between the model elevation results and the observations for the two categories, open water, and at the edge of, or under the ice shelf. For the open water comparison, the differences were determined both for the satellite data and the tide gauge data. The corresponding percentages are shown for the amplitudes. The number of points used in each comparison is shown, with the number in parentheses indicating the number for the M_2 constituent if a different number was used for its comparison. The standard deviations of the differences in open water are also shown for the *Egbert et al.* [1994] (TPXO.3), *Le Provost et al.* [1994] (FES95.2), and Andersen-Grenoble [*Jet Propulsion Laboratory*, 1996] (AG95) models.

a variety of reasons for mismatches between the model output and data. The two error sources that are believed to be most important are model response to errors in bathymetry and constituent errors in the data due to short analysis record lengths as identified on Figure 3.7. Points where the model amplitude estimates differ by more than 25% from data are examined in Appendix A. The phases agree well for most measurement locations and constituents (Figures 3.7e-h).

3.5.3.2. *Velocities*

The model velocities were compared with the sixty velocity measurements described in section 3.4.2. Except for the major axis, the tidal ellipse descriptors are very unstable when velocities are low. We therefore compared only the modeled and measured major axes of the tidal ellipses, and ignored the other three descriptors, the minor axis, inclination, and phase. Model velocities at each location were adjusted by the ratio of the model water depth to the reported depth for the measurement site; i.e., we actually compared the depth-integrated barotropic transports. The domain was broken into three water depth categories, the continental shelf, the continental slope, and deep water, and a fourth category for the area under the ice shelf or at its edge (Table 3.2). Eight data points are located on the continental shelf, which was defined as having a depth of less than 500 m and not being under an ice shelf. Twenty-five data points are located on the continental slope, with depths ranging from 500 to 3000 m. Twenty-five data points are located in deep water, with depths greater than 3000 m. Two points are in the ice shelf category.

The standard deviation of the differences between the major axis from the model and that of the measurement (Table 3.4) was calculated in the same manner as for the elevations (section 3.5.3.1, above). In deep water, velocities were small and the standard deviations of the differences were less than or equal to 1.5 cm s^{-1}. For the continental slope, the standard deviations of the differences were larger 1.2-4.8 cm s^{-1} (57-131%). On the continental shelf, standard deviations were as large as 1.9 cm s^{-1} (55%) for semidiurnal constituents, and 6.8 cm s^{-1} (266%) for the diurnal constituents. The large

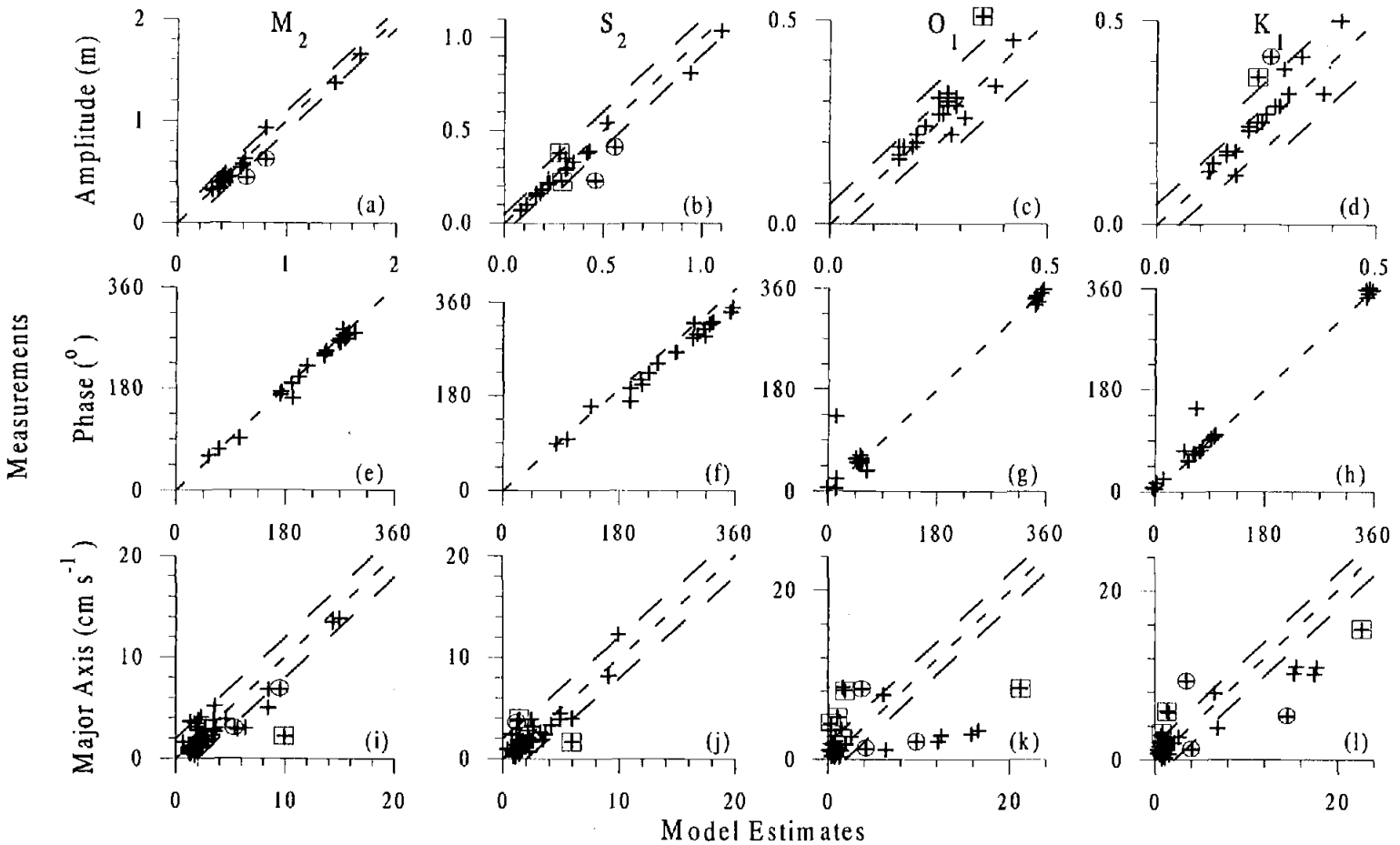

Figure 3.7. The correlation between the model results and the observed harmonic constituents for (a-d) the tidal elevation, (e-h) phase for the elevation, and (i-l) major axis for the M_2, S_2, O_1, and K_1 constituents, respectively. The short-dashed line represents perfect agreement between the model results and the measurements: the area above the line indicates under-prediction by the model. The long-dashed lines represent estimates of general measurement uncertainties. Observations with short record lengths have been indicated with squares and those believed to have inaccurate topography with circles.

Category	M_2	S_2	O_1	K_1
Continental Shelf	1.9 (55 %)	0.8 (21 %)	6.8 (266 %)	5.2 (84 %)
Continental Slope	2.0 (83 %)	1.2 (57 %)	4.8 (131 %)	2.7 (57 %)
Deep	0.7 (43 %)	0.5 (35 %)	1.5 (95 %)	0.9 (26 %)
Ice Shelf	1.4 (44 %)	2.8 (97 %)	2.7 (32 %)	3.5 (45 %)

Table 3.4. Standard deviations of the differences between the model major axes and the observations for the four categories shown, with the corresponding percentages.

errors for the diurnal constituents are probably associated with the presence of topographically trapped, diurnal shelf waves [*Middleton et al.*, 1987]. These waves are sensitive to both the along-slope and cross-slope topography. Our model predicts amplification for the O_1 constituent that was not observed by *Middleton et al.* [1987]. For the ice shelf regions, the standard deviations of the model misfits reached 3.5 cm s^{-1}.

The correlations between the model and measured velocities are shown for the four constituents in Figures 3.7i-l. The convention is the same as used for the elevation comparisons. The primary error sources are again inaccurate model bathymetry and measurement errors, particularly due to short record lengths. Baroclinicity is an additional error source for the velocities. The largest discrepancies between the model velocities and the measurements are discussed in Appendix B.

3.5.4. Comparison of Model Results with Three Global Models

We evaluate the effect of increased resolution, improved bathymetric data, and the explicit inclusion in our model of the ocean cavity under the FRIS, by comparing the results of our model with three global tidal models: TPXO.3 [*EBF*], FES95.2 [*Le Provost et al.*, 1994], and AG95 [*Andersen*, 1995]. These comparisons were only made for the open water regions. The standard deviations of the elevation differences were calculated

for this model, following the procedure described in section 3.5.3.1. Since the model domains cover slightly different areas, some of the tidal gauge locations are not included in all domains. The number of locations used for each of the calculations is given in Table 3.3. Our model reproduced measured tidal elevations slightly better than TPXO.3 and FES95.2 in the open water for the semidiurnal constituents. The AG95 model has lower standard deviations for the differences, but higher percentage errors. As its does not include some areas where several of the shallower tide gauges were located, the AG95 standard deviations are biased toward the smaller elevations of deeper water, resulting in smaller values with higher corresponding percentages. Thus, the smaller standard deviations of the differences for AG95, which does not include our entire model domain, do not necessarily indicate improved performance.

Velocities were not available for the FES95.2 and AG95 models. Therefore, only the TPXO.3 model was used for a velocity comparison. Although the elevations were similar, the TPXO.3 model does not generate the high velocities seen in our model. This was particularly evident in the shallower water in the southern portion of the domain and at the continental shelf/slope break. The velocities at the southern slope/shelf break, where short-wavelength, topographically trapped shelf waves occur, were underpredicted by ~10 cm s^{-1} by *EBF* for K_1, compared to our overprediction of ~5 cm s^{-1}. The higher currents in our model can be attributed to improved bathymetry and higher grid resolution.

3.6. Tidal Energy Balance

3.6.1. Tidal Energy Flux

For any region of the model domain, the tidal energy balance can be written as:

$$\oint_L \langle E_n\, dl \rangle + \iint_{Area} \langle \mathbf{F}(x,y)\cdot\mathbf{u} \rangle dx\, dy - \iint_{Area} \langle D(x,y) \rangle dx\, dy = 0 \qquad (3.4)$$

where E_n is the energy flux normal to the closed boundary (L), $\mathbf{F}(x,y)$ represents local astronomical forcing corrected for solid earth tides, $D(x,y)$ represents the sum of local dissipation terms, and angle brackets represent time averaging. The dissipation term includes bottom friction and lateral friction, which are both parameterized in our model. Recall that the friction between the glacial ice shelves and the ocean has been represented by doubling C_D in these regions. Other dissipative terms that we have not modeled include stress at the interface between sea ice and the ocean, "topographic drag" (i.e., energy input into baroclinic motion such as internal tides), and ice shelf flexure.

The first term in (3.4) is the energy flux divergence, which balances any energy production ($\langle \mathbf{F} \cdot \mathbf{u} \rangle$) and dissipation ($D$) within the area enclosed by L. For each constituent, the components of energy flux at any point in the model domain, averaged over a complete tidal period, are

$$E_u = 0.5 \rho g \beta H A_u A_\eta \cos(\theta_u - \theta_\eta), \tag{3.5a}$$

and

$$E_v = 0.5 \rho g \beta H A_v A_\eta \cos(\theta_v - \theta_\eta). \tag{3.5b}$$

In (3.5), H is the water depth, A_u, A_v, and A_η are the constituent amplitudes for the east/west velocity, the north/south velocity, and the elevation respectively, and θ_u, θ_v, and θ_η are the associated phases. As in (3.2), the factor β=0.9 is applied as a simple correction for ocean loading and self-attraction [*Egbert*, 1997]. The factor of 0.5 arises from time averaging over a complete tidal cycle.

On average, the energy flux is clockwise around the Weddell Sea for all constituents. For M_2 (Figure 3.8a), the flux is westward along the Antarctic coast, turning southward under the FRIS, primarily through the Filchner Depression. This energy under the FRIS propagates clockwise and emerges at the western end of the Ronne Ice Shelf, then flows northwards along the eastern side of the Antarctic Peninsula, across Drake Passage and up the east coast of South America. Significant energy also flows around the Patagonian shelf from the South Pacific into the South Atlantic. For the O_1 constituent (Figure 3.8b),

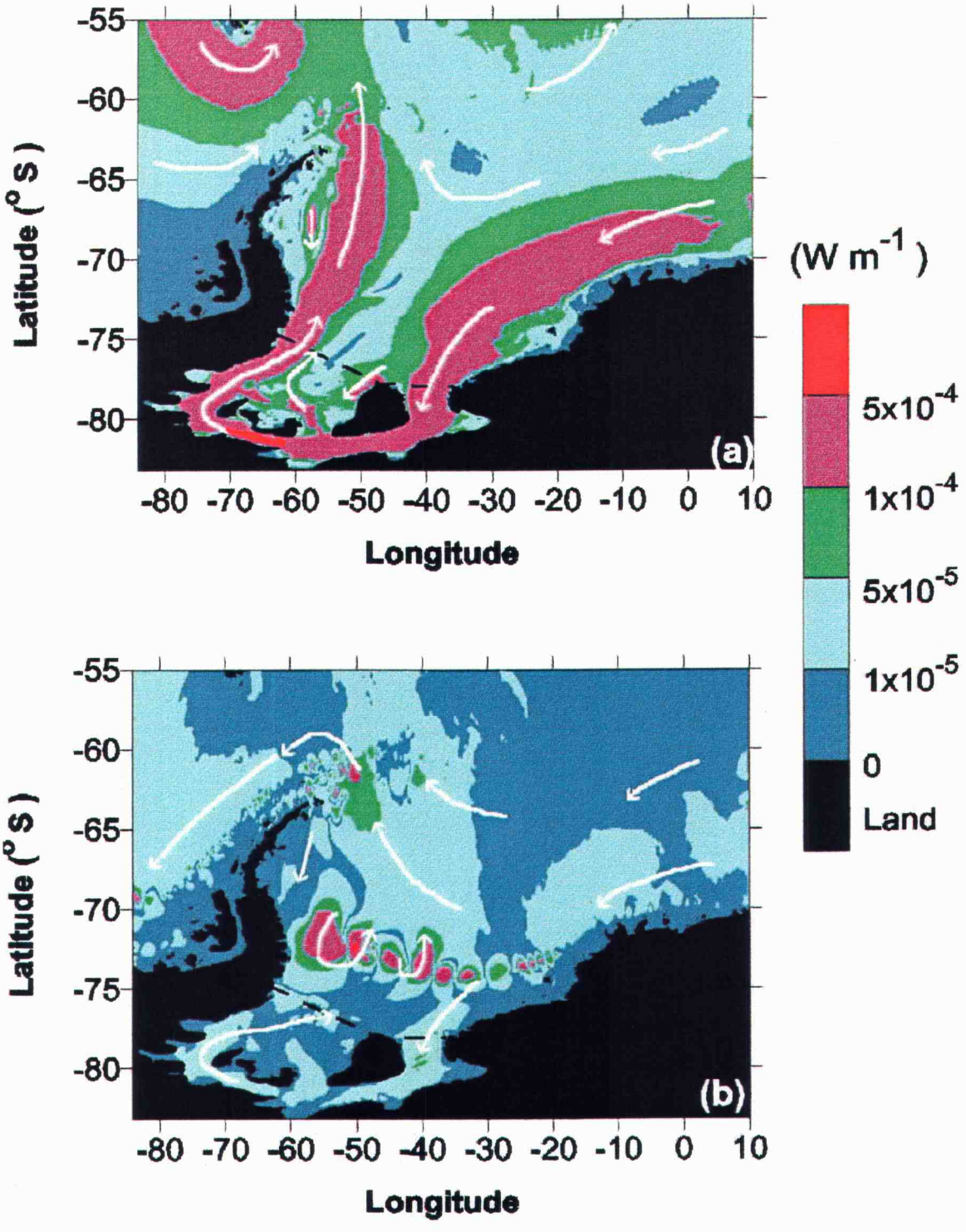

Figure 3.8. Depth-integrated energy flux (W m^{-1}) for the (a) M_2 and (b) O_1 constituents. Shading indicates flux magnitude according to the color scale: white arrows indicate flux direction. The 500, 1000, and 3000 m isobaths (or water column thickness isolines under the FRIS) are shown. Black dashed lines indicate the approximate location of the FRIS Ice Front.

the energy flux is generally westward. Most of the energy approaching the tip of the Antarctic Peninsula from the southeast turns around the peninsula to continue westward along the Antarctic coast in the Bellingshausen Sea (Figure 3.8b). There is a small clockwise energy flux under the FRIS. At the continental shelf break in the southern Weddell Sea, the O_1 energy flux is very complicated. Diurnal energy on the southern shelf break has been previously characterized as being due to the large wave number mode of energetic, diurnally-forced, barotropic shelf waves [*Middleton et al.*, 1987]. There is, however, a strong correlation between the flux direction and the sequence of troughs along the southern slope (the gap between the peninsula and the General Belgrano Bank; the Ronne Depression; and the Filchner Depression). Our model appears to overpredict currents along the southern slope (see section 3.5.3.2, and *Padman et al.*, [1998]). The diurnal tidal current along the southern slope will be considered in more detail in future model studies, but we believe that additional bathymetric information will be required before models can adequately describe ocean currents in this region.

3.6.2. Energy Losses Due to Bottom Stress

Tidal energy in the real ocean is dissipated by several mechanisms, including bottom friction, lateral friction, friction between the pack ice and the water, topographic drag, and flexure of the ice shelves. Our model parameterizes the first two of these sinks, however, the others are ignored. The time-averaged dissipation of energy per unit area by bottom friction, $\langle D_B(t) \rangle$, was evaluated as

$$\langle D_B \rangle = \rho_w C_D \langle |\mathbf{u}|^3 \rangle, \qquad (3.6)$$

where $\mathbf{u}$ is the barotropic velocity, and the angle brackets denote time averaging over the 45-day tidal analysis period of the model run.

Area-averaged and area-integrated values of $\langle D_B \rangle$ for 12 subregions of our model domain (Figure 3.9) are presented in Table 3.5. The highest average value, 0.067 W m^{-2},

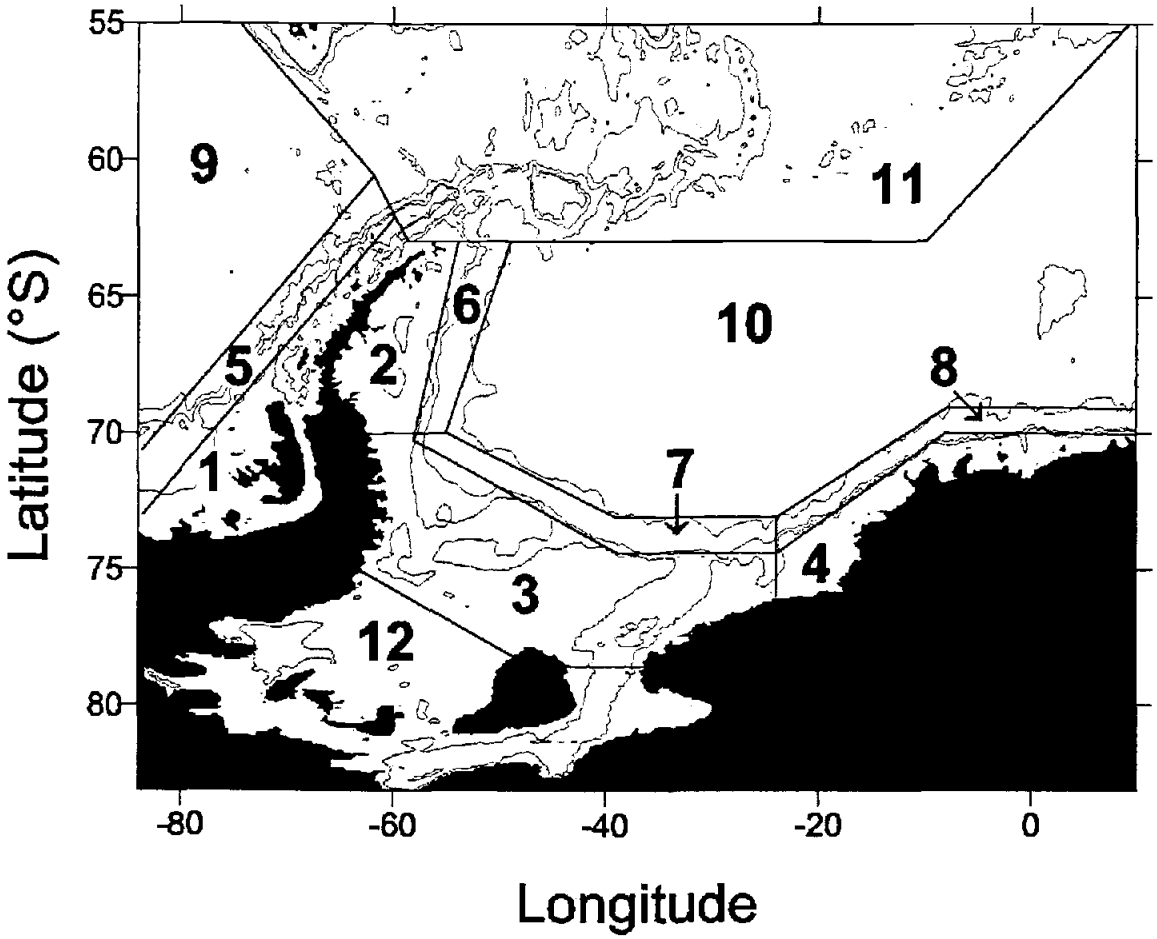

Figure 3.9. Subregions for which area-averaged values of energy dissipation by bottom friction have been calculated (see Table 3.5). The 500 and 3000 m isobaths (or water column thickness isolines under the FRIS) are indicated.

occurs under FRIS and large values are also found for the slope in the southern Weddell Sea and the continental shelf subregions, except in the eastern Weddell Sea. Through the $|\mathbf{u}|^3$ dependence in (3.6), the actual distribution of $\langle D_B \rangle$ is clearly directly related to the spatial structure of u_{typ} (Figure 3.6). For example, most of the total energy loss for the FRIS (27 GW) occurs at the front of the Ronne Ice Shelf, and most of the energy loss for the continental shelf regions occurs in the high velocity region over the General Belgrano Bank. The energy lost to dissipation in the deep water of the Weddell Sea (region 10) is small, since velocities are small throughout this region. Although the deep basins (regions 9-11) cover most of the domain (~75%), they account for less than 12% of the

Region		Area (10^6 km^2)	$\iint D_B(x,y)$ (GW)	$\langle D_B \rangle$ (10^{-3} W m^{-2})
Shelf				
	S. Pacific (1)	0.34	6	18
	W. Weddell (2)	0.21	2	9
	S. Weddell (3)	0.51	32	63
	E. Weddell (4)	0.18	3	17
Slope				
	S. Pacific (5)	0.29	0.29	1.0
	W. Weddell (6)	0.13	0.48	3.7
	S. Weddell (7)	0.17	5.1	29
	E. Weddell (8)	0.22	0.14	0.6
Deep				
	S. Pacific (9)	1.17	0.05	0.04
	Weddell (10)	2.74	0.10	0.03
	Scotia (11)	3.49	10	2.8
	FRIS (12)	0.40	27	67
Total		9.9	86	8.7
[Baroclinic tide generation]		—	33	3.0

Table 3.5. Area, area-integrated tidal dissipation rate due to bottom friction (GW = 10^9 W), and mean dissipation rate per unit area, for specified sub-regions of the model domain (Figure 3.9). Baroclinic tide generation is the domain-averaged energy flux from the barotropic tides to the internal waves as determined following *Sjöberg and Stigebrandt* [1992].

total energy loss to bottom friction. Nearly all of this dissipation occurs in the Scotia Sea near the tip of the Antarctic Peninsula, and along the Scotia Ridge.

The total tidal energy lost to bottom friction in our 4-constituent model is about 86 GW, giving a domain-averaged value of $\langle D_B \rangle \approx 0.0087$ W m^{-2}. The flux divergence across the open boundaries of our model domain is approximately -32 GW (i.e., a net flux into the domain) for all 4 tidal constituents combined. The 54 GW difference is primarily due to local astronomical forcing (67 GW), with a small additional term due to lateral viscosity.

3.7. Some Implications of Model Results

In this section we discuss two ways in which tidal currents can modify the general circulation and hydrography of the Weddell Sea. These are: the influence of tides on the effective friction experienced by the mean flow; and the generation of baroclinic tides and other internal gravity waves that can then lead to significantly higher effective diffusivities in the pycnocline. We also briefly review the implications of our model for estimates of the energy losses to ice shelf flexure. One of the most significant effects of tides in ice-covered seas, the distortion of the sea-ice cover, is discussed by *Padman et al.* [1998].

3.7.1. Relationship Between Tides and Mean Currents

The general circulation in the Weddell Sea is dominated by the Weddell Gyre, which flows clockwise [*Orsi et al.*, 1993]. The total volume transport of the gyre is about 30 Sv (1 Sv=10^6 m^3s^{-1}), which is concentrated in boundary currents on the southern and western sides of the basin [*Fahrbach et al.*, 1994]. A maximum mean speed of 16 cm s^{-1} has been reported in the Weddell coastal current, but 6 cm s^{-1} is a more typical value for the mean velocity over the shelf, and speeds less than 1 cm s^{-1} are typical for the deep basins [*Fahrbach et al.*, 1994].

Various studies have demonstrated that the tides can have a significant effect on the mean circulation, by generating residual currents and increasing the effective bottom friction felt by the mean flow. Generation of residual velocities has been described by *Loder* [1980], *Robinson* [1981], *Padman et al.* [1992], and *Kowalik and Proshutinsky* [1995], among others. While most of the processes responsible for residual currents will not be discussed here, we note that the necessary conditions for significant residual currents do exist within our model domain. Here, we only consider the role of tides in modifying the effective friction felt by the non-tidally-forced mean flow, which is driven primarily by wind stress and thermohaline forcing (air/sea and ice/ocean salt and heat exchanges). The increased effective friction due to the mean flow also affects tidal velocities. However, since tidal currents are usually much stronger (see below), they will have a more significant effect on the mean flow than the mean flow has upon them.

Mean currents along the southern and western margins of the Weddell Gyre were assumed to vary with water depth, from a maximum of 6 cm s^{-1} at the 500 m isobath (i.e., the continental shelf) to a minimum of 0.5 cm s^{-1} at the 3500 m isobath (following *Fahrbach et al.* [1994]). The ratio of the model typical tidal speed (u_{typ}: (3)) to the mean current $\langle|\mathbf{u}|\rangle$, was then determined at each location. Tidal currents generally exceed the mean currents in the Weddell Gyre. At the Ronne Ice Shelf edge and over the General Belgrano Bank, $u_{typ}/\langle|\mathbf{u}|\rangle$ is about 5-10; over the continental shelf and slope, the ratio is 2-5.

The effect of the additional velocity variance from the tidal flows on the effective benthic friction felt by the subtidal, or "mean", currents can be estimated following *Noble et al.* [1983]. They noted that the bottom stress experienced by the subtidal flow can be written as

$$\tau_b = C_D(\mathbf{u}|\mathbf{u}|)_{\text{lowpass-filtered}} = C_E\mathbf{u}_s|\mathbf{u}_s| \,. \tag{3.7}$$

Here, $\mathbf{u}$ is the total near-bottom current, and $\mathbf{u}_s$ is the subtidal current. When the tidal current amplitude, $|\mathbf{u}_{tide}|$, is much larger than $|\mathbf{u}_s|$, the effective drag coefficient, C_E, is related to the bottom drag coefficient, C_D, by

$$C_E \approx \frac{|\mathbf{u}_{tide}|}{|\mathbf{u}_s|} C_D \tag{3.8}$$

If the mean bottom velocity in the absence of tides ($\mathbf{u}_{\text{no tides}}$) is the velocity required for the bottom stress to balance the forcing (e.g., wind stress), then the mean velocity with tides included will be given by $\mathbf{u}_s/\mathbf{u}_{\text{no tides}} \approx (C_D/C_E)^{1/2}$. That is, for our case of $|\mathbf{u}_{tide}|/|\mathbf{u}_s| \approx 2.5$, the mean flow with tides added is about 60-70% of the current in the absence of tides. In our ideal ocean, this is equivalent to reducing the gyre volume transport by the same fraction.

Gordon et al. [1981] estimated the mean circulation for the Weddell Basin to be 76 Sv, based on integrating the Sverdrup transport without bottom friction. A reduced estimate of 46 Sv was obtained by applying the model of *Bye and Veronis* [1979], where

linear friction and the gyre "aspect ratio" are taken into account. This latter estimate is 1.5 times the 30 Sv obtained by *Fahrbach et al.* [1994] from current meter measurements. From our crude estimate and model (wind stress balances bottom friction), the inclusion of the tides in a circulation model would reduce the mean transport by a factor of about 1.5, thereby reconciling the value based on *Bye and Veronis* [1979] with *Fahrbach's* measurements. This simple approach cannot provide accurate Gyre transport values, but it is clear that the potential exists for tides to significantly modify the transport, and efforts should be made to include this influence in general circulation models. This could be easily achieved by using a spatially-dependent drag coefficient, $C_E(x,y)$ that has been evaluated following the analysis technique described above.

3.7.2. Baroclinic Tide Generation

Energy dissipation in our tidal model occurs primarily through bottom friction, with a smaller contribution from lateral viscosity. Other dissipative terms, such as stress at the base of the sea ice, have not been included in our model formulation. In a stratified ocean energy can also be lost from the barotropic tide by the generation of baroclinic tides and other internal gravity waves. While the baroclinic kinetic energy density may be small compared with the barotropic component, the velocity shear associated with baroclinic tides can be a major source of turbulent mixing in the Weddell Sea pycnocline [*Stanton et al.*, 1998].

Bell [1975] studied the generation of internal waves when currents flow over rough topography, and estimated an average energy loss from the barotropic tide of about 0.001 W m^{-2} (see also, *Polzin et al.* [1997]). *Sjöberg and Stigebrandt* [1992] estimated fluxes from the barotropic tide into the internal tide, using a model that calculated the baroclinic modes that are required to satisfy boundary conditions at bathymetry represented by steps. Their mean deep-ocean value was about 0.004 W m^{-2}. Some of this baroclinic energy can be made available to turbulent mixing in the pycnocline through non-linear processes such as wave-wave interactions. We would expect the strongest mixing to occur near regions of strongest generation. This is consistent with observations in the eastern Arctic Ocean, where higher kinetic energy dissipation in the pycnocline was linked to energetic

tidal currents over the Yermak Plateau [*Padman et al.*, 1992; *Padman*, 1995]. A baroclinic model of the Arctic Ocean that included simple mixing parameterizations [*Polyakov*, 1995] found enhanced mixing over continental slopes, with resultant generation of near-surface mean geostrophic currents. Similarly, *Parsons* [1995] found that temperature differences over topographic features were consistent with enhanced mixing due to internal tides. In the Weddell Sea, baroclinic tides have been observed near Maud Rise [*Robertson et al.*, 1995b; *Stanton et al.*, 1998] and in the northwestern Weddell Sea by *Foster* [1994].

We used the formulation of *Sjöberg and Stigebrandt* [1992] to determine the energy loss to internal tides for our model domain (Figure 3.10). We assumed that the maximum buoyancy frequency was 3 cycles per hour, and that the scaling thickness (δ) for the permanent pycnocline was 50 m when the water depth was greater than 500 m. For water depths less than 500 m, δ was taken to be 10% of the water depth. Calculations were performed for both the M_2 and S_2 constituents, with the energy loss being summed for the first ten baroclinic modes. Since the diurnal constituents have frequencies that are much less than f, only the semidiurnal constituents can generate freely propagating baroclinic tides. The modeled energy loss to baroclinic tides was greater than 0.01 W m^{-2} for parts of the continental shelf/slope break, the front of the Ronne Ice Shelf, and much of the Bransfield Strait and elsewhere over the rough bathymetry of the Scotia Ridge (Figure 3.10). Energy losses exceeding 1 W m^{-2} are predicted in some small areas in the Bransfield Strait. Strong baroclinic tides are not predicted to be locally generated at either the AnzFlux (Antarctic Zone Flux Experiment) or *Foster* [1994] locations (marked "A" and "F" on Figure 3.10) where they have been observed. They could, however, be generated over nearby bathymetric features, such as the shelf edge and Maud Rise, then propagate to these locations. The domain-averaged energy loss is about 0.003 W m^{-2} for the M_2 and S_2 constituents combined.

It is interesting to speculate on the amount of mixing that might be generated in the pycnocline in response to baroclinic tide generation. Assume that, through internal wave propagation, all the baroclinic energy is uniformly distributed in the model, and is also dissipated within the model domain at the same rate at which it is generated. If the

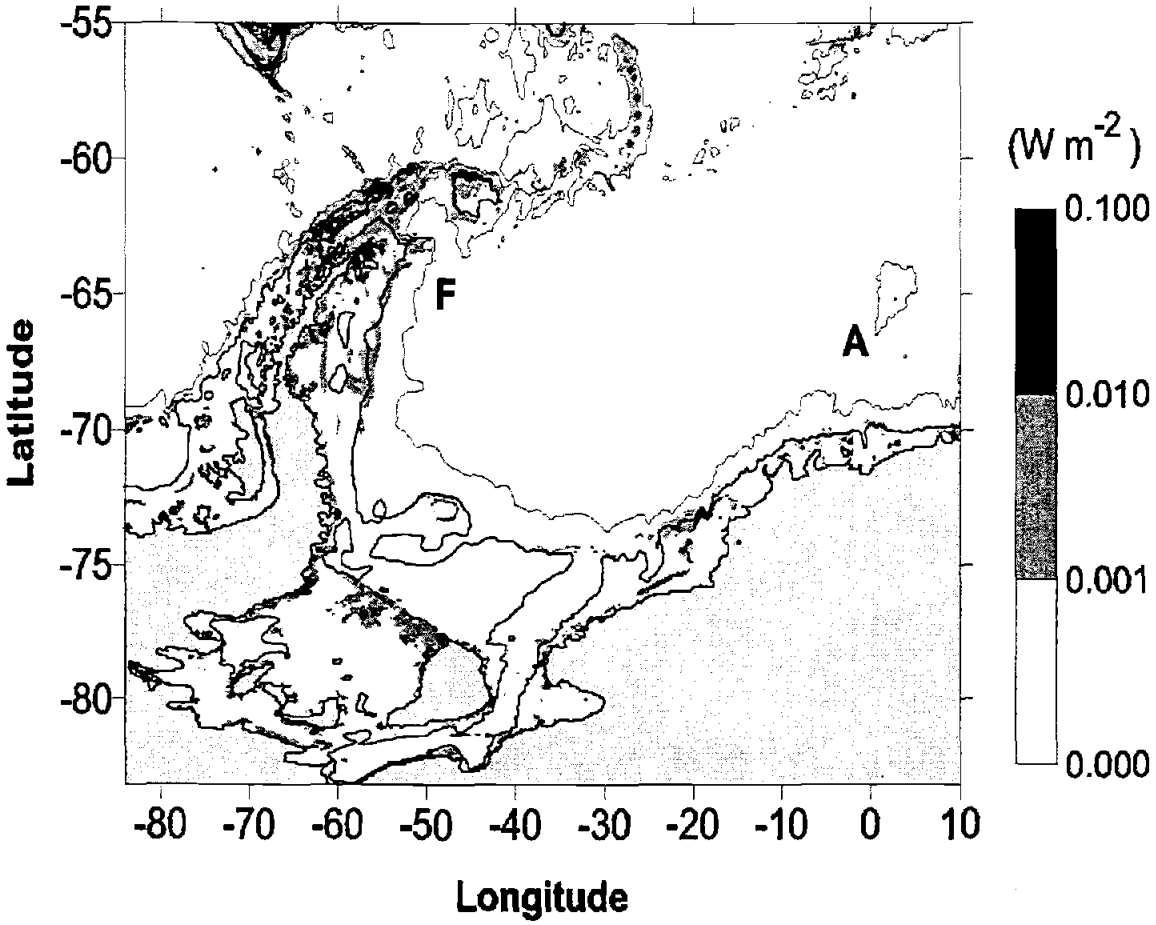

Figure 3.10. The energy flux from barotropic tides to internal waves, following *Sjöberg and Stigebrandt* [1992]. The 500 and 3000 m isobaths (or water column thickness isolines under the FRIS) are shown. The location of the Anzflux baroclinic tide observation is denoted with an "A" and that of *Foster* [1994] with an "F".

0.003 W m^{-2} mean production is balanced by uniform dissipation in a 100 m thick pycnocline ($H_{pyc} \approx 2\delta$), then the mean dissipation rate, $\langle \varepsilon \rangle$ is about 3×10^{-8} W kg^{-1}. Following *Osborn* [1980], we then estimate the vertical turbulent eddy diffusivity from $K_v = \Gamma \varepsilon / N^2$, where Γ is the "mixing efficiency", taken to be 0.2. For N = 3 cph, we obtain $K_v \approx 2 \times 10^{-4}$ $m^2 s^{-1}$. If the mean temperature difference across the pycnocline is 2.5°C, i.e., $\langle \partial T/\partial z \rangle = 0.025$°C m^{-1}, then the heat flux is $F_H = \rho c_p K_v \langle \partial T/\partial z \rangle \approx 25$ W m^{-2} (c_p is the specific heat capacity of seawater). This heat flux is the same order of magnitude as the average value required to balance the heat budget for the Weddell Sea [*Fahrbach et al.*, 1994] and an order of magnitude higher than the diapycnal heat fluxes of 3 W m^{-2}

estimated from observations in the western Weddell Sea [*Robertson et al.*, 1995a]. There are many caveats to the above calculation, including the possibility that much of the generated baroclinic energy is actually dissipated close to the seabed [*Polzin et al.*, 1997] rather than in the strongly-stratified pycnocline. Nevertheless, we believe that generation of baroclinic tides may play a significant role in the upward flux of WDW heat towards the ocean surface. Furthermore, Figure 3.10 identifies the regions where baroclinic tide generation is expected to be strongest: many of these areas are also important for larger-scale processes occurring in the Weddell Sea. For example, generation is high along the shelf break, where mixing at the shelf/slope front between shelf water types and WDW can lead to bottom water formation [*Foster et al.*, 1987]. Generation is large in the Bransfield Strait and along the Scotia Ridge, where the water of the Antarctic Circumpolar Current interacts with Weddell Gyre water in the Weddell-Scotia Confluence. Generation is also strong at the FRIS front, suggesting a mechanism for mixing between the open shelf circulation and the dynamically isolated circulation under the ice shelves [*Grosfeld et al.*, 1997]. From their model of circulation under ice shelves *Grosfeld et al.* suggest that very little advective transport occurs across the ice front (because of the strong cross-frontal gradient in f/H), thus isolating the ice-shelf circulation from the adjacent continental shelf. The energetic tides along the ice front suggest that strong cross-frontal mixing could occur in this region, reducing the isolation of these two flow regimes.

3.7.3. Ice Shelf Energy Losses

Early studies suggested that the interaction of tides with the glacial ice shelves surrounding Antarctica might be a major component of the total global tidal power dissipation of about 2500 GW [*Doake*, 1978]. The proposed dissipation mechanism, flexing of the glacial ice by spatial gradients in tidal elevation, is not included in our model. As we have shown above, however, our model predicts the tidal elevation field of the non-ice-shelf portion of the model domain quite well. Tidal energy fluxes must also, therefore, be reasonably well represented. In our model, a total of 66 GW of tidal energy enters the ice shelf cavity, and this is, therefore, approximately the maximum that can be

lost by all dissipative processes under FRIS. Benthic and ice/water friction in our model accounts for about 27 GW. *Ray and Egbert* [1997] noted that most energy dissipated by the Antarctic ice shelves must first cross 60°S, since very little forcing of the dominant M_2 tide occurs south of this latitude. They used two different global tidal models to estimate an energy flux for the M_2 constituent of 1 and 42 GW northwards across the 60°S latitude line for all longitudes. In our regional model we find a total flux of about 63 GW northward across 60°S between 84°W and 10°E, with a similar pattern to *Ray and Egbert* [1997]. Hence, neither the global models nor our regional tidal model support the hypothesis of significant (in global terms) dissipation through ice shelf flexure. *Ray and Egbert* [1997] attributed *Doake*'s overestimation to the use of a few poor tidal observations and an incorrect model for the tidal energy absorbed by ice shelf flexure. *Vaughan* [1995] investigated the flexure of the ice shelves due to tides and reached a similar conclusion. Despite this result, the interaction of tides with ice shelves remains a potentially significant process [*Makinson and Nicholls*, 1996; *Smithson et al.*, 1996].

3.8. Conclusions

We have developed a high-resolution barotropic model of tides in the Weddell Sea. The ocean cavity under the Filchner-Ronne Ice Shelf was explicitly included in the model domain. Four constituents were modeled, M_2, S_2, O_1, and K_1. Modeled tidal elevation amplitudes exceed 1 m at the back of the FRIS and the Larsen Ice Shelf. Modeled typical tidal speeds are greater than 0.1 m s^{-1} over most of the continental shelves. The highest speeds, greater than 75 cm s^{-1}, occur in the shallow water over the General Belgrano Bank and near the front of the Ronne Ice Shelf. Typical tidal currents over most of the Weddell Sea are 2-10 times greater than mean flows associated with wind and thermohaline forcing. Tides therefore provide a significant fraction of the total oceanic kinetic energy, with a commensurately important influence on the oceanography of the region.

Most of the modeled tidal elevations agreed very well with available measurements, which include both tide gauges and satellite altimetry. Agreement between model predictions of major-axis currents and available measurements is less satisfactory, although still reasonable given the large potential errors that can be ascribed to

inadequate bathymetric data. For the open ocean areas, standard deviations for the differences between modeled and measured tidal constituent elevations ranged from 2-5 cm in amplitude and up to 8° in phase. Similar comparisons against satellite altimetry data gave *rms* differences of 1-3 cm in amplitude. The major axis for the tidal velocity ellipses showed standard deviations of about 1 cm s^{-1} for deep-water regions, where tidal currents are small. Larger differences were seen for measurements under and near the Filchner/Ronne Ice Shelf. The elevation coefficients in this region had standard deviations of 8-14 cm in amplitude and 12-70° in phase when compared with tidal gauge data. For velocities under the ice shelf, the standard deviations of the major axis of the velocity ellipses ranged from 1.4 to 3.5 cm s^{-1}.

The tidal energy budget for our model is dominated by an energy influx through the eastern boundary, efflux through the northern and western boundaries, local astronomical forcing, and dissipation by bottom stress within the domain. The highest energy loss to bottom stress occurs in shallow regions with rapidly changing bathymetry, particularly under the ice shelves and on the continental slope. Mean energy losses in these areas are 0.009-0.067 W m^{-2}: the energy loss over the entire domain is 86 GW. We used the formulation of *Sjöberg and Stigebrandt* [1992] to estimate the potential in the real, stratified ocean for an additional loss of about 0.003 Wm^{-2} by generation of baroclinic tides (33 GW for the total model domain). This term is significantly smaller than the domain-integrated bottom frictional losses. Nevertheless, it may represent the largest single source of energy available to drive diapycnal mixing within the pycnocline. Spatial variability of pycnocline mixing rates could lead to significant geostrophic velocities in some areas.

Rough estimates for the increase in mean effective bottom stress due to the addition of tides with a quadratic bottom stress formulation ($\tau_b=C_D|\mathbf{u}|^2$) suggest that the mean gyre transport could be reduced by about 30% by incorporating tidal motion into general circulation models.

In the future, additional tidal constituents will be included in an effort to raise the total explained tidal variance. A dynamic/thermodynamic coupled ice model could be added to explore the influence of the ocean tides on the ice cover, and vice versa. With a

realistic ice model, seasonal effects of the ice cover on the tides can then be investigated. For a similar model for the Arctic Ocean, *Kowalik and Proshutinsky* [1994] found that ocean tides can have a profound effect on the ice cover and the heat and salt exchanges at the air/ice/water interface, although the addition of sea ice to their tidal model had little influence on the ocean tides. The dissipation of energy due to the flexure of the ice shelves could also be parameterized in our model. While we have shown that the ice shelves are not a major sink of global tidal energy, there is a potential for significant modification to tidal predictions for the western Weddell Sea, since much of the tidal energy in this region has previously circulated under the Filchner/Ronne Ice Shelf. Baroclinic effects could be incorporated into the model by adding another dimension and including stratification. Additionally, as more data become available, "data assimilation" methods could be used to improve the model results.

These modifications should improve our understanding of the relationships between tides and other processes that have a direct bearing on topics of both regional and global significance. These processes include stability of the sea ice cover (therefore, the regional mean albedo and oceanic heat loss to the atmosphere), and stability of the ice shelves, which contribute to the global freshwater budget. However, the most fundamental limitation to our tidal model is the paucity of good bathymetric data, especially in the southwestern Weddell Sea. This limitation, which is highlighted by model sensitivity studies [*Padman et al.* 1998], is likely to apply also to regional, non-tidal models such as might be used to estimate Warm Deep Water and Ice Shelf Water production and their influence on AABW formation.

3.9. References

Aanderaa Instruments, RCM4/5 Operating Manual, *Technical Publication No. 119*, Aanderaa Instruments, Bergen, Norway, 1979.

Andersen, O. B., New ocean tide models for loading computations, *Bull. Int. Mare Terr.*, *102*, 9256-9264, 1995.

Andersen, O. B., P. L. Woodworth, and R. A. Flather, Intercomparison of recent ocean tide models, *J. Geophys. Res.*, *100*, 25,261-25,282, 1995.

Barber, M., and D. Crane, Current flow in the northwest Weddell Sea, *Antarctic Science*, *7*, 39-50, 1995.

Bell, T. H., Topographically generated internal waves in the open ocean, *J. Geophys. Res.*, *80*, 320-327, 1975.

Bersch, M., G. A. Becker, H. Frey, and K. P. Koltermann, Topographic effects of the Maud Rise on the stratification and circulation of the Weddell Gyre, *Deep-Sea Res.*, *39*, 303-331, 1992.

Broecker, W. S., and T. H. Peng, *Tracers in the Sea*, Eldigio Press, Palisades, NY, 690 pp., 1982.

Bye, J. A. T., and G. Veronis, A correction to the Sverdrup transport, *J. Phys. Oceanog.*, *9*, 649-651, 1979.

Carmack, E. C., Water characteristics of the Southern Ocean south of the Polar Front, in *A Voyage of Discovery*, edited by M. Angel, pp. 15-41, Pergamon Press, Inc., Oxford, 1977.

Cartwright, D. E., and R. J. Taylor, New computations of the tide generating potential, *Geophys. J. R. Astron. Soc.*, *23*, 45-74, 1971.

Central Intelligence Agency, *World Data Bank, 2*, Central Intelligence Agency, Washington, D. C., 1972.

Doake, C. S. M., Dissipation of tidal energy by Antarctic ice shelves, *Nature*, *275*, 304-305, 1978.

Doake, C. S. M., Gravimetric tidal measurements on Filchner Ronne Ice Shelf, in *Filchner-Ronne Ice Shelf Programme Report No. 6*, edited by H. Oerter, Alfred-Wegener Institute for Polar and Marine Research, Bremerhaven, Germany, 34-39, 1992.

Egbert, G. D., Tidal data inversion: interpolation and inference, *Prog, in Oceanogr.*, in press, 1997.

Egbert, G. D., A. F. Bennett, and M. G. G. Foreman, TOPEX/POSEIDON tides estimated using a global inverse model, *J. Geophys. Res., 99*, 24,821-24,852, 1994.

Eckstaller, A., and H. Miller, Gezeiten-Vertikalbewegung des Filchner Schelfeises (Tides and vertical movement of the Filchner Ice Shelf), *Ber. Polarforsch., 19*, 82-97, 1984.

Fahrbach, E., G. Rohardt, and G. Krause, The Antarctic coastal current in the southeastern Weddell Sea, *Polar Biology, 12,* 171-182, 1992.

Fahrbach, E., G. Rohardt, M. Schröder, and V. Strass, Transport and structure of the Weddell Gyre, *Ann. Geophysicae, 12,* 840-855, 1994.

Ffield, A., and A. L. Gordon, Tidal mixing signatures in the Indonesian Seas, *J. Phys. Oceanogr., 26*, 1924-1937, 1996.

Foldvik, A., and T. Kvinge, Bottom currents in the Weddell Sea, *Rep. No. 37,* 43 pp., University of Bergen, Bergen, Norway, 1974.

Foldvik, A., and T. Gammelsrød, Notes on southern ocean hydrography, sea-ice and bottom water formation, *Palaeogeog., Palaeoclim., Palaeoecol., 67,* 3-17, 1988.

Foldvik, A., T. Gammelsrød, N. Slotsvik, and T. Tørresen, Oceanographic conditions on the Weddell Sea shelf during the German Antarctic Expedition 1979/80, *Polar Res., 3,* 209-226, 1982a.

Foldvik, A., T. Gammelsrød and T. Tørresen, Physical oceanographic studies in the Weddell Sea shelf during the Norwegian Antarctic Research Expedition 1978/79, *Polar Res., 3,* 195-207, 1982b.

Foldvik, A., T. Gammelsrød and T. Tørresen, Circulation and water masses in the southern Weddell Sea shelf, in *Oceanology of the Antarctic Continental Shelf,* Antarc. Res. Series, *43,* edited by S. S. Jacobs, 5-20, AGU, Washington, D. C., 1985a.

Foldvik, A., T. Kvinge, and T. Tørresen, Bottom currents near the continental shelf break in the Weddell Sea, in *Oceanology of the Antarctic Continental Shelf,* Antarc. Res. Series, *43,* edited by S. S. Jacobs, 21-34, AGU, Washington, D. C., 1985b.

Foldvik, A., J. H. Middleton, and T. D. Foster, The tides of the southern Weddell Sea, *Deep-Sea Res., 37,* 1345-1362, 1990.

Foreman, M. G. G., *Manual for tidal current analysis and prediction*, Pacific Marine Science Report No. 78-6, Institute of Ocean Sciences, Patricia Bay, Sidney, B.C., 70 pp., 1978.

Foster, T. D., Large, steplike temperature and salinity structures observed in the central Weddell Sea, , *Antarct. J. of the U.S., 29,* 99-100, 1994.

Foster, T. D., A. Foldvik, and J. H. Middleton, Mixing and bottom water formation in the shelf break region of the southern Weddell Sea, *Deep-Sea Res., 34,* 1771-1794, 1987.

Furevik, T., and A. Foldvik, Stability at M_2 critical latitude in the Barents Sea, *J. Geophys. Res., 101*, 8823-8837, 1996.

Gallagher, B. S., and W. H. Munk, Tides in Shallow Water: Spectroscopy, *Tellus, 23,* 346-363, 1971.

Gammelsrød, T., A. Foldvik, O. A. Nøst, Ø. Skagseth, L. G. Anderson, E. Fogelqvist, K. Olsson, T. Tanhua, E. P. Jones, and S. Østerhus, Distribution of water masses on the continental shelf in the southern Weddell Sea, in *The Polar Oceans and Their Role in Shaping the Global Environment*, Geophysical Monograph 85, edited by O. M. Johannessen, R. D. Muench, and J. E. Overland, AGU, Washington, D.C., p. 159-176, 1994.

Genco, M. L., F. Lyard, and C. Le Provost, The oceanic tides in the South Atlantic Ocean, *Ann. Geophysicae, 12,* 868-886, 1994.

Gordon, A. L., D. G. Martinson, and M. W. Taylor, The wind driven circulation in the Weddell-Enderby Basin, *Deep-Sea Res., 28A,* 151-163, 1981.

Grosfeld, K., R. Gerdes, and J. Determann, Thermohaline circulation and interaction between ice shelf cavities and the adjacent open ocean, *J. Geophys. Res., 203,* 15,595-15,610, 1997.

Haltiner G. J., and R. T. Williams, *Numerical Prediction and Dynamic Meteorology,* John Wiley and Sons, Inc., New York, 477 pp., 1980.

Hatayama, T., T. Awaji, and K. Akitomo, Tidal currents in the Indonesian Seas and their effect on transport and mixing, *J. Geophys. Res., 101*, 12,353-12,373, 1996.

Hisdal, V., On the tides at Norway Station, and adjacent coastal areas of Antarctica, Norwegian Antarctic Expedition, 1956-60, *Sci. Res., 9,* 21 pp, Norwegian Polar Institute, Oslo, 1965.

Jet Propulsion Laboratory, A collection of ocean tide models on CD-ROM, CD-ROM distributed by the *Jet Propulsion Laboratory*, Pasadena, California, 1996.

Kowalik, Z., and A. Y. Proshutinsky, The Arctic Ocean Tides, in *The Polar Oceans and Their Role in Shaping the Global Environment*, Geophysical Monograph 85, edited by O. M. Johannessen, R. D. Muench, and J. E. Overland, pp. 137-158, AGU, Washington, D. C., 1994.

Kowalik, Z., and A. Y. Proshutinsky, Topographic enhancement of tidal motion in the western Barents Sea, *J. Geophys. Res., 100*, 2613-2637, 1995.

LaBrecque, J. L., and M. E. Ghidella, Estimates of bathymetry, depth to magnetic basement, and sediment thickness for the western Weddell Basin, *Antarct.. J. of the U. S., 27*, 68-70, 1993.

Le Provost, C., M. L. Genco, F. Lyard, P. Vincent, and P. Canceil, Spectroscopy of the world ocean tides from a finite element hydrodynamic model, *J. Geophys. Res., 99*, 24,777-24,797, 1994.

Levine, M. D., L. Padman, R. D. Muench, and J. H. Morison, Internal waves and tides in the western Weddell Sea: Observations from Ice Station Weddell, *J. Geophys. Res, 102*, 1073-1089, 1997.

Loder, J.W., Topographic rectification of tidal currents on the sides of Georges Bank, *J. Phys. Oceanogr., 10*, 1399-1416, 1980.

Lutjeharms, J. R. E., C. C. Stavropolous, and K. P. Koltermann, Tidal measurements along the Antarctic coastline, in *Oceanology of the Antarctic Continental Shelf*, Antarc. Res. Series, *43*, edited by S. S. Jacobs, pp. 273-289, AGU, Washington, D. C., 1985.

MacAyeal, D. R., Numerical simulations of the Ross Sea Tides, *J. Geophys. Res, 89*, 607-615, 1984.

Makinson, K., and K. W. Nicholls, Modeling tidal currents beneath Filchner-Ronne Ice Shelf, *Filchner-Ronne Ice Shelf Programme*, Report 10, 58-67, 1996.

Middleton, J. H., and T. D. Foster, Tidal currents in the central Weddell Sea, *Deep-Sea Res., 24*, 1195-1202, 1977.

Middleton, J. H., T. D. Foster, and A. Foldvik, Low-frequency currents and continental shelf waves in the southern Weddell Sea, *J. Phys. Oceanogr., 12*, 618-634, 1982.

Middleton, J. H., T. D. Foster, and A. Foldvik, Diurnal shelf waves in the southern Weddell Sea, *J. Phys. Oceanogr., 17*, 784-791, 1987.

National Geophysical Data Center, GEODAS CD-ROM worldwide marine geophysical data, *Data Announce. 92-MGG-02*, Natl. Oceanic and Atmos. Admin. U.S. Dep. Commer., Boulder, Colo., 1992.

Noble, M., B. Butman, and E. Williams, On the longshelf structure and dynamics of subtidal currents on the eastern United States continental shelf, *J. Phys. Oceanogr., 13,* 2125-2147, 1983.

Nygaard, E., Preliminary results from current measurements in position R2 (76°29' S, 53°00' W) outside the Ronne Ice Shelf in the southern Weddell Sea 1993-1994, unpublished report, Geophysical Institute, Bergen, Norway, 25 pp., 1995.

Orsi, A. H., W. D. Nowlin, Jr., and J. Whitworth III, On the circulation and stratification of the Weddell Gyre, *Deep Sea Res., 40*, 169-203, 1993.

Osborn, T.R., Estimates of the local rate of vertical diffusion from dissipation measurements, *J. Phys. Oceanogr., 10*, 83-89, 1980.

Padman, L., Small-scale physical processes in the Arctic Ocean, in *Arctic Oceanography: Marginal Ice Zones and Continental Shelves,* Coastal and Estuarine Studies, *49*, edited by W. O. Smith and J. M. Grebmeier, pp. 97-129, AGU, Washington, D.C., 1995.

Padman, L., A. J. Plueddemann, R. D. Muench, and R. Pinkel, Diurnal tides near the Yermak Plateau, *J. Geophys. Res, 97*, 12,639-12,652, 1992.

Padman, L., C. H. Kottmeier, and R. Robertson, Tidal ice motion in the Weddell Sea, submitted to *J. Geophys. Res.,* 1998.

Parker, B. B., *Tidal Hydrodynamics*, 883 pp., John Wiley and Sons, New York, 1991.

Parsons, A. R., On the Barents Sea polar front in summer and interpretations of the associated regional oceanography using an Arctic Ocean general circulation model, Ph.D. thesis, 178 pp., Naval Postgraduate School at Monterey, September 1995.

Pedley, M., J. G. Paren, and J. R. Potter, The tidal spectrum underneath Antarctic Ice Shelves, *J. Geophys. Res., 91*, 13,001-13,009, 1986.

Polyakov, I.V., Maintenance of the Arctic Ocean large-scale baroclinic structure by the M2 tide, *Polar Research, 13*, 219-232, 1995.

Polzin, K. L., J. M. Toole, J. R. Ledwell, and R. W. Schmitt, Spatial variability of turbulent mixing in the abyssal ocean, *Science, 276*, 93-96, 1997.

Pond, S., and G. L. Pickard, *Introductory Dynamical Oceanography*, Butterworth-Heinemann Ltd., Oxford, England, 329 pp., 1978.

Potter, J. R., J. G. Paren, and M. Pedley, Tidal behaviour under an Antarctic ice shelf, *Br. Antarc. Survey Bull., 68*, 1-18, 1985.

Pratt, J. G. D., Tides at Shackleton, Weddell Sea, Trans-Antarctic Expedition, 1955-1958, *Sci. Rep. 4*, 21 pp., American Philosophical Society, Philadelphia, 1960.

Ramming, H. G., and Z. Kowalik, *Numerical Modeling of Marine Hydrodynamic: Applications to Dynamic Physical Processes,* Elsevier Oceanography Series, *26*, 368 pp., Elsevier, Amsterdam, 1980.

Ray, R. D., and G. D. Egbert, The flux of tidal power across latitude 60°S, *Geophys. Res. Let., 24*, 543-546, 1997.

Robertson, R. A., L. Padman, and M. D. Levine, Fine structure, microstructure, and vertical mixing processes in the upper ocean in the western Weddell Sea, *J. Geophys. Res., 100*, 18,517-18,535, 1995a.

Robertson, R. A., L. Padman, M. D. Levine, R. D. Muench, and M. G. McPhee, Internal waves in the eastern Weddell Sea during AnzFlux, IAPSO XXI General Assembly, Honolulu, HI, 318, 1995b.

Robinson, I. S., Tidal vorticity and residual circulation, *Deep-Sea Res., 28A,* 195-212, 1981.

Schwiderski, E. W., Ocean tides, I, Global ocean tidal equations, *Mar. Geod., 3*, 161-217, 1980.

Sjöberg, B., and A. Stigebrandt, Computations of the geographical distribution of the energy flux to mixing processes via internal tides and the associated vertical circulation in the ocean, *Deep-Sea Res., 39,* 269-291, 1992.

Smith, A. M., The use of tiltmeters to study the dynamics of Antarctic ice-shelf grounding lines, *J. Glaciol., 37,* 51-58, 1991.

Smith, W. H. F., On the accuracy of digital bathymetric data, *J. Geophys. Res, 98*, 9591-9603, 1993.

Smithson, M. J., Pelagic tidal constants 3, *IAPSO Publication Scientifique No.35*, 191 pp., 1992.

Smithson, M. J., A. V. Robinson, and R. A. Flather, Ocean tides under the Filchner-Ronne Ice Shelf, Antarctica, *Annals. of Glaciology, 23*, 217-225, 1996.

Stanton, T. P., L. Padman, and R. A. Robertson, Heat fluxes through the permanent pycnocline in the eastern Weddell Sea, submitted to *J. Geophys. Res.*, 1998.

Stephenson, S. N., C. S. M. Doake, and J. A. C. Horsfall, Tidal flexure of ice shelves measured by tiltmeter, *Nature*, *282*, 496-497, 1979.

Thiel, E., A. P. Crary, R. A. Haubrich, and J. C. Behrendt, Gravimetric determination of ocean tide, Weddell and Ross Seas, Antarctica, *J. Geophys. Res.*, *65*, 629-636, 1960.

Vaughan, D. G., Tidal flexure at ice shelf margins, *J. Geophys. Res.*, *100*, 6213-6224, 1995.

Vaughan, D. G., J. Sievers, C. S. M. Doake, G. Grikurov, H. Hinze, V. S. Pozdeev, H. Sandhäger, H. W. Schenke, A. Solheim, and F. Thyssen, Map of the subglacial and seabed topography; Filchner-Ronne-Schelfeis/ Weddell Sea, Antarktis, scale 1:2,000,000, *Institut für Angewandte Geodäsie*, Frankfurt am Main, Germany, 1994.

Viehoff, T., and A. Li, Iceberg observations and estimation of submarine ridges in the western Weddell Sea, *Int. J. Remote Sensing*, *16*, 3391-3408, 1995.

Chapter 4

THE PRINCETON OCEAN MODEL AND EFFECTS OF THE CRITICAL LATITUDE ON INTERNAL TIDE GENERATION FOR THE SOUTHERN WEDDELL SEA

Robin Robertson, Laurie Padman and Murray D. Levine

Submitted to *Journal of Atmos. and Oceanic Tech.*,
February, 1999, in press.

4.1. Abstract

In the southern Weddell Sea, several water masses with the capability to form Antarctic Bottom Water (AABW) meet near the continental shelf break. The internal tidal field over the continental shelf break in the Weddell Sea is of interest due to its potential to mix these waters and to form AABW. An attempt was made to utilize a modified version of the Princeton Ocean Model (POM) to investigate the internal tidal fields generated by the interaction of the M_2 barotropic tide with topography over the continental shelf and slope in the southern Weddell Sea. The model was implemented as a two-dimensional (cross-slope and vertical) transect. The effect on the baroclinic response to proximity to the critical latitude (ψ_{crit}) was investigated. Internal tides were generated over the upper continental slope when the continental shelf break was in the vicinity of ψ_{crit}, as predicted by linear internal wave theory. However, near ψ_{crit} an apparent internal tide signal was generated by POM even with a homogeneous water column. Further investigation showed that this apparent internal tide was a field of vertically dependent inertial oscillations induced through resonant forcing near ψ_{crit} by erroneous baroclinic pressure gradient terms. Although POM does give some indication that internal waves are generated at the continental shelf break in the southern Weddell Sea near ψ_{crit}, the erroneous inertial oscillations significantly contaminate the internal wave signature of the weak stratification typical for the Weddell Sea. Consequently, POM in its present form is unsuitable for investigating internal tide/wave generation near ψ_{crit} especially for weak stratification. The specific causes of the errors in POM are discussed and two possible model modifications to remove or reduce the errors are investigated.

4.2. Introduction

The Weddell Sea is the major single source of Antarctic Bottom Water (AABW), providing about 80-90 % of the deep and bottom water production for the Southern Ocean [*Weppernig et al.*, 1996]. Weddell Sea Deep Water (WSDW), a subclass of AABW [*Carmack*, 1977], can be formed through several different water mass

combinations. The two most frequently cited combinations mix Warm Deep Water (WDW) with either Western Shelf Water (WSW) or Ice Shelf Water (ISW) [*Gordon*, 1998]. Modified versions of these schemes also incorporate Winter Water (WW) and/or Modified Warm Deep Water (MWDW). The potential for AABW formation increases at locations where these water masses lie in close proximity, notably along the upper continental slope in the southern and western Weddell Sea (Figure 4.1). Because of the potential for AABW formation, processes that cause mixing of these water masses are of significant interest to large-scale modeling efforts.

Tides are recognized as a significant factor in ocean mixing (see [*Munk and Wunsch*, 1998]). Tides have been observed to increase mixing rates in regions as diverse as the Indonesian Seas [*Ffield and Gordon*, 1996; *Hatayama et al.*, 1996], the deep ocean [*Polzin et al.*, 1997], and the Arctic Ocean [*Padman et al.*, 1992; *Polyakov*, 1995]. Tides affect ocean mixing through several mechanisms. Interactions between the barotropic

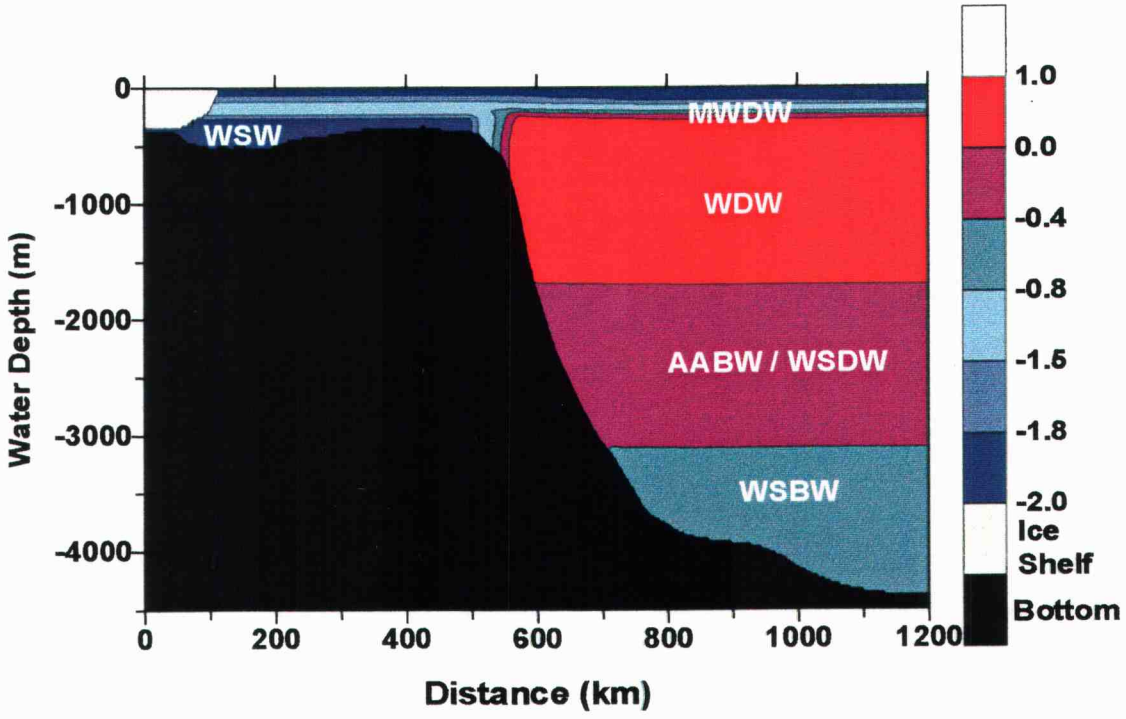

Figure 4.1. Typical potential temperature, θ, field for the southern Weddell Sea. The ice shelf is indicated by gray shading and the bottom by black. Several water masses have been identified in a). These include Western Shelf Water (WSW), Modified Warm Deep Water (MWDW), Warm Deep Water (WDW), Weddell Sea Deep Water (WSDW) or Antarctic Bottom Water (AABW), and Weddell Sea Bottom Water (WSBW). Ice Shelf Water (ISW) and Winter Water (WW) are not indicated.

tide and topography, such as ridges or the continental slope, generate baroclinic tides, internal waves, and continental shelf waves. *Munk and Wunsch* [1998] postulate that of ~900 GW of M_2 barotropic tidal energy loss over deep sea ridges, ~200-600 GW (1 GW = 10^9 W) is converted from barotropic tides to baroclinic tides. A larger amount of energy is likewise converted over continental boundaries. Baroclinic tides set up the conditions for shear or advective instabilities, which can then increase mixing through the pycnocline.

Do internal tides occur in the Weddell Sea? If they do, are they energetic enough to significantly influence other oceanic processes such as AABW formation, upper-ocean heat fluxes to the sea ice, or upper-ocean tidal currents? A few observations suggest the presence of internal tides. Their locations are indicated by stars in Figure 4.2a. Analyses of mooring data from the southern shelf and slope by *Middleton and Foster* [1977] showed that semidiurnal tidal currents in a benthic layer extending to 100 m above the seabed were strongly depth-dependent. They described these tides as "baroclinic", however, in a later paper [*Foldvik et al.*, 1990] they noted that the vertical structure was consistent with the ocean's barotropic response when tidal constituents were close to their critical latitude, i.e., the latitude at which the tidal frequency equals the Coriolis frequency, f. There are two issues here that are relevant to later discussions. First, throughout most of the Weddell Sea, f is close to the frequency of the dominant semidiurnal M_2 tidal constituent, and thus short data records cannot distinguish between near-inertial (possibly wind-forced) motion, and tidal motion. Second, significant vertical structure of tidal currents can exist under certain circumstances, even without any density stratification.

Other observations of semidiurnal-band ocean variability in the Weddell Sea have been reported by *Foster* [1994] and *Robertson et al.* [1995]. *Foster* saw large vertical displacements of the pycnocline in one day of CTD data in the northwestern Weddell Sea, while *Robertson et al.* found strong semidiurnal-band velocity shear across the pycnocline in the eastern Weddell Sea near Maud Rise. Recently recovered current meter moorings from the northern Filchner Trough [*Woodgate et al.*, 1998] show similar semidiurnal-band velocity structure to that described by *Foldvik et al.* [1990], with most

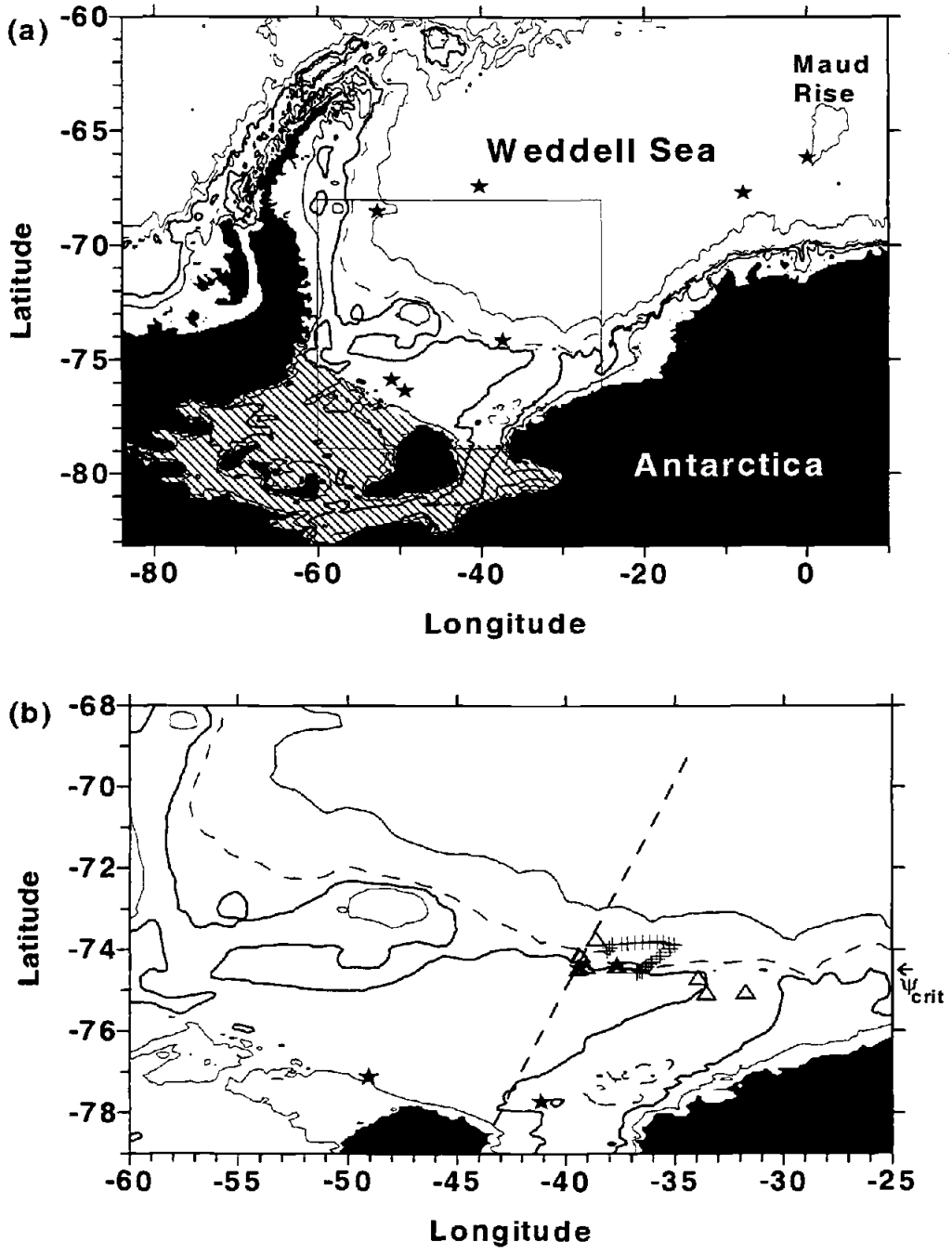

Figure 4.2. a) The water column thickness for the Weddell Sea, contoured at 200, 500 (thick line), 1000 (dashed line), and 3000 m. The Filchner-Ronne Ice Shelf area is indicated by hatching. Stars indicate the location of observations of internal tides. b) The water column thickness for the boxed region in a) with identical contouring intervals. The location of the transect used for the model domain is shown as a dashed line. The location of observations of tidal elevations are indicated by stars, those of tidal currents by triangles, and those of the Ropex profiles by crosses. The location of the M_2 critical latitude is indicated by ψ_{crit}, on the right axis.

of the depth-dependence explained by the thick boundary layer near the M_2 critical latitude rather than by baroclinicity.

The available database (stars in Figure 4.2a and triangles in Figure 4.2b) is clearly inadequate for evaluating the overall relevance of baroclinic tides to Weddell Sea oceanography. *Robertson et al.* [1998] (hereinafter referred to as *RPE*) developed a high-resolution, depth-integrated ocean tidal model to improve our understanding of the distribution of barotropic tidal kinetic energy in the Weddell Sea. They postulated that, based on the magnitude of tidal currents over the continental shelf and slope, adding tides to a general circulation model should significantly decrease the transport of the Weddell Gyre by increasing the effective bottom drag coefficient. Furthermore, a parameterization of the energy flux going from the barotropic to the baroclinic tide suggested that baroclinic tides may be sufficiently strong to play a role in water mass modification near the shelf break (Figure 4.3a).

Motivated by these previous studies, the primary goal of this study was to improve the understanding of internal tide generation beyond the simple parameterization of baroclinic tides described by *RPE*. The area of focus is the southern shelf and slope of the Weddell Sea, since this is the region in which tidal kinetic energy is known to be strong and simple models suggest that the baroclinic tide should be significant (Figure 4.3a). For this investigation, a numerical model (a modified version of the Princeton Ocean Model) was used in an attempt to simulate internal tide generation for conditions that are typical of the southern slope.

The numerical model is described in section 4.3. Models have been successfully used to determine the internal tidal fields in mid-latitude regions such as the Hudson-Raritan Basin [*Oey*, 1985], the Hebrides Sea [*Xing and Davies*, 1996], Monterey Bay [*Petruncio,* 1996], the Australian Northwest Shelf [*Holloway*, 1996], and Georges Bank [*Chen and Beardsley*, 1998]. Theoretical considerations for different wave types, including internal waves, and their generation and propagation are discussed in section 4.4. Section 4.5 evaluates the model results, including comparisons with existing observations and an evaluation of critical latitude effects. A summary is provided in section 4.6.

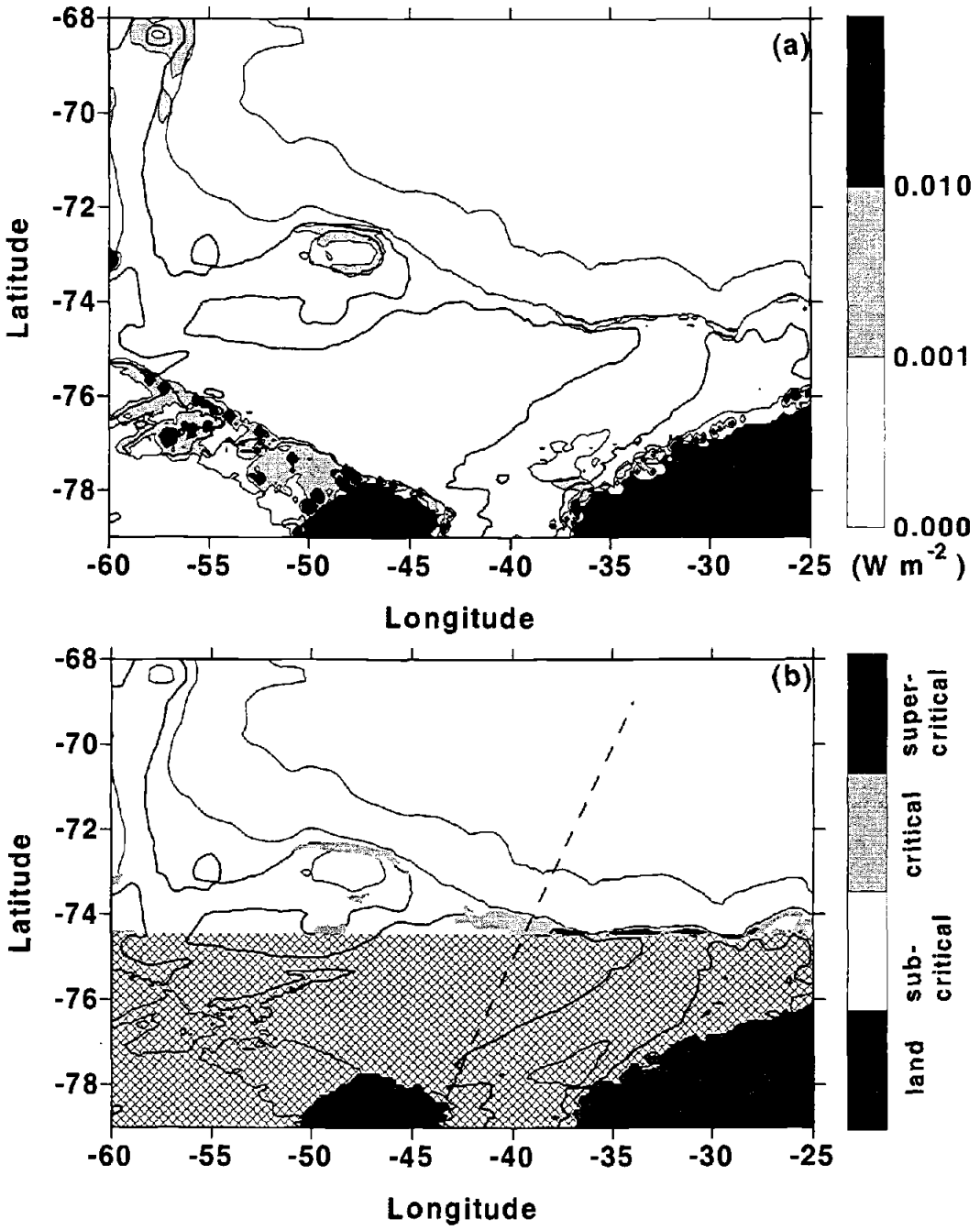

Figure 4.3. a) The energy loss from the barotropic tide to the baroclinic tide as determined by *Robertson et al.* [1998] following the method of *Sjöberg and Stigebrandt* [1992]. b) The internal wave generation criteria parameter, $\gamma(M_2)$, for the Weddell Sea. The locations of the transect is shown as a dashed line. The subcritical, critical, and critical regimes of $\gamma(M_2)$ are indicated. Water column thickness is contoured at 200, 500 (thick line), 1000, and 3000 m in both a) and b). In b), the area poleward of the critical latitude where the linear theory is no longer applicable is indicated by gray hatching. $\gamma(M_2)$ is defined as zero for flat slopes.

4.3. Modeling Approach

4.3.1. Model Description

A slightly modified version of the Princeton Ocean Model (POM) was utilized to simulate the generation and propagation of internal tides for two-dimensional cross-sections over the continental shelf and slope. POM has been previously applied for this purpose in mid-latitude regions by *Holloway* [1996] and *Chen and Beardsley* [1998]. Only the major points and the modifications of POM, primarily to accommodate the presence of an ice shelf, will be covered here; a full description of POM can be found in *Mellor* [1993].

POM is a three-dimensional, non-linear, primitive equation model, developed by *Blumberg and Mellor* [1987]. The model has a free surface and makes both the Boussinesq and hydrostatic approximations. It uses the Mellor-Yamada level 2.5 turbulence closure scheme for vertical mixing of momentum, heat, and salt. The Smagorinsky diffusivity scheme was used to determine the horizontal momentum viscosity and horizontal temperature and salinity diffusivity coefficients. In this scheme, diffusivity is dependent on grid size, horizontal velocity shear, and an adjustable constant. This constant was set to 0.2 as suggested by the model developers, although smaller values have been used [*Oey*, 1985]. Potential density, σ_θ, is determined from potential temperature, θ, and salinity, S, fields using the UNESCO equation of state [*Mellor*, 1993]. POM was modified to accommodate the existence of an ice shelf as a frictional stress surface by adding a term for surface friction against the ice shelf in the surface stress calculation. The ice shelf was assumed to float. Sea ice was not included in the model. A quadratic stress formulation was used for both the sea bed and the ice shelf with the drag coefficient, $C_D = 0.0025$. Because of the existence of an ice shelf over part of the domain, boundary layers were used at both the surface and bottom (see section 4.3.2). The leap-frog scheme was used for time stepping. The model utilizes the "barotropic-baroclinic mode" splitting technique to reduce the number of computations for the baroclinic mode. A barotropic time step of 2 seconds was used, which was within the stability requirement of the Courant-Friedrichs-Levy condition for the grid size and

domain bathymetry [*Haltiner and Williams*, 1980, p. 119]. A baroclinic time step of 72 seconds was used. Most of the simulations were run for fifty-five days; exceptions are noted. This simulation length was selected because the domain-integrated energy in the baroclinic mode of the model stabilized after approximately fifty days.

Other modifications were made to POM to reduce the effective stratification, which resulted from the normalization of density. These modifications include using double-precision for all variables, using a mean density (ρ_o) based on the potential temperature and salinity biases at the ocean surface, normalizing the density by the mean density (ρ_o) as opposed to 1000., and using 1449.2 instead of 1449.1 in the calculation of the speed of sound in the density pressure corrections. These modifications effectively change the set of density calculations from

$$\begin{aligned}
\rho &= \frac{\rho_{P,\theta,S} - \rho_o}{1000.} \\
\rho_o &= 1027.0 \\
\rho_{P,\theta,S} &= \rho_{\theta,S} + 10^4 \, {}^{p}\!/_{c^2}\left(1 - 0.2 \, {}^{p}\!/_{c^2}\right) \\
p(\sigma) &= -\rho_o \, g \, 10^{-4}(H + \eta)\sigma \\
c &= 1449.1 + 0.00821p + 4.55\theta - 0.45\theta^2 + 1.34(S - 35.)
\end{aligned} \tag{4.1}$$

to

$$\begin{aligned}
\rho &= {}^{\rho_{P,\theta,S}}\!/_{\rho_o} - 1. \\
\rho_o &= \rho_{\theta,S}(\theta_{Bias}, S_{Bias}, P = 0) \\
\rho_{P,\theta,S} &= \rho_{\theta,S} + 10^4 \, {}^{p}\!/_{c^2}\left(1 - 0.2 \, {}^{p}\!/_{c^2}\right) \\
p(\sigma) &= -\rho_o \, g \, 10^{-4}(H + \eta)\sigma \\
c &= 1449.2 + 0.00821p + 4.55\theta - 0.45\theta^2 + 1.34(S - 35.)
\end{aligned} \tag{4.2}$$

where ρ is the normalized in-situ density (no units), ρ_o is a typical mean density (kg m^{-3}), $\rho_{P,\theta,S}$ is the *in-situ* density for the potential temperature and salinity (kg m^{-3}), $\rho_{\theta,S}$ is the density for the potential temperature and salinity at the surface (kg m^{-3}), p is the pressure (decibars), c is the speed of sound (m s^{-1}), g is the gravitational acceleration (9.8 m s^{-2}), θ is the potential temperature (°C), S is the salinity (psu), H is the water depth (m), η is the surface elevation (m), σ is the vertical coordinate ((surface) $0 \geq \sigma \geq -1$ (bottom)) (no

units), and the 'Bias' subscript refers to bias reference values used by POM. (Biases of $\theta_{Bias} = 0.0$ °C; $S_{Bias} = 34.4$ psu were chosen.) A full discussion of the errors in the equation of state is given in *Mellor* [1991].

4.3.2. Model Domain, Grid, Bathymetry, and Initial Hydrography

A transect across the continental shelf/slope break was selected for the model domain (dashed line in Figure 4.2b). It was selected to be aligned with the direction of tidal propagation at the continental shelf/slope break and to pass in the vicinity of existing tidal observations (triangles and stars in Figure 4.2b). Due to the curving coastline of this region, however, the direction of tidal propagation varies over the transect and only is aligned with the transect at the continental shelf/slope break. The transect is roughly perpendicular to the continental shelf/slope break.

The model uses an Arakawa C-grid in the horizontal dimensions. Although the model was operated in a three-dimensional mode, this was essentially a two-dimensional application, using the cross-slope, y, and vertical, z, directions. The grid was composed of 5 cells in the along-slope direction, x, and 600 in the cross-slope direction, y. The horizontal grid spacing was 2 km in both the along-slope and cross-slope directions. The model utilizes a sigma-coordinate system with σ scaled to the sum of the water column thickness, $H(y)$, and the surface elevation, $\eta(y,t)$. This quantity is also defined as the effective water depth, $D(y,t)$, ($D(y,t) = H(y) + \eta(y,t)$). Under the ice shelf, the coordinate system is offset from the surface by the ice shelf thickness in order to account for the pressure head associated with the ice shelf. Sixty-six sigma levels were used, of which sixty were spaced evenly through the water column excluding the numerical boundary layers. Another three sigma layers were spaced in each of the numerical surface and benthic boundary layers. These three sigma layers occupy the equivalent of one of the mid-water column sigma layers and their thicknesses decrease as 0.5, 0.25, and 0.25 of one of the mid-water column layer heights, respectively, with the smaller sigma layers near the surface and the bottom.

Modified ETOPO5 bathymetry was used for the model depth, with the modifications described in *RPE*. Estimates of the bathymetry under the Filchner-Ronne Ice Shelf and

ice shelf thickness came from the map of *Vaughan et al.* [1994]. The water column thickness, H, was the difference between the bathymetry and the ice shelf thickness, if any. The ice shelf depth thickness was limited to 340 m to allow the southern boundary to be open. Since the real three-dimensional flow is not blocked by Berkner Island but flows under the ice shelves at the southern end, an open boundary is required in the two-dimensional application to simulate equivalent topographic conditions. We are attempting to simulate an open basin. With a wall at the southern boundary, this two-dimensional application would be that of a closed basin and a standing wave would be set up by the wave reflecting from the southern end. This is not the condition we are trying to simulate.

To reduce potential problems with the noise in observational hydrographic data, an idealized stratification scheme with a similar density gradient to that of observed winter stratification was used. The observed winter stratification hydrography (black lines in Figures 4.4a and 4.4b) was based on data from Ice Station Weddell [*Huber et al.*, 1994] and from the southern slope region [*Foster and Carmack*, 1976]. The idealized scheme has a constant potential temperature (gray line in Figure 4.4a) and a salinity, which increased with depth (gray line in Figure 4.4b). The observed winter stratification profiles (black lines) and the hypothetical winter stratification profiles (gray lines) of σ_θ and the Brunt- Väisälä frequency (N) are shown in Figures 4.4c and 4.4d, respectively. The value of N (s^{-1}) , was determined from the stratification according to

$$N = \left(\frac{-g}{\rho_o} \partial \rho_s / \partial z + \frac{g^2}{c^2} \right)^{1/2}, \tag{4.3}$$

where ρ_s is the non-normalized *in-situ* density (kg m^{-3}) (with the mean density ρ_o = 1027.8 kg m^{-3}). These profiles were used over the entire domain. This ignores the front existing over the continental shelf break in Figure 4.1, which results from different hydrography for the deep basin and the shelf. The hydrography over the shelf in Figure 4.1 was estimated from data of *Foster and Carmack* [1976], *Foster et al.* [1987], and *Gammelsrød et al.* [1994].

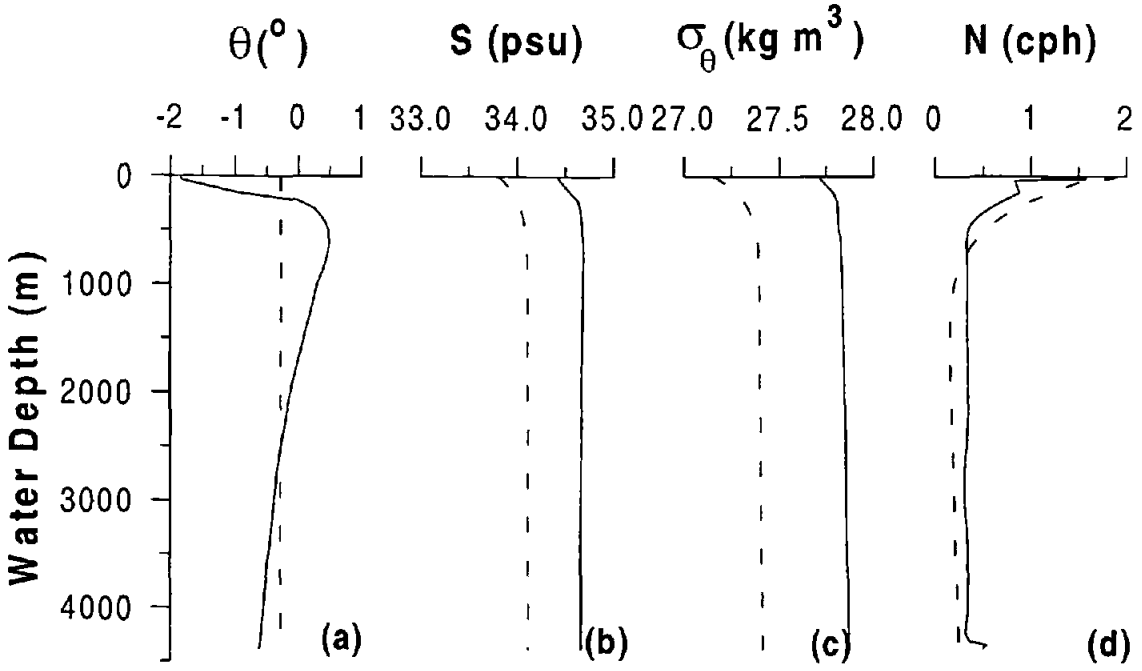

Figure 4.4. The a) potential temperature, θ, b) salinity, S, c) potential density, σ_θ, and d) Brunt-Väisälä frequency, N, profiles for the observed winter stratification (solid lines) and the idealized winter stratification (dashed lines).

Cases with uniform potential temperature and salinity fields, in other words a homogeneous ocean, were run to define the background barotropic elevation and velocity fields. These homogeneous simulations were run for only 30 days, since the domain-averaged energy for the "baroclinic mode" of the solution stabilized after 25 days.

4.3.3. Boundary Conditions and Forcing

Since land was not included in the model domain, four open boundaries were present. For the cross-slope boundaries, cyclic boundary conditions were used for all variables. In this application, this condition along with the geometry of the domain results in all variables being constant in the along-slope direction. At both the deep basin and continental shelf open boundaries, tidal forcing was implemented by setting the elevations, η, using coefficients taken from a barotropic tidal model for the Weddell Sea [*RPE*]. Only the most energetic constituent, M_2, was used for tidal forcing. The tidal

forcing was modified by a ramp over the first day to reduce the high frequency noise generated by an initial impulse [*Holloway*, 1996].

After consideration of several alternative open boundary conditions [see *Palma and Matano*, 1998], the *Lewis et al.* [1994] partially clamped radiative boundary condition was chosen for the depth-independent cross-slope velocity, V_A, and an advective scheme for depth-independent along-slope velocities, U_A, on the shelf (southern) and deep basin (northern) boundaries [*Petruncio*, 1996]. The boundary conditions for V_A were tuned as suggested by *Lewis et al.* [1994]. This tuning was required in order to achieve elevation amplitudes comparable to the specified elevation. *Martinsen and Engedahl*'s [1987] flow relaxation scheme was used over five cells for the depth-dependent horizontal velocities, U and V, at both the shelf and deep basin boundaries. A detailed description of *Martinsen and Engedahl*'s boundary scheme can be found in *Holloway* [1996]. The boundary conditions for the vertical velocity, W, were no flow through the surface and bottom sigma layers and zero at the open continental shelf and deep basin boundaries. The open continental shelf and deep basin boundary conditions for θ and S used a interpolation boundary condition equivalent to *Martinsen and Engedahl*'s [1987] flow relaxation scheme.

4.4. Theoretical Considerations

4.4.1. Wave Types and Wave Generation

In the southern ocean, the M_2 tide consists primarily of a barotropic Kelvin wave propagating westward around Antarctica. Even without stratification, interaction of the tide with topography may cause the excitation of inertial oscillations, gyroscopic waves, and/or barotropic Poincaré waves [*Huthnance*, 1981; *Middleton and Denniss*, 1993; *LeTareau and Maze*, 1996]. Where stratification exists, variations in topography may cause some of the barotropic Kelvin wave energy to be converted to baroclinic Kelvin waves [*Baines*, 1986], baroclinic Poincaré waves, or higher frequency internal gravity waves [*Gill*, 1982, pp. 142]. Higher frequency internal waves may also be generated

through non-linear interactions and result in energy being transferred to harmonics of the original frequency.

Poincaré waves, sometimes referred to as Sverdrup waves [*Gill*, 1982, pp. 250], are gravity waves with rotation, and a balance exists between pressure, the Coriolis force, and acceleration [*Kundu*, 1990, pp. 506-507]. They have frequencies greater than or equal to the inertial frequency, and elliptical orbits, which become circular at near-inertial frequencies. When the frequency equals the inertial frequency, they are denoted inertial oscillations and pressure no longer plays a role, so the momentum balance is between the Coriolis force and acceleration.

In an unstratified fluid with rotation, gyroscopic waves can exist [*LeBlond and Mysak*, 1978, pp. 37-40]. They have frequencies less than or equal to the inertial frequency and the Coriolis force balances acceleration. Their group velocity propagates horizontally, perpendicular to the phase velocity. At the inertial frequency, the group velocity goes to zero, only a vertical wavenumber exists, and the particle motion lies in the horizontal plane. This particle motion can impart a vertical structure to the horizontal velocities similar to that of baroclinic internal waves.

Generation of internal waves is primarily dependent on the steepness of the topography, the strength of the barotropic current, and the stratification. *Baines* [1986] developed a parameter for determining the necessary conditions for internal wave generation. This parameter, γ, is the ratio of the bottom slope, $\partial H/\partial y$, to the slope of the internal wave characteristic ,α, i.e.,

$$\gamma = \frac{\partial H/\partial y}{\alpha}, \tag{4.4}$$

where

$$\alpha = \left(\frac{\omega^2 - f^2}{N^2 - \omega^2} \right)^{1/2}. \tag{4.5}$$

Here, ω is the wave frequency (s^{-1}) and f is the Coriolis parameter (s^{-1}), determined from $f = 2\,\Omega \sin \psi$, where Ω is the earth's angular rotation ($7.292 \times 10^{-5}\ s^{-1}$) and ψ is the

latitude. For internal tides, ω is the tidal frequency (1.40518×10^{-4} s^{-1} for M_2). The value of N near the seabed is used for this calculation.

When $\gamma \approx 1.0$, the slope is critical and the generation of internal waves is the greatest. Internal waves generated on a critical slope propagate along the slope, since their ray paths lie on the slope. Where γ is less than 1.0, the slope is called subcritical and few, if any, internal waves are generated. Any waves which are formed can propagate either on- or offshore. Where γ is greater than 1.0, the slope is supercritical and internal waves are generated but the energy can only propagate offshore [*Sherwin*, 1991]. Note that as $\omega \rightarrow f$, $\alpha \rightarrow 0$; consequently, even for weakly stratified conditions (small N) gentle bottom slopes can lead to a critical or supercritical values for γ. A flat bottom, however, will only result in subcritical values for γ ($\gamma = 0$). Since internal wave generation occurs not only exactly at $\gamma = 1$ but also in a band around this value, a range between 0.5 and 2.0 was defined as the range of critical γ, with values below this range being subcritical and values above being supercritical.

The value of γ for the M_2 frequency was estimated for the southern Weddell Sea (Figure 4.3b). For this calculation, a generalized N was used that was dependent on the water depth, with N equal to 2.0 cph for depths less than 500 m, varying linearly from 2.0 to 0.2 cph for depths between 500 and 1000 m, and equal to 0.2 cph for depths below 1000 m. This estimate predicts that internal tides can be generated in localized areas along the continental shelf break with water depths of approximately 500-800 m and that a critical slope region exists within the transect.

The value of $\gamma(M_2)$ was also determined for the transect using N at the bottom determined from the model's initial hydrography. $\gamma(M_2)$ (solid black line in Figure 4.5a) is critical over the upper continental slope at roughly 520 to 600 km distance from the transect origin (See Figure 4.5c for the topography). The generally subcritical values of γ are due to the weak stratification.

The latitude where the tidal frequency, ω, equals the inertial frequency, f, is referred to as the critical latitude, ψ_{crit}. The critical latitude for M_2 is at 74° 28.5' S, which is near the top of the continental slope 522 km from the origin of the transects (Figures 4.2b and

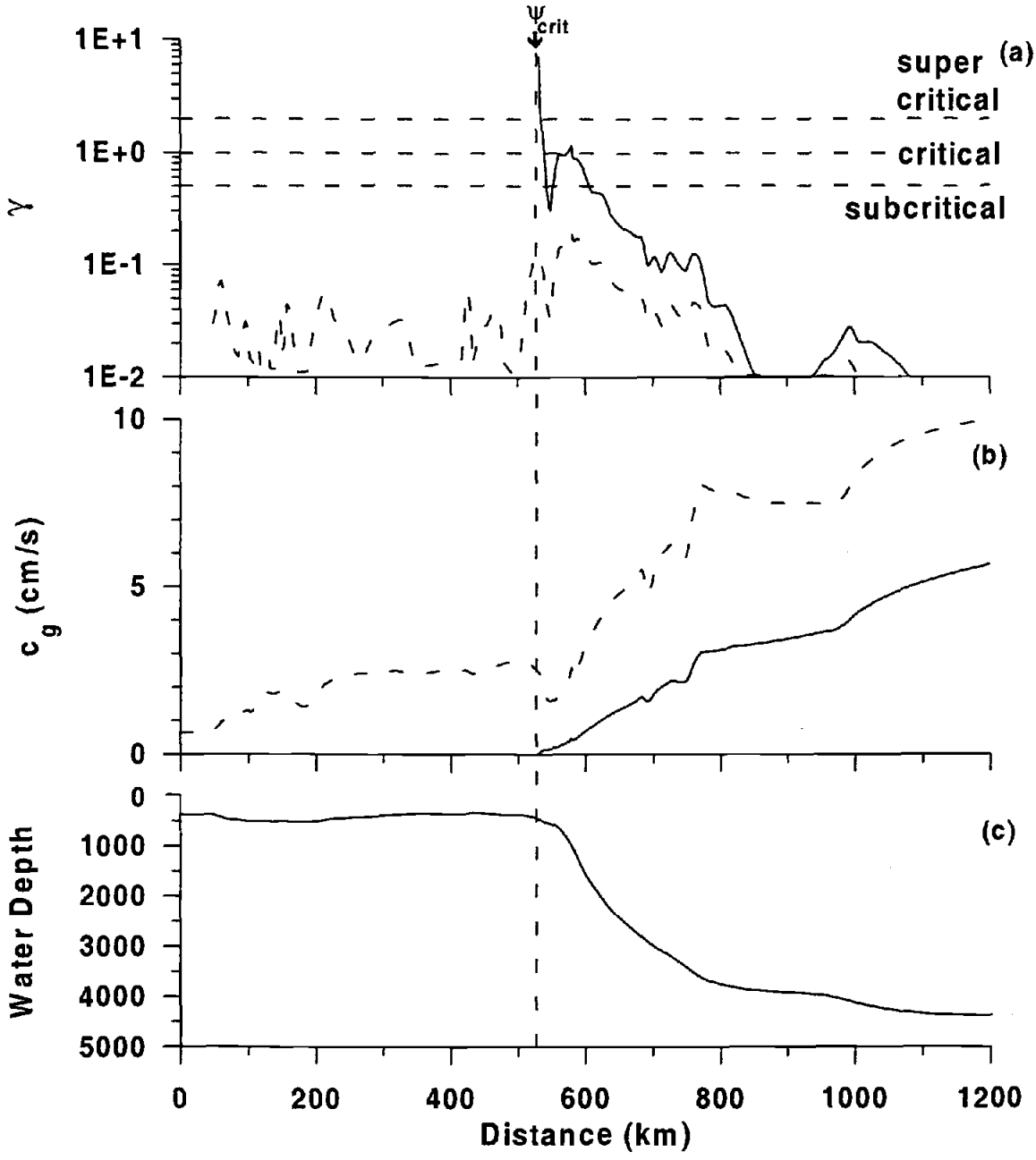

Figure 4.5. a) The internal wave generation criterion parameter, $\gamma(M_2)$, b) the internal wave horizontal group speed, c_g, and c) the water depth, D, and ice shelf thickness for the transect with the hypothetical winter stratification. In a) and b), the values when the transect is in the actual location are indicated by black lines and by dashed lines when the transect is shifted 10° north so the critical latitude is not present in the domain. The critical, subcritical, and supercritical ranges are denoted in a). The location of the M_2 critical latitude is denoted with ψ_{crit} in b) and the effective critical latitude range by ECLR. The corresponding fields for a strong stratification of $N = 2.6$ cph throughout the water column are shown in d), e), and f).

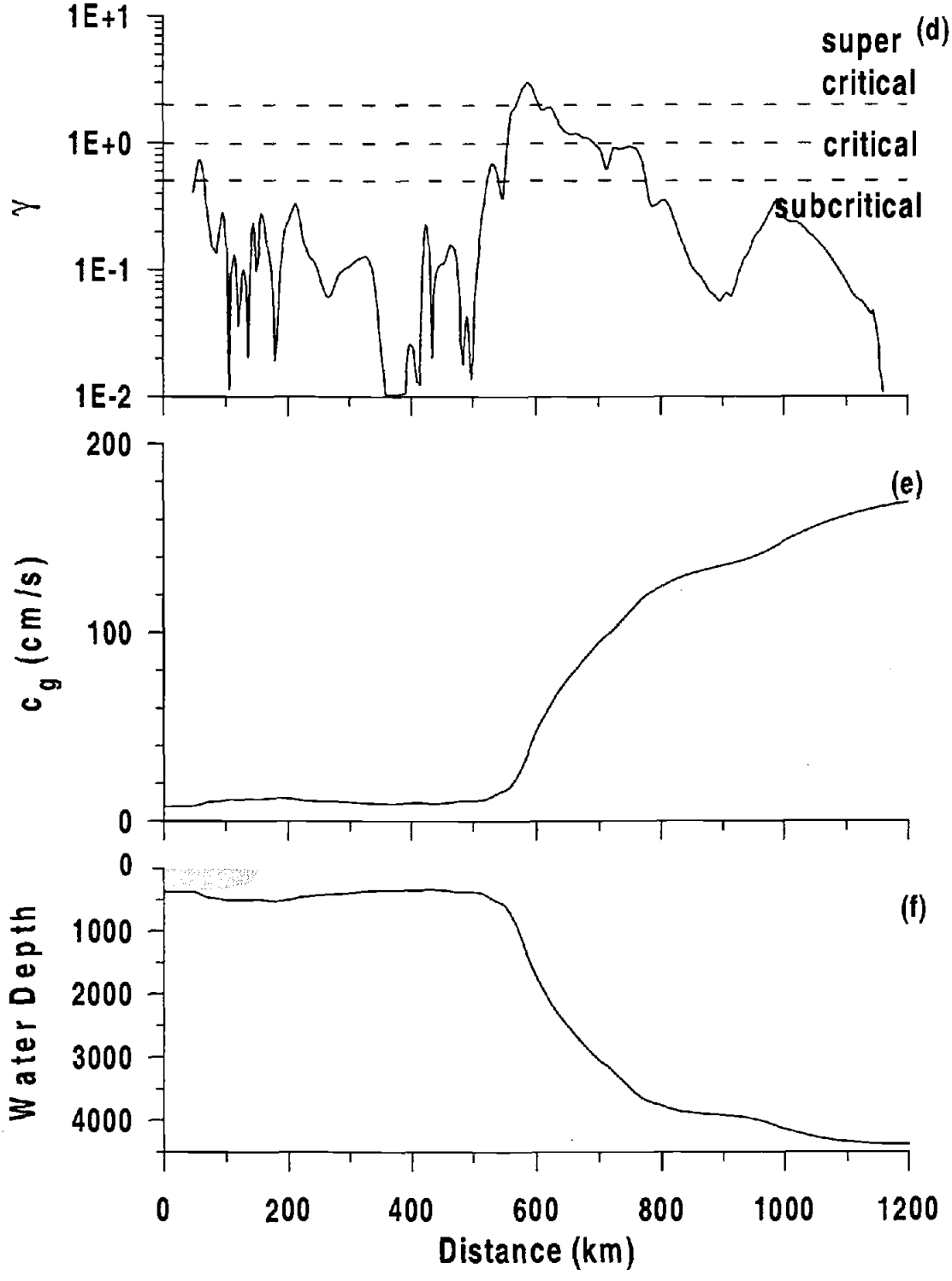

Figure 4.5. (continued)

4.5b). Since at ψ_{crit}, $f = -\omega$ (Southern Hemisphere), α becomes zero and γ goes to infinity there. Obviously, the linear theory used to determine γ fails at this point and γ (M_2) is not shown poleward of ψ_{crit} in Figure 4.5a.

If the domain is shifted northward 10° so that ψ_{crit} is no longer in the domain, γ never reaches the critical level (dashed line in Figure 4.5a). However for strong stratification such as $N = 2.6$ cph throughout the water column, γ (M_2) (Figure 4.5d) is critical over most of the continental slope and supercritical over the upper continental slope.

4.4.2. Wave Propagation

While the regions for wave generation may be highly localized, the resultant waves may be observed over a broader area, dependent on their propagation characteristics. Wave propagation is characterized by the dispersion relation and the horizontal group speed, c_g. These relations are shown in Table 4.1 for Kelvin waves, Poincaré waves, gyroscopic waves, and internal waves, where k, l, and m are the along-slope, cross-slope, and vertical wavenumbers (m^{-1}), respectively. Most of the tidal energy in the Weddell Sea propagates as a barotropic Kelvin wave, independently of changes in latitude, with c_g dependent only on the water column thickness (Table 4.1). However, in some areas tidal energy propagates as Poincaré waves, whose propagation is dependent on latitude, ψ, through f. Since $|\omega| > |f|$ for M_2 Poincaré waves, they do not develop poleward of ψ_{crit}. Furthermore, the critical latitude acts as a turning latitude, ψ_{turn}, for poleward-propagating Poincaré waves and prevents them from propagating further poleward. *Middleton and Denniss* [1993] note the turning latitude, ψ_{turn}, does not always coincide with ψ_{crit}; however, using their evaluation for the transect resulted in $\psi_{turn} \approx \psi_{crit}$. It should be noted that due to the long barotropic wavelengths (Table 4.1), ψ_{crit} does not act as a complete wall, but allows some energy to propagate through. This is also true for reflection from the slope, since the wavelengths are long in comparison to the shelf width (~150 km). The propagation of gyroscopic waves is also latitude-dependent through f and they do not develop equatorward of ψ_{crit}.

Wave Type	Dispersion Relation	Group Speed Relation	Typical Group Speed*	Typical Wavelength♦
Barotropic Kelvin	$\omega^2 = g\,H\,l^2$	$c_g = \pm\sqrt{gH}$	$c_g = 76.7\,m\,s^{-1}$	$L_y(600) \sim 3{,}400\,km$ $L_y(4000) \sim 8{,}850\,km$
Barotropic Poincaré	$\omega^2 = f^2 + g\,H(k^2+l^2)$	$c_g = \pm\dfrac{gHl}{\sqrt{f^2+g\,H(k^2+l^2)}}$	$c_g = 3.0\,m\,s^{-1}$	$L_y(600) \sim 73{,}000\,km$ $L_y(4000) \sim 103{,}000\,km$
Baroclinic Poincaré	$\omega^2 = f^2 + \dfrac{N^2(k^2+l^2)}{m^2}$	$c_g = \pm\dfrac{N^2 l}{m^2\sqrt{f^2+\dfrac{N^2(k^2+l^2)}{m^2}}}$	$c_g = 2x10^{-5}\,m\,s^{-1}$	$L_y(600) \sim 85\,km$ $L_y(4000) \sim 72\,km$
Internal Waves in a Continuously Stratified Fluid	$\omega^2 = f^2 + \dfrac{N^2(k^2+l^2)}{(k^2+l^2+m^2)}$	$c_g = \pm\dfrac{m(N^2-f^2)\sqrt{(k^2+l^2)}}{(k^2+l^2+m^2)^{3/2}\sqrt{f^2+\frac{(k^2+l^2)N^2}{m^2}}}$	$c_g = 0.04\,m\,s^{-1}$	$L_y(600) \sim 80\,km$ $L_y(4000) \sim 60\,km$

in two dimensions, the cross-slope direction, y, and the vertical direction, z

c_g is in the cross-slope direction

* calculated using $H = 600$ m, $N = 1.2$ cph, $\Psi = 74°\,14.7'$ S, and assuming mode one internal waves ($m = \pi/H$)

♦ calculated using $H = 600$ m and $H = 4000$ m

Table 4.1. The dispersion relations, the cross-slope horizontal group speed relations, and typical group speed and wavelength values for Kelvin waves, Poincaré waves, gyroscopic waves, and internal waves in a continuously stratified fluid.

The internal wave dispersion relation and group speed are also dependent on latitude (Table 4.1). To investigate the propagation rate, the cross-slope component of the internal horizontal group speed, c_g, was determined using

$$c_g = \partial\omega/\partial l = \frac{N^2}{m\omega}\left(\frac{\omega^2 - f^2}{N^2 - f^2}\right)^{1/2} \tag{4.6}$$

[*Gill*, 1982, pp. 261]. This formulation is equivalent to that in Table 4.1 when the WKB approximation ($N(z)$ varies slowly) is used and

$$m^2 = \frac{l^2\left(N^2 - \omega^2\right)}{\left(\omega^2 - f^2\right)} . \tag{4.7}$$

For the purpose of calculating typical values, the internal waves were assumed to be of mode one (i.e., $m=\pi H^{-1}$), where H is the water column thickness. Internal waves are only generated for frequencies between f and N. Internal tides are internal waves at the tidal frequencies and follow these relationships. The estimated values of c_g are low, roughly 1-6 cm s^{-1}, for the M_2 internal tides over the upper continental slope and decreasing to zero at ψ_{crit}, as seen by the solid black line in Figure 4.5b. The low c_g values imply that internal tides propagate only very slowly from the generation site. The low c_g values result from weak stratification and the proximity to ψ_{crit}. When the domain is moved north 10° so that ψ_{crit} is no longer in the domain, c_g increases (dashed line in Figure 4.5b). Furthermore when stronger stratification is present (N = 2.6 cph throughout the water column) and the domain is shifted 10° N, c_g increases by more than an order of magnitude (Figure 4.5e).

Another way to look at internal waves is through internal wave ray theory. According to ray theory, any locally generated internal tidal energy should propagate along internal wave ray paths. Characteristic ray paths for the M_2 internal tides for the latitude, stratification, and topography of the model domain are shown in Figure 4.6a. The steepness of the ray paths is due to the weak stratification. It should be noted that there are no internal wave rays poleward of the critical latitude. Also over the upper slope, the angle of the internal wave rays is quite parallel to the bottom slope. Figure 4.6b shows the corresponding ray paths for the stratification and domain if the latitude was shifted

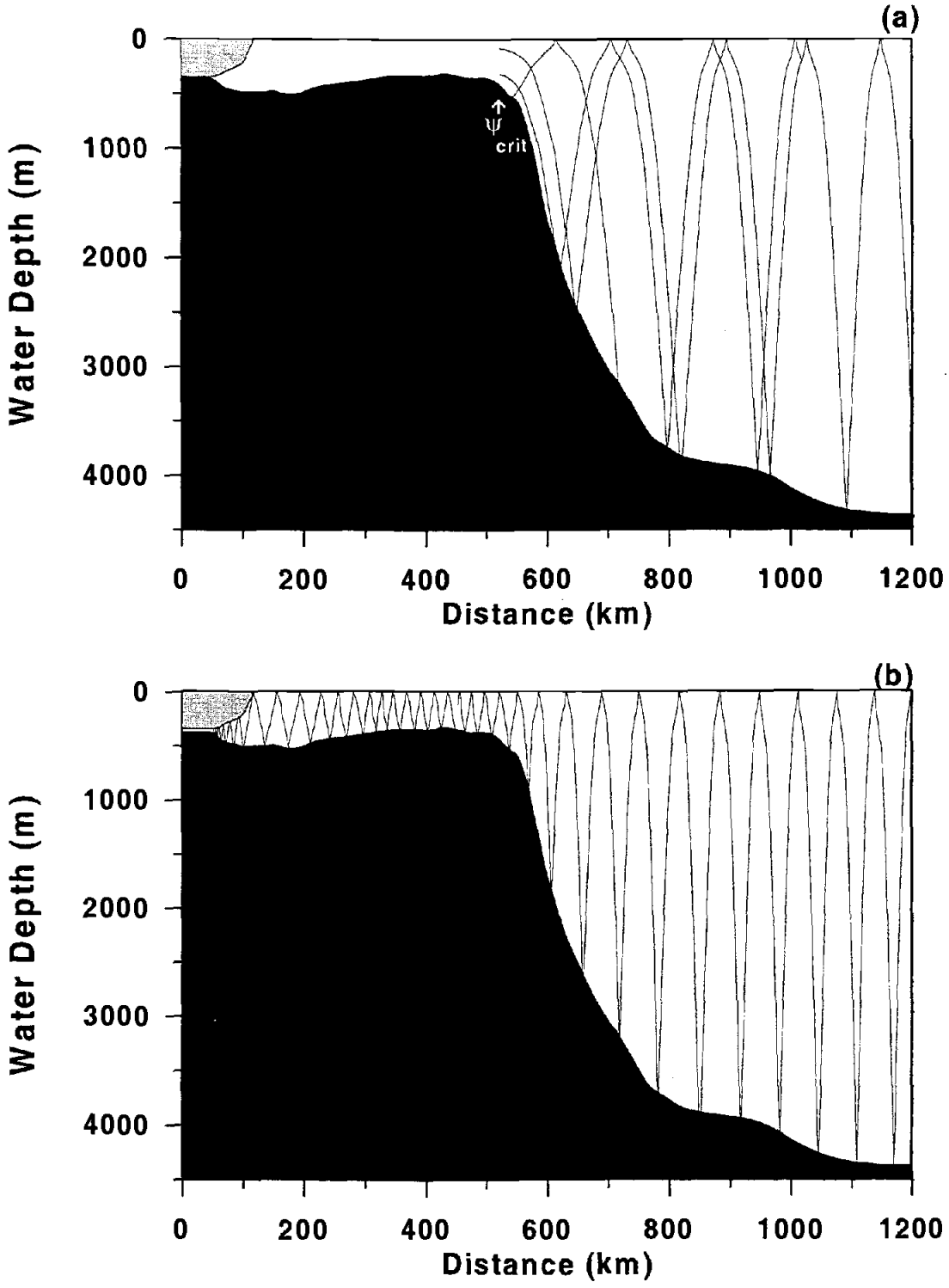

Figure 4.6. Characteristic internal waves ray paths for the M_2 tide a) with the critical latitude present in the domain and b) without the critical latitude in the domain. The location of the critical latitude is indicated by ψ_{crit} in a).

10° to the north, so ψ_{crit} was no longer present in the domain. The internal wave rays exist throughout the domain, but are not parallel to the bottom slope, since $\gamma(M_2)$ is subcritical. Values of c_g for this scenario are much higher (dashed line in Figure 4.5b) than those at the original latitude, so internal tidal energy will propagate away from the generation site faster. However, since $\gamma(M_2)$ for this shifted latitude range is always below the critical level (dashed line in Figure 4.5a), internal tides are unlikely to be generated.

The foregoing discussion has been based on linear theory and there is a question of how well this theory approximates reality. *Eriksen* [1998] investigated internal wave reflection and mixing at Fieberling Guyot and found that the linear theory for generation and reflection of internal waves off a sloping bottom predicted the enhanced peak at the frequency of the critical slope quite well. However, he noted that the linear wave theory failed to predict either the amplitude of the peak or the off-slope decay scale. Linear wave theory neglects advection, frictional stress and other non-linear effects that POM includes. Consequently, differences are expected between POM results and linear theory predictions. From the linear analysis, however, we expect internal tides to be generated only in a narrow band over the upper continental slope in the neighborhood of the critical latitude.

4.4.3. Boundary Layer Effects

Frictional stress causes a boundary layer at the seabed and at the surface under the ice shelf. Both the boundary layers and the vertical structure of the horizontal velocities can be affected by proximity to the critical latitude. To evaluate this effect, it is useful to decompose the tidal velocity into two rotary components, clockwise and anticlockwise. These components respond differently to proximity to ψ_{crit}. The amplitude of the positive rotary current (anticlockwise) should be depth-dependent and the amplitude of the negative rotary current (clockwise) should be depth-independent in the Southern Hemisphere [*Prinsenberg and Bennett*, 1989; *Foldvik et al.*, 1990]. *Furevik and Foldvik* [1996] used a formulation for the boundary layer thickness scale for the two rotary components (λ_+ and λ_-, respectively). The boundary layer thickness is defined as the

distance that the velocity magnitude is reduced by e^{-1} and the scales can be approximated by

$$\lambda_+ = \sqrt{\frac{K_M}{\omega + f}} \qquad \text{and} \qquad \lambda_- = \sqrt{\frac{K_M}{\omega - f}}, \tag{4.8}$$

where K_M is a constant vertical eddy viscosity ($m^2\ s^{-1}$). Over the upper continental slope at the latitude for the model domain, this theory predicts a λ_+ of 17 m at 70° S and 55 m at 74° S using $K_M = 0.001\ m^2\ s^{-1}$. At ψ_{crit}, $\omega = -f$ (Southern Hemisphere), these equations reduce to

$$\lambda_+ \to \infty \quad \text{and} \quad \lambda_- = \sqrt{\frac{-A_M}{2f}}, \tag{4.9}$$

i.e., the boundary layer for the positive rotary current becomes infinite; however, the theory breaks down here. Even though the theory cannot be applied precisely at the critical latitude, good agreement was found between theory and observations in both the Arctic [*Furevik and Foldvik*, 1996] and Weddell Sea [*Foldvik et al.*, 1990]. Thus, the observations support use of the theory except at the singular point (ψ_{crit}).

4.5. Model Results and Discussion

4.5.1. Model Result Considerations

4.5.1.1. *Model Outputs*

The model output includes cross-slope transects of elevation (η) and the depth-independent horizontal velocities (U_A and V_A) from the "barotropic mode", and two-dimensional fields of the depth-dependent velocities (U, V, and W), potential temperature (θ), and salinity (S) in the cross-slope (y) and vertical (z) directions from the "baroclinic mode". Hourly fields from the last two days for η, U_A, V_A, U, V, and W were analyzed using *Foreman*'s [1977; 1978] tidal analysis routines to obtain the tidal elevation and phases, major axes of the tidal ellipses for both the depth-independent and depth-dependent velocities, and the tidal vertical velocity amplitudes for the M_2 constituent.

4.5.1.2. *Sigma-Coordinate Effects*

One drawback of working in sigma coordinates is that false depth-dependent velocities can be generated by the model due to the choice of coordinate system in areas of rapidly changing water depth [*Blumberg and Mellor*, 1987; *Mellor*, 1993]. To investigate the magnitude of this false velocity for the model topography, the model was run without any forcing. The maximum false velocities generated over the continental shelf and slope were ~0.002 cm s^{-1} in the cross-slope direction and ~0.0003 cm s^{-1} in the vertical direction with the largest cross-slope. Velocities under the ice shelf were larger, reaching 0.1 cm s^{-1} in the cross-slope direction. Since the region under the ice shelf is of little interest, these velocity errors are acceptable for our investigation.

4.5.1.3. *Boundary Layer Effects*

Vertical structure in the horizontal velocities in an unstratified or stratified ocean can result from frictional effects and generally appears as a benthic boundary layer. *Furevik and Foldvik* [1996] investigated the effect of the critical latitude on seasonally ice-covered regions of the Barents Sea in the Northern Hemisphere. They observed that vertical structure in their horizontal velocity observations was related to proximity to the critical latitude (see section 4.4.3). They found that the benthic boundary layer was thicker near the critical latitude. They noted that for the Southern hemisphere, the positive rotary current (anticlockwise) will be affected by proximity to ψ_{crit} and its amplitude will be depth-dependent.

To see whether POM simulates this effect, a simulation was run with a flat bottom with a water depth of 400 m for a homogeneous water column. Profiles of the normalized amplitude of the anticlockwise component of the depth-dependent velocities show a dependence on the critical latitude (Figures 4.7a-4.7c). The boundary layer from POM (~300 m at 74°S and ~250 m at 70°S) is much thicker than that estimated following *Furevik and Foldvik* [1996] (55 m at 74°S and 17 m at 70°S). This difference in the boundary layer thicknesses primarily results from the differences in the vertical viscosity coefficient, but also is affected by the different tidal structure of the two studies. The *Furevik and Foldvik* scheme uses a $K_M = 0.001$ $m^2 s^{-1}$, whereas POM uses a variable K_M,

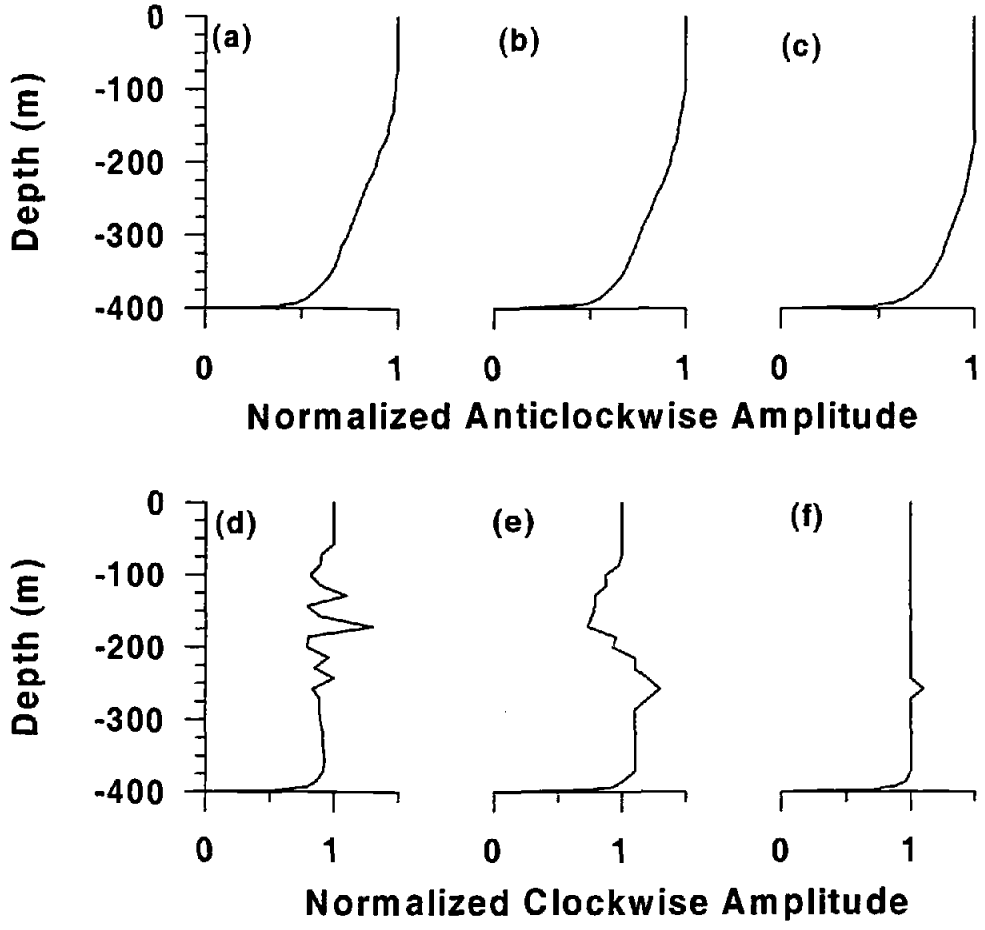

Figure 4.7. Profiles of the normalized amplitudes for the anticlockwise component of the baroclinic velocity from a simulation with a flat bottom and no stratification at a) the critical latitude and distances of b) 500 and c) 1400 km equatorward of the critical latitude. The corresponding normalized amplitude profiles for the clockwise component are shown in d), e), and f), respectively. The amplitudes were normalized by the amplitude for the surface values (uppermost cell). The normalized amplitudes for the clockwise component are roughly one tenth of those for the anticlockwise.

which is typically much larger especially in an unstratified ocean. The vertical viscosity from POM as determined by the Mellor- Yamada 2.5 level closure scheme became quite large, reaching 0.1 $m^2 s^{-1}$. Using $K_M = 0.1$ $m^2 s^{-1}$ in the *Furevik and Foldvik* formulation, the boundary layer thickness estimates became ~550 m at 74°S and ~170 m at 70°S, which are comparable to the POM values. The clockwise component also appears to have a critical latitude dependence (Figures 4.7d-4.7f). However, since the clockwise amplitude is quite small, roughly an order of magnitude less than the

anticlockwise amplitude, and the dependence is quite noisy, the dependence is probably due more to numerical noise than to critical latitude effects. The different tidal structure modeled by the two studies precludes an exact quantitative comparison: *Furevik and Foldvik* used a barotropic tidal field in polar coordinates around the M_2 amphidromic point of the central Barents Sea, whereas this study specifies tides along a straight coast. In conclusion, POM qualitatively simulates the expected effects of the critical latitude on the benthic boundary layer.

4.5.2. Stratified Ocean Without the Critical Latitude

To simplify the physics, the latitude of the domain was altered 10° to the north so that ψ_{crit} did not fall within the domain. The M_2 tidal elevations, η, from this simulation had an amplitude ranging from 0.44 m at the deep water end to 0.49 m at the ice shelf end (solid line in Figure 4.8a), and a phase of approximately 289° which was relatively constant over the transect (not shown). The major axes for the depth-independent velocities for the M_2 constituent (solid line in Figure 4.8b) are strongly influenced by the topography (gray line in 4.8b) increasing dramatically over the outer continental shelf and under the ice shelf.

As predicted by linear theory (Figure 4.5a), internal tides were not generated in these conditions. As a result, the depth dependence of the cross-slope velocity consisted only of ice shelf and benthic boundary layers. The benthic boundary layer is apparent in the profiles of the cross-slope depth-dependent velocities at a time near the peak offshore depth-independent tidal flow (t = 54.708 days) over the upper continental slope (dashed lines in Figure 4.9a) with a boundary layer thickness ranging from 50 to 100 m, from a POM generated K_M in the range of 10^{-3} to 10^{-6} $m^2 s^{-1}$. (t is the time since the start of the simulation.) Stratification reduces the K_M in POM from the high values of the homogeneous, flat bottom simulation of section 4.5.1.3.

4.5.3. Stratified Ocean With the Critical Latitude

To investigate the effect of the critical latitude, simulations were run with the transect in its original location (Figure 4.2b). The amplitudes of the elevation for simulations

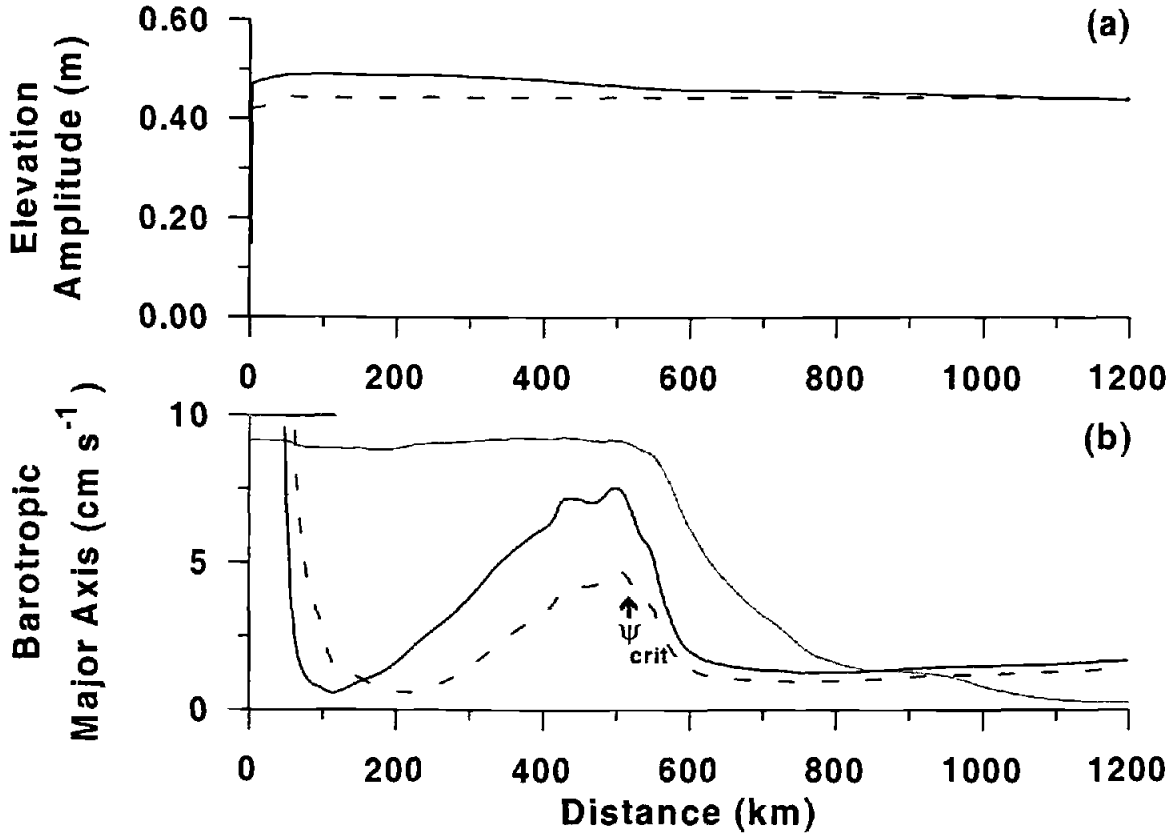

Figure 4.8. a) The elevation amplitude from simulations with (dashed line) and without (solid line) the critical latitude crossing through the domain. b) The major axis of the depth-independent velocities from simulations with (dashed line) and without (solid line) the M_2 critical latitude crossing through the domain. The topography is indicated in b) by thick gray lines. The location of the critical latitude is denoted with ψ_{crit} in b).

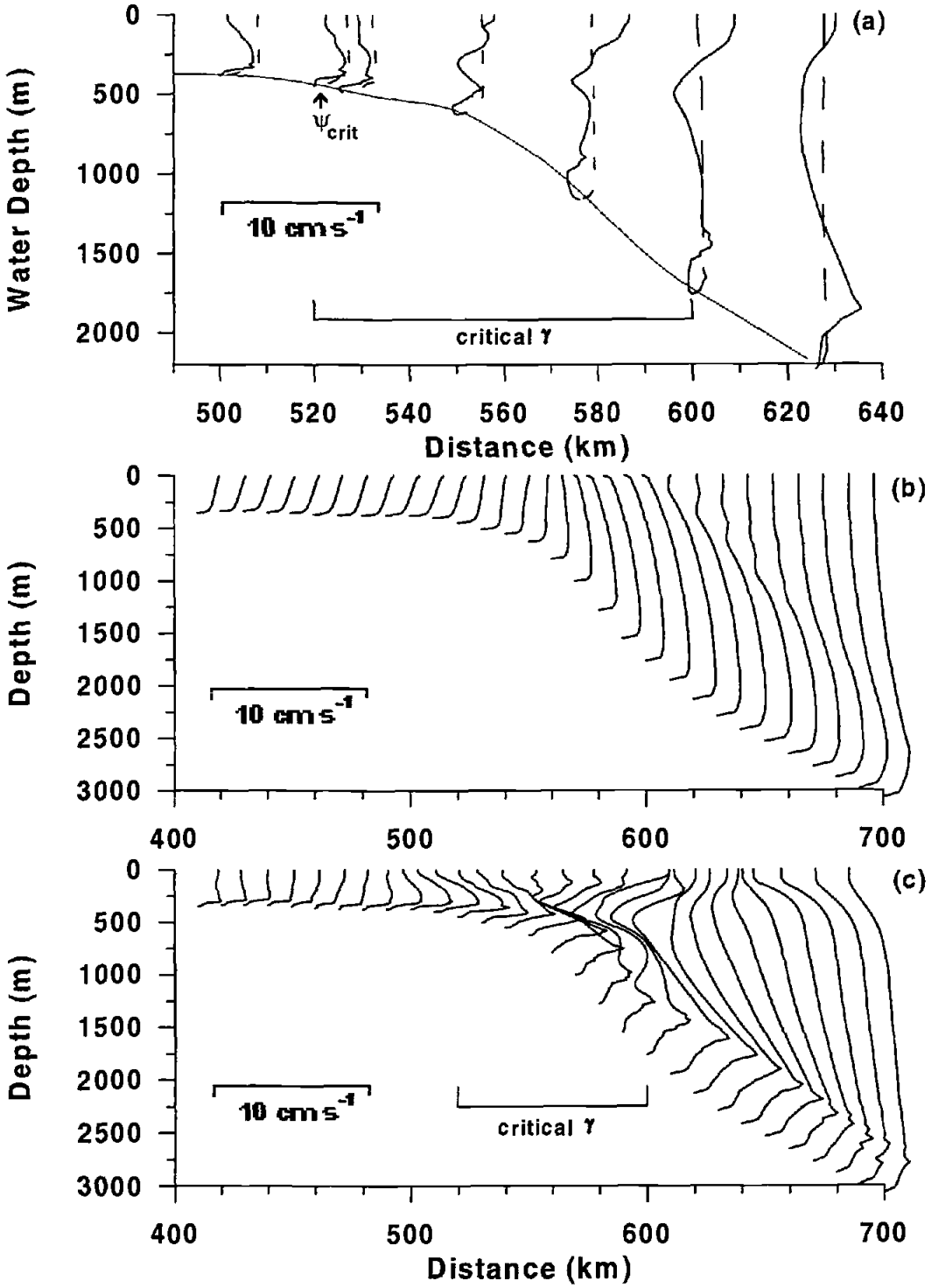

Figure 4.9. a) Cross-slope velocity profiles at t = 54.708 days over the upper continental slope with (solid line) and without (dashed line) the critical latitude and with stratification. Cross-slope velocity profiles over the continental slope from simulations b) without (at t = 29.833 days) and c) with (at t = 54.708 days) stratification with the critical latitude. The locations of ψ_{crit} and the critical γ range are indicated in a).

with M_2 forcing without the critical latitude passing through the domain (solid line in Figure 4.8a) increase slightly south of the critical latitude, whereas those with the critical latitude (dashed line in Figure 4.8a) are constant over nearly the entire transect. The difference between the elevation amplitudes for the two simulations increases with distance from the critical latitude to a maximum of about 3 cm at the front of the ice shelf. The major axes of the depth-independent velocities are significantly smaller over the continental shelf than those of the simulation without the critical latitude. There is apparently more kinetic and potential energy in the barotropic mode of the model simulation when the critical latitude is not present, particularly over the continental shelf poleward of the critical latitude. And, as will be shown later, there is more energy in the baroclinic mode of the model simulation when the critical latitude is present.

4.5.3.1. *Comparison with Observations*

Tidal observations in this region consist of four observations of tidal elevations (stars in Figure 4.2b) and nineteen current meter records measured at nine different moorings (triangles in Figure 4.2b). Due to the paucity of observations for this region, all nearby tidal observations have been included. The locations of the elevation observations are listed in Table 4.2 and those of the velocity observations with their depths in Table 4.3. A fuller discussion of the observations and their errors can be found in *RPE*.

The model results from the simulation with the critical latitude in the domain and with idealized stratification were compared with existing observational data in the region and with the results of a barotropic model. The elevation amplitudes and phases from this simulation are shown as solid lines and the predicted tidal elevation amplitudes and phases along the transect from the *RPE* barotropic model as dashed lines in Figures 4.10a and 4.10b, respectively.

The *RPE* elevation phases agree with the observations (Figure 4.10b), however, three of the elevation amplitude predictions slightly disagree with the observations (Figure 4.10a). This disagreement can be attributed to the distance from the transect. Only one of the observations actually lies on the transect, *Foldvik et al.*'s [1985] observation at 74° 26' S, 39° 24' W (y=526 km). For this observation, the *RPE* predictions disagree by 4 cm.

Location	Latitude		77° 42.6' S	77° 7' S	74° 26' S	74° 23' S
	Longitude		41° 8.0' W	49° 3' W	39° 24' W	37° 39' W
Reference			*Thiel* [1960]	*Foldvik* [1982]	*Foldvik* [1985]	*Middleton* [1982]
No. of Days			30	4.2	30	180
Water Depth	Observation		792	260	450	470
(m)	Model	Transect A	492	458	483	518
On or Off Transect			A: Off	A: Off	A: On	A: Off
M_2	Observation	Amplitude	0.44±.02	0.49±.03	0.54±.01	0.58±.04
		Phase	286	280	238	242
	POM - A	Amplitude	0.44 (0.00)	0.44 (-0.05)	0.44 (-0.10)	0.44 (-0.14)
		Phase	289 (+3)	289 (+9)	289 (+51)	289 (+47)
	RPE	Amplitude	0.64 (+0.20)	0.44 (-0.05)	0.58 (+0.04)	0.60 (-)
		Phase	274 (-12)	294 (+14)	244 (+6)	244 (+2)

Differences shown in parentheses
- for difference indicates the value fell within the uncertainty range

Table 4.2. Comparison between the POM and *RPE* tidal predictions and the observations for the elevation amplitude (m) and phase (°) at the observation locations. The differences are shown in parentheses. A dash indicates a difference less than the observational uncertainty. The location, water depth, and length of the record are given for each of the observations along with the principal author and year of the reference.

Location	Reference	No. of Days	On or Off Transect	Water Depth (m)			M_2 Major Axis for Tidal Velocity Ellipse			
				Observation	Model	Instrument	Observation	POM- Depth Independent	POM -Depth Dependent	*RPE*
75° 1' S 31° 46' W	*Woodgate* [1998]	828	Off	610	362 (601)♦	257	5.7	3.6 (-2)	2.4 (-3)	8.1 (-)
		828				378	6.3		8.8 (+3)	
		837				484	6.4		10.3 (+4)	
		691				590	5.3		2.1 (-3)	
75° 2' S 33° 33' W	*Woodgate* [1998]	829	Off	574	365 (582)♦	191	7.1	3.5 (-3)	5.5 (-)	8.9 (+2)
		829				342	6.3		6.0 (-)	
		837				448	5.5		13.0 (+8)	
		693				554	3.3		6.1 (+3)	
74° 40' S 33° 56' W	*Middleton* + [1982]	410	Off	475	379	375	6.8	4.7 (-2)	6.9 (-)	9.5 (+3)
		410				450	4.5		5.4 (-)	
74° 26' S 39° 24' W	*Middleton* + [1982]	630	On	475	483	375	6.8	4.1 (-3)	9.1 (+2)	8.5 (-)
		630				450	3.4		5.1 (-)	
74° 24' S 39° 6' W	*Middleton* + [1982]	510	On	465	507	400	5.0	3.9 (-)	9.8 (+5)	8.4 (+3)
		510				450	2.6		2.7 (-)	
74° 23' S 37° 39' W	*Foldvik* [1990]	31	Off	475	518	450	2.2	3.9 (-)	3.1 (-)	9.9 (+8)
74° 8' S 39° 19' W	*Foldvik* [1990]	460	On	650	828	627	3.0	2.7 (-)	6.0 (+3)	6.3 (+3)
74° 6' S 39° 22' W	*Middleton* + [1982]	600	On	720	868	620	2.9	2.6 (-)	9.2 (+6)	5.7 (+3)
73° 43' S 38° 36' W	*Middleton* + [1982]	620	On	1915	1906	1815	1.3	1.3 (-)	6.8 (+6)	2.3 (-)
		620				1890	0.9		5.7 (+5)	

+ *Foldvik et. al* [1990] is a more useful reference for these observations

♦ depth for the altered position

Table 4.3. Comparison between POM and *RPE* predictions and the observations for the velocity major axis (cm s^{-1}) at the observation locations. The location, water depth, and length of the record are given for each of the observations along with the principal author and year of the reference. The differences are shown in parentheses. A dash indicates a difference less than the observational uncertainty.

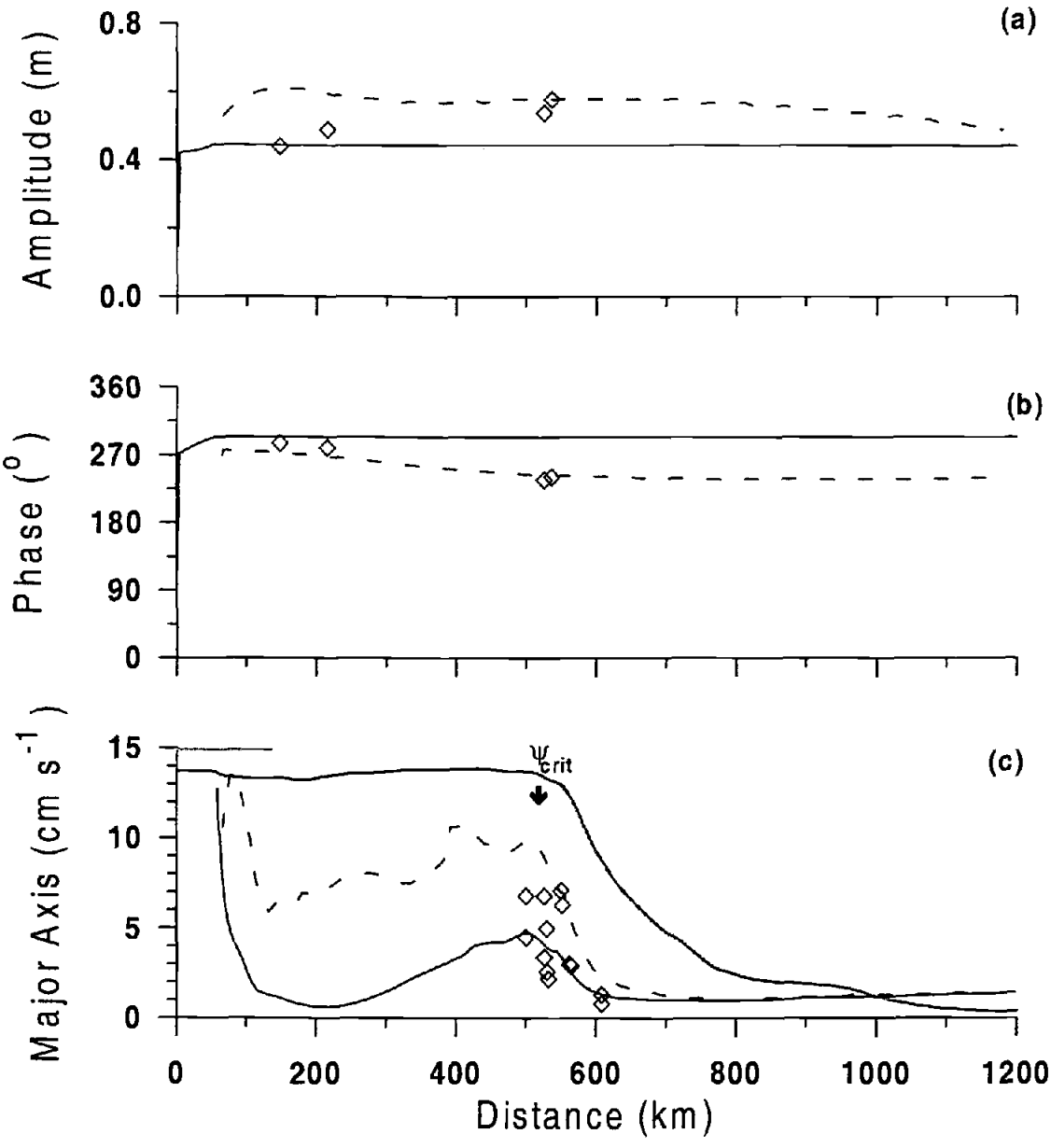

Figure 4.10. The elevation a) amplitude and b) phase and c) the major axis of the depth-independent velocities as determined by POM (solid line) and *RPE* (dashed line). Observations are shown by diamonds located at the distance on the transect corresponding to their latitude. The water depth profile is indicated in c) as a dark gray line and the area covered by the ice shelf is indicated by a light gray bar at the top of c). The location of the critical latitude is indicated by ψ_{crit} in c).

When a comparison is made for *RPE* values at the model locations (Table 4.2), the agreement for *RPE* improves except for *Thiel*'s [1960] observation, which was disregarded in the *RPE* study, because it utilized a tiltmeter and the accuracy of tiltmeters has been questioned. Distance from the transect also accounts for the phase differences between the observations (diamonds in Figure 4.10b) and *RPE* (dashed line in Figure 4.10b).

The predicted major axes from *RPE* (dashed line in Figure 4.10c) differ from the observations, with *RPE* overestimating all observations. However, since we are comparing the depth-independent major axes and the velocity observations were often taken in pairs with one instrument near the bottom in the bottom frictional boundary layer (roughly the lowest 60-100 m), the uppermost of the paired values in Figure 4.10c is more appropriate for the comparison. The major axes predicted by *RPE* agree within instrument and analysis uncertainties (2 cm s^{-1}) for three out of seven of the observations 50 m or greater above the seabed and are slightly larger than the uncertainty for the other four (Table 4.3). Note, however, that the *Foldvik et al.* [1990] theoretical model and recent observations by *Woodgate et al.* [1998] suggest that the M_2 boundary layer can be much thicker than 100 m near ψ_{crit}. Thus, even the uppermost current meter of the pairs may still be in the benthic boundary layer and not represent the depth-averaged current.

The elevations predicted by POM (solid line in Figure 4.10a) disagree slightly with the observations (diamonds in Figure 4.10a). The barotropic Kelvin wave traveling along the curving Antarctic coastline influences the elevation differently due to the different distances offshore and its changing propagation direction. *RPE* includes this effect; however, because this application of POM is essentially two-dimensional, this version of POM in this application cannot. Consequently, the disagreement between POM and the observations can be attributed to the neglect of variation in the along-slope direction in this application. This is discussed more fully in section 4.5.3.2.

POM predicted major axes for the depth-independent velocities (solid line in Figure 4.10c) agree within the uncertainty for three of the seven observations 50 m or more above the seabed (diamonds in Figure 4.10c and Table 4.3). Three of the four observations which don't agree are off the transect and the fourth is near the critical

latitude and is probably influenced by boundary layer effects since the boundary layer is thicker there. When the major axes for the depth-dependent velocities are compared using the model velocities at the corresponding distance off the bottom as the instruments for the observations, the differences exceed the uncertainties for twelve of nineteen observations (Table 4.3). It should be noted that the *Woodgate* observations were not compared at the distance along the transect corresponding to their latitude, but instead to a location along the transect with a similar depth. The depths for these observations at the corresponding latitude are shown in Table 4.3, with the depth for the altered location used for the comparison in parentheses. Most of the instruments were located in the lower water column. The model often places these locations in the benthic boundary layer (solid line in Figure 4.9a). Due to the strong velocity gradient here, a slight change in depth may result in a large velocity difference. Thus, due to differences in the bottom depths for the model and the observations and the sensitivity to the depth location resulting from the large gradients, comparisons should be restricted to those between the non-boundary layer observations and the depth-independent major axes of the model.

From their observations, *Middleton et al.* [1977] estimated the M_2 tide to be 50% "baroclinic" over the upper continental slope in this region. These observations consisted of a pair of instruments at each of two locations (74° 26' S and 74° 24' S). Both locations had one instrument that was clearly in the benthic boundary layer, either 15 or 25 m from the bottom, and another instrument either 60 or 100 m from the bottom. POM predicts a reduction of velocity of about 44% at the 74° 26' location and 73% at the other (74° 24'), which is closer to the bottom and further into the benthic boundary layer (Table 4.3).

4.5.3.2. *Limitations of the Two-Dimensional Approach*

In the Weddell Sea, the tides are generally thought of as Kelvin waves propagating along the Antarctic coast [e. g., *MacAyeal*, 1984]). This generally results in a wave propagating along-slope. Due to the geometry of the southern Weddell Sea, however, the Kelvin wave propagating along the Antarctic coast splits with a portion of its energy propagating westward along the continental slope and another portion propagating southward across the continental slope following the coast [*RPE*]. A similar situation

occurs in the Ross Sea [*MacAyeal*, 1984]. The model domain lies in the region where the coast-following Kelvin wave propagates across the continental slope. Since a wall does not exist along the eastern boundary of the model domain, the elevation gradient and the accompanying pressure gradient necessary for a Kelvin wave cannot be set up. Thus, the two-dimensional transect approach is unable to simulate a Kelvin wave propagating along the coast for this region. Likewise, the lack of a southern barrier precludes the existence of an along-slope propagating Kelvin wave. The tidal forcing at the boundary results in the tide propagating along-slope through the domain as a Poincaré wave with the M_2 frequency instead of as a cross-slope propagating Kelvin wave. The existence of this Poincaré wave propagating through the domain is supported both by the relative size of the Coriolis force in the terms of the momentum equation and by the ratio of the tidal ellipse axes agreeing with the ratio predicted by linear theory (not shown). Theoretically, Poincaré waves cannot propagate past the critical latitude. Therefore, when the critical latitude is in the domain, any north-south portion of the forcing wave is blocked and it is turned around. As a result, the elevation phase will not increase as it would for a propagating wave. Shallow water, flat bottom simulations without the critical latitude in the domain and with a large phase difference corresponding to the smaller phase speed for shallow water showed the elevation phase to vary as it would for a propagating wave. An equivalent simulation with the critical latitude in the domain showed the elevation phase to be relatively constant but with a maximum at the critical latitude, reflecting the blockage of a portion of the Poincaré wave. (The nearly constant phase from the simulation without the critical latitude is associated with a small phase difference along the transect and is not a result of this effect. The small phase difference is a result of the larger deep water group speed.) It should be noted that due to the long wavelength, not all of the wave energy will be blocked. The difference between the elevation amplitudes for the simulations with and without the critical latitude in the domain (solid and dashed lines in Figure 4.8a, respectively) could be a result of the blockage of a portion of the north-south propagating Poincaré forcing wave. When the critical latitude is absent, the elevation amplitude would increase over the continental shelf reflecting the propagation of the wave into shallower water (solid line in Figure 4.8a). However, when the critical

latitude is present, the north-south component of the Poincaré forcing wave would be blocked and the amplitude would remain constant (dashed line in Figure 4.8a). Additionally, since there are no gradients in the alongslope direction in this application of the model, topographic Poincaré waves, also known as continental shelf waves, cannot exist.

4.5.3.3. *Shortcomings of POM with the Critical Latitude*

Our two-dimensional simulations with a homogeneous ocean and a sloping bottom with ψ_{crit} in the domain show significant vertical variation in the depth-dependent horizontal velocities over the outer shelf and upper slope, with the strongest variation roughly between 600-700 km (Figures 4.11a and 4.11b). This vertical variation in the horizontal velocities only occurs when ψ_{crit} is near or on a slope. Although frictional effects can cause vertical variation, they do not predict a mid-water column minimum [*Lamb*, 1879, pp. 623]. Observations with multiple velocity measurements on a single mooring do not give evidence of such a vertical structure in the velocities [*Foldvik et al.*, 1990; *Woodgate et al.*, 1998]. Additionally, most of the mismatch between the observed and the POM velocities coincides with the location of this vertical variation in the horizontal velocities for the homogeneous ocean simulation with POM overestimating the velocities, particularly in the lower water column.

Since this vertical variation in the homogeneous solution is unlikely to be real, what causes it? It was first postulated to be a frictional effect. Although the boundary layer does cause some vertical variation near the bottom and vertical viscosity affects the vertical structure, most of the vertical variation was found to occur without friction being present. The variation showed most of the characteristics of an internal tide or baroclinic Poincaré wave generated over the upper slope. The wavelength and group speed from the model simulation agreed with the theoretical values for a baroclinic Poincaré wave at the M_2 frequency and the model value of N, supporting this hypothesis. However, internal tides or waves do not exist in a homogeneous ocean. Further investigation revealed that the density normalization in POM resulted in an effective N of about 0.6 cph for a uniform potential temperature and salinity. This effective stratification could be sufficient

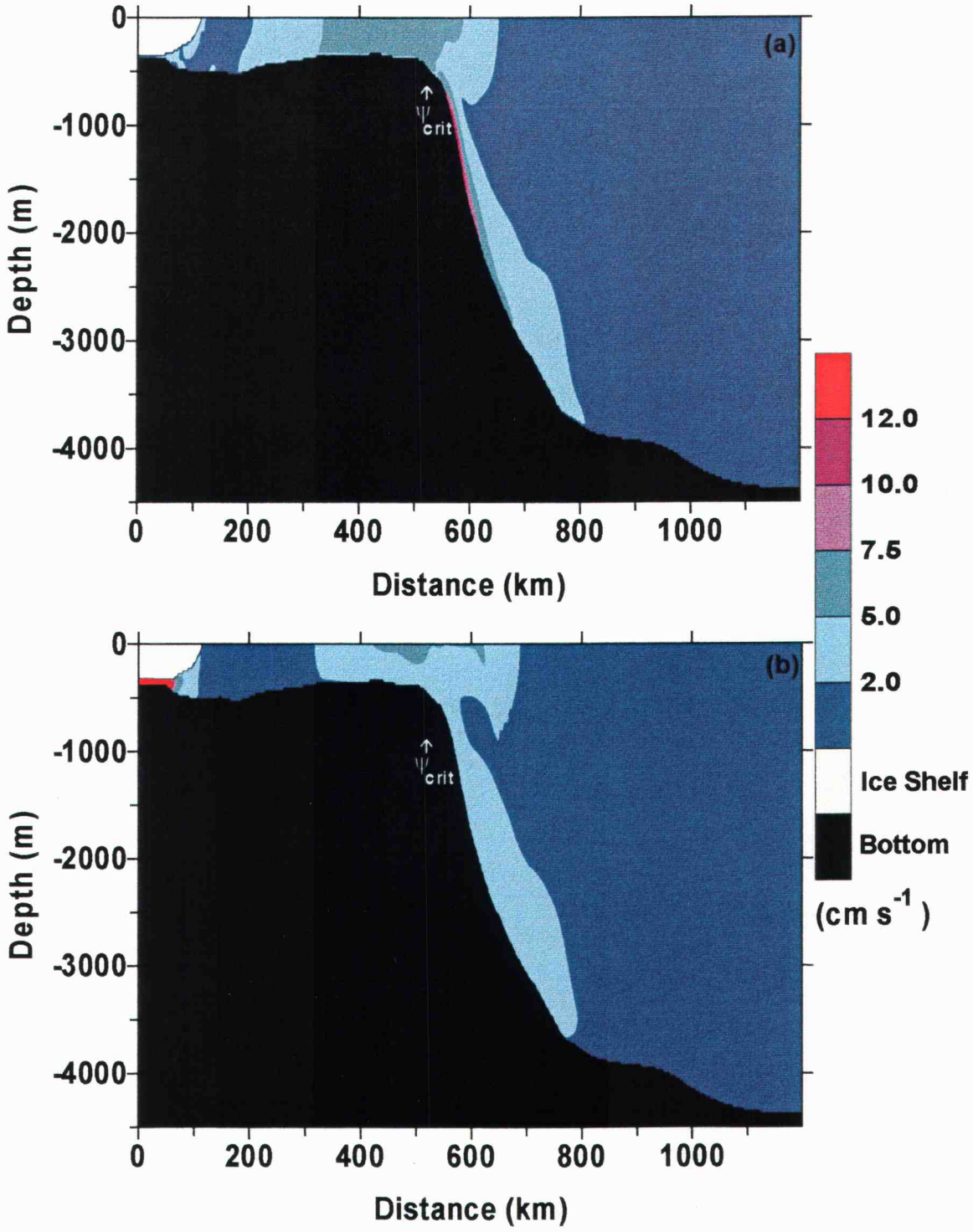

Figure 4.11. The major axes of the tidal ellipses of the depth-dependent velocities from simulations with a homogeneous ocean with ψ_{crit} in the domain using a) equation set (4.1) and b) equation set (4.2). The location of the critical latitude is indicated in a) and b) by ψ_{crit}.

for internal wave generation near ψ_{crit} due to the sensitivity of the baroclinic pressure gradient term calculation in POM. Modifications (discussed in section 4.3.1) were made to POM in order to remove this effective stratification. The effective N was reduced to ~0.01 cph. The remaining N is a result of the mismatch of the pressure corrections for the density (equation (4.2) and N (equation (4.3)) calculations. It results from the second order pressure correction term in the density and the dependence of c on η. Consequently, N fluctuates in time as c^2 resulting in a frequency twice the M_2 frequency. Likewise, the vertical variation of the horizontal velocities was reduced with the lower N, but still persisted (Figures 4.9b and 4.11b).

To verify that the modified version of POM was still capable of generating realistic internal waves, a simulation was performed with a strong stratification (N = 2.6 cph throughout the water column) and with the domain away from the critical latitude. The internal tide wave rays for this scenario can be clearly seen propagating over the continental shelf in the cross-slope horizontal baroclinic velocities at t = 54.9 days, a time near the maximum depth-independent on-shore flow (Figure 4.12a). The baroclinic velocity is defined as the depth-dependent velocity with the depth-independent velocity removed (= V - V_A). These internal tides are basically mode one with opposite velocities at the surface and the bottom, except over the upper continental slope where they are mode two. The maximum velocities occur over the upper continental slope where a supercritical γ is predicted (Figure 4.5d). There the internal tides only propagate offshore as predicted by a super-critical γ.

Investigation of the amplitudes and phases (phase for anticlockwise component) of the depth-dependent velocities from a sigma layer just below the numerical surface boundary layer (σ = 5) for two homogeneous ocean simulations with (Figure 4.13b) and without (Figure 4.13a) ψ_{crit} in the domain shows a distinct influence of ψ_{crit} in both the velocity amplitude and phase. When ψ_{crit} is not in the domain, the amplitude (solid line in Figure 4.13a) increases with decreasing water depth (gray dashed line in Figure 4.13a) and is essentially identical to the barotropic amplitude (dashed line in Figure 4.8b). The phase is nearly constant (crosses in Figure 4.13b) except near the ice shelf. When ψ_{crit} is

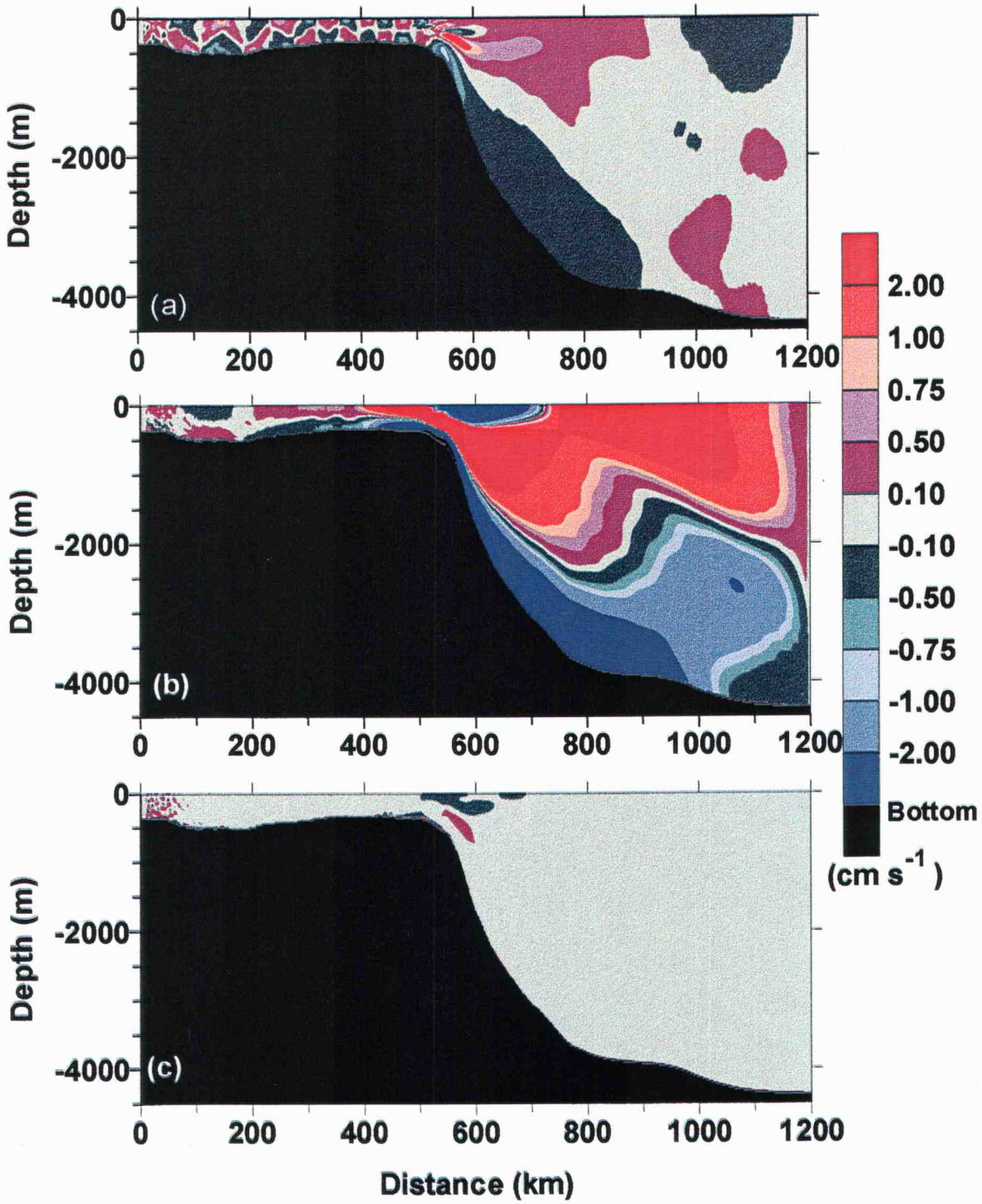

Figure 4.12. a) The cross-shore horizontal baroclinic velocities at t= 54.9 days, a time near the peak on-shore flow, from a simulation with strong stratification (N = 2.6 cph) without ψ_{crit} in the domain. The cross-shore horizontal baroclinic velocities at t = 54.9 days, a time near the peak on-shore flow, from simulations with strong stratification (N = 2.6 cph) and with ψ_{crit} in the domain both b) with and c) without using η in the pressure calculation used for the density determination.

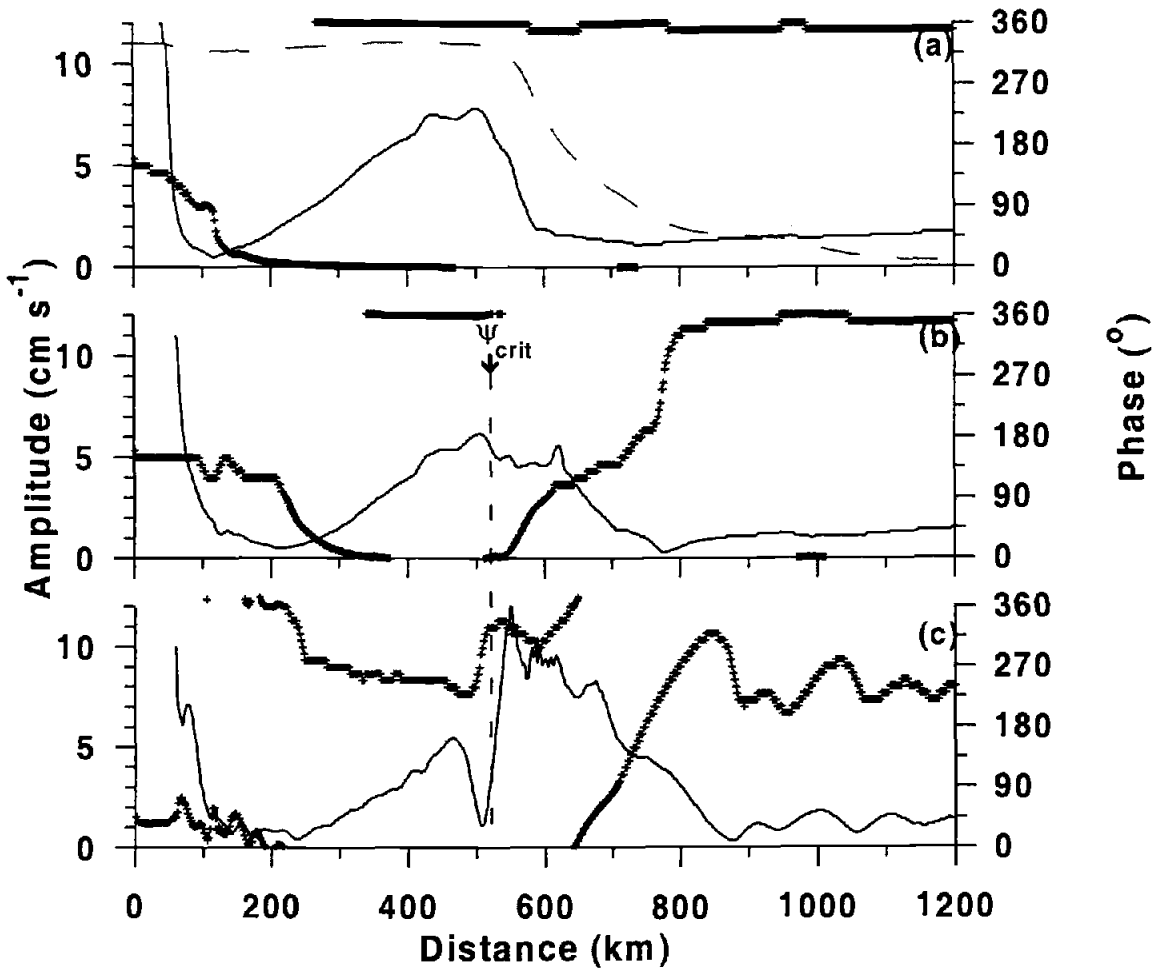

Figure 4.13. The amplitudes of the depth-dependent velocities (black line) and phases for the anticlockwise component (gray crosses) from the fifth sigma level from the surface for simulations: with a) an unstratified ocean without the critical latitude in the domain, b) an unstratified ocean with the critical latitude in the domain, and c) a idealized stratified winter ocean with the critical latitude in the domain. The topography is indicated in a) by thick gray lines. The location of the critical latitude is indicated in b) by ψ_{crit}.

in the domain, the amplitude over the continental slope equatorward of ψ_{crit} shows a definite increase and the phase varies like that of a propagating wave. The phase slope indicates a wavelength of ~300-500 km for a wave propagating poleward from ψ_{crit}. However, this wavelength does not coincide with that of either a barotropic or baroclinic

Poincaré wave for the reduced N ($N \sim 0.01$ cph) ($L_{\text{baroclinic}} \approx 0.4$ km; $L_{\text{barotropic}} \approx 73{,}000$ km).

However, this type of phase signal could also result from the excitation of inertial oscillations and the beating of the inertial oscillations with the M_2 tidal signal. The two-day time series of model results used for the analysis is too short to distinguish inertial oscillations from the M_2 tide. The inertial frequency is slightly different at each latitude, consequently the inertial oscillations will resonate differently with the M_2 tidal frequency. As a result, the phase difference will vary with distance from ψ_{crit}. Likewise the amplitude of the inertial oscillations will decrease with distance from ψ_{crit} as the resonance decreases with increasing frequency differences. Additionally, although inertial oscillations are not themselves vertically dependent, they can support a vertical dependence, since "the particles move on horizontal sheets, each layer decoupled from the one above and below it" Kundu [pp. 509, 1990]. Vertical viscosity will, however, act to couple the layers over some vertical distance.

But how would vertical variation be imparted to the inertial oscillations? To illuminate this, we need to examine the "baroclinic mode" equations used by the model. These equations are the continuity equation (4.10), the equations of motion for the along-slope (4.11) and cross-slope (4.12) directions and equations for the conservation of heat (4.13) and salt (4.14).

$$\frac{\partial DU}{\partial x} + \frac{\partial DV}{\partial y} + \frac{\partial W'}{\partial \sigma} + \frac{\partial \eta}{\partial t} = 0 \tag{4.10}$$

$$\frac{\partial UD}{\partial t} + \frac{\partial UUD}{\partial x} + \frac{\partial UVD}{\partial y} + \frac{\partial UW'}{\partial \sigma} - fVD + gD\frac{\partial \eta}{\partial x} + g\,D^2 \int_{\sigma}^{0} \left[\frac{\partial \rho'}{\partial x} - \frac{\sigma'}{D}\frac{\partial \rho'}{\partial \sigma'}\frac{\partial D}{\partial x} \right] d\sigma' = \frac{\partial}{\partial \sigma}\left[\frac{K_M}{D}\frac{\partial U}{\partial \sigma} \right] + \frac{\partial}{\partial x}\left[2D\,A_M \frac{\partial U}{\partial x} \right] + \frac{\partial}{\partial y}\left[D\,A_M \left(\frac{\partial U}{\partial y} + \frac{\partial V}{\partial x} \right) \right] \tag{4.11}$$

$$\frac{\partial VD}{\partial t}+\frac{\partial UVD}{\partial x}+\frac{\partial VVD}{\partial y}+\frac{\partial VW'}{\partial \sigma}+fUD+gD\frac{\partial \eta}{\partial y}+$$
$$gD^2\int_{\sigma}^{0}\left[\frac{\partial \rho'}{\partial y}-\frac{\sigma'}{D}\frac{\partial D}{\partial y}\frac{\partial \rho'}{\partial \sigma'}\right]d\sigma' = \tag{4.12}$$
$$\frac{\partial}{\partial \sigma}\left[\frac{K_M}{D}\frac{\partial V}{\partial \sigma}\right]+\frac{\partial}{\partial x}\left[DA_M\left(\frac{\partial U}{\partial y}+\frac{\partial V}{\partial x}\right)\right]+\frac{\partial}{\partial y}\left[2DA_M\frac{\partial V}{\partial y}\right]$$

$$\frac{\partial TD}{\partial t}+\frac{\partial TUD}{\partial x}+\frac{\partial TVD}{\partial y}+\frac{\partial TW'}{\partial \sigma}=\frac{\partial}{\partial \sigma}\left[\frac{K_H}{D}\frac{\partial T}{\partial \sigma}\right]+\frac{\partial}{\partial x}\left[DA_M\frac{\partial T}{\partial x}\right]+\frac{\partial}{\partial y}\left[DA_M\frac{\partial T}{\partial y}\right] \tag{4.13}$$

$$\frac{\partial SD}{\partial t}+\frac{\partial SUD}{\partial x}+\frac{\partial SVD}{\partial y}+\frac{\partial SW'}{\partial \sigma}=\frac{\partial}{\partial \sigma}\left[\frac{K_H}{D}\frac{\partial S}{\partial \sigma}\right]+\frac{\partial}{\partial x}\left[DA_M\frac{\partial S}{\partial x}\right]+\frac{\partial}{\partial y}\left[DA_M\frac{\partial S}{\partial y}\right] \tag{4.14}$$

where W' is the cross-sigma component of the vertical velocity, A_M is the horizontal viscosity coefficient ($m^2\ s^{-1}$), K_M is the vertical viscosity coefficient ($m^2\ s^{-1}$), and K_H is the heat diffusivity coefficient ($m^2\ s^{-1}$). The equation of motion for the cross-slope depth-dependent velocity (4.12) includes terms for acceleration, advection in the along-slope, cross-slope, and vertical directions, Coriolis force, surface elevation pressure gradient, baroclinic pressure gradient, vertical diffusion, and horizontal diffusion, respectively.

To illustrate what is happening, time series of the values for these terms are shown in Figures 4.14a-c for three σ levels (upper, mid-, and lower water column, σ = 10, 30, and 50, respectively) at a location over the upper continental slope (y = 600 km) from a simulation with a homogeneous ocean. It should be noted that the horizontal diffusion has been combined with the horizontal advection and that the vertical diffusion term is not shown. Also in order for the other terms to be visible, the Coriolis term has been shown at a different scale (right-hand side axes). The term with the most influence is obviously the Coriolis term (cyan lines in Figures 4.14a-c). A balance between the Coriolis term and acceleration is typical for inertial oscillations or gyroscopic waves. However, since this location is equatorward of the critical latitude, these cannot be gyroscopic waves. The next largest term in the upper and mid- water column is the surface elevation pressure gradient term (green lines in Figures 4.14a-c). However, the surface pressure gradient term is constant with depth and cannot be the source of the vertical variation. On the other hand, the baroclinic pressure gradient term (red lines in

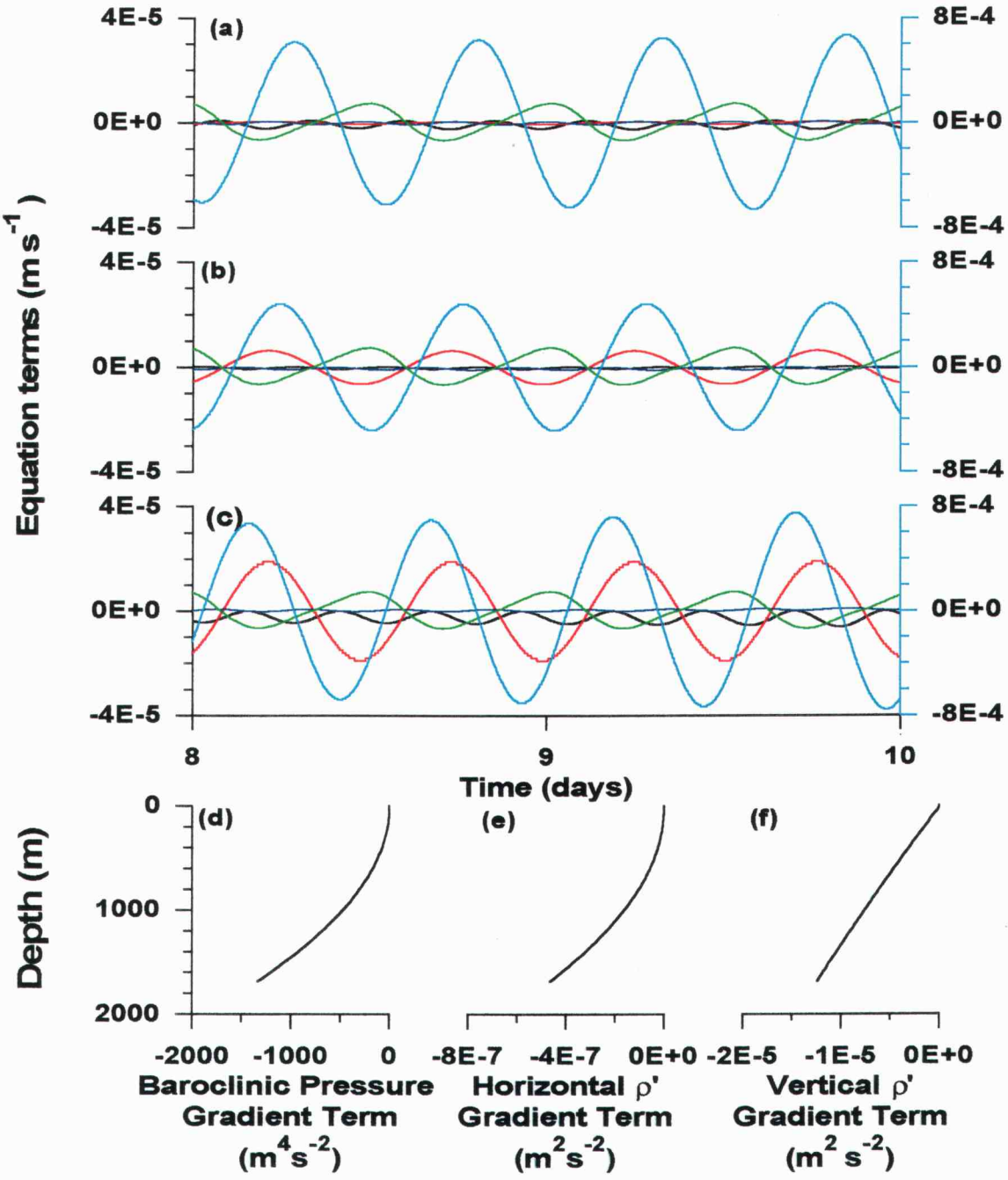

Figure 4.14. Time series of the terms used to determine the acceleration of the cross-slope depth-dependent velocity at 600 km distance along the transect in the a) upper, b) mid-, and c) lower water column for a simulation of a homogeneous ocean with ψ_{crit} in the domain. The terms shown are Coriolis (light blue), baroclinic pressure gradient (red), surface pressure gradient (green), vertical advection (blue), and the combined horizontal advection and diffusion (black). Vertical diffusion is not shown. The Coriolis term is scaled using the axes on the right-hand side in a)-c). Profiles of d) the baroclinic pressure gradient term and e) the horizontal and f) vertical gradients of the perturbation density used for that term at a distance of 600 km and at t = 10 days.

Figures 4.14a-c) is vertically dependent, increases with depth, and is the second largest term in the lower water column (Figure 4.14c). Therefore, the baroclinic pressure gradient term is the most probable candidate for the vertical variation seen in the horizontal velocity field.

Further investigation linked the vertical variation of the horizontal velocities to the vertical variation of the baroclinic pressure gradient term in POM. In sigma coordinates, the baroclinic pressure gradient term consists of "horizontal" (along-sigma) and vertical (across-sigma) gradients:

$$g D^2 \int_{\sigma}^{0} \left[\frac{\partial \rho'}{\partial y} - \frac{\sigma'}{D} \frac{\partial D}{\partial y} \frac{\partial \rho'}{\partial \sigma'} \right] d\sigma'. \tag{4.15}$$

ρ' is the perturbation density (no units) determined from the normalized density, ρ, and a background density, ρ_{MEAN}, according to

$$\rho' = \rho - \rho_{MEAN} \tag{4.16}$$

ρ_{MEAN} is the normalized density for the initial θ, S and pressure field, with η equal to zero. σ represents the vertical distance in the water column from the surface ($-1 \leq \sigma \leq 0$), y the horizontal cross-slope distance (km), and D the depth (m), $D = H + \eta$. The baroclinic pressure gradient term and errors associated with it have been the subject of investigation by *Mellor et al.* [1994; 1998], although no critical latitude effects have yet been reported. The use of a perturbation density, ρ', drastically reduces the numerical error in the baroclinic pressure gradient term [*Mellor et al.*, 1994; 1998], although a higher order error of unknown origin remains in this term [*Mellor et al.*, 1998]. Theoretically for a homogeneous ocean the baroclinic pressure gradient term should be zero, with the horizontal and vertical gradients canceling each other. Vertical profiles of the baroclinic pressure gradient term for a homogeneous ocean at a location on the upper slope at $t = 10$ days show that the values used by the model are not zero and systematically increase with depth in a non-linear manner (Figure 4.14d). These erroneous values for the baroclinic pressure gradient term have been traced to the vertical gradient term (Figure 4.14f) and its integration with depth (Figure 4.14d). Although the two gradients should cancel each other for the homogenous ocean, the vertical gradient

(Figure 4.14f) was two orders of magnitude greater than the horizontal gradient term (Figure 4.14e). Since the baroclinic pressure gradient term arises from the tidal fluctuations of η, it fluctuates at the tidal frequency. Near ψ_{crit}, the fluctuating baroclinic pressure gradient term is nearly resonant with the inertial frequency and can, therefore, induce inertial oscillations and resonate with them, increasing their amplitude. This occurs even though the magnitude of the baroclinic pressure gradient term is much less than that of the Coriolis term (Figures 4.14a-c). Independent investigation found that a baroclinic pressure gradient term with a magnitude on the order of 1% of the initial Coriolis term was sufficient to induce significant inertial oscillations during a period of time equivalent to the duration of a model run. For the lower water column over the upper continental slope the baroclinic pressure gradient term was 3% or more of the Coriolis term and was seen to accelerate the velocities at the near-inertial frequency (not shown). Two factors act to stabilize the growth of the inertial oscillations. When the velocities become large enough, friction and diffusion stabilize the inertial oscillations and prevent them from growing further. Secondly, the synchronization of the forcing from the M_2 pressure gradient with the inertial oscillations deteriorates with time. When the forcing term is out of phase with the inertial oscillation, the baroclinic pressure gradient term will decelerate the inertial oscillation.

Away from ψ_{crit}, the tidal and inertial frequencies are sufficiently separated that resonance is too weak to be significant. For example, this effect was negligible for a simulation of a homogeneous ocean with the domain shifted 10° N of ψ_{crit} (not shown). Since most previous internal tide investigations, such as those of *Holloway* [1996] on the Australian slope or *Chen and Beardsley* [1998] over Georges Bank, have not been located near ψ_{crit} for the tidal constituent being studied, these studies have not encountered this vertically dependent inertial oscillation response.

The vertical variation results both from the depth-dependence of this erroneous baroclinic pressure gradient term and vertical diffusion through friction. Since most of the forcing occurs at the greater depths, the inertial oscillation signal is stronger there. However, in the upper water column the M_2 tidal signal still dominates. Due to the slightly different frequencies, these two signals come in and out of phase, resulting in a

phase difference, which varies with distance from ψ_{crit}. The tidal and inertial frequencies are too close to distinguish without a much longer time series. Additionally, the larger velocities of the lower water column diffuse upwards since K_M is non-zero. The Mellor-Yamada 2.5 level closure scheme calculates large values for K_M for a homogeneous water column ($K_M \approx 0.1$ m^2 s^{-1}). The large K_M values result in increased diffusion of the higher velocities. The upward diffusion of the inertial oscillation velocities also affects the phase lag between the surface and the bottom. Both of these effects combine to produce an apparent internal wave-like velocity structure. Continuity and advection may play secondary roles. The apparent cross-slope wavelength is related to the slope width and the effectiveness of the erroneous baroclinic pressure gradient terms in forcing a near-resonant response (a function of distance from ψ_{crit}).

How should this vertical variation be removed? Obviously, the calculation of the baroclinic pressure gradient, particularly the vertical gradient component, needs improvement. In sigma coordinates, the baroclinic pressure gradient term comes not only from the horizontal gradient in the perturbation density, ρ' (equation 4.15), but there is also a vertical component due to the coordinate transformation. The vertical gradient includes both the changes in pressure due to density changes when θ and/or S vary and changes in pressure due to variation in the locations of the σ levels relative to the surface as η varies. These two changes are apparent when the pressure is substituted in ρ' and it is rewritten as

$$\rho' = \rho - \rho_{Mean}$$

$$\rho' = \frac{\rho(t \neq 0) - \rho(t = 0)}{\rho_o}$$

$$\rho' = \rho_{\theta,S}(t \neq 0) - g(H+\eta)\sigma/c^2 - \left(2x10^{-5}\rho_o g^2 (H+\eta)^2 \sigma^2 / c^4 \right)\Big|_{t\neq 0} \quad (4.17)$$

$$- \rho_{\theta,S}(t = 0) + gH\sigma/c^2 + \left(2x10^{-5}\rho_o g^2 H^2 \sigma^2 / c^4 \right)\Big|_{t=0}$$

In a homogeneous ocean, ρ' reduces to

$$\rho' = -g\eta\sigma/c^2 - 2x10^{-5}\rho_o g^2 \eta^2 \sigma^2 / c^4 - 4x10^{-5}\rho_o g^2 H\eta\sigma^2 / c^4 \quad (4.18)$$

when the changes in the sound speed (less than 1% for these depths in a homogeneous ocean) are ignored. Since there are no density changes due to θ or S, only the η-dependent changes remain. Since the C-grid does not provide exact density differences at the velocity points but both the horizontal and vertical density gradients are averages of two differences, error is introduced in these terms due to its use. The error in the baroclinic pressure gradient term was found linked to the pressure correction of the density and the use of the perturbation density. To remove the error in the baroclinic pressure gradient term, specifically the vertical gradient, two suggestions would be 1) remove η from the pressure calculation used for ρ' or 2) use a derivative approach to determine the vertical difference for ρ'.

To investigate the first two of these possibilities, an independent test was set up for the homogeneous ocean at a location on the upper slope using $\eta = 0.5$ m. The values for the baroclinic pressure gradient term from this test were slightly reduced when the modifications of section 4.3.1 were made to the density calculation (short-dashed line compared to solid line in Figure 4.15). Using the first suggestion, when η is removed from the pressure calculation in equation set (4.2), i.e., $P = -\rho_o g H$, ρ' will become zero. This also resulted in a baroclinic pressure gradient term of zero (dotted line in Figure 4.15). The vertical variation in the horizontal depth-dependent velocities over the continental slope disappeared when this modification was applied to a simulation with POM. Removal of η from the pressure calculation in equation set (4.2) is not, however, an acceptable solution to this problem for a stratified ocean, since it also removes any real variations in pressure due to the shifting of the σ levels relative to the sea surface. To see the effect this has on the internal wave field when stratification is present, two simulations were run with strong stratification ($N \sim 2.6$ cph) near the critical latitude, one with η (Figure 4.12b) and one without η (Figure 4.12c) in the pressure correction calculation. The removal of η in the pressure calculation for the density calculation resulted in the loss of nearly the entire internal tidal signal (Figure 4.12c compared to Figure 4.12b).

The second suggestion is quite complicated for a stratified ocean, however, for a homogeneous ocean, the derivative of the perturbation density can be substituted for the

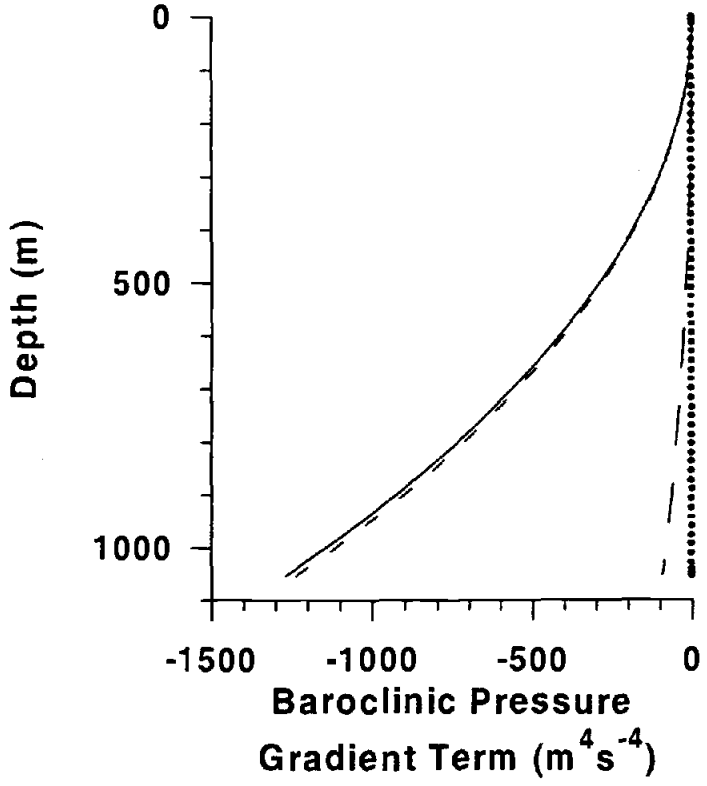

Figure 4.15. The baroclinic pressure gradient term as determined in a test program for a location on the upper continental slope and a surface elevation of 0.5 m using the original density calculation (solid line), the modified density calculation (short-dashed line), the modified density calculation with a surface elevation of zero (dotted line), and the modified density calculation using a gradient of the perturbation density instead of the density difference for the vertical gradient in the baroclinic pressure gradient term (long-dashed line).

difference. Differentiating equation (4.18) with respect to σ, the vertical gradient of ρ' becomes

$$\partial\rho'/\partial\sigma = -g\eta/c^2 - 4x10^{-5}\rho_o g^2\eta^2\sigma/c^4 - 8x10^{-5}\rho_o g^2 H\eta\sigma/c^4 . \qquad (4.19)$$

For typical values, the first of these terms is roughly three orders of magnitude larger than the second or third. Substituting this term in for the vertical gradient of ρ' in the baroclinic pressure gradient term in the independent test significantly reduces the error in the baroclinic pressure gradient term (long-dashed line in Figure 4.15). However, this

solution is not acceptable for a stratified ocean, since in this form it is limited to a homogeneous ocean.

The real solution to correctly determining the baroclinic pressure gradient term must handle a stratified ocean correctly without inducing errors for the homogeneous ocean. One suggestion would be to develop a method of interpolating the vertical difference, which will reduce the errors associated with the C-grid and better represent the non-linear differences resulting from the pressure correction to the density. The bottom line is that due to the handling of pressure in the density calculation and the sensitivity of the baroclinic pressure gradient term calculation in POM, vertically variable inertial oscillations are induced near ψ_{crit}. These inertial oscillations have been shown to be a model artifact resulting from errors in the baroclinic pressure gradient term and have many characteristics which can result in their being confused with an internal tidal signal.

4.5.3.4. *Internal Wave Field*

In the stratified ocean, internal waves are apparent in vertical profiles of the cross-slope depth-dependent velocities at a time near the peak offshore barotropic tidal flow (t = 54.708 days;) (Figure 4.9c and solid line in Figure 4.9a). These profiles reveal much more vertical shear existing over the upper continental slope with stratification (Figure 4.9c and solid line in Figure 4.9a) than without stratification (Figure 4.9b). Although some of this signal is attributable to a larger inertial oscillation response due to the smaller K_M, there is also evidence of an internal tidal response and of propagation of a internal tide in Figure 4.9c. The internal tides appear to respond both in a mode and in a ray manner and to have a wavelength of ~200 km (Figure 4.13c).

In order to further evaluate the internal tides, the major axes of the tidal ellipses were determined by using tidal analysis routines of *Foreman* [1978] on the depth-dependent velocities for each respective location. Larger major axes are seen near the surface and the bottom over the upper continental slope (Figure 4.16b compared to 4.16a). The maxima are roughly aligned along the angle of the internal wave ray paths (Figure 4.6a).

The internal wave propagation is apparent in the amplitudes and phases (phase for anticlockwise component) of the depth-dependent velocities from a sigma layer just

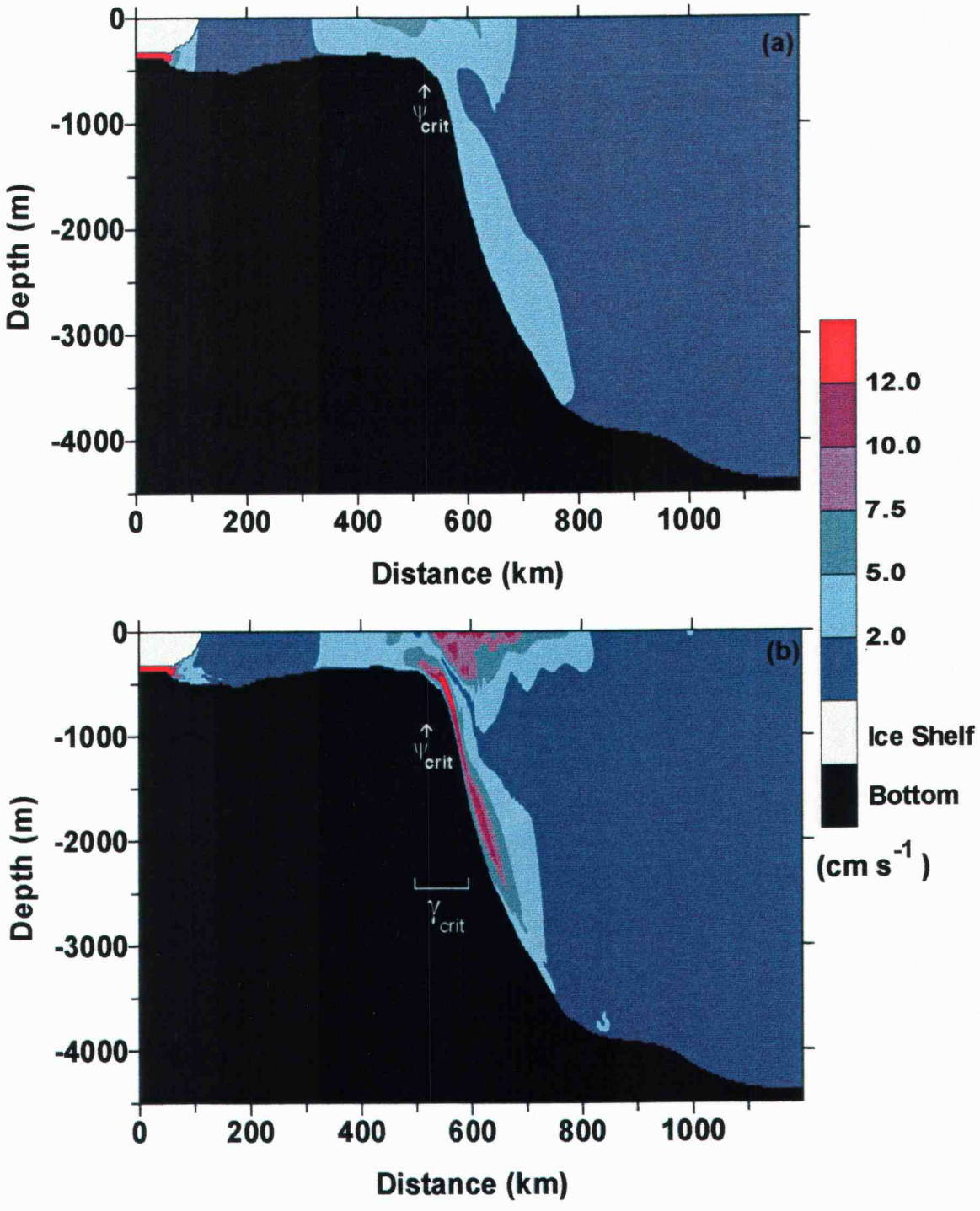

Figure 4.16. The major axes of the tidal ellipses of the depth-dependent velocities from simulations with ψ_{crit} in the domain and a) without and b) with stratification. The location of the critical latitude is indicated in a) and b) by ψ_{crit}.

below the numerical surface boundary layer (Figure 4.13c). It should be noted that this sigma level does not represent a single depth, but its depth changes as the water column thickness changes. When stratification is present, the amplitude peaks slightly equatorward of ψ_{crit} and is much higher than that of the homogeneous ocean over the entire slope (Figure 4.13c compared to Figure 4.13b) indicating generation of internal tides or inertial oscillations and/or the propagation of internal tides there. Due to the short time series, it is impossible to distinguish internal tides from inertial oscillations. Equatorward of ψ_{crit} between 600 and 800 km distance, the phase increases suggesting an internal tide propagating through this sigma level. Although the POM results indicate that internal tides are generated over the upper continental slope for a stratified ocean, the magnitudes of the internal tides over much of the continental slope are not much greater than the velocities associated with the erroneous inertial oscillations generated by POM for the homogeneous ocean (Figure 4.11b compared to Figure 4.11a). Consequently, much of the internal tidal signal predicted by POM is questionable and the results are not reliable enough for a quantitative analysis. Furthermore, I believe that in its present form POM is unsuitable for predicting internal tides or waves in polar regions near the critical latitude, particularly where weak stratification exists.

4.6 Summary

An attempt was made to utilize the Princeton Ocean Model (POM) to investigate the generation of internal tides at the M_2 frequency over the outer continental shelf and slope in the southern Weddell Sea. The model was run as a two-dimensional transect, assuming that bathymetry and tidal forcing were constant in the along-slope direction. Appropriate boundary conditions were chosen for the northern and southern boundaries to generate currents near the shelf break that were comparable to measurements and predictions from a barotropic regional model.

Linear theory predicts that 10° equatorward of the M_2 critical latitude ($\psi_{crit}(M_2) \approx 74°28'$), bottom slopes are not steep enough to support the generation of internal tides. The extremely weak stratification of the Weddell Sea is responsible for this lack of baroclinic response. Near $\psi_{crit}(M_2)$, however, the slope of the internal tidal wave

characteristics become almost zero, and so it becomes possible for internal tide generation to occur despite the weak stratification. This latitude is close to the shelf break in the southern Weddell Sea, in a region where much of the interaction occurs between shelf-resident water types and the intermediate water types of the deep basin. Thus, any mixing associated with the internal tides along the southern shelf would contribute to the water mass mixing that ultimately generates WSDW and WSBW, which both then contribute to the global production of AABW.

Unfortunately, POM in its present form was found to be unsuitable for simulation of internal tides near $\psi_{crit}(M_2)$, which makes it unsuitable for simulating internal tides in the southern Weddell Sea. The major difficulty encountered using POM near ψ_{crit} was the development of a vertically variable inertial oscillation response over the continental slope. Since this inertial oscillation has not been observed, it is believed to be unreal and a model artifact. Further investigation found that the inertial oscillation stemmed from errors in the calculation of the baroclinic pressure gradient term. Near ψ_{crit}, errors in the baroclinic pressure gradient term were found to induce resonant forcing at the inertial frequency resulting in the erroneous inertial oscillations. Since the error in this term increased with depth, the inertial oscillations were stronger in the lower water column over the continental slope. These inertial oscillations exhibited many of the characteristics of an internal tide; however, they occurred both with and without stratification. They had higher velocities with stratification than without, since increased vertical diffusion and friction reduced the vertical variation, and the vertical viscosity coefficient is reduced with increased stratification in the Mellor-Yamada 2.5 level closure scheme. The inertial oscillation response was found to decrease with shallower slopes and also with distance from ψ_{crit}. The slope dependence results from a reduction in the error in the baroclinic pressure gradient term for shallower slopes and the distance dependence from the decrease in resonance with distance from ψ_{crit}. The error in the baroclinic pressure gradient term resulted from errors in the vertical gradient of the perturbation density used in POM. The error was found to be linked to the inclusion of the surface elevation in the pressure correction to the perturbation density. Modifications made to POM in an attempt to resolve the erroneous behavior, which developed when

ψ_{crit} was in the domain, reduced the error but were unable to remove it. Additionally, it was determined that for this region, a two-dimensional application of POM is unable to simulate the forcing wave driving the dynamics.

4.7. References

Baines, P. G., Internal tides, internal waves, and near-inertial motions, in *Baroclinic Processes on Continental Shelves*, Coastal and Estuarine Science 3, edited by C. N. K. Mooers, AGU, Washington, D.C., 19-31 pp., 1986.

Blumberg, A. F., and G. L. Mellor, A description of a three-dimensional coastal ocean circulation model, in *Three-Dimensional Coastal Ocean Models*, 4, edited by N. Heaps, 208 pp., AGU, Washington, D. C., 1987.

Carmack, E. C., Water characteristics of the Southern Ocean south of the Polar Front, in *A Voyage of Discovery*, edited by M. Angel, pp. 15-41, Pergamon Press, Inc., Oxford, 1977.

Chen, C., and R. C. Beardsley, Tidal mixing and cross-frontal particle exchange over a finite amplitude asymmetric bank: A model study of Georges Bank, *J. Mar. Res., 56*, 1163-1201, 1998.

Eriksen, C. C., Internal wave reflection and mixing at Fieberling Guyot, *J. Geophys. Res., 103*, 2977-2994, 1998.

Ffield, A., and A. L. Gordon, Tidal mixing signatures in the Indonesian Seas, *J. Phys. Oceanogr., 26*, 1924-1937, 1996.

Foldvik, A., T. Gammelsrød, and T. Tørresen, Physical oceanographic studies in the Weddell Sea shelf during the Norwegian Antarctic Research Expedition 1978/79, *Polar Res., 3*, 195-207, 1982.

Foldvik, A., T. Gammelsrød, and T. Tørresen, Circulation and water masses in the southern Weddell Sea shelf, in *Oceanology of the Antarctic Continental Shelf, Antarc. Res. Series, 43*, edited by S. S. Jacobs, pp. 5-20, AGU, Washington, D. C., 1985.

Foldvik, A., J. H. Middleton, and T. D. Foster, The tides of the southern Weddell Sea, *Deep-Sea Res., 37*, 1345-1362, 1990.

Foreman, M. G. G., *Manual for tidal height analysis and prediction*, Pacific Marine Science Report No. 77-10, Institute of Ocean Sciences, Patricia Bay, Sidney, B.C., 58 pp., 1977.

Foreman, M. G. G., *Manual for tidal current analysis and prediction*, Pacific Marine Science Report No. 78-6, Institute of Ocean Sciences, Patricia Bay, Sidney, B.C., 70 pp., 1978.

Foster, T. D., Large, steplike temperature and salinity structures observed in the central Weddell Sea, *Antarct. J of the U.S., 29*, 99-100, 1994.

Foster, T. D., and E. C. Carmack, Frontal zone mixing and Antarctic Bottom Water formation in the southern Weddell Sea, *Deep-Sea Res., 23,* 301-317, 1976.

Foster, T. D., A. Foldvik, and J. H. Middleton, Mixing and bottom water formation in the shelf break region of the southern Weddell Sea, *Deep-Sea Res., 34,* 1771-1794, 1987.

Furevik, T., and A. Foldvik, Stability at M_2 critical latitude in the Barents Sea, *J. Geophys. Res., 101*, 8823-8837, 1996.

Gammelsrød, T., A. Foldvik, O. A. Nøst, Ø. Skagseth, L. G. Anderson, E. Fogelqvist, K. Olsson, T. Tanhua, E. P. Jones, and S. Østerhus, Distribution of water masses on the continental shelf in the southern Weddell Sea, in *The Polar Oceans and Their Role in Shaping the Global Environment*, Geophysical Monograph 84, edited by O. M. Johannessen, R. D. Muench, and J. E. Overland, AGU, Washington, D.C., 159-176 pp., 1994.

Gill, A. E., *Atmosphere-Ocean Dynamics*, Academic Press, Inc., San Diego, CA, 662 pp., 1982.

Gordon, A. L., Western Weddell Sea thermohaline stratification, in *Ocean, Ice and Atmosphere: Interactions at the Antarctic Continental Margin, Antarc. Res. Series, 75,* edited by S. S. Jacobs and R. F. Weiss, 215-240 pp., AGU, Washington, D. C., 1998.

Haltiner G. J., and R. T. Williams, *Numerical Prediction and Dynamic Meteorology,* John Wiley and Sons, Inc., New York, 477 pp., 1980.

Hatayama, T., T. Awaji, and K. Akitomo, Tidal currents in the Indonesian Seas and their effect on transport and mixing, *J. Geophys. Res., 101*, 12,353-12,373, 1996.

Holloway, P. E., A numerical model of internal tides with application to the Australian north west shelf, *J. Phys. Oceanogr., 26,* 21-37, 1996.

Huber, B.A., P. A. Mele, W. E. Haines, A. L. Gordon, and V. I. Lutkin, *Ice Station Weddell, 1*, CTD/Hydrographic Data, Tech. Rep. *LDEO-94-2*, Lamont-Doherty Geol. Obs., Palisades, N.Y., 1994.

Huthance, J. M., Internal tides and waves near the continental shelf edge, *Geophys. Astrophys. Fluid Dyn., 48*, 81-105, 1989.

Kundu, P. *Fluid Mechanics*, Academic Press, Inc., San Diego, CA, 668 pp., 1990.

Lamb, H., *Hydrodynamics*, Cambridge Univ. Press, Cambridge, 738 pp., 1879.

Le Blond, P. H., and L. A. Mysak, *Waves in the Ocean*, Elsevier Scientific Publishing, Amsterdam, 602 pp., 1978.

Le Tareau, J. Y., and R. Maze, On barotropic and baroclinic tides over an arbitrary sloping topography, *Ann. Geophysicae, 14,* 961-975, 1996.

Lewis, J. K., Y. L. Hsu, and A. F. Blumberg, Boundary forcing and a dual-mode calculation scheme for coastal tidal models using step-wise bathymetry, Estuarine and Coastal Modeling III, Proceedings of the 3rd International Conf., Oakbrook, IL, Sept. 1993, M. L. Spaulding, K. Bedford, A. Blumberg, R. Cheng, and C. Swanson editors, ASCE, NY, 1994.

MacAyeal, D. G., Numerical simulation of the Ross Sea tides, *J. Geophys. Res., 89,* 607-615, 1984.

Martinsen, E. A., and H. Engedahl, Implementation and testing of a lateral boundary scheme as an open boundary condition in a barotropic ocean model, *Coastal. Eng., 11,* 603-627, 1987.

Mellor, G. L., User's guide for a three-dimensional, primitive equation, numerical ocean model. Unpublished report, Atmospheric and Ocean Sciences Program, 35 pp., Princeton University, Princeton, NJ, 1993.

Mellor, G. L., An equation of state for numerical modeling of oceans and estuaries, *J. Atmos. and Ocean. Tech., 8,* 609-611, 1991.

Mellor, G. L., T. Ezer, and L.-Y. Oey, The pressure gradient conundrum of sigma coordinate models, *J. Atmos. Ocean. Tech., 11,* 1126-1134, 1994.

Mellor, G. L., L.-Y. Oey, and T. Ezer, Sigma coordinate gradient errors and the seamount problem, *J. Atmos. Ocean. Tech., 15,* 1122-1131, 1998.

Middleton, J. H., and T. Denniss, The propagation of tides near the critical latitude, *Geophys. Astrophys. Fluid Dynam., 68,* 1-13, 1993.

Middleton, J. H., and T. D. Foster, Tidal currents in the central Weddell Sea, *Deep-Sea Res., 24,* 1195-1202, 1977.

Middleton, J. H., T. D. Foster, and A. Foldvik, Low-frequency currents and continental shelf waves in the southern Weddell Sea, *J. Phys. Oceanogr., 12,* 618-634, 1982.

Munk, W., and C. Wunsch, The moon and mixing: abyssal recipes II, *Deep-Sea Res., 45,* 1977-2010, 1998.

National Geophysical Data Center, GEODAS CD-ROM worldwide marine geophysical data, *Data Announce. 92-MGG-02*, Natl. Oceanic and Atmos. Admin. U.S. Dep. Commer., Boulder, Colo., 1992.

Oey, L.-Y., G. L. Mellor, and R. I. Hires, A three-dimensional simulation of the Hudson-Raritan Estuary. Part I: Description of the model and model simulations, *J. Phys. Oceanogr., 15*, 1676-1692, 1985.

Padman, L., K. W. Nicholls, and R. A. Woodgate, The 1998 Ronne Polynya Experiment (ROPEX), *Antarct. J of the U.S.*, in press, 1998.

Padman, L., A. J. Plueddemann, R. D. Muench, and R. Pinkel, Diurnal tides near the Yermak Plateau, *J. Geophys. Res, 97*, 12,639-12,652, 1992.

Palma, E. B., and R. P. Matano, On the implementation of passive open boundary conditions for a general circulation model: The barotropic mode, *J. Geophys. Res, 103*, 1319-1342, 1998.

Petruncio, E. T., Observations and modeling of the internal tide in a submarine canyon, Ph.D. thesis, 181 pp., Naval Postgraduate School at Monterey, CA, September 1996.

Polyakov, I.V., Maintenance of the Arctic Ocean large-scale baroclinic structure by the M_2 tide, *Polar Research, 13*, 219-232, 1995.

Polzin, K. L., J. M. Toole, J. R. Ledwell, and R. W. Schmitt, Spatial variability of turbulent mixing in the abyssal ocean, *Science, 276*, 93-96, 1997.

Prinsenberg, S. J., and E. B. Bennett, Vertical variations of tidal currents in shallow land fast ice-covered regions, *J. Phys. Oceanogr., 19*, 1268-1278, 1989.

Robertson, R. A., L. Padman, and G. D. Egbert, Tides in the Weddell Sea, in *Ocean, Ice and Atmosphere: Interactions at the Antarctic Continental Margin, Antarc. Res. Series, 75*, edited by S. S. Jacobs and R. F. Weiss, 341-369 pp., AGU, Washington, D. C., 1998.

Robertson, R. A., L. Padman, M. D. Levine, R. D. Muench, and M. G. McPhee, Internal waves in the eastern Weddell Sea during AnzFlux, IAPSO XXI General Assembly, Honolulu, HI, 1995.

Sherwin, T. J., Evidence of a deep internal tide in the Faeroe-Shetland Channel, in *Tidal Hydrodynamics*, edited by B. B. Parker, 469-488 pp., John Wiley and Sons, New York, 1991.

Sjöberg, B., and A. Stigebrandt, Computations of the geographical distribution of the energy flux to mixing processes via internal tides and the associated vertical circulation in the ocean, *Deep-Sea Res., 39,* 269-291, 1992.

Thiel, E., A. P. Crary, R. A. Haubrich, and J. C. Behrendt, Gravimetric determination of ocean tide, Weddell and Ross Seas, Antarctica, *J. Geophys. Res., 65,* 629-636, 1960.

Vaughan, D. G., J. Sievers, C. S. M. Doake, G. Grikurov, H. Hinze, V. S. Pozdeev, H. Sandhäger, H. W. Schenke, A. Solheim, and F. Thyssen, Map of the subglacial and seabed topography; Filchner-Ronne-Schelfeis/ Weddell Sea, Antarktis, scale 1:2,000,000, *Institut für Angewandte Geodäsie,* Frankfurt am Main, Germany, 1994.

Weppernig, R. P., Schlosser, S. Khatiwala, and R. G. Fairbanks, Isotope data from Ice Station Weddell: Implications for deep water formation in the Weddell Sea, *J. Geophys. Res., 101*, 25,723-25,739, 1996.

Woodgate, R. A., M. Schröder, and S. Østerhus, Moorings from the Filchner Trough and the Ronne Ice Shelf Front: Preliminary results, Filchner-Ronne Ice Shelf Program, Report No. 12, Alfred-Wegener Institute, 1998.

Xing, J., and A. M. Davies, Processes influencing the internal tide, its higher harmonics, and tidally induced mixing on the Malin-Hebrides Shelf, *Prog. in Ocean.*, *38*, 155-204, 1996.

5: GENERAL SUMMARY

Heat loss by the ocean to the ice and atmosphere in the polar regions plays an important role in global climate and ocean circulation through Antarctic Bottom Water (AABW) formation. Most AABW formation occurs in the Weddell Sea, where the basin-averaged heat loss from the ocean to the atmosphere has been estimated at 19 W m^{-2} [*Fahrbach et al.*, 1994]. Two field programs involving Oregon State University (OSU) personnel show that the local vertical heat flux varies by at least an order of magnitude over the Weddell Sea. From the CISW drift camp in the western Weddell Sea, the average heat flux from the ocean to the atmosphere was estimated at 2 W m^{-2} [*Robertson et al.*, 1995a; *Levine et al.*, 1997], whereas from the AnzFlux experiment in the eastern Weddell Sea, the equivalent heat flux was estimated at 30-40 W m^{-2} [*Robertson et al.*, 1995b; *Stanton et al.*, 1999], more than an order of magnitude higher (Figure 5.1). These and other studies indicate that not only does the average heat loss to the ice and atmosphere vary within the Weddell Sea, but also that the relative importance of different heat flux mechanisms varies greatly. Several studies [e.g., *Foster et al.*, 1987; *Foldvik et al.*, 1990; *Gammelsrød et al.*, 1994] indicated that processes related to tides were probably contributing to the heat flux in many areas where large fluxes have been inferred. As a result, this summary will focus on the observed heat fluxes for the eastern and western Weddell Sea and the influence of the tides on circulation, mixing, and heat transport from the results of both barotropic and baroclinic tidal models. Note that the analyses of the eastern Weddell Sea data [*Robertson et al.*, 1995b; *Stanton et al.*, 1999] were not included as a chapter in this thesis.

Heat fluxes observed in the western Weddell Sea (Chapter 2) were quite low, with an average heat loss to the atmosphere of only 2 W m^{-2}, an order of magnitude less than the basin average value of ~20 W m^{-2}. Although higher surface heat fluxes, up to 15 W m^{-2}, were observed during storms, even these are still less than the basin average. The western Weddell Sea is perennially covered by thick, second year sea ice, which reduces the wind-induced and convective surface mixing. The lower heat fluxes in this region both reflect the influence of the ice cover, and are a result of it. The heat flux through the

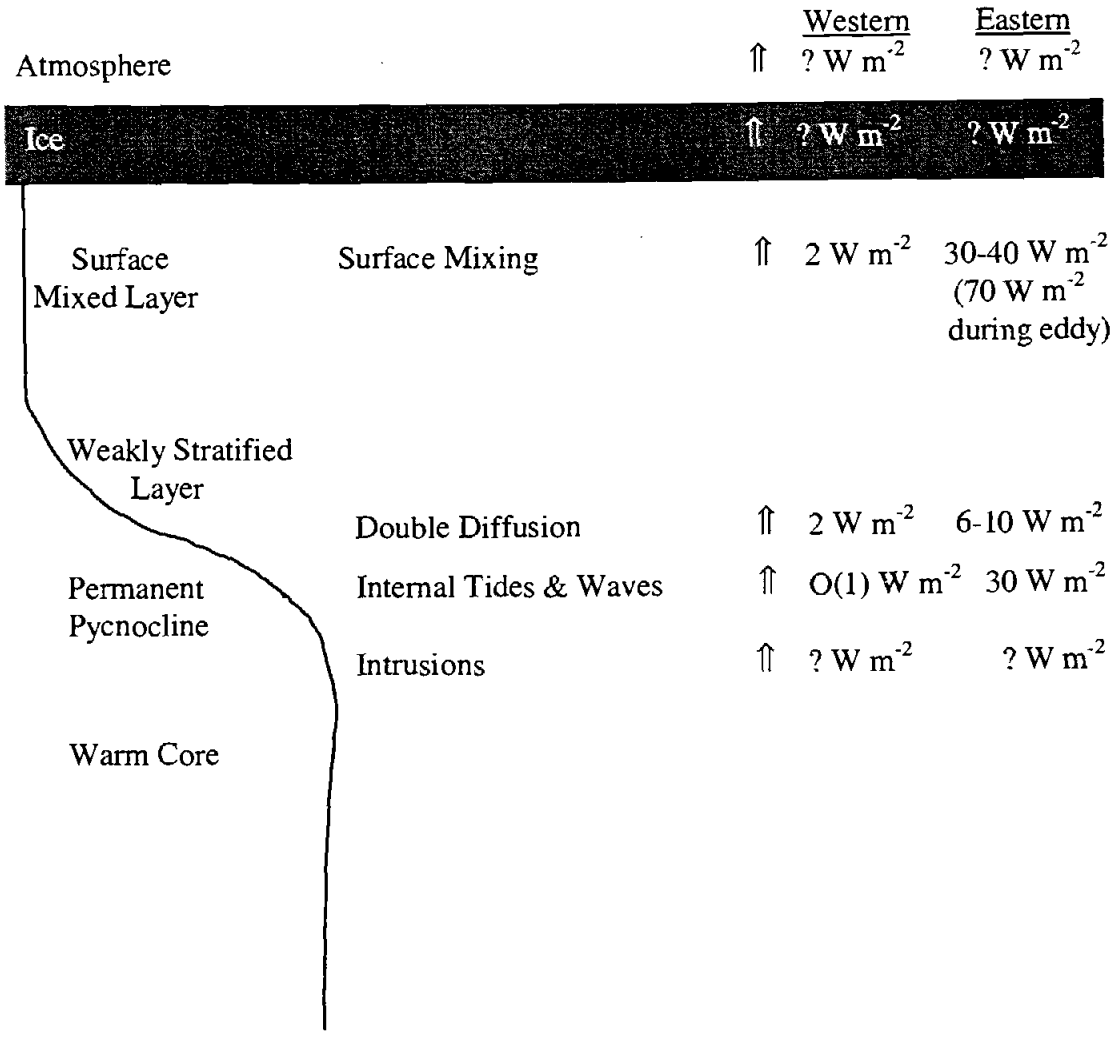

Figure 5.1 Observed heat fluxes in the Weddell Sea. Estimates for the eastern Weddell Sea are taken from *Robertson et al.*, [1995b] and Stanton et al. [1999].

upper ocean is dominated by double diffusion in the western Weddell Sea, being roughly twice the contribution by internal tides and waves (Figure 5.1). Other mechanisms such as intrusions may contribute to the upper ocean heat flux in certain regions, however we were unable to estimate the heat flux attributable to intrusions for the western Weddell Sea.

The heat fluxes observed in the eastern Weddell Sea were higher than those of the western Weddell Sea, with an average heat loss to the atmosphere of 30-40 W m^{-2} in winter. The elevation of the permanent pycnocline during an eddy increased the surface

heat flux to ~70 W m^{-2} [*Robertson et al.*, 1995b; *Stanton et al.*, 1999]. Although the double-diffusive contribution was 6-10 W m^{-2}, which is three to five times higher than that in the western Weddell Sea, the heat flux through the upper ocean was dominated by shear instabilities resulting from internal tides and waves, which provide approximately 30 W m^{-2} to the total flux through the pycnocline.

These heat flux observations were made only in a small part of each basin. For comparison with basin scale budget estimates [e.g. *Fahrbach et al.*, 1994,] we need to know the total distribution of upper-ocean heat flux. Some flux mechanisms are limited to local areas and may not be represented by the limited observations. For example, tides are believed to affect the generation of internal tides and waves over the upper continental shelf, but not in the deep basin. However, neither of the OSU flux measurement programs took place in a region with strong anticipated internal tide activity.

While tides have been postulated to influence mixing and heat flux [e.g., *Foster et al.*, 1987; *Foldvik et al.*, 1990], chapter three of this thesis represents the most detailed analysis to date of possible tidal effects. Our results support the previous hypotheses of the relevance of tide-related ocean mixing and also describe the geographical regions where this mixing is likely to be the most energetic. Spatial gradients of ocean tidal velocities cause the ice cover to deform and diverge, and cause lead formation. Since the heat flux through open water is roughly two orders of magnitude higher than that through ice [*Launianinen and Vihma*, 1994], even a lead fraction of just 1% of the total area could double the mean heat flux. Lead fractions of this size are predicted over the continental shelf/slope break in the southern and eastern Weddell Sea using the velocities predicted by the barotropic tidal model [*Padman et al.*, 1999]. Higher lead fractions are predicted when the baroclinic M_2 tide is added to the barotropic tide.

Evaluation of the amount of barotropic tidal energy going into internal waves using the barotropic model results and following the method of *Sjöberg and Stigebrandt* [1992]. This study indicated that significant energy for internal tide and wave generation occurs over the upper continental shelf/slope in the southern Weddell Sea. Unfortunately, further investigation of the M_2 internal tides generated across the continental shelf and slope in this region using a three-dimensional primitive equation model in a two-

dimensional transect mode was unable to determine if there was significant generation of M_2 internal tides. The primitive equation model which was used proved to be unsuitable for this purpose. In its present form, it is incapable of reliably simulating internal tides near the critical latitude due to systematic errors in the calculation of the baroclinic pressure gradient component for the cross-slope velocity acceleration. However, the model does give some indication that internal tides are generated over the upper continental slope and the velocities generated by the model agree reasonably well with observations in this region.

BIBLIOGRAPHY

Aanderaa Instruments, RCM4/5 Operating Manual, *Technical Publication No. 119*, Aanderaa Instruments, Bergen, Norway, 1979.

Andersen, O. B., New ocean tide models for loading computations, *Bull. Int. Mare Terr., 102*, 9256-9264, 1995.

Andersen, O. B., P. L. Woodworth, and R. A. Flather, Intercomparison of recent ocean tide models, *J. Geophys. Res., 100*, 25,261-25,282, 1995.

Baines, P. G., Internal tides, internal waves, and near-inertial motions, in *Baroclinic Processes on Continental Shelves*, Coastal and Estuarine Science 3, edited by C. N. K. Mooers, AGU, Washington, D.C., 19-31 pp., 1986.

Baker, M. A. and C. H. Gibson, Sampling turbulence in the stratified ocean: Statistical consequences of strong interactions, *J. Phys. Oceanogr., 17*, 1817-1836, 1987.

Barber, M., and D. Crane, Current flow in the northwest Weddell Sea, *Antarctic Science, 7*, 39-50, 1995.

Bathmann, U., V. Smetacek, H. De Baar, E. Fahrbach, and G. Krause, The expeditions ANTARKTIS X/6-8 of the research vessel "*Polarstern*" in 1992/93, *Rep. Polar Res. 135*, Alfred-Wegener Institute for Polar and Marine Research, Germany, 1994.

Bell, T. H., Topographically generated internal waves in the open ocean, *J. Geophys. Res., 80*, 320-327, 1975.

Bersch, M., G. A. Becker, H. Frey, and K. P. Koltermann, Topographic effects of the Maud Rise on the stratification and circulation of the Weddell Gyre, *Deep-Sea Res., 39*, 303-331, 1992.

Blumberg, A. F., and G. L. Mellor, A description of a three-dimensional coastal ocean circulation model, in *Three-Dimensional Coastal Ocean Models*, 4, edited by N. Heaps, 208 pp., AGU, Washington, D. C., 1987.

Boyd, T. J., and E. A. D'Asaro, Cooling of the West Spitsbergen Current, *J. Geophys. Res., 99*, 22,597-22,618, 1994.

Broecker, W. S., and T. H. Peng, *Tracers in the Sea*, Eldigio Press, Palisades, NY, 690 pp., 1982.

Bye, J. A. T., and G. Veronis, A correction to the Sverdrup transport, *J. Phys. Oceanogr.*, *9*, 649-651, 1979.

Caldwell, D. R., T. M. Dillon, and J. N. Moum, The rapid-sampling vertical profiler: An evaluation, *J. Atmos. Oceanic Technol.*, 2, 615-625, 1985.

Carmack, E. C., Water characteristics of the Southern Ocean south of the Polar Front, in *A Voyage of Discovery*, edited by M. Angel, 15-41 pp., Pergamon Press, Inc., Oxford, 1977.

Carmack, E. C., Circulation and mixing in ice-covered waters, in *The Geophysics of Sea Ice*, edited by N. Untersteiner, 641-712 pp., Plenum, New York, 1986.

Cartwright, D. E., and R. J. Taylor, New computations of the tide generating potential, *Geophys. J. R. Astron. Soc.*, *23*, 45-74, 1971.

Central Intelligence Agency, *World Data Bank, 2*, Central Intelligence Agency, Washington, D. C., 1972.

Chen, C., and R. C. Beardsley, Tidal mixing and cross-frontal particle exchange over a finite amplitude asymmetric bank: A model study of Georges Bank, *J. Mar. Res.*, *56*, 1163-1201, 1998.

Dillon, T. M., The energetics of overturning structures: Implications for the theory of fossil turbulence, *J. Phys. Oceanogr.*, *14*, 541-549, 1984.

Doake, C. S. M., Dissipation of tidal energy by Antarctic ice shelves, *Nature, 275*, 304-305, 1978.

Doake, C. S. M., Gravimetric tidal measurements on Filchner Ronne Ice Shelf, in *Filchner-Ronne Ice Shelf Programme Report No. 6*, edited by H. Oerter, Alfred-Wegener Institute for Polar and Marine Research, Bremerhaven, Germany, 34-39, 1992.

Egbert, G. D., Tidal data inversion: interpolation and inference, *Prog. in Oceanogr.*, in press, 1997.

Egbert, G. D., A. F. Bennett, and M. G. G. Foreman, TOPEX/POSEIDON tides estimated using a global inverse model, *J. Geophys. Res.*, *99*, 24,821-24,852, 1994.

Eckstaller, A., and H. Miller, Gezeiten-Vertikalbewegung des Filchner Schelfeises (Tides and vertical movement of the Filchner Ice Shelf), *Ber. Polarforsch.*, *19*, 82-97, 1984.

Eriksen, C. C., Internal wave reflection and mixing at Fieberling Guyot, *J. Geophys. Res.*, *103*, 2977-2994, 1998.

Fahrbach, E., G. Rohardt, and G. Krause, The Antarctic coastal current in the southeastern Weddell Sea, *Polar Biology, 12,* 171-182, 1992.

Fahrbach, E., G. Rohardt, M. Schröder, and V. Strass, Transport and structure of the Weddell Gyre, *Ann. Geophysicae, 12,* 840-855, 1994.

Fernando, H. J. S., Oceanographic implications of laboratory experiments on diffusive interfaces, *J. Phys. Oceanogr., 19,* 1707-1715, 1989.

Ffield, A., and A. L. Gordon, Tidal mixing signatures in the Indonesian Seas, *J. Phys. Oceanogr., 26,* 1924-1937, 1996.

Fofonoff, N. P., Some properties of sea water influencing the formation of Antarctic bottom water, *Deep Sea Res., 4,* 32-35, 1956.

Foldvik, A., and T. Kvinge, Bottom currents in the Weddell Sea, *Rep. No. 37,* 43 pp., University of Bergen, Bergen, Norway, 1974.

Foldvik, A., and T. Gammelsrød, Notes on southern ocean hydrography, sea-ice and bottom water formation, *Palaeogeog., Palaeoclim., Palaeoecol., 67,* 3-17, 1988.

Foldvik, A., T. Gammelsrød, N. Slotsvik, and T. Tørresen, Oceanographic conditions on the Weddell Sea shelf during the German Antarctic Expedition 1979/80, *Polar Res., 3,* 209-226, 1982a.

Foldvik, A., T. Gammelsrød and T. Tørresen, Physical oceanographic studies in the Weddell Sea shelf during the Norwegian Antarctic Research Expedition 1978/79, *Polar Res., 3,* 195-207, 1982b.

Foldvik, A., T. Gammelsrød and T. Tørresen, Circulation and water masses in the southern Weddell Sea shelf, in *Oceanology of the Antarctic Continental Shelf,* Antarc. Res. Series, *43,* edited by S. S. Jacobs, 5-20, AGU, Washington, D. C., 1985a.

Foldvik, A., T. Kvinge, and T. Tørresen, Bottom currents near the continental shelf break in the Weddell Sea, in *Oceanology of the Antarctic Continental Shelf,* Antarc. Res. Series, *43,* edited by S. S. Jacobs, 21-34, AGU, Washington, D. C., 1985b.

Foldvik, A., J. H. Middleton, and T. D. Foster, The tides of the southern Weddell Sea, *Deep-Sea Res., 37,* 1345-1362, 1990.

Foreman, M. G. G., *Manual for tidal height analysis and prediction*, Pacific Marine Science Report No. 77-10, Institute of Ocean Sciences, Patricia Bay, Sidney, B.C., 58 pp., 1977.

Foreman, M. G. G., *Manual for tidal current analysis and prediction*, Pacific Marine Science Report No. 78-6, Institute of Ocean Sciences, Patricia Bay, Sidney, B.C., 70 pp., 1978.

Foster, T. D., An analysis of the cabbeling instability in sea water, *J. Phys. Oceanogr.*, *2*, 294-301, 1972.

Foster, T. D., Large, steplike temperature and salinity structures observed in the central Weddell Sea, *Antarct. J. of the U.S., 29*, 99-100, 1994.

Foster, T. D., and E. C. Carmack, Temperature and salinity structure in the Weddell Sea, *J. Phys. Oceanogr.*, *6*, 36-44, 1976a.

Foster, T. D., and E. C. Carmack, Frontal zone mixing and Antarctic Bottom Water formation in the southern Weddell Sea, *Deep Sea Res.*, *23*, 301-317, 1976b.

Foster, T. D., A. Foldvik, and J. H. Middleton, Mixing and bottom water formation in the shelf break region of the southern Weddell Sea, *Deep Sea Res.*, *34*, 1771-1794, 1987.

Furevik, T., and A. Foldvik, Stability at M_2 critical latitude in the Barents Sea, *J. Geophys. Res.*, *101*, 8823-8837, 1996.

Gallagher, B. S., and W. H. Munk, Tides in shallow water: Spectroscopy, *Tellus*, *23*, 346-363, 1971.

Gammelsrød, T., A. Foldvik, O. A. Nøst, Ø. Skagseth, L. G. Anderson, E. Fogelqvist, K. Olsson, T. Tanhua, E. P. Jones, and S. Østerhus, Distribution of water masses on the continental shelf in the southern Weddell Sea, in *The Polar Oceans and Their Role in Shaping the Global Environment*, Geophysical Monograph 85, edited by O. M. Johannessen, R. D. Muench, and J. E. Overland, AGU, Washington, D.C., 159-176 pp., 1994.

Genco, M. L., F. Lyard, and C. Le Provost, The oceanic tides in the South Atlantic Ocean, *Ann. Geophysicae, 12*, 868-886, 1994.

Gill, A. E., Circulation and bottom water production in the Weddell Sea, *Deep Sea Res.*, *20*, 111-140, 1973.

Gordon, A. L., Western Weddell Sea thermohaline stratification, in *Ocean, Ice and Atmosphere: Interactions at the Antarctic Continental Margin, Antarc. Res. Series, 75*, edited by S. S. Jacobs and R. F. Weiss, 215-240 pp., AGU, Washington, D. C., 1998.

Gordon, A. L., and B. A. Huber, Southern Ocean winter mixed layer, *J. Geophys. Res.*, *95*, 11,655-11,672, 1990.

Gordon, A. L., B. A. Huber, H. H. Hellmer, and A. Ffield, Deep and bottom water of the Weddell Sea's western rim, *Science*, *262*, 95-97, 1993a.

Gordon, A. L., and Ice Station Weddell Group of Principal Investigators and Chief Scientists, Weddell Sea exploration from ice station, *EOS Trans., AGU*, *74*, 121-126, 1993b.

Gordon, A. L., D. G. Martinson, and M. W. Taylor, The wind driven circulation in the Weddell-Enderby Basin, *Deep-Sea Res., 28A,* 151-163, 1981.

Gouretski, V., and A. Danilov, Weddell Gyre: Structure of the eastern boundary, *Deep-Sea Res.*, 40, 561-582, 1993.

Gregg, M. C., Diapycnal mixing in the thermocline: A review, *J. Geophys. Res.*, *92*, 5249-5286, 1987.

Gregg, M. C., Scaling turbulent dissipation in the thermocline, *J. Geophys. Res.*, *94*, 9686-9698, 1989.

Grosfeld, K., R. Gerdes, and J. Determann, Thermohaline circulation and interaction between ice shelf cavities and the adjacent open ocean, *J. Geophys. Res., 203,* 15,595-15,610, 1997.

Haltiner G. J., and R. T. Williams, *Numerical Prediction and Dynamic Meteorology,* John Wiley and Sons, Inc., New York, 477 pp., 1980.

Hatayama, T., T. Awaji, and K. Akitomo, Tidal currents in the Indonesian Seas and their effect on transport and mixing, *J. Geophys. Res., 101*, 12,353-12,373, 1996.

Hisdal, V., On the tides at Norway Station, and adjacent coastal areas of Antarctica, Norwegian Antarctic Expedition, 1956-60, *Sci. Res., 9,* 21 pp, Norwegian Polar Institute, Oslo, 1965.

Holloway, P. E., A numerical model of internal tides with application to the Australian north west shelf, *J. Phys. Oceanogr., 26,* 21-37, 1996.

Huber, B. A., P. A. Mele, W. E. Haines, A. L. Gordon, and V. I. Lukin, Ice Station Weddell 1, CTD/Hydrographic Data, *Tech. Rep. LDEO-94-2*, Lamont-Doherty Earth Obs., Palisades, N. Y., 1994.

Huthance, J. M., Internal tides and waves near the continental shelf edge, *Geophys. Astrophys. Fluid Dyn.*, *48*, 81-105, 1989.

Jet Propulsion Laboratory, A collection of ocean tide models on CD-ROM, CD-ROM distributed by the *Jet Propulsion Laboratory*, Pasadena, California, 1996.

Kelley, D., Effective diffusivities within thermohaline staircases, *J. Geophys. Res.*, *89*, 10,484-10,488, 1984.

Kelley, D., Fluxes through diffusive staircases: A new formulation, *J. Geophys. Res.*, *95*, 3365-3371, 1990.

Kowalik, Z., and A. Y. Proshutinsky, The Arctic Ocean Tides, in *The Polar Oceans and Their Role in Shaping the Global Environment*, Geophysical Monograph 85, edited by O. M. Johannessen, R. D. Muench, and J. E. Overland, 137-158, AGU, Washington, D. C., 1994.

Kowalik, Z., and A. Y. Proshutinsky, Topographic enhancement of tidal motion in the western Barents Sea, *J. Geophys. Res.*, *100*, 2613-2637, 1995.

Kundu, P. *Fluid Mechanics*, Academic Press, Inc., San Diego, CA, 668 pp., 1990.

LaBrecque, J. L., and M. E. Ghidella, Estimates of bathymetry, depth to magnetic basement, and sediment thickness for the western Weddell Basin, *Antarc. J. U.S.*, *27*, 68-70, 1993.

Lamb, H., *Hydrodynamics*, Cambridge Univ. Press, Cambridge, 738 pp., 1879.

Launiainen, J. and T. Vihma, On the surface heat fluxes in the Weddell Sea, in *The Polar Oceans and Their Role in Shaping the Global Environment*, Geophysical Monograph 85, edited by O. M. Johannessen, R. D. Muench, and J. E. Overland, AGU, Washington, D.C., 399-419, 1994.

Le Blond, P. H., and L. A. Mysak, *Waves in the Ocean*, Elsevier Scientific Publishing, Amsterdam, 602 pp., 1978.

Le Provost, C., M. L. Genco, F. Lyard, P. Vincent, and P. Canceil, Spectroscopy of the world ocean tides from a finite element hydrodynamic model, *J. Geophys. Res.*, *99*, 24,777-24,797, 1994.

Le Tareau, J. Y., and R. Maze, On barotropic and baroclinic tides over an arbitrary sloping topography, *Ann. Geophysicae, 14*, 961-975, 1996.

Ledwell, J. R., A. J. Watson, and C. S. Law, Evidence for the slow mixing across the pycnocline from an open-ocean tracer-release experiment, *Nature*, *364*, 701-703, 1993.

Levine, M. D., L. Padman, R. D. Muench, and J. H. Morison, Internal waves and tides in the western Weddell Sea: Observations from Ice Station Weddell, *J. Geophys. Res*, *102*, 1073-1089, 1997.

Lewis, J. K., Y. L. Hsu, and A. F. Blumberg, Boundary forcing and a dual-mode calculation scheme for coastal tidal models using step-wise bathymetry, Estuarine and Coastal Modeling III, Proceedings of the 3rd International Conf., Oakbrook, IL, Sept. 1993, M. L. Spaulding, K. Bedford, A. Blumberg, R. Cheng, and C. Swanson editors, ASCE, NY, 1994.

Loder, J.W., Topographic rectification of tidal currents on the sides of Georges Bank, *J. Phys. Oceanogr., 10,* 1399-1416, 1980.

Lutjeharms, J. R. E., C. C. Stavropolous, and K. P. Koltermann, Tidal measurements along the Antarctic coastline, in *Oceanology of the Antarctic Continental Shelf,* Antarc. Res. Series, *43*, edited by S. S. Jacobs, 273-289 pp., AGU, Washington, D. C., 1985.

Lytle, V. I., and S. F. Ackley, Heat flux through sea ice in the western Weddell Sea: Convective and conductive transfer processes, *J. Geophys. Res., 101*, 8853-8868, 1996.

MacAyeal, D. R., Numerical simulations of the Ross Sea tides, *J. Geophys. Res, 89*, 607-615, 1984.

Makinson, K., and K. W. Nicholls, Modeling tidal currents beneath Filchner-Ronne Ice Shelf, *Filchner-Ronne Ice Shelf Programme,* Report 10, 58-67, 1996.

Marmorino, G. O., and D. R. Caldwell, Heat and salt transport through a diffusive thermohaline interface, *Deep Sea Res., 23*, 59-67, 1976.

Martinsen, E. A., and H. Engedahl, Implementation and testing of a lateral boundary scheme as an open boundary condition in a barotropic ocean model, *Coastal. Eng., 11*, 603-627, 1987.

McPhee, M. G., Analysis and prediction of short-term ice drift, *J. Offshore Mech. Arct. Eng., 110*, 94-100, 1988.

McPhee, M. G., Turbulent heat flux in the upper ocean under sea ice, *J. Geophys. Res., 97*, 5365-5379, 1992.

McPhee, M. G., On the turbulent mixing length in the oceanic boundary layer, *J. Phys. Oceanogr., 24*, 2014-2031, 1994.

McPhee, M. G., and D. G. Martinson, Turbulent mixing under drifting pack ice in the Weddell Sea, *Science*, *263*, 219-220, 1994.

Mellor, G. L., User's guide for a three-dimensional, primitive equation, numerical ocean model. Unpublished report, Atmospheric and Ocean Sciences Program, 35 pp., Princeton University, Princeton, NJ, 1993.

Mellor, G. L., An equation of state for numerical modeling of oceans and estuaries, *J. Atmos. and Ocean. Tech.*, *8*, 609-611, 1991.

Mellor, G. L., T. Ezer, and L.-Y. Oey, The pressure gradient conundrum of sigma coordinate models, *J. Atmos. Ocean. Tech.*, *11*, 1126-1134, 1994.

Mellor, G. L., L.-Y. Oey, and T. Ezer, Sigma coordinate gradient errors and the seamount problem, *J. Atmos. Ocean. Tech.*, *15*, 1122-1131, 1998.

Middleton, J. H., and T. Denniss, The propagation of tides near the critical latitude, *Geophys. Astrophys. Fluid Dynam.*, *68*, 1-13, 1993.

Middleton, J. H., and T. D. Foster, Tidal currents in the central Weddell Sea, *Deep Sea Res.*, *24*, 1195-1202, 1977.

Middleton, J. H., T. D. Foster, and A. Foldvik, Low-frequency currents and continental shelf waves in the southern Weddell Sea, *J. Phys. Oceanogr.*, *12*, 618-634, 1982.

Middleton, J. H., T. D. Foster, and A. Foldvik, Diurnal shelf waves in the southern Weddell Sea, *J. Phys. Oceanogr.*, *17*, 784-791, 1987.

Muench, R. D., and A. L. Gordon, Circulation and transport of water along the western Weddell Sea margin, *J. Geophys. Res.*, *100*, 18,503-18,516, 1995.

Muench, R. D., H. J. S. Fernando, and G. R. Stegun, Temperature and salinity staircases in the northwesten Weddell Sea, *J. Phys. Oceanog.*, *20*, 295-306, 1990.

Muench, R. D., M. D. Morehead, and J. T. Gunn, Regional current measurements in the western Weddell Sea, *Antarc. J. U.S.*, *27*, 108, 1993.

Munk, W., and C. Wunsch, The moon and mixing: abyssal recipes II, *Deep-Sea Res.*, *45*, 1977-2010, 1998.

National Geophysical Data Center, GEODAS CD-ROM worldwide marine geophysical data, *Data Announce. 92-MGG-02*, Natl. Oceanic and Atmos. Admin. U.S. Dep. Commer., Boulder, Colo., 1992.

Noble, M., B. Butman, and E. Williams, On the longshelf structure and dynamics of subtidal currents on the eastern United States continental shelf, *J. Phys. Oceanogr., 13,* 2125-2147, 1983.

Nygaard, E., Preliminary results from current measurements in position R2 (76°29' S, 53°00' W) outside the Ronne Ice Shelf in the southern Weddell Sea 1993-1994, unpublished report, Geophysical Institute, Bergen, Norway, 25 pp., 1995.

Oey, L.-Y., G. L. Mellor, and R. I. Hires, A three-dimensional simulation of the Hudson-Raritan Estuary. Part I: Description of the model and model simulations, *J. Phys. Oceanogr., 15,* 1676-1692, 1985.

Orsi, A. H., W. D. Nowlin, Jr., and T. Whitworth III, On the circulation and stratification of the Weddell Gyre, *Deep Sea Res., 40,* 169-203, 1993.

Osborn, T. R., Estimates of the local rate of vertical diffusion from dissipation measurements, *J. Phys. Oceanogr., 10,* 83-89, 1980.

Osborn, T. R., and W. R. Crawford, An airfoil probe for measuring turbulent velocity fluctuations in water, in *Air-Sea Interactions: Instruments and Methods*, 369-386 pp., Plenum, New York, 1980.

Padman, L., Small-scale physical processes in the Arctic Ocean, in *Arctic Oceanography: Marginal Ice Zones and Continental Shelves,* Coastal and Estuarine Studies, *49,* edited by W. O. Smith and J. M. Grebmeier, 97-129 pp., AGU, Washington, D.C., 1995.

Padman, L., and T. M. Dillon, Vertical heat fluxes through the Beaufort Sea thermohaline staircase, *J. Geophys. Res., 92,* 10,799-10,806, 1987.

Padman, L., and T. M. Dillon, On the horizontal extent of the Canada Basin thermohaline steps, *J. Phys. Oceanogr., 18,* 1458-1462, 1988.

Padman, L., and T. M. Dillon, Turbulent mixing near the Yermak Plateau during the Coordinated Eastern Arctic Experiment, *J. Geophys. Res., 96,* 4769-4782, 1991.

Padman, L., C. Kottmeier, and R. Robertson, Tidal-Band ice motion and divergence in the Weddell Sea, submitted to *J. Geophys. Res.,* 1999.

Padman, L., K. W. Nicholls, and R. A. Woodgate, The 1998 Ronne Polynya Experiment (ROPEX), *Antarct. J of the U.S.*, in press, 1998.

Padman, L., A. J. Plueddemann, R. D. Muench, and R. Pinkel, Diurnal tides near the Yermak Plateau, *J. Geophys. Res, 97,* 12,639-12,652, 1992.

Padman, L., R. Robertson, and K. Nicholls, Modelling tides in the southern Weddell Sea: Updated model with new bathymetry from ROPEX, Filchner Ronne Ice Shelf Programme Report No. 12, Alfred-Wegener-Institute for Polar and Marine Research, Bremerhaven, Germany, 1998.

Palma, E. B., and R. P. Matano, On the implementation of passive open boundary conditions for a general circulation model: The barotropic mode, *J. Geophys. Res, 103*, 1319-1342, 1998.

Parker, B. B., *Tidal Hydrodynamics*, 883 pp., John Wiley and Sons, New York, 1991.

Parsons, A. R., On the Barents Sea polar front in summer and interpretations of the associated regional oceanography using an Arctic Ocean general circulation model, Ph.D. thesis, 178 pp., Naval Postgraduate School at Monterey, September 1995.

Pedley, M., J. G. Paren, and J. R. Potter, The tidal spectrum underneath Antarctic Ice Shelves, *J. Geophys. Res., 91*, 13,001-13,009, 1986.

Petruncio, E. T., Observations and modeling of the internal tide in a submarine canyon, Ph.D. thesis, 181 pp., Naval Postgraduate School at Monterey, CA, September 1996.

Polyakov, I.V., Maintenance of the Arctic Ocean large-scale baroclinic structure by the M2 tide, *Polar Research, 13*, 219-232, 1995.

Polzin, K. L., J. M. Toole, J. R. Ledwell, and R. W. Schmitt, Spatial variability of turbulent mixing in the abyssal ocean, *Science, 276*, 93-96, 1997.

Pond, S., and G. L. Pickard, *Introductory Dynamical Oceanography*, Butterworth-Heinemann Ltd., Oxford, England, 329 pp., 1978.

Potter, J. R., J. G. Paren, and M. Pedley, Tidal behaviour under an Antarctic ice shelf, *Br. Antarc. Survey Bull., 68*, 1-18, 1985.

Pratt, J. G. D., Tides at Shackleton, Weddell Sea, Trans-Antarctic Expedition, 1955-1958, *Sci. Rep. 4*, 21 pp., American Philosophical Society, Philadelphia, 1960.

Prinsenberg, S. J., and E. B. Bennett, Vertical variations of tidal currents in shallow land fast ice-covered regions, *J. Phys. Oceanogr., 19*, 1268-1278, 1989.

Ramming, H. G., and Z. Kowalik, *Numerical Modeling of Marine Hydrodynamic: Applications to Dynamic Physical Processes*, Elsevier Oceanography Series, *26*, 368 pp., Elsevier, Amsterdam, 1980.

Ray, R. D., and G. D. Egbert, The flux of tidal power across latitude 60°S, *Geophys. Res. Let., 24*, 543-546, 1997.

Robertson, R. A., L. Padman, and G. D. Egbert, Tides in the Weddell Sea, in *Ocean, Ice and Atmosphere: Interactions at the Antarctic Continental Margin, Antarc. Res. Series, 75,* edited by S. S. Jacobs and R. F. Weiss, 341-369 pp., AGU, Washington, D. C., 1998.

Robertson, R. A., L. Padman, and M. D. Levine, Fine structure, microstructure, and vertical mixing processes in the upper ocean in the western Weddell Sea, *J. Geophys. Res., 100,* 18,517-18,535, 1995a.

Robertson, R. A., L. Padman, M. D. Levine, R. D. Muench, and M. G. McPhee, Internal waves in the eastern Weddell Sea during AnzFlux, IAPSO XXI General Assembly, Honolulu, HI, 318, 1995b.

Robinson, I. S., Tidal vorticity and residual circulation, *Deep-Sea Res., 28A,* 195-212, 1981.

Ruddick, B., A practical indicator of the stability of the water column to double-diffusive activity, *Deep Sea Res., 30,* 1105-1107, 1983.

Ruddick, B., and D. Walsh, Observations of the density perturbations which drive thermohaline intrusions, in *Proceedings of the Chapman Conference on Double-Diffusive Convection*, Scottsdale, AZ, 1995.

Rudels, B., The diffusive interface at low stability: The importance of non-linearity and turbulent entrainment, *Tellus Series A 43,* 153-167, 1991.

Schmitt, R. W., Double diffusion in oceanography, *Ann. Rev. Fluid Mech., 26,* 255-285, 1994.

Schwiderski, E. W., Ocean tides, I, Global ocean tidal equations, *Mar. Geod., 3,* 161-217, 1980.

Sherwin, T. J., Evidence of a deep internal tide in the Faeroe-Shetland Channel, in *Tidal Hydrodynamics*, edited by B. B. Parker, 469-488 pp., John Wiley and Sons, New York, 1991.

Sjöberg, B., and A. Stigebrandt, Computations of the geographical distribution of the energy flux to mixing processes via internal tides and the associated vertical circulation in the ocean, *Deep-Sea Res., 39,* 269-291, 1992.

Smith, W. H. F., On the accuracy of digital bathymetric data, *J. Geophys. Res., 98,* 9591-9603, 1993.

Smithson, M. J., Pelagic tidal constants 3, *IAPSO Publication Scientifique No.35,* 191 pp., 1992.

Smithson, M. J., A. V. Robinson, and R. A. Flather, Ocean tides under the Filchner-Ronne Ice Shelf, Antarctica, *Annals of Glaciology, 23,* 217-225, 1996.

Stanton, T. P., L. Padman, and R. A. Robertson, Heat fluxes through the permanent pycnocline in the eastern Weddell Sea, submitted to *J. Geophys. Res.,* 1999.

Stephenson, S. N., C. S. M. Doake, and J. A. C. Horsfall, Tidal flexure of ice shelves measured by tiltmeter, *Nature, 282,* 496-497, 1979.

Stillinger, D. C., K. N. Helland, and C. W. Van Atta, Experiments of the transition of homogeneous turbulence to internal waves in a stratified fluid, *J. Fluid Mech., 131,* 91-122, 1983.

Taylor, J., The fluxes across a diffusive interface at low values of the density ratio, *Deep-Sea Res., 35,* 555-567, 1988.

Tennekes, H., and J. L. Lumley, *A First Course in Turbulence,* 300 pp., MIT Press, Cambridge, MA, 1992.

Thiel, E., A. P. Crary, R. A. Haubrich, and J. C. Behrendt, Gravimetric determination of ocean tide, Weddell and Ross Seas, Antarctica, *J. Geophys. Res., 65,* 629-636, 1960.

Toole, J. M., and D. T. Georgi, On the dynamics and effects of double-diffusively driven intrusions, *Prog. in Oceanogr., 10,* 123-145, 1981.

Turner, J. S., *Buoyancy Effects in Fluids,* 368 pp, Cambridge University Press, New York, 1973.

Vaughan, D. G., Tidal flexure at ice shelf margins, *J. Geophys. Res., 100,* 6213-6224, 1995.

Vaughan, D. G., J. Sievers, C. S. M. Doake, G. Grikurov, H. Hinze, V. S. Pozdeev, H. Sandhäger, H. W. Schenke, A. Solheim, and F. Thyssen, Map of the subglacial and seabed topography; Filchner-Ronne-Schelfeis/Weddell Sea, Antarktis, scale 1:2,000,000, *Institut für Angewandte Geodäsie,* Frankfurt am Main, Germany, 1994.

Viehoff, T., and A. Li, Iceberg observations and estimation of submarine ridges in the western Weddell Sea, *Int. J. Remote Sensing, 16,* 3391-3408, 1995.

Walsh, D., and B. Ruddick, Double-diffusive interleaving: The influence of non-constant diffusivities, *J. Phys. Oceanogr., 25,* 348-358, 1995.

Weppernig, R. P., Schlosser, S. Khatiwala, and R. G. Fairbanks, Isotope data from Ice Station Weddell: Implications for deep water formation in the Weddell Sea, *J. Geophys. Res., 101*, 25,723-25,739, 1996.

Wijesekera, H. W., L. Padman, T. M. Dillon, M. D. Levine, C. A. Paulson, and R. Pinkel, The application of internal wave dissipation models to a region of strong mixing, *J. Phys. Oceanogr., 23*, 269-286, 1993.

Woodgate, R. A., M. Schröder, and S. Østerhus, Moorings from the Filchner Trough and the Ronne Ice Shelf Front: Preliminary results, Filchner-Ronne Ice Shelf Program, Report No. 12, Alfred-Wegener Institute, 1998.

Xing, J., and A. M. Davies, Processes influencing the internal tide, its higher harmonics, and tidally induced mixing on the Malin-Hebrides Shelf, *Prog. in Ocean., 38*, 155-204, 1996.

APPENDICES

Appendix A: Review of Large Discrepancies Between the Model Elevations and the Measurements

The differences for the model elevation estimates greater than a cutoff of 25% will be examined below for each of the constituents. The largest discrepancies occurred with the *Thiel et al.* [1960] observations (77°42'S , 41°8'W). The model overestimates the M_2 and S_2 constituents by 20 cm (46%) and 23 cm (100%), respectively, and underestimates K_1 by 15 cm (-37%) (circled points in Figures 3.7a, 3.7b and 3.7d). The differences at this location are believed to be due to errors in the bathymetry or the location of the ice shelf. Although this location was on an ice shelf when the measurement was obtained, the present estimates do not show an ice shelf at this location. A significant difference was found at *Doake* [1992] site under the Ronne Ice Shelf (77°45'S, 64°30'W). Here the model underpredicts O_1 by 16 cm (-31%) (denoted with a square in Figure 3.7c). This measurement has a short record length (9 days). The short record length (20 days) at the *Lutjeharms et al.* [1985] site (70°12'S, 2°44'W) is probably the cause for the underestimates of 10 cm (-26%) and 13 cm (-36%) for the S_2 and K_1 constituents at this site (denoted with squares in Figures 3.7b and d). The difference of 6 cm (26%) for S_2 at the *Hisdal* [1965] site (70°30'S, 2°32'W) is also due to its short record length of 3 days (denoted with a square in Figure 3.7b). The *Middleton et al.* site (74°28'S,37°39'W) was underestimated by the model by 13 cm (-36%) for the K_1 constituent. This underestimate may be measurement error or a result of continental shelf waves. The continental shelf/slope edge in this area generates continental shelf waves that amplify the diurnal constituents. The overestimate of 6 cm (50%) for K_1 at the *Smithson* [1992] site (60°51'S, 54°43'W) may result from the same mechanism.

Appendix B: Review of Large Discrepancies Between the Model Velocity Ellipse Major Axes and the Measurements

The largest differences occur at the *Foldvik et al.* [1982a] site with a short record length (4.2 days), where all constituents had large differences, 7.7 (351%), 4.2 (248%), 12.8 (152%), and 7.3 cm s^{-1} (47%) for the M_2, S_2, O_1, and K_1 constituents, respectively (denoted with squares in Figures 3.7i-l). Short record lengths may be responsible for the under-predictions at four of the *Levine et al.* [1997] sites (15 days). These points also have squares around them in Figures 3.7j-l. Bathymetric error probably accounts for errors in the S_2, O_1, and K_1 constituents at one of the *Fahrbach et al.* [1992;1994] sites near 71°3'S, 11°45'W. Bathymetric errors are also believed to be the source of the differences at the *Nygaard* [1995] site, where the model underpredicted the diurnal constituents by 4.6 (-55%) and 5.8 cm s^{-1} (-62%) for the O_1 and K_1 constituents, respectively (circled in Figures 3.7k and l). For this site, however, baroclinic effects are another possibility, since the base of the ice shelf is near 200 m depth and some differences were observed between the two meters on this mooring. This location is near the ice shelf edge and in an area where the bathymetry is not well known. One of the three long record length *Fahrbach et al.* [1992;1994] sites located near 71°3'S, 11°45'W shows a difference exceeding 25% for S_2, which has been attributed to bathymetric errors (circled in Figure 3.7j). However, measurement errors are also a possible cause since the differences are less than the uncertainties for two of the three locations. Bathymetric errors are the probable source for the differences in M_2, O_1, and K_1 at the *Middleton et al.* [1982] site near the edge of the Filchner Depression (74°40'S, 33°56'W) (circled in Figures 3.7i, k, and l) and the *Fahrbach et al.* [1992, 1994] site in a region of complicated bathymetry (63°30'S, 52°6'W) (circled in Figure 3.7k).

Of the remaining differences, the largest for M_2 occur for a group of sites near 74°S (the group of points below the uncertainty band in Figure 3.7i). The critical latitude, where the M_2 tidal frequency equals the inertial frequency, occurs at 74°28'30' S. Two of the four *Middleton et al.* [1987, 1982] and the *Foldvik et al.* [1990] locations near this critical latitude show differences greater than 2.0 cm s^{-1} (ranging from 40 to 111%). These discrepancies between the model predictions and the measurements may be a result

of effects of the critical latitude. *Furevik and Foldvik* [1996] found that both the benthic boundary layer and water column turbulence were significantly increased near the critical latitude. These changes are neglected in the model where the drag parameterization is independent of the latitude and tidal frequency.

Five other points for the diurnal constituents lie significantly below the uncertainty band (Figures 3.7k and l). These are the *Middleton et al.* [1982, 1987] and *Foldvik et al.* [1990] measurements near 74°S and 37°-39°W. These discrepancies, along with those for four *Fahrbach* [1992, 1994] observations near 71°3'S, 11°45'W and a *Fahrbach et al.* [1992, 1994] observation further east on the continental shelf (70°26'S, 8°18'W), are believed to be associated with inadequate model representation of continental shelf waves.